

2017

Cross-Scale Energy Transport and Kinetic Wave Properties Associated with Kelvin-Helmholtz Instability

Thomas W. Moore

Follow this and additional works at: <https://commons.erau.edu/edt>



Part of the [Plasma and Beam Physics Commons](#)

Scholarly Commons Citation

Moore, Thomas W., "Cross-Scale Energy Transport and Kinetic Wave Properties Associated with Kelvin-Helmholtz Instability" (2017). *Dissertations and Theses*. 317.
<https://commons.erau.edu/edt/317>

This Dissertation - Open Access is brought to you for free and open access by Scholarly Commons. It has been accepted for inclusion in Dissertations and Theses by an authorized administrator of Scholarly Commons. For more information, please contact commons@erau.edu.

**Cross-Scale Energy Transport and Kinetic Wave Properties Associated
with Kelvin-Helmholtz Instability**

by

Thomas W. Moore

A Thesis Submitted to the Physical Sciences Department
in Partial Fulfillment of the Requirements
for the Degree of

DOCTOR OF PHILOSOPHY

(Engineering Physics)

Embry-Riddle Aeronautical University

Daytona Beach, FL 32114

2017

Copyright by Thomas W. Moore 2017

All Rights Reserved

Cross-Scale Energy Transport and Kinetic Wave Properties Associated with
Kelvin-Helmholtz Instability

By


Thomas W. Moore

This Dissertation was prepared under the direction of the candidate's Dissertation
Committee Chair, Dr. Katariina Nykyri and has been approved by the members of his
dissertation committee. It was submitted to the College of Arts and Sciences and was
accepted in partial fulfillment of the requirements for the


Degree of
Doctor of Philosophy in Engineering Physics



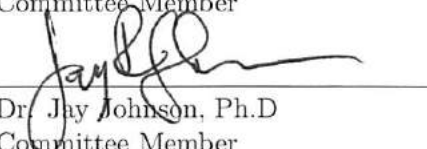
Dr. Katariina Nykyri, Ph.D
Committee Chair



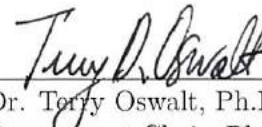
Dr. Anatoly Streltsov, Ph.D
Committee Member



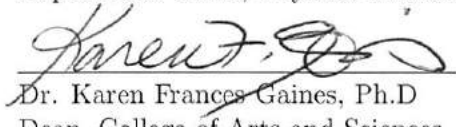
Dr. Matthew Zettergren, Ph.D
Committee Member



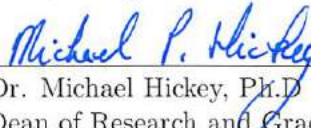
Dr. Jay Johnson, Ph.D
Committee Member



Dr. Terry Oswald, Ph.D
Department Chair, Physical Sciences



Dr. Karen Frances Gaines, Ph.D
Dean, College of Arts and Sciences



Dr. Michael Hickey, Ph.D
Dean of Research and Graduate Studies

April 10th 2017

Date

Acknowledgments

The research in this dissertation was supported by National Science Foundation Grants 0847120 and 1502774. I would like to acknowledge the work performed by the Cluster FGM, EFW, CIS and PEACE instrument teams as well as the Cluster Science Archive, Cluster Active Archive and OMNIWeb for the use of their data. I would also like to acknowledge the International Space Science Institute for sponsoring me as a young scientist to attend and participate in international working groups. Special thanks to Dr. Andrew Dimmock for his collaborative contributions, mentorship and friendship. Special thanks to Emily Dougal for her loving support, friendship and most of all for saying yes.

Most of all, I would like to thank my advisor, Dr. Katariina Nykyri, for taking me on as her student, sharing her passion for research, and greatly supporting my telecommute. Without her, I would not have had a graduate experience so full of learning, accomplishment and opportunity.

Contents

1	Introduction	3
1.1	The Sun and Solar Wind	4
1.2	The Near-Earth System	7
1.2.1	Magnetosheath	7
1.2.2	Magnetosphere	9
1.2.3	Low-Latitude Boundary Layer	14
1.3	Physical Processes at the Magnetopause	15
1.3.1	Magnetic Reconnection	16
1.3.2	Kelvin-Helmholtz Instability	22
1.3.3	Plasma Wave Modes	25
1.4	Processes Associated with KHI	33
1.4.1	Reconnection inside Kelvin-Helmholtz Instability	34
1.4.2	Mode Conversion	35
1.5	Dawn-Dusk Asymmetries	36
1.5.1	Asymmetries in the Source (Magnetosheath) Plasma	36
1.5.2	Asymmetric Evolution of Magnetopause Processes	40
1.6	Motivation	42
2	Methodology	45
2.1	Identifying KH Signatures in the LLBL	45
2.2	Boundary Normal Coordinate System and Variance Analysis	47
2.3	Kinetic Theory	51
2.3.1	WHAMP	55
2.3.2	MHD Physics	60
2.4	Local 2-D MHD Simulations	64

2.5	Identifying High-Frequency Waves	68
2.6	Experimental Dispersion Relation	69
2.7	Statistical Study	70
2.7.1	Data Binning Process	70
2.7.2	Ion-scale MVAB Wave Intervals	72
2.8	Ellipticity Calculation	74
3	Case Study	84
3.1	Introduction	84
3.2	Cross-Scale Observations	88
3.3	Cold Component Ion Heating	99
3.4	KHI Observations and Simulations	102
3.5	Wave Analysis	106
4	Statistical Study	116
4.1	Introduction	116
4.2	Broad Band Statistics	120
4.2.1	Degree of Polarization	120
4.2.2	Magnetic Compressibility	120
4.3	Ion-scale Wave Intervals	122
4.3.1	Mean Total Magnetic Wave Power, P_{tot}	123
4.3.2	Total Integrated Poynting Flux	125
4.3.3	Polarization Dispersion: FMW	125
4.3.4	Mean $\delta E/\delta B$ Polarization Dispersion	128
4.3.5	Plasma Parameters	128
4.4	Discussion	135
4.4.1	Broad Band Statistics	136
4.4.2	Ion-Scale Wave Intervals	137
4.5	Effects of Solar Wind Speed on Plasma Parameters	141
4.6	Doppler Shift Effects	148
5	Summary	153
5.1	Case Study	153
5.2	Statistical Study	154

6 Discussion and Future Work	157
A Appendix	160
A.1 Binning and Sorting Statistical Figures and Summary Plots	160
A.1.1 KHI Events	160
A.1.2 Non-KHI Events	174
A.2 Extreme Doppler Shift Effects	191

Abstract

In the Earth's magnetosphere, the magnetotail plasma sheet ions are much hotter than in the shocked solar wind. On the dawn-sector, the cold-component ions are more abundant and hotter by 30-40 percent when compared to the dusk sector. Recent statistical studies of the flank magnetopause and magnetosheath have shown that the level of temperature asymmetry of the magnetosheath is unable to account for this (Dimmock et al., 2015), so additional physical mechanisms must be at play, either at the magnetopause or plasma sheet, that contribute to this asymmetry. This thesis focuses on ion heating across the magnetopause boundary separating the magnetosheath and the magnetospheric plasmas, which is driven by mechanisms operating on fluid, ion and electron scales. One of the pending problems in collisionless astrophysical plasmas is to understand the plasma heating and transport across three fundamental scales: fluid, ion and electron. Presented here is evidence of the energy transport between the fluid and ion scales: energy is provided by a velocity shear at the magnetopause generating fluid-scale Kelvin-Helmholtz Instability and their rolled-up vortices, where an ion-scale fast magnetosonic wave packet located in the center of a Kelvin-Helmholtz vortex has sufficient energy to account for observed cold-component ion heating. In addition, a statistical analysis is performed on the ion-scale wave properties in the three main plasma regimes common to flank magnetopause boundary crossings when the boundary is unstable to KHI: hot and tenuous magnetospheric, cold and dense magnetosheath and mixed (H. Hasegawa, Fujimoto, Phan, et al., 2004). The statistical analysis shows that during KH events there is enhanced non-adiabatic heating calculated during ion scale wave intervals when compared to non-KH events. This suggests that during KH events there is more free energy for ion-scale wave generation, which in turn can heat ions more effectively when compared to cases when KH waves are absent. This

may contribute to the dawn favored temperature asymmetry of the plasma sheet, because KH waves are statistically more abundant on the dawn sector. Furthermore, the present findings have universal consequences in understanding cross-scale energy transport from fluid to ion-scales, applicable to a variety of environments experiencing velocity shears with comparable plasma regimes.

Chapter 1

Introduction

The face of the sun is not without expression, but it tells us precious little of what is in its heart. – Armin J. Deutsch, Scientific American magazine, November 1948

The solar wind is a supermagnetosonic magnetized plasma streaming far into the heliosphere. Although cooling as it flows, it is rapidly heated upon encountering planetary obstacles. At Earth, this interaction forms the magnetosphere and its sub-regions. The goal of this present research is to explore particle heating across the boundary separating the shocked solar wind and magnetospheric plasma, which is driven by mechanisms operating on fluid, ion and electron scales Moore et al. (2016). To accomplish this, the following thesis will be structured as follows: (1) Introduction of the Sun, solar wind, near-Earth space system, magnetopause processes and associated asymmetries; (2) Formulation and derivation of the tools and physics used to conduct this research; (3) present the results of the case study and statistical study; and (4) summarize the results by discussing the relevance, impact and future work.

1.1 The Sun and Solar Wind

As its name might suggest, the “solar” system is dominated by processes at the Sun. The Earth and other celestial bodies are coupled to the Sun by fields and the interplanetary medium, plasma – no, space is not a vacuum. Sitting at the center of the heliosphere, the Sun is the powerhouse of the solar system. Fueled by fusion reactions, energy generated at its core is delivered to its surface via radiative diffusion and convection. Energy then leaves the Sun as radiation from the visible photosphere and via solar wind from the outermost layer, the corona. At around 1 million Kelvin, the solar corona is in a state of steady expansion (Parker, 1958). Because it is not in hydrostatic equilibrium with the local interstellar medium (LISM), the corona “evaporates” as a steady state release of plasma into the heliosphere known as the solar wind.

The solar wind comprises magnetic streams of hot tenuous plasma, and cools as it expands away from the corona (Bittencourt, 2004). Intermittent bouts of coronal mass ejections (CMEs) also contribute to the solar wind. Although the solar wind has a radial trajectory, Archimedean spirals in IMF are formed due to the Sun’s rotation. The solar wind is a well-behaved MHD plasma (more on this in § 2.3.2) and as such, it carries portions of the Sun’s magnetic field into the heliosphere, forming the IMF. The IMF is predominantly comprised of open field lines, which is a convenient description for field lines are not locally “closed”. The Archimedean spirals of solar wind carrying IMF intercept the Earth’s magnetic field at a 45° angle in the orbital plane. However, this is not always the case; there exists a differential rotation in the Sun (the poles maintain a smaller rotational period than the equator) causing the Sun’s magnetic fields to become twisted. This twisting of field lines along with disturbances from CMEs can cause relatively small deformations in the standard IMF configuration resulting in a broad spectrum of IMF orientations intercepted by Earth’s orbit. IMF orientation is often categorized with respect to Earth’s

bow shock geometry – a region upstream of Earth’s magnetic field. The relative motion of the Earth into the solar wind is faster than the speed at which information travels (e.g the magnetosonic speed) in the local medium (the solar wind plasma). Because the solar wind is super-magnetosonic, information about the solar wind cannot reach the magnetopause before the solar wind plasma, and as a result a standing shock wave is formed. There are five main IMF orientations mentioned in the literature: Parker-Spiral (PS), Ortho-Parker-Spiral (OPS), radial, northward and southward. The IMF can never be purely in any one of these directions, rather it typically assumes a superposition of one two or more orientations. Common practice is to denote the IMF orientation with which configuration the IMF most strongly aligns with; for example strongly northward IMF would be used to designate an IMF orientation that has a mostly northward component.

The preceding nomenclature is best understood in the context of the Geocentric Solar Magnetic (GSM) coordinate system. Let us first introduce the Geocentric Solar Ecliptic (GSE) coordinate system, in which \hat{x}_{GSE} is pointing sunward in the Sun-Earth line, \hat{z}_{GSE} points in the direction perpendicular to the ecliptic plane and \hat{y}_{GSE} completes the system (Russell, 1971). In the GSM coordinate system $\hat{x}_{GSM} = \hat{x}_{GSE}$, \hat{z}_{GSM} is in the direction of Earth’s magnetic dipole axis (positive towards geographic north), and \hat{y}_{GSM} completes the system (Russell, 1971). When the IMF is exactly in PS orientation it makes a 45° angle between the sun-Earth line (x -axis in GSE and GSM coordinates); from segment I of Figure 1.1 the IMF is parallel to the shock normal at the dawn flank. Because there is small variation about the about exact parallel alignment, the term ”quasi-parallel” is preferred. Similarly, in OPS orientation, the IMF is ”quasi-perpendicular” to the dawn flank shock normal (see segment II of Figure 1.1).

For strongly northward (southward) IMF, the magnetic field lies predominantly in the positive (negative) z direction. Radial IMF orientation has a magnetic field predominantly in the x direction. IMF orientation is stressed in this chapter because it has been shown

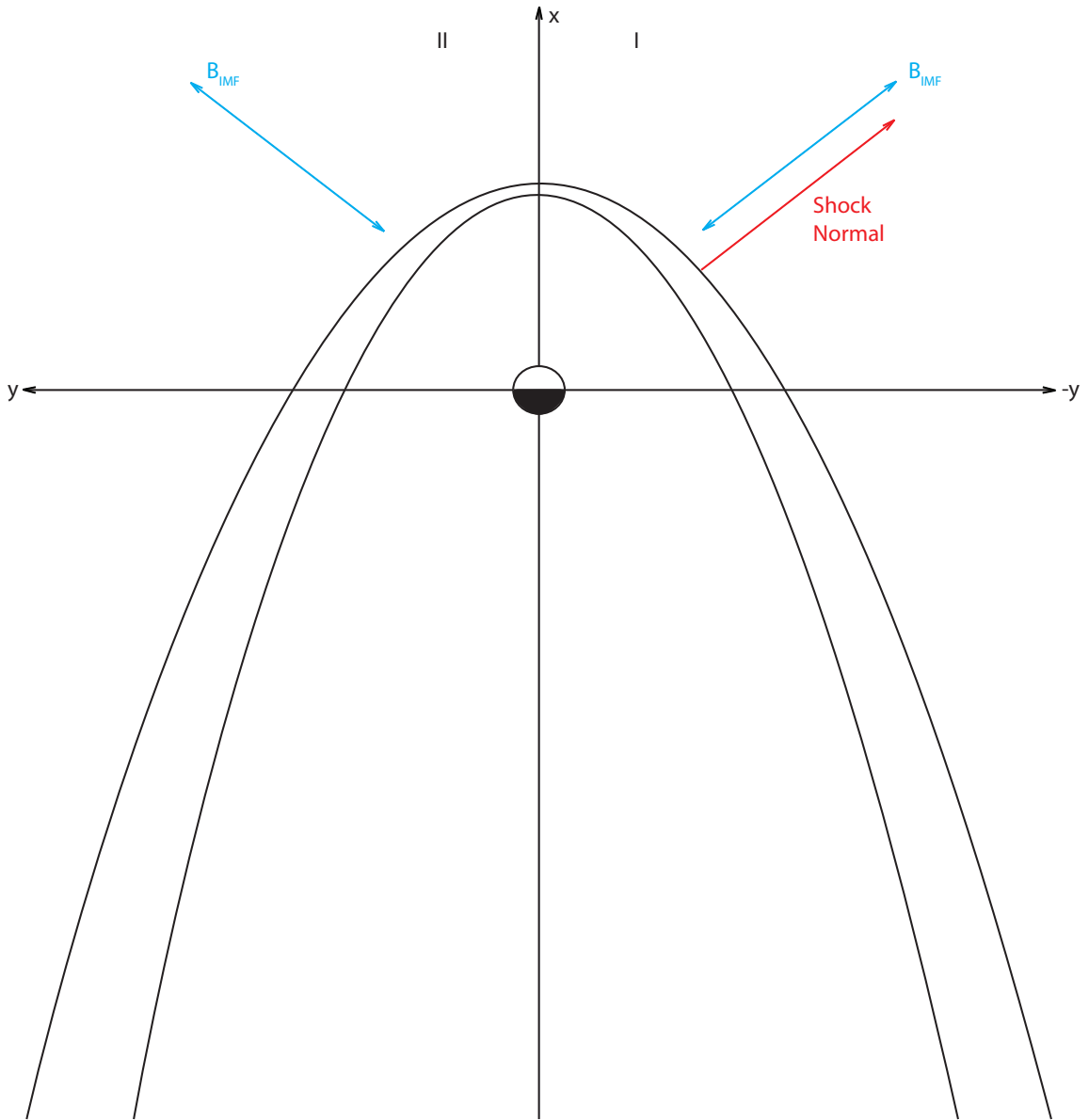


Figure 1.1: IMF orientation relative to shock normal in the x-y plane (GSE) for PS (segment I) and OPS (segment II).

to have a crucial effect on the onset of the two major physical mechanisms, the Kelvin-Helmholtz instability and magnetic reconnection, occurring at Earth's magnetopause (see § 1.3).

1.2 The Near-Earth System

Radially inward from the bow shock is the magnetosheath which consists of shocked solar wind plasma, followed by the Earth's magnetosphere – separated from the magnetosheath by the magnetopause (see Figure 1.2). For the purpose of this thesis, we will focus on the sections pertinent to the mechanisms discussed in § 1.3.

Figure 1.2 depicts the entirety of Earth's magnetosphere including the sheath (magnetosheath) and bow shock.

1.2.1 Magnetosheath

From Figure 1.2, the magnetosheath is located between the magnetopause (the farthest extent of Earth's magnetic field) and the bow shock.

Air Force Pioneer I was the first spacecraft to observe the magnetosheath, first launched in 1958 to explore plasma regions between the Earth and Moon (Sonett et al., 1960), shortly followed by IMP 1 (Ness & Wilcox, 1965), Ogo 1 (Holzer et al., 1966), Mariner 4 (Siscoe et al., 1967) and IMP 2 (Fairfield, 1967).

Plasma in the magnetosheath is cold (hotter than solar wind, colder than magnetosphere) and dense, with typical ion number densities of about 10 cm^{-3} , and temperatures of a few million Kelvin. The cold dense plasma in the magnetosheath is supplied by shocked solar wind plasma, where solar wind plasma undergoes compression and heating at the shock, as well as a decrease in the flow speed following the continuity equation. This shocked solar

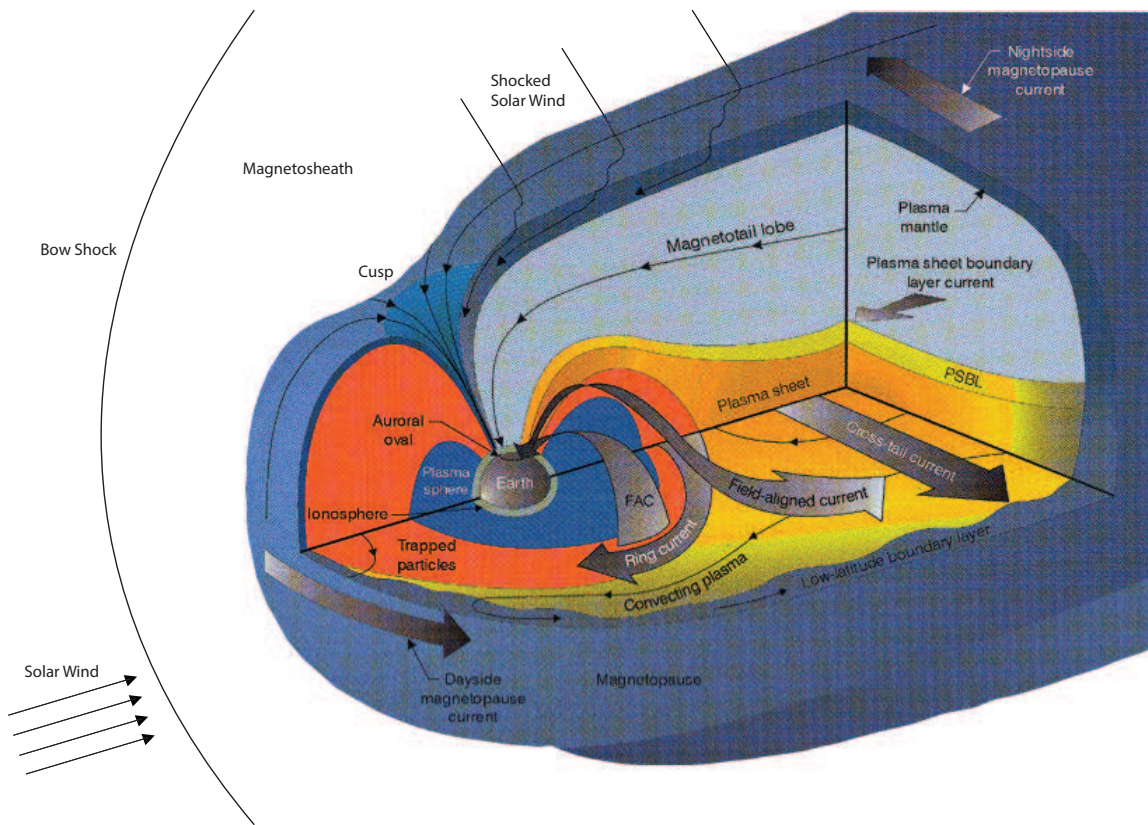


Figure 1.2: The Earth's magnetosphere, magnetosheath and bow shock. Image courtesy of Imperial College London (London, 2009).

wind plasma populating the magnetosheath carries with it the IMF, however the component of the magnetic field tangential to the magnetopause is increased across the shock due to a “draping effect”. The bow shock is technically speaking, a fast-shock, because the upstream solar wind speed is super magnetosonic; magnetosonic waves are commonly referred to as fast-mode waves. A fast-shock mode causes the downstream magnetic field to bend away from the shock normal (Kivelson & Russell, 1995) (Please see Figure 1.3); kinetic energy is converted to magnetic and thermal energy, increasing the total downstream magnetic field strength.

1.2.2 Magnetosphere

The magnetosphere, lying just within the magnetosheath separated by current sheets, is a dynamic system influenced by solar wind input. As briefly mentioned in § 1.2.1, the magnetopause represents the location of the farthest extent of Earth’s magnetic field, a boundary separating magnetosheath and magnetospheric plasmas. It’s location is governed by a pressure balance between the magnetosphere and shocked solar wind plasmas. The stand-off distance of the magnetopause is defined by the radial distance from Earth at which the total pressure of the magnetospheric plasma (dominated by magnetic pressure) and the total pressure of the magnetosheath plasma (dominated by the dynamic pressure at the subsolar point) are in equilibrium. The stand-off distance is dynamic and varies with changing solar wind conditions.

Approximately 99% of Earth’s magnetic field is generated by a hydromagnetic dynamo in the outer core (2900 - 5100 *km* depth) (Juusola, 2015). Other influences include magnetized rock in the lithosphere (< 50 *km* depth) and solar activity driving currents in the ionosphere (Juusola, 2015). Collectively this forms a complex magnetic field structure.

Assuming a superposition of fields created by multipole magnets, multipole expansion

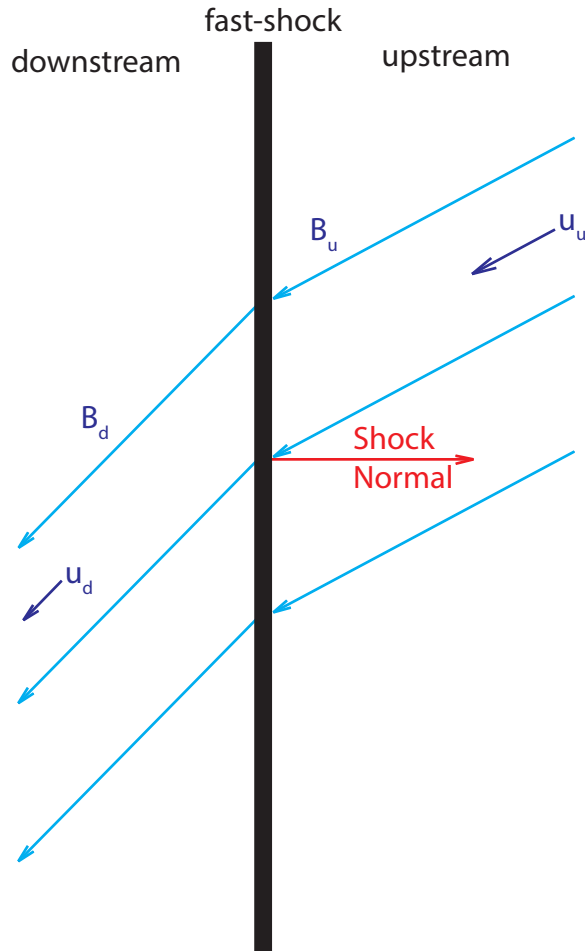


Figure 1.3: Fast-shock mode. The magnetic field lines bend away from the shock normal on the downstream of the shock (left side).

is used to describe Earth’s complex magnetic field structure (Juusola, 2015). From the first order approximation is the dipole field (Juusola, 2015). The n^{th} order approximation includes the dipole field $n = 1$, anomalous effects $2 \leq n < 14$ and crustal anomalies $n \leq 14$ (Juusola, 2015). Because the dipole nature of Earth’s magnetic field is the main contributor, it is often generalized as dipole-like.

The dipole-like nature of the magnetic field diverges near the dayside-nightside terminator, where “open” field lines trail behind the Earth. The term open is a commonly used expression in space physics however it is a misnomer as the existence of magnetic monopoles have not been observed (but still theoretically possible) and all field lines must close, so “locally open” is more appropriate. Due to the interaction of the solar wind at the dayside magnetopause, magnetic reconnection can occur, breaking Earth’s field and connecting it with the solar wind IMF. These reconnected, or open field lines (with one footprint in the ionosphere, and the other in the solar wind IMF) are then transported tailward by the solar wind to the tail of the magnetosphere, where they can reconnect again forming newly closed (to Earth’s ionosphere) field lines which are then transported back to the dayside in a process known as the Dungey Cycle (Dungey, 1961; University, 2017). Footprints of the open and closed field lines originate in the ionosphere, forming the magnetic cusps. The open field lines form the northern and southern tail lobes and nestled between them is the plasma sheet, comprising closed field lines.

The plasma sheet, lying near the equatorial plane, is located just inside the magnetopause separated by the Low-Latitude Boundary Layer (LLBL) and separated from the plasmasphere by the plasmapause. This region is populated by hot tenuous plasma (Baumjohann et al., 1989) which has a much lower ion number density ($\approx 1 \text{ cm}^{-3}$) and approximately 50 times hotter than its neighboring magnetosheath plasma. However, under extended periods of northward IMF the plasma sheet has been shown to become cold and dense (Terasawa et al., 1997; Fujimoto et al., 1998; Stenuit et al., 2002; Øieroset et al.,

2005).

In a statistical survey of GEOTAIL observations in the near-Earth plasma sheet ($-15 R_E < X_{GSM} < -50 R_E$), Terasawa et al. (1997) showed that the plasma sheet became “significantly” colder and denser. Terasawa et al. (1997) suggested that “cold” ions of MSH origin were being transported across the magnetopause because colder and denser ions were observed near the dawn and dusk flanks compared to the central region of the plasma sheet.

In a later study, ion temperatures and number densities in the equatorial plasma sheet – inferred from ionospheric data using the Defense Meteorological Satellite Program (DMSP) – were analyzed on much smaller spatial scales as a function of B_Z ; it was shown that these plasma properties differ from northward to southward IMF (Wing & Newell, 2002) (see Figure 1.4). Even though cold and dense ions were shown to be present under both northward and southward IMF, the dusk flank ion number density profiles suggest that far more MSH ions enter from the dusk LLBL under northward IMF (Wing & Newell, 2002) (see Panel (b) of Figure 1.4). The plasma sheet temperatures were also shown to be much hotter under Southward IMF. Periods of southward IMF solar wind are known to trigger substorms (McPherron, 1991), which have been associated with ion energization in the plasma sheet (Hones et al., 1976).

Geotail crossings of the flank LLBL have shown evidence of a “stagnant” ion population inside the plasma sheet at the dawn and dusk flanks (Fujimoto et al., 1998); omnidirectional ion spectrograms show that the stagnant ion population is composed of hot ($> 1 keV$) and cold ($< 1 keV$) ions at the dusk flank, referred to as a “mixing effect”. In fact, there exist two distinct ion populations in the plasma sheet, hot component ions of magnetospheric origin and cold component ions of magnetosheath origin (H. Hasegawa et al., 2003; H. Hasegawa, Fujimoto, Phan, et al., 2004). Furthermore, omnidirectional ion spectrograms from Geotail show a distinct dawn-dusk asymmetry among the dense ions in

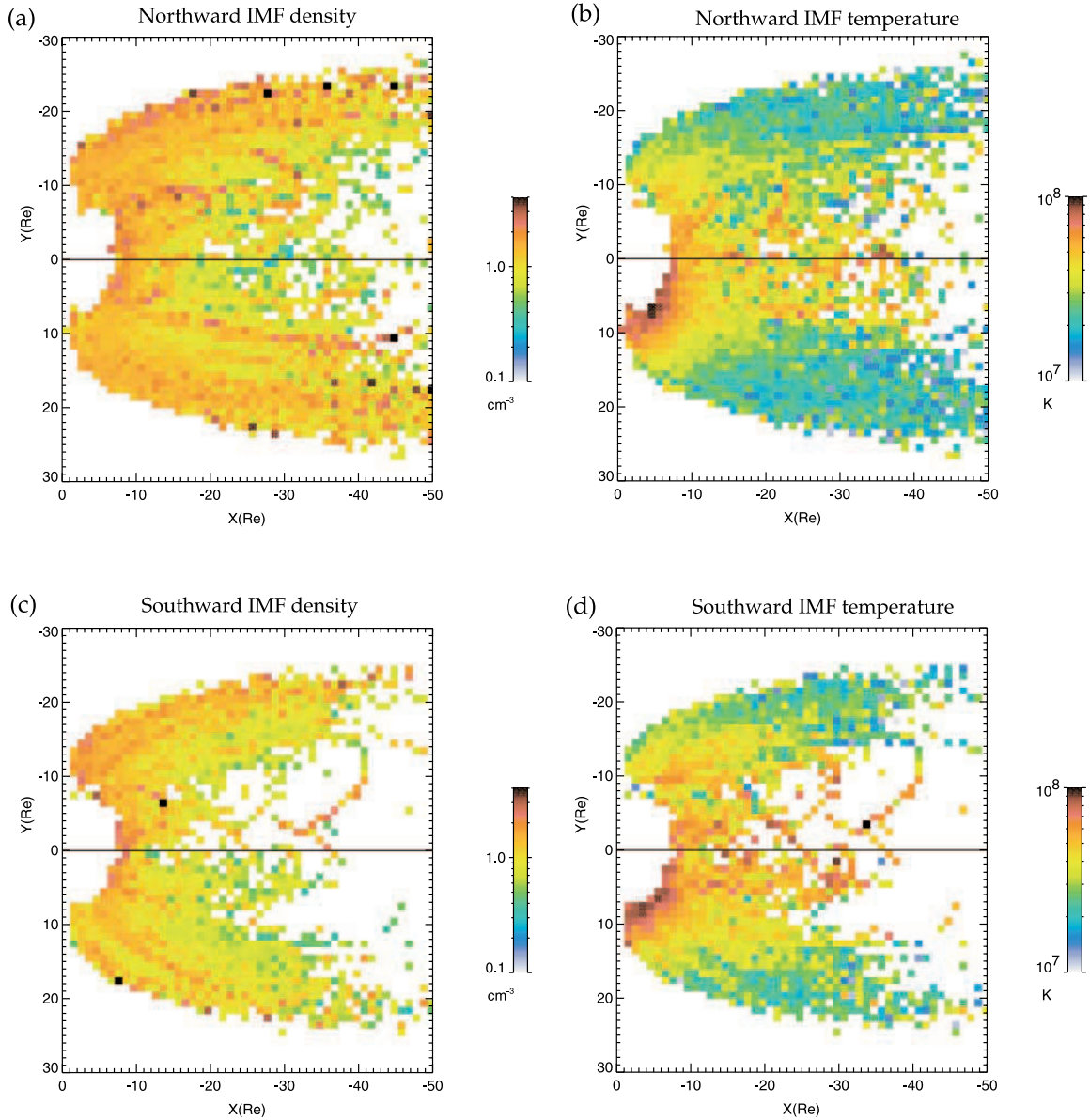


Figure 1.4: B_Z IMF dependance on plasma sheet ion number density (Left Panels) and ion temperature (Right Panels) for northward (Top Panels) and southward (Bottom Panels) IMF (Wing & Newell, 2002).

the mixing region where these dense ions at the dawn side have a higher average energy (H. Hasegawa et al., 2003). Using DMSP ionospheric data, inferred plasma sheet ion temperatures show a hotter cold component population on the dawn flank compared to the dusk flank (Wing et al., 2005).

In a case study combining data from the solar wind (Ace and Wind spacecraft) and plasma sheet (Geotail spacecraft), Wing et al. (2006) calculated the timescale for which the plasma sheet becomes cold and dense. Approximately a few hours after the solar wind IMF turned northward, ion temperatures dropped below 2 keV and the ion densities were observed to raise up to 1 cm^{-3} after ≈ 8 hours; these observations were consistent with their previous statistical study (Wing et al., 2005).

1.2.3 Low-Latitude Boundary Layer

Eastman & Hones (1979) confirmed the existence of a boundary layer at the dayside magnetosphere with observations from the IMP 6 spacecraft. IMP 6 observations of the dawn and dusk flanks of the dayside magnetosphere unveiled a region wherein the local plasma parameters (e.g. ion number density, bulk flow and energy) and magnetic field are mixed between that typical of the magnetosheath and magnetosphere. For all IMP 6 crossings of the magnetopause, the boundary layer was "nearly always present at all latitudes and longitudes". The boundary layer thickness ranges from about 100 km at the dayside magnetosphere to several Earth radii tailward of the dawn-dusk terminator (Eastman & Hones, 1979). This boundary layer is known today as the LLBL.

The low-latitude boundary layer (LLBL) is a region of mixed plasma located in the low latitude magnetospheric flanks. The LLBL begins as a very thin layer at the dayside magnetosphere, expanding tailward and is most pronounced in the equatorial plane. Formation of the LLBL is a result of double high-latitude reconnection (Lavraud et al., 2005;

Li et al., 2005), reconnection in Kelvin-Helmholtz (KH) vortices (Nykyri & Otto, 2001), ion diffusion in KH vortices (Fujimoto & Terasawa, 1994, 1995) and Kinetic Alfvén waves (KAW) (Johnson & Cheng, 1997; Johnson et al., 2001) which are discussed in greater detail in § 1.3. These processes are responsible for mass and energy transport across the magnetopause boundary, capable of injecting cold and dense magnetosheath plasma into the magnetosphere. As a result, the LLBL is comprised of plasma with mixed magnetosheath and magnetospheric typical number densities and temperatures. The LLBL acts as a buffer between the magnetopause and the plasma sheet such that the processes that occur at the magnetopause are coupled to the plasma sheet.

1.3 Physical Processes at the Magnetopause

The two main processes at the magnetopause that can produce the transport of mass, momentum and energy are magnetic reconnection and viscous interaction. Axford & Hines (1961) first proposed that a “viscous-like” interaction between Earth’s outer magnetosphere and the solar wind drives convection in the magnetosphere, a process that could also account for the auroral “spiral” motion. In a later study using Explorer 18 data to analyze the magnetopause stability to KHI, Boller & Stolov (1973) claimed that KHI might be the “viscous interaction” proposed by Axford & Hines (1961). In the same year that Axford & Hines (1961) published their convection model, Dungey (1961) proposed that ionospheric convection was driven by a cycle of magnetic reconnection.

As discussed mentioned briefly in § 1.2.3, magnetic reconnection, KHI and KAWs play an important role in the formation of the LLBL. In this section, we will discuss the two main physical processes which occur at the magnetopause that can produce the transport of mass, momentum and energy: magnetic reconnection and KHI, as well as offer a brief overview of important plasma wave modes and their basic properties.

1.3.1 Magnetic Reconnection

Theory

Magnetic reconnection occurs in a plasma when anti-parallel magnetic field components (carried by charged particles) converge to very small spatial scales, where diffusion can occur. The ion and electron diffusion regions are defined as the areas where ions and electrons become decoupled from the magnetic field lines, respectively. The decoupling of charged particles from the magnetic field lines is a clear violation of the “frozen-in” condition (i.e. Alfvén’s Frozen-in Theorem). For an ideal MHD plasma, that is a fluid with an infinite magnetic conductivity, the magnetic field lines are frozen into the fluid (Alfvén, 1942, 1943).

From an ideal MHD approximation, the change in magnetic field is governed by this frozen-in condition, $\mathbf{E} + (\mathbf{v} \times \mathbf{B}) = \mathbf{0}$, and thus magnetic reconnection is not possible from a theoretical standpoint. However, for a resistive fluid (i.e. resistive MHD), the plasma is not infinitely conductive and thus Faraday’s Equation retains its diffusive term (see § 2.3.2 for a more in-depth description).

$$\nabla \times \mathbf{B} = \mu_0 \mathbf{J} \tag{1.1}$$

$$\nabla \times \mathbf{E} = -\frac{\partial \mathbf{B}}{\partial t} \tag{1.2}$$

$$\mathbf{J} = \sigma(\mathbf{E} + \mathbf{v} \times \mathbf{B}) \tag{1.3}$$

From Ampere’s Law (Equation 1.1), Faraday’s Law (Equation 1.2 and the resistive Ohm’s Law (Equation 1.3) the resistive induction equation becomes

$$\frac{\partial \mathbf{B}}{\partial t} = \nabla \times (\mathbf{v} \times \mathbf{B}) - \eta \nabla^2 \mathbf{B} \quad (1.4)$$

Where η is the resistivity such that it is inversely proportional to the conductivity $\eta \equiv \frac{1}{\sigma \mu_0}$. The first term on the right hand side of Equation 1.4 is the frozen-in term and the second term is the diffusion term. It is useful to approximate these quantities in terms of length scales. Let $\nabla \approx 1/l_0$, so that the ratio of the frozen-in to diffusion term is given by

$$R_M = \frac{\frac{1}{l_0} v B}{\eta \frac{1}{l_0^2} B} = \frac{l_0 v}{\eta} = \sigma \mu_0 l_0 v \quad (1.5)$$

Equation 1.5 is the Reynold's number (i.e. the Lundquist number). This plasma parameter describes the magnetic field "slippage" – how coupled the field is to the fluid. For typical space plasmas the Reynold's number is quite large, and for magnetic reconnection to operate $R \lesssim 1$. However, taking into account other terms from the full form of the Generalized Ohm's law can break the "frozen-in" condition. The Generalized Ohm's law is shown in Equation 1.6 below and is derived in § 2.3.2.

Generalized Ohm's Law (MHD)

$$\mathbf{E} + \mathbf{u} \times \mathbf{B} = \frac{m_e m_i}{e^2 \rho} \left[\frac{\partial \mathbf{j}}{\partial t} + \nabla \cdot (\mathbf{u} \mathbf{j} + \mathbf{j} \mathbf{u}) \right] - \frac{M}{e \rho} \nabla \cdot \underline{\underline{\mathbf{P}}}_e + \frac{m_i}{e \rho} \mathbf{j} \times \mathbf{B} + \eta \mathbf{j} \quad (1.6)$$

On the right hand side of Equation 1.6, the first term is the electron inertial term, the second term is the electron pressure term, the third term is the Hall term and the fourth term is the resistivity. These terms are designated by the scale size at which they dominate: the electron inertial term is scaled by the square of the electron inertial length (c^2/ω_{pe}^2); the electron pressure term ion and the Hall term are scaled by the inertial length (c/ω_{pi}); and the resistivity term is scaled by the inverse of the Lundquist number. The Lundquist number is a special case of the magnetic Reynold's number when the Alfvén velocity is the

typical velocity scale of the system. As an example in the MHD approximation, when the anti-parallel components of the field lines converge to the ion inertial scale lengths, the electron pressure and Hall terms have a large relative weight to the rest of the terms from the Generalized Ohm's law. Therefore at smaller length scales, the "frozen-in" condition can break down, however only the electron inertial term, off diagonal components of the electron pressure tensor and resistivity term can break the "frozen-in" condition. Although the Hall term cannot break the "frozen-in" condition, inclusion of the Hall term along side the resistivity or other terms which can break the "frozen-in" condition in MHD models makes fast reconnection possible (e.g. comparable to Hybrid and full kinetic models) (Birn et al., 2001). These small length scales can form naturally due to solar wind interaction with the magnetosphere – the curl in the magnetic field between resulting from the close proximity of the IMF and Earth's geomagnetic field create thin current sheets which form the magnetopause.

Reconnection is known to occur at the dayside magnetopause, in the magnetotail, in the cusps and in the LLBL. At the magnetopause, it is useful to consider magnetic reconnection in two-dimensional (2D) space, with a separatrix separating the magnetic connection topology (see Figure 1.5). From Figure 1.5, the separatrix divides the original connection topology from the newly connected, or reconnected topology. Visually, the separatrix also defines four quadrants: two inflow and two out flow regions, as well as an x-line at the center. The inflow region marks the influx of plasma carrying fields from the original connectivity. Plasma velocity in the inflow region will have a considerable perpendicular component with respect to the magnetic field. Magnetic reconnection can release large amounts of energy as energy stored in the magnetic field is released as kinetic energy, thermal energy and etc. The newly connected field lines act as a rubber band, expelling plasma in the outflow region in field aligned jets as magnetic tension is released.

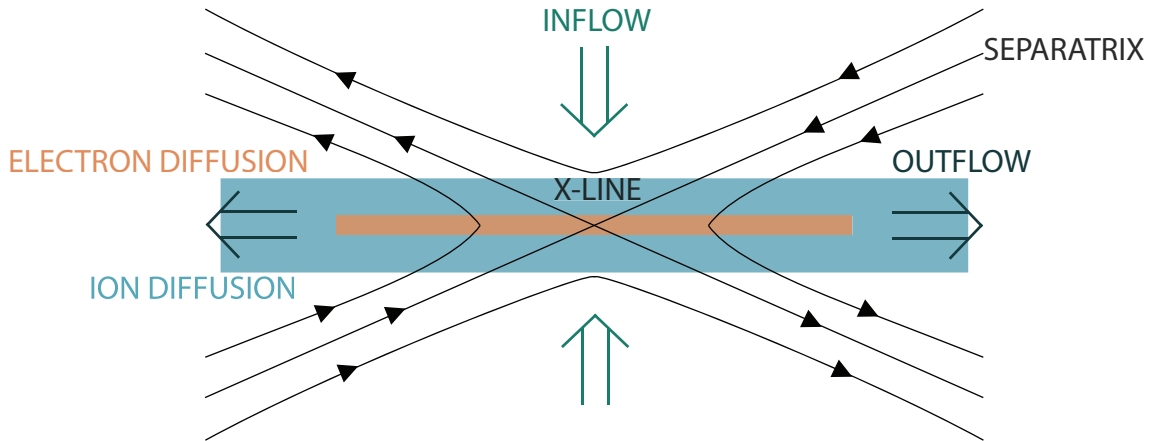


Figure 1.5: Illustration of magnetic reconnection.

Observations

Dungey (1961) first proposed that plasma convection was driven by a cycle of magnetic reconnection at the dayside and nightside magnetosphere. Under southward IMF, magnetic reconnection at the dayside magnetopause between the Earth's geomagnetic field and the solar wind IMF can occur. In the context of Figure 1.5, the inflow regions consist of the original shocked solar wind IMF in the magnetosheath and the original magnetospheric magnetic topologies. The outflow regions are the newly connected magnetic topologies containing the magnetosheath plasma: field lines with one foot connected to the Earth's poles and the other connected to the solar wind. This outflow plasma and its associated magnetic field are carried tailward over the polar regions to magnetotail. As these magnetic field lines accumulate in the magnetotail, anti-parallel field components from the northern and southern hemispheres converge to length scales where magnetic reconnection can occur, forming two sets of magnetic topologies: (1) magnetic field lines that have both feet attached to the solar wind IMF and (2) magnetic field lines that have both feet in the Earth's magnetic poles, one in the north and the other in the south. The plasma connected to the solar wind IMF is ejected tailward. Magnetic tension in the newly polar connected field carries

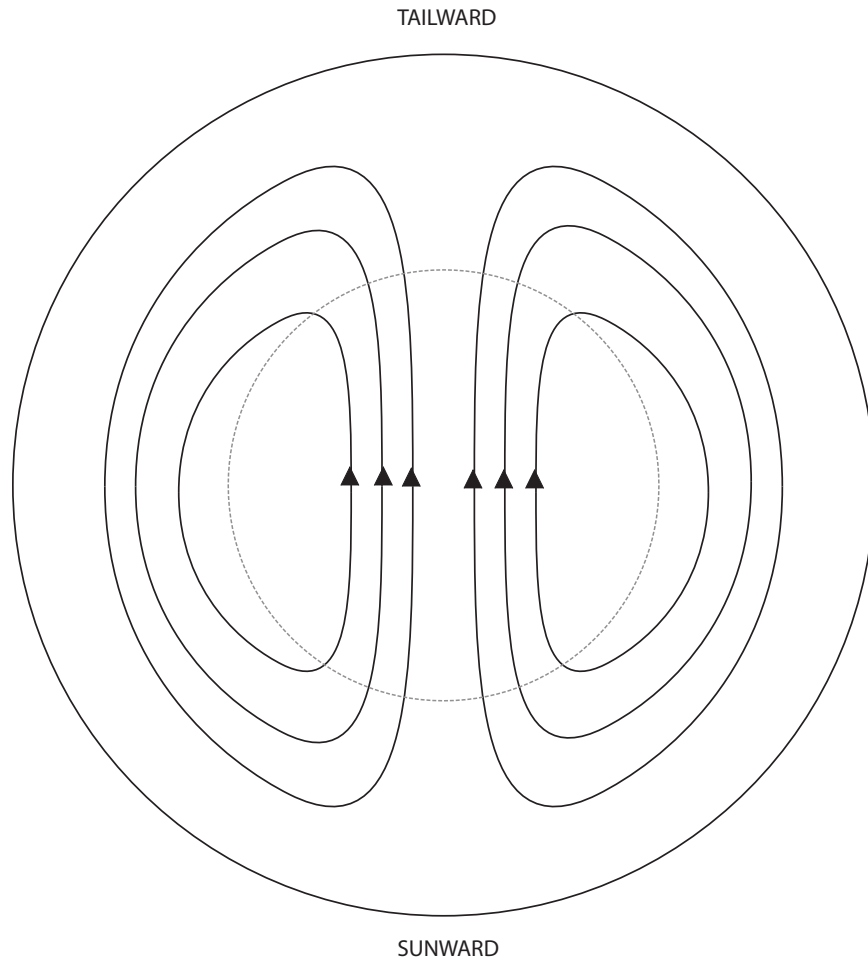


Figure 1.6: Magnetic field motion in the ionosphere.

the "frozen-in" plasma sunward. Dungey used the analogy of a doughnut to describe the convection pattern in the ionosphere. Figure 1.6 shows the magnetic field line motion in the ionosphere, where the open field line topology from dayside reconnection is represented in the doughnut hole and the closed field line topology from reconnection in the tail is represented by the doughnut (Dungey, 1961; Egeland & Burke, 2012).

The first evidence of magnetic reconnection at the magnetopause was published in 1979 (Paschmann et al., 1979) just two years after the launch of ISEE 1 and 2. Paschmann et al.

1.3. PHYSICAL PROCESSES AT THE MAGNETOPAUSE

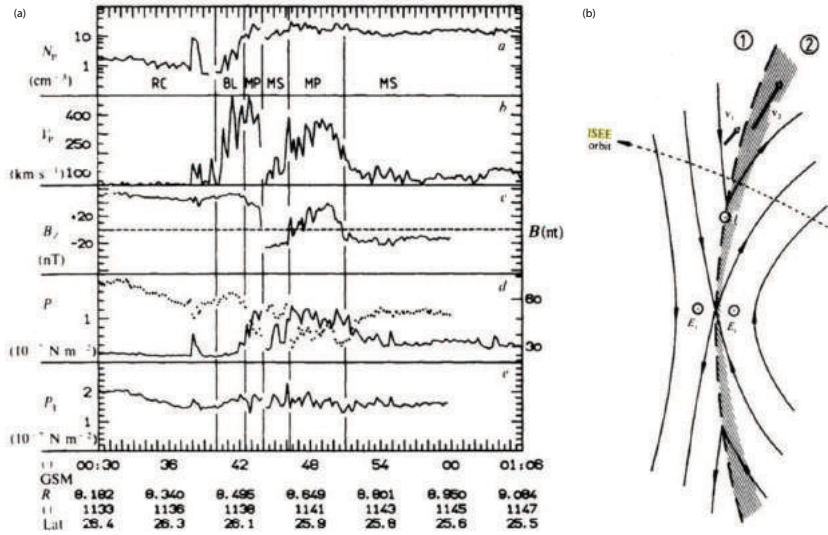


Figure 1.7: First evidence of magnetic reconnection (a) from ISEE traversal of the dayside magnetopause (b). Figure courtesy of Paschmann et al. (1979).

(1979) showed ISEE observations of fast plasma flows at the dayside magnetopause when traversing from the ring current to the magnetosheath (see Figures 1.7 (a) and (b)). These results were consistent with magnetic reconnection theory and the Dungey model – plasma is accelerated in the outflow region and carried poleward by the solar wind. In 1981, B. U. O. Sonnerup et al. (1981) analyzed 11 ISEE magnetopause crossings, in which the plasma velocity in the vicinity of the magnetopause was much greater than in the magnetosheath, reporting results consistent with magnetic reconnection theory. B. U. O. Sonnerup et al. (1981) showed, in part, that the increase in the tangential plasma velocity was consistent with the theoretical value derived from the Maxwell stresses on the plasma.

Observational evidence of reconnection in the tail had already been reported prior to Paschmann et al. (1979) and B. U. O. Sonnerup et al. (1981). A statistical analysis of the magnetic field structure in the magnetotail during substorm activity provided the location of the neutral line (Nishida & Nagayama, 1973).

In 1978, Russell & Elphic (1978) showed evidence of magnetic reconnection in the form of “flux transfer events” (FTEs) from ISEE observations, concluding that the periodic switching on and off of dayside reconnection caused the tearing of flux tubes from the magnetosphere. Russell & Elphic (1978) proposed that FTEs could be a major source of magnetopause oscillations. Typical signatures of FTEs include bipolar variation in the normal component of the magnetic field (Russell & Elphic, 1978; Russell & Elphic, 1979), enhancements in the magnetic field magnitude (Russell & Elphic, 1978; Russell & Elphic, 1979; Paschmann et al., 1982) and total magnetic pressure (Paschmann et al., 1982) separated by a median and mode of approximately 8 and 3 minutes respectively (Russell et al., 1996).

Due to observational similarities between FTEs and KHI at the magnetospheric flanks – such as the quasi-periodic nature of plasma property and field fluctuations including bipolar variation in the normal component of the magnetic field – special care must be taken in order to accurately differentiate between the two processes.

1.3.2 Kelvin-Helmholtz Instability

KHI occurs at the interface of two viscous fluids that have non zero relative velocity and is known to occur in astrophysical plasmas including the solar corona (Foullon et al., 2011; Nykyri & Foullon, 2013) and the terrestrial magnetopause (Fairfield et al., 2000; H. Hasegawa, Fujimoto, Phan, et al., 2004; Nykyri et al., 2006). In fact, it has been shown to occur quite frequently at the terrestrial magnetopause. A recent statistical study found the KHI occurrence rate to be approximately 19% at Earth’s magnetopause (Kavosi & Raeder, 2015). The magnetopause acts as an interface between the fast tailward moving shocked solar wind plasma in the magnetosheath and the relatively stagnant plasma in the magnetosphere. Small perturbations in this shear flow interface (e.g. the

magnetopause boundary) allow for the growth of KHI. In a magnetized plasma however, the magnetic field can act to stabilize the interface. More specifically, the magnetic field tangential to the propagation direction (or wavevector) of the growing KH wave, can stabilize the boundary, which is apparent from the onset condition. The onset condition for KHI in a magnetized plasma is given by the following (Treumann & Baumjohann, 1997):

$$[\mathbf{k} \cdot (\mathbf{V}_1 - \mathbf{V}_2)]^2 \geq \frac{n_1 + n_2}{4\pi m_0 n_1 n_2} [(\mathbf{k} \cdot \mathbf{B}_1)^2 + (\mathbf{k} \cdot \mathbf{B}_2)^2] \quad (1.7)$$

Where \mathbf{V}_i , \mathbf{B}_i and n_i are the velocity, magnetic field and number density for the i^{th} side of the boundary (e.g. shear flow interface); \mathbf{k} is the KH wavevector. From Equation 1.7, the onset of KHI is dependent upon the magnetic field orientation $[(\mathbf{k} \cdot \mathbf{B}_1)^2 + (\mathbf{k} \cdot \mathbf{B}_2)^2]$ in relation to the shear flow $\mathbf{k} \cdot (\mathbf{V}_1 - \mathbf{V}_2)$ relative to the propagation direction of the growing KH wave. The boundary becomes unstable to KHI when the shear flow along \mathbf{k} is large relative to the amount of magnetic field along \mathbf{k} . The right hand side of Equation 1.7 goes to zero as the angle between the \mathbf{B} and \mathbf{k} approaches 90° , maximizing the onset. At the magnetopause, KHI onset is maximized in the equatorial plane at the magnetospheric flanks under northward facing IMF, assuming \mathbf{k} lies in the equatorial plane. Here the angle between the Earth's field and \mathbf{k} , and the angle between the solar wind IMF and \mathbf{k} is approximately 90° . In an incompressible plasma (e.g. $\nabla \cdot \mathbf{v} = 0$), with a constant $|\mathbf{k} \cdot \mathbf{B}|$, Equation 1.7 can be reduced to:

$$[\mathbf{k} \cdot \frac{1}{2}(\mathbf{V}_1 - \mathbf{V}_2)]^2 > \mathbf{k} \cdot (\mathbf{V}_{A,1} - \mathbf{V}_{A,2})^2 \quad (1.8)$$

Where the velocity shear along \mathbf{k} must be greater than Alfvén velocity along \mathbf{k} for KHI to occur (Nykyri, 2013). Equation 1.8 is somewhat analogous to shock formation when the flow speed exceeds the local information speed. In the 3-D system, the 2-D dynamics still exist, however curvature of the magnetic field can act to stabilize KHI (Ma et al., 2014).

KHI has been observed at the magnetopause under northward IMF (Fairfield et al., 2000; H. Hasegawa, Fujimoto, Phan, et al., 2004; Taylor et al., 2008; Eriksson et al., 2009). However, in the real 3D system, KH can grow wherever the onset condition is satisfied (Adamson et al., 2016). Indeed, KHI has been observed under a diverse set of solar wind conditions including PS orientation (Nykyri et al., 2006; Moore, 2012), OPS orientation (Taylor et al., 2012) and even southward IMF (Hwang et al., 2011; Yan et al., 2014). As a function of clock angle, the normalized occurrence rate of KHI is $\approx 35\%$ for northward IMF, $\approx 20\%$ for IMF near the equatorial plane (both PS and OPS combined) and $\approx 10\%$ for southward IMF according to a recent statistical study that analyzed 7 years of THEMIS magnetopause crossings (Kavosi & Raeder, 2015).

Field-aligned currents generated from the twisting of magnetic field lines inside of evolving KH vortices have been suggested to cause small-scale effects in the ionosphere. Furthermore, theoretical work by A. Hasegawa (1976) suggests that discrete auroral signatures can be attributed to the electron acceleration mechanism of Kinetic Alfvén Wave (KAWs), mode converted from MHD surface waves at the magnetopause. Auroral bright spots have been suggested to result from KHI activity in the magnetosphere (Lui et al., 1989; Farrugia et al., 1994). Dougal et al. (2013) estimated the ionospheric location and size of the quasi-periodic signatures from the flank magnetopause associated with KHI. Global MHD and quasi-empirical Tsyganenko models were used for mapping of the magnetic field lines from the location of the spacecraft in the magnetosphere to the ionosphere. Local 2-D MHD model to estimate the size of the MHD vortex in the flank magnetopause. Assuming a time lag derived from the Alfvén speed along the mapped field line from the magnetosphere to the ionosphere and assuming the area to be proportional to the magnetosphere to ionospheric total magnetic field ratio, Dougal et al. (2013) estimated location and vortex sizes in the ionosphere. The calculated vortex sizes (at an altitude of 100 *km*) were between approximately 40 and 600 *km* were within the same order of magnitude of

estimates from Lui et al. (1989) and Farrugia et al. (1994). Dougal et al. (2013) estimated travel times from the magnetosphere to the closest ionospheric location ranging between approximately 1 to 4 minutes. Dougal et al. (2013) were able to map KHI events to stationary and traveling convection vortices observed by SuperDARN with vortices ranging in size between 1000 and 1800 *km*.

KHI can result in the mass transport across the magnetopause via two methods: (1) the “blobby” macroscopic mass transport provided by magnetic reconnection inside of the KH vortices (Nykyri & Otto, 2001; Nykyri et al., 2006; H. Hasegawa et al., 2009) and (2) diffusive transport (Fujimoto & Terasawa, 1994, 1995; H. Hasegawa, Fujimoto, Phan, et al., 2004; Cowee et al., 2010). Mass transport across the magnetopause associated with reconnection in KHI vortices has been quantified and shown to be efficient in generating a cold-dense plasma sheet in the time scale of about 2 hours (Nykyri & Otto, 2001) during strongly northward IMF. KHI can also drive diffusive transport via ion transport through thin current sheets (Fujimoto & Terasawa, 1994, 1995; H. Hasegawa, Fujimoto, Phan, et al., 2004; Cowee et al., 2010) and through the generation of KAWs Johnson & Cheng (1997). § 1.4 contains more information on KHI associated reconnection and diffusion.

1.3.3 Plasma Wave Modes

In our universe, information and energy is carried through waves which travel through all sorts of media, and just like any other media, waves propagate through plasmas. However, because plasma is composed of ionized particles, the way waves propagate through a plasma is different than any other media. In a plasma, there exists a “zoo” of wave modes, each have unique dispersion properties.

A plasma wave’s dispersion relation is an expression which describes how its frequency relates to its wavevector (i.e. $\omega(\mathbf{k})$). For example, a non-dispersive wave has a linear rela-

tionship between its frequency and wavevector, whereas a dispersive wave has a non-linear relationship. Because the dispersion relation for a non-dispersive wave is linear, its phase velocity ($v_\phi = \omega/k$) is equal to its group velocity $v_g = d\omega/dk$. An example of a non-dispersive wave is a common electromagnetic wave propagating in a vacuum $c = \omega/k$, where c is the speed of light; in a plasma there is the compressional Alfvén wave $v_A = \omega/k$, where v_A is the Alfvén speed.

MHD Modes

For the MHD modes, dispersion relations are derived from the MHD description of a plasma. The MHD system of equations are derived and discussed in § 2.3.2. The ideal MHD equations can be simplified using linear perturbation theory, where fields and state properties are approximated by a linear combination of time independent background and time varying perturbation terms – analogous to a constant DC offset with an overlying time-varying AC signal. Using linear perturbation theory, the fields and state properties are defined as follows:

$$\mathbf{B} = \mathbf{B}_0 + \delta\mathbf{B}_1$$

$$\mathbf{v} = \mathbf{v}_0 + \delta\mathbf{v}_1$$

$$\rho = \rho_0 + \delta\rho_1$$

$$p = p_0 + \delta p_1$$

For the ideal MHD case, these expressions are plugged into the Equation 2.24 (Continuity), Equation 2.25 (Momentum), Equation 2.27 (Energy) and Faraday’s Law of Induction ($\nabla \times \mathbf{E} = -\partial\mathbf{B}/\partial t$) using the ideal form of the Generalized Ohm’s Law ($\mathbf{E} = -\mathbf{u} \times \mathbf{B}$) to define

the electric field. Derivatives of the constant terms are zero, assuming that the time varying perturbations are very small, all of their higher order terms go to zero. Thus, the linearized ideal MHD equations are as follows:

Continuity

$$\frac{\partial \delta \rho}{\partial t} + \rho_0 \nabla \cdot (\delta \mathbf{u}) = 0 \quad (1.9)$$

Momentum

$$\rho_0 \frac{\partial \delta \mathbf{u}}{\partial t} = -\nabla \delta p + \frac{1}{\mu_0} (\nabla \times \delta \mathbf{B}) \times \mathbf{B}_0 \quad (1.10)$$

Energy

$$\frac{\partial \delta p}{\partial t} = -\gamma p_0 \nabla \cdot \delta \mathbf{u} \quad (1.11)$$

Faraday's Law

$$\frac{\delta \partial \mathbf{B}}{\partial t} = \nabla \times (\delta \mathbf{u} \times \mathbf{B}_0) \quad (1.12)$$

Taking the time derivative of Equation 1.10 (Momentum) and plugging Equation 1.11 into the result yields the following result:

$$\rho_0 \frac{\partial^2 \delta \mathbf{u}}{\partial t^2} = \gamma p_0 \nabla (\nabla \cdot \delta \mathbf{u}) + \frac{B_0^2}{\mu_0} (\nabla \times (\nabla \times (\delta \mathbf{u} \times \mathbf{e}_B))) \times \mathbf{e}_B \quad (1.13)$$

where $\mathbf{B}_0 = B_0 \mathbf{e}_B$ and \mathbf{e}_B is the unit vector denoting the direction of the background magnetic field. With a little algebra, Equation 1.13 reduces to

$$\frac{\partial^2 \delta \mathbf{u}}{\partial t^2} = c_s^2 \nabla (\nabla \cdot \delta \mathbf{u}) + v_A^2 (\nabla \times (\nabla \times (\delta \mathbf{u} \times \mathbf{e}_B))) \times \mathbf{e}_B \quad (1.14)$$

where c_s is the sound speed ($c_s^2 = \gamma p_0 / \rho_0$) and v_A is the Alfvén speed ($v_A^2 = B_0^2 / \mu_0 \rho_0$). Assuming plane wave solutions (e.g. $\delta \mathbf{B} = |\delta \mathbf{B}| e^{i(\mathbf{k} \cdot \mathbf{x} - \omega t)}$, where \mathbf{x} is the position vector and $\mathbf{k} = k_\perp \mathbf{e}_x + k_\parallel \mathbf{e}_z$ where $\mathbf{e}_B = \mathbf{e}_z$), and taking the Fourier transform of Equation 1.14 yields the following system of equations in matrix form $\underline{\underline{W}} \cdot \delta \mathbf{u} = 0$:

$$\begin{bmatrix} \omega^2 - v_A^2 k_{\parallel}^2 - (c_s^2 + v_A^2) k_{\perp}^2 & 0 & -c_s^2 k_{\parallel} k_{\perp} \\ 0 & \omega^2 - v_A^2 k_{\parallel}^2 & 0 \\ -c_s^2 k_{\parallel} k_{\perp} & 0 & \omega^2 - c_s^2 k_{\parallel}^2 \end{bmatrix} \begin{pmatrix} \delta u_x \\ \delta u_y \\ \delta u_z \end{pmatrix} = 0 \quad (1.15)$$

The non-trivial solutions to Equation 1.15 are found by taking the determinant of matrix $\underline{\underline{W}}$ and setting it equal to zero, such that $Det(\underline{\underline{W}}) = 0$ since a nonsingular matrix will yield only trivial solutions. The three solutions are the Shear Alfvén Wave, the Fast Mode Wave and the Slow Mode Wave.

Shear Alfvén Waves

The first of the three non-trivial solutions, the Shear Alfvén Wave, is shown in Equation 1.16.

$$\omega = k_{\parallel} v_A = k v_A \cos(\theta) \quad (1.16)$$

The Shear Alfvén Wave is a non-dispersive wave that carries momentum and energy along magnetic field lines. As the Shear Alfvén Wave propagates along, or at some small angle to the background magnetic field θ_{kB} , small perpendicular perturbations (to \mathbf{B}_0) move the the frozen-in plasma (see Figure 1.8). The Shear Alfvén Wave is an incompressible wave ($\nabla \cdot \delta \mathbf{u} = 0$); the $\delta \mathbf{u}$ and $\delta \mathbf{B}$ perturbations are perpendicular to both \mathbf{k} and \mathbf{B}_0 and the phase speed approaches zero as $k_{\parallel} \rightarrow 0$. Because these waves are efficient at carrying momentum and energy along magnetic field lines they are important to magnetospheric-ionospheric coupling (Nykyri, 2011).

Fast and Slow Modes

The second and third non-trivial solutions to Equation 1.15 are the Fast (+) and Slow (−) Wave modes shown in the following expression:

$$\omega^2 = \frac{k^2}{2} \left(c_s^2 + v_A^2 \pm \left[(c_s^2 + v_A^2)^2 - 4v_A^2 c_s^2 \frac{k_{\parallel}^2}{k^2} \right]^{1/2} \right) \quad (1.17)$$

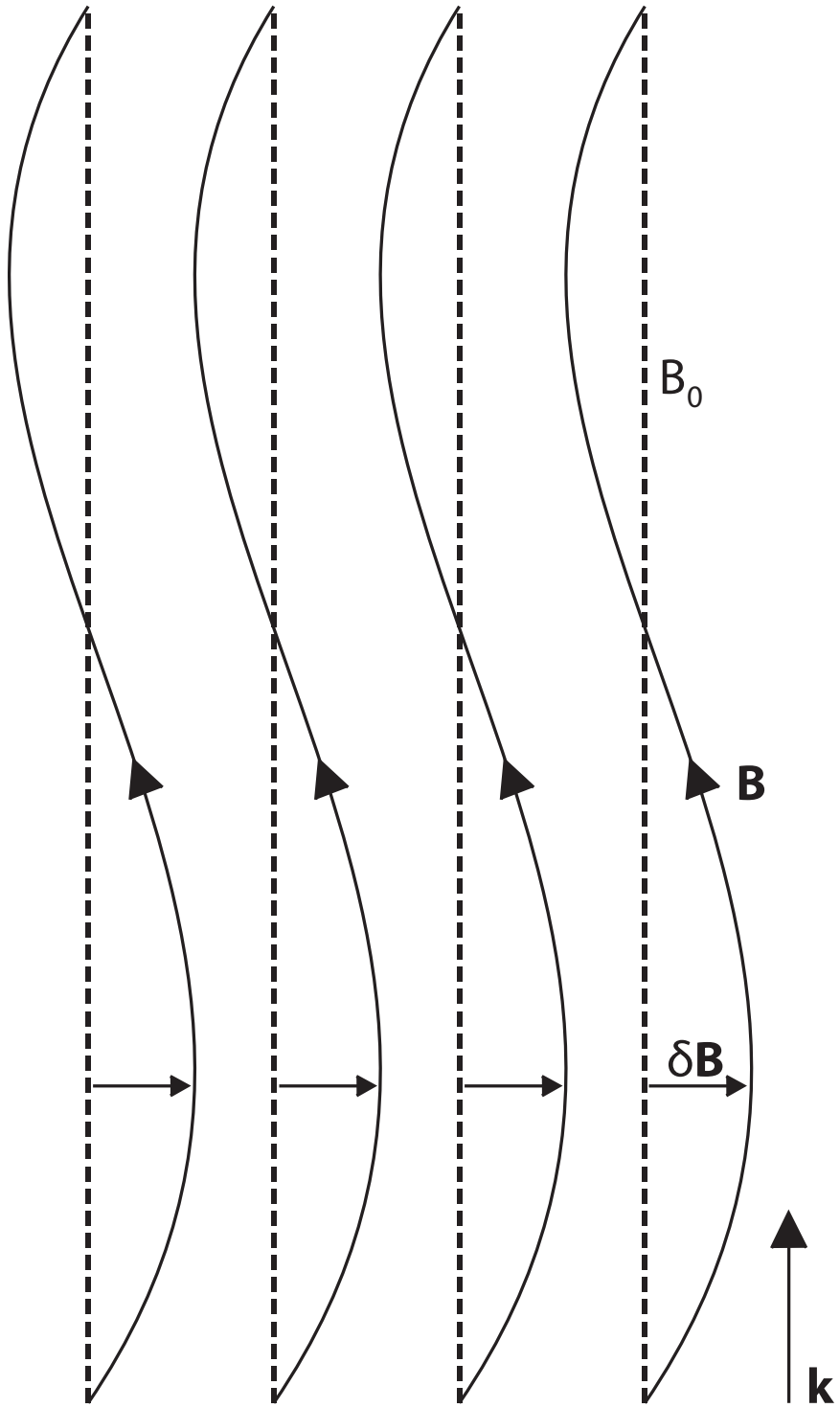


Figure 1.8: Shear Alfvén wave propagating along the magnetic field.

As with the Shear Alfvén Wave, the Slow Mode Wave carries information along magnetic field lines. The phase speed along the magnetic field line is the minimum between the sound and Alfvén speeds, whereas the phase speed perpendicular to the magnetic field is zero.

Fast Magnetosonic Waves

The Fast Mode Wave also known as the Fast Magnetosonic Wave (FMW) has the largest group speed and thus defines the maximum speed at which information can be carried through an MHD plasma. Recall that the super-magnetosonic solar wind forms the “fast-shock” (bow shock) upstream of the magnetopause. These waves are exceptionally important because they can carry energy across field lines (i.e. perpendicular to the magnetic field). The phase speed along the magnetic field line is the maximum between the sound speed and Alfvén speed, whereas the phase speed perpendicular to the magnetic field is the magnetosonic speed $c_{ms}^2 = c_s^2 + v_A^2$. Because FMWs can carry energy perpendicular to \mathbf{B}_0 , it is worthwhile to write its dispersion relation in terms of the perpendicular wavenumber k_\perp as shown in Equation 1.17. As $k_\parallel \rightarrow 0$, the FMW becomes a Compressional Alfvén Wave.

$$\omega^2 = \frac{k^2}{2} \left(c_{ms}^2 + \left[(v_A^2 - c_s^2)^2 + 4v_A^2 c_s^2 \frac{k_\perp^2}{k^2} \right]^{1/2} \right) \quad (1.18)$$

Compressional Alfvén Waves

Also in the cold plasma limit ($c_s \ll v_A^2$), the Fast Mode Wave reduces to the Compressional Alfvén wave (see Equation 1.19).

$$\omega = kv_A \quad (1.19)$$

The Compressional Alfvén wave is a compressional longitudinal wave that causes compressions and rarefactions in the plasma. Due to the plasma being “frozen-in” to the magnetic field lines, compressions and rarefactions cause the magnetic field strength to fluctuate in

the wake of the passing waves (see Figure 1.9).

Kinetic Alfvén Waves

The KAW is an important wave in part because of its association with magnetopause processes (A. Hasegawa, 1976; A. Hasegawa & Chen, 1976; Johnson et al., 2001) and ion heating (A. Hasegawa, 1976; A. Hasegawa & Chen, 1976; Johnson & Cheng, 2001) in both space and laboratory plasmas. Theoretical work by A. Hasegawa (1976) has shown that KAWs can accelerate “aurora-forming” electrons, manifested by geometric signatures consistent with auroral observations. The dispersion relation for the KAW, shown in Equation 1.20, can be derived from a two fluid approximation of the plasma (Stasiewicz et al., 2000). This is accomplished by combining Equation 2.19 (Fluid Momentum) for both electrons and ions with Maxwell’s equations. The KAW is a dispersive wave that propagates below the ion cyclotron frequency and generally has a left-hand polarization. The KAW has a finite k_{\perp} with a wavelength comparable to the ion gyroradius (perpendicular to the magnetic field) (A. Hasegawa, 1976).

$$\omega = k_{\parallel} v_A \omega_{ic} \sqrt{\frac{1 + k_{\perp}^2 (\rho_s^2 + \rho_i^2)}{\omega_{ic}^2 + k_{\parallel}^2 v_A^2 (1 + k_{\perp}^2 \rho_i^2)}} \quad (1.20)$$

Ion Cyclotron Waves

Like the KAW, the Ion Cyclotron Wave (ICW) is a dispersive left-hand polarized wave which propagates below the ion cyclotron frequency. ICWs can energize ions via ion cyclotron resonance when $\omega \rightarrow \omega_{ic}$, because it resonates with the ions motion about the background magnetic field. The ICW dispersion relation (Stix, 1992), shown in Equation 1.21, is derived from kinetic theory. Roots from Equation 2.11 are found by deriving the dielectric tensor $\underline{\underline{\epsilon}}$ (see Equation 2.12) for a cold magnetized plasma and assuming parallel (with respect to the magnetic field) propagation. The ICW dispersion relation is solved from the root

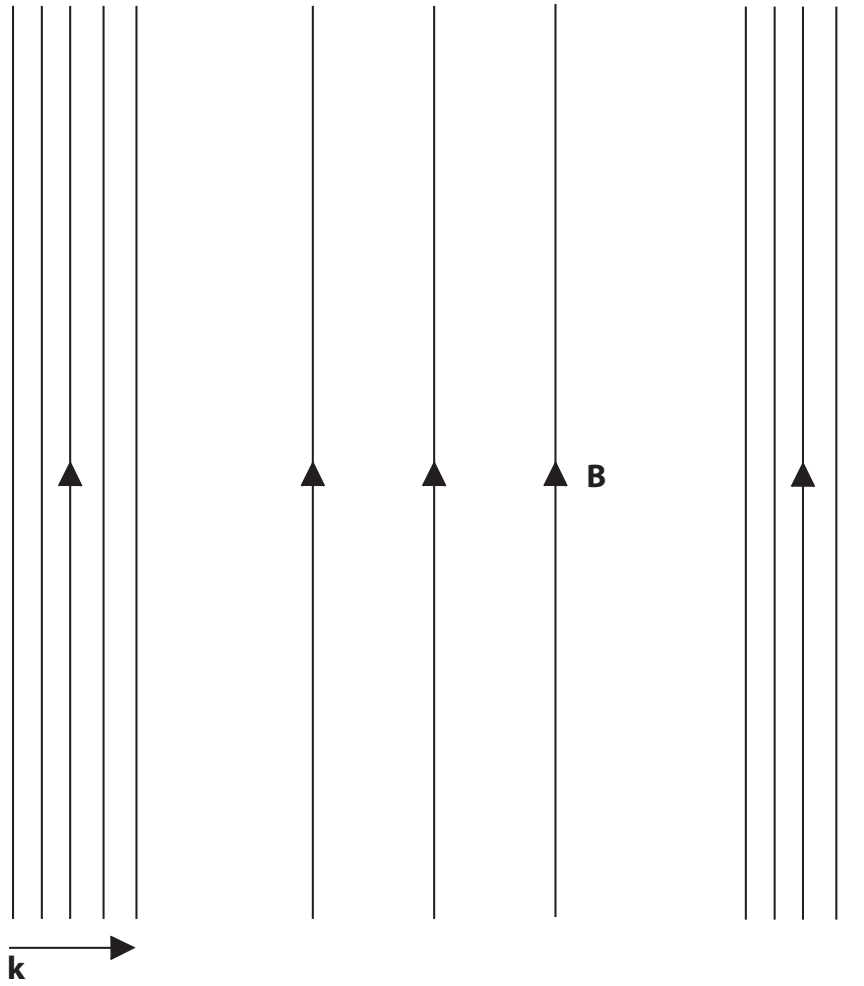


Figure 1.9: Compressional Alfvén wave propagating perpendicular to the magnetic field.

associated with left-hand polarization, and is given by the following expression:

$$\omega = \omega_{ic} \left(1 + \frac{\omega_{pi}^2}{k_{\parallel}^2 c^2} + \frac{\omega_{pi}^2}{k_{\parallel}^2 c^2 + k_{\perp}^2 c^2} \right)^{-1/2} \quad (1.21)$$

1.4 Processes Associated with KHI

Understanding the transport and heating of plasma across different spatial and temporal scales is particularly important in laboratory and space plasmas. The specific entropy, $S_i = T_i/n^{2/3}$ (where T_i is the ion temperature in eV/cm and n is the ion number density) increases by two orders of magnitude – from 2.5 - 70 eV cm² in the magnetosheath to 700 - 16000 eV cm² in the magnetosphere (Borovsky & Cayton, 2011). As such, it is highly plausible that mechanisms acting across multiple scales are at play at Earth’s magnetopause. Magnetic reconnection which operates on ion and electron scales is known to be produced by the non-linear evolution of KH vortices (Otto & Fairfield, 2000; Nykyri & Otto, 2001; Nykyri et al., 2006; H. Hasegawa et al., 2009). Reconnection inside KH vortices has been associated with the production of field aligned ion beams (Nykyri et al., 2006; Nishino, Fujimoto, Terasawa, et al., 2007; Nishino, Fujimoto, Ueno, et al., 2007), where non-Maxwellian distributions provide energy capable of promoting wave growth. In addition, KHI has also been associated with the excitation of KAWs at the magnetopause via a process called mode conversion (A. Hasegawa, 1976; Johnson et al., 2001) which can accelerate particles parallel to the ambient field (A. Hasegawa, 1976) and heat ions stochastically (Johnson & Cheng, 2001) and has been associated with energy transport across the magnetopause (Chaston et al., 2007).

1.4.1 Reconnection inside Kelvin-Helmholtz Instability

Magnetic reconnection associated with KHI was first proposed by Hu and Liu in 1986. They theorized that the twisting of magnetic field lines by the growing KHI generation at the magnetopause can lead to the formation of magnetic islands. 2D MHD simulations have been used to study the generation of so-called vortex-induced reconnection; these simulations showed linear (Pu et al., 1990) and non-linear (Chen et al., 1997) coupling between KHI and magnetic reconnection.

Not to be confused with vortex-induced reconnection, 2D MHD simulations have shown that the twisting of magnetic field lines inside of KH vortices can generate thin current sheets on the scale of the ion-inertial length where reconnection can occur (Otto & Fairfield, 2000; Nykyri & Otto, 2004). Reconnection driven by the evolution of the KH vortices forms magnetic islands allowing for the transport of magnetosheath plasma into the magnetosphere as shown in Figure 1.10. Nykyri & Otto (2001, 2004) quantified the plasma transport rate inside of KH vortices using MHD and Hall MHD approximations respectively; they found that that reconnection inside the vortices can provide transport velocities on the order of $1 - 2 \text{ km/s}$ corresponding to a diffusion coefficient of $10^9 \text{ m}^2/\text{s}$. These findings suggested that magnetic reconnection inside KH vortices might be a viable mechanism for transporting mass across the magnetopause. In fact, reconnection inside KH vortices has been shown to occur at the flank magnetopause (Nykyri et al., 2006; H. Hasegawa et al., 2009; Eriksson et al., 2016).

Bridging the gap between fluid and ions scales is the observation of ion-beams during reconnection inside of KH vortices (Nykyri et al., 2006). Ion-beam distributions are non-Maxwellian and are a source of energy which may drive ion-scale wave activity. The big picture in relation to cross-scale coupling is as follows: fluid scale KHI can generate thin boundaries with anti-parallel facing magnetic fields which favor magnetic reconnection.

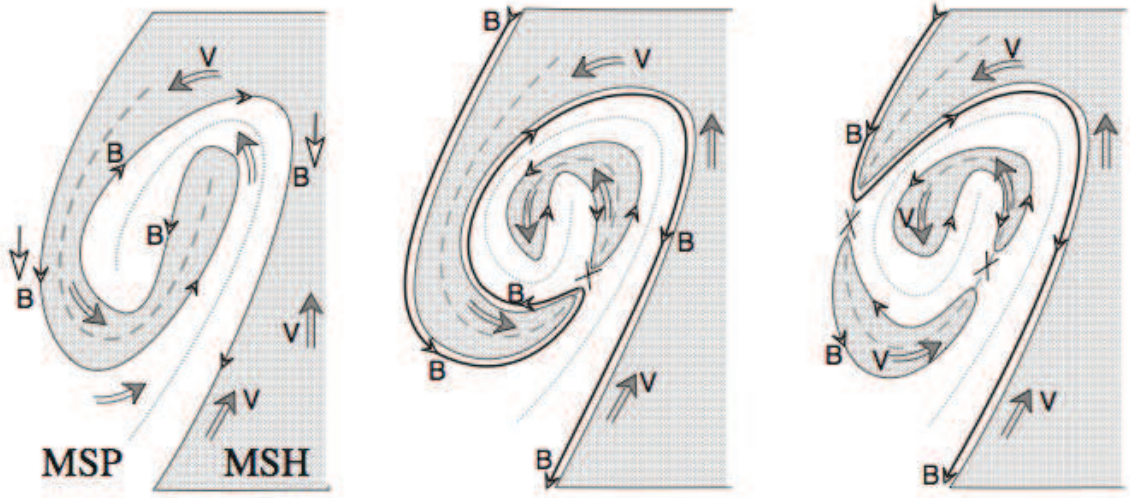


Figure 1.10: Illustration of magnetic reconnection inside a KH vortex (Nykyri & Otto, 2001). As the magnetic field lines become twisted inside the KH vortex, magnetic reconnection creates magnetic islands.

tion. Associated ion-beams can then drive ion-scale wave activity inside the fluid-scale KH vortices.

1.4.2 Mode Conversion

Theoretical work by A. Hasegawa (1976) has shown that MHD surface waves excited by either an MHD instability or externally applied impulse can “resonantly mode convert” to KAWs. Further theoretical work suggests that stochastic ion heating (perpendicular to the magnetic field) via kinetic Alfvén wave (KAW) turbulence may to some extent be responsible for particle heating (A. Hasegawa, 1976; Johnson et al., 2001; Johnson & Cheng, 2001) and transport (Johnson et al., 2001; Johnson & Cheng, 2001). Amplification of perpendicular wave power at the Earth’s magnetopause can be explained by the theory of mode conversion of compressional MHD waves into KAWs (Johnson et al., 2001). As the compressional Alfvén mode propagates into regions with sharp gradients in the $k_{\parallel}v_A$, Alfvén resonance

($k_{\parallel}^2 = k_A^2$) can excite KAWs (A. Hasegawa, 1976; Cheng & Johnson, 1999; Johnson et al., 2001). It should be noted that KH waves are compressional surface waves, or surface Alfvén modes – a fast-mode wave containing a non-zero tangential (to the current sheet) component of \mathbf{k} (Pu & Kivelson, 1983). Amplification of the transverse magnetic field at the magnetopause is seen by the increase in the ratio of transverse to compressional magnetic wave power (P_{\perp}/P_{\parallel}) at the Alfvén resonance location – see bottom panel of Figure 1.11 – was shown to be consistent with theoretical calculations of compressional wave absorption (Johnson et al., 2001). Furthermore, observations of mode conversion from KHI driven surface waves to KAWs supporting transport of both electromagnetic energy and plasma at the Alfvén resonance location have been made (Chaston et al., 2007) (please see Figure 1.12).

1.5 Dawn-Dusk Asymmetries

The shocked solar wind which populates the magnetosheath is the source plasma for entry into the magnetosphere across the magnetopause via FTEs, magnetic reconnection as well as diffusion in KH vortices and reconnection associated with KHI. The solar wind IMF is statistically configured in the PS orientation which creates a quasi-parallel shock at the dawnside bow shock responsible for generating various wave modes, instabilities and interactions that could be responsible for heating ions (Eastwood et al., 2002, 2003, n.d., 2005; Blanco-Cano et al., 2006). In this section we will discuss the inherent asymmetries in the source magnetosheath plasma and the asymmetric evolution of magnetopause processes.

1.5.1 Asymmetries in the Source (Magnetosheath) Plasma

Results from a statistical study using data from IMP 8, ISEE 3, ISEE 1 and WIND spacecraft showed significant dawn-dusk asymmetry in the plasma density where a higher plasma

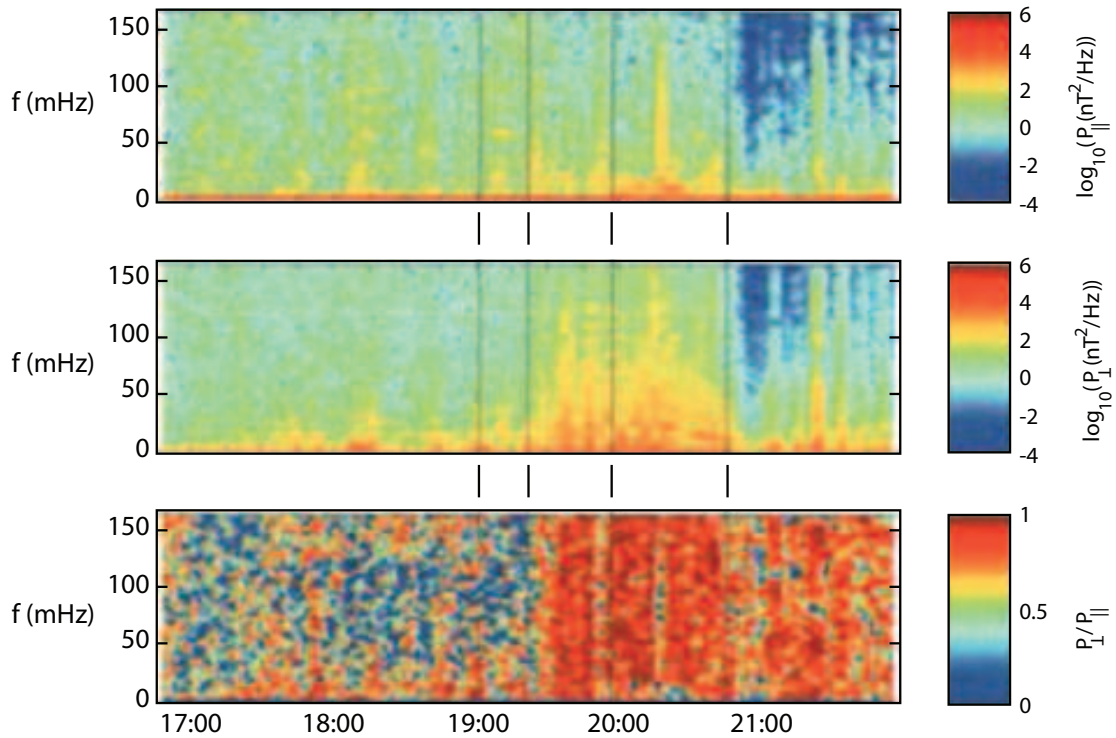


Figure 1.11: WIND magnetopause crossing. Wave power spectral density of the parallel magnetic field (top panel), perpendicular magnetic field (middle panel) and ratio of the perpendicular to total wave power. The wave power become more strongly perpendicular at the magnetopause (Johnson et al., 2001).

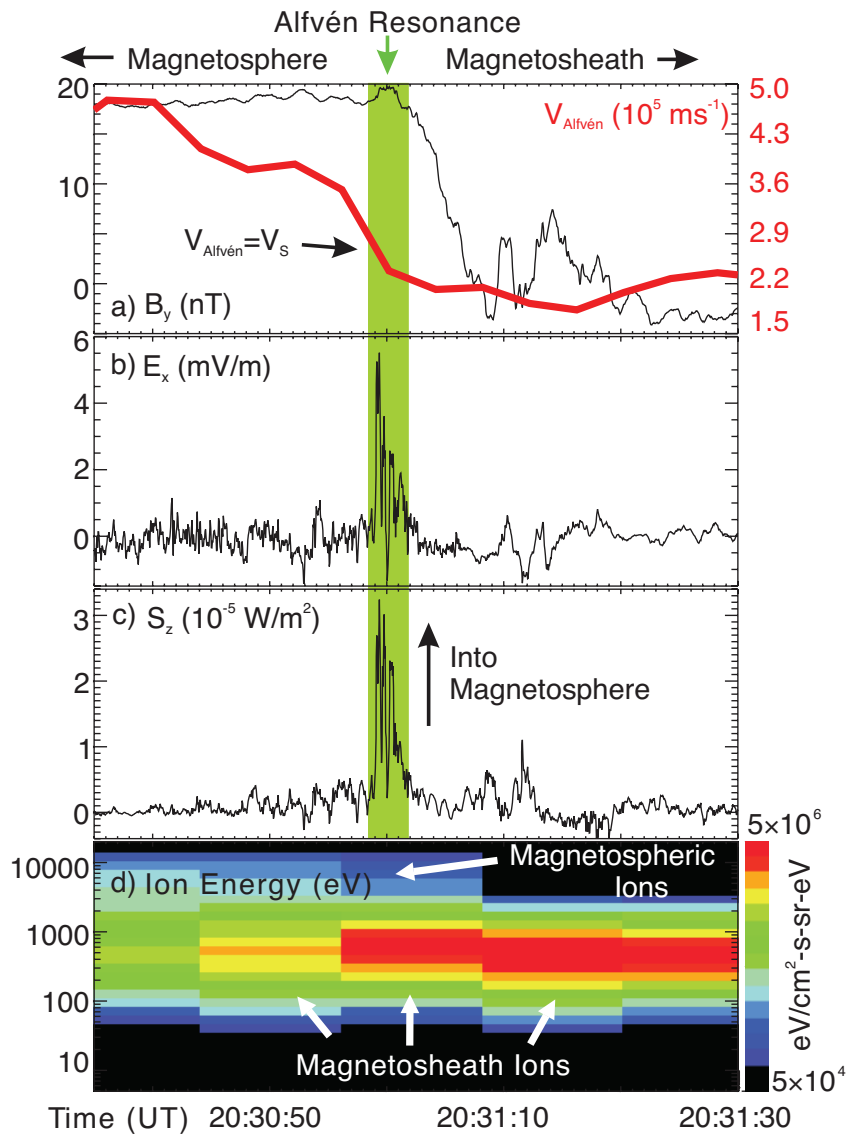


Figure 1.12: Cluster observations: mode conversion from Kelvin-Helmholtz Instability driven surface waves to Kinetic Alfvén Waves. Poynting flux (wave energy) into the magnetopause is observed at the Alfvén Resonance location, coinciding with mixed ion region (Chaston et al., 2007).

density was reported at the dawn flank magnetopause (Paularena et al., 2001). This dawn favored asymmetry was reported to be dependent upon the upstream solar wind conditions during the solar minimum, however not for the solar maximum.

Longmore et al. (2005) reported a dawn-dusk asymmetry in the velocity magnitudes and densities in the northern hemisphere from a statistical study of Cluster orbits. Lower velocity magnitudes and higher densities were measured at the dawn flank magnetosheath with no apparent dependency on solar wind IMF.

Walsh et al. (2012) conducted a statistical analysis of 1114 dayside boundary crossings from 3 years of THEMIS spacecraft data. The study concluded several dawn-dusk asymmetries near the sheath side magnetopause in the proton number density and temperature as well as in the bulk flow and magnetic field strengths driven by a statistically PS orientated IMF. The proton number density and temperature are both higher at the dawn flank, whereas the bulk flow and magnetic field strengths are both higher at the dusk flank. These results were found to be consistent with BATS-R-US global MHD simulations.

In a recent statistical analysis, Dimmock et al. (2014) reported that the magnetic field fluctuation amplitudes in the magnetosheath interplanetary medium reference frame (MIPM) were reduced by 20% - 25% on the dusk flank when compared to that of the dawn flank under a statistically PS orientated IMF. These results are in agreement with previous studies, which have shown strong magnetic field fluctuations downstream of the quasi-parallel shock (Fairfield et al., 2003; Luhmann et al., 1986; Zastenker et al., 2002; Němeček et al., 2002; Shevyrev & Zastenker, 2005; Shevyrev et al., 2006, 2007).

Dimmock et al. (2015) showed evidence of a temperature asymmetry in the magnetosheath plasma from 7 years of THEMIS data, where the dawn flank is statistically hotter than the dusk flank. The dawn flank was shown to be approximately 10% hotter when the upstream solar wind IMF is in PS orientation (Dimmock et al., 2015). However, the observed temperature asymmetry in the magnetosheath plasma is not sufficient to produce

the observed scale of plasma sheet temperature asymmetry (Dimmock et al., 2015).

1.5.2 Asymmetric Evolution of Magnetopause Processes

Ten years of ISEE 1 and 2 observations of magnetopause crossings have shown that the largest amplitudes of magnetopause oscillations occur at the dayside dawn-flank when the IMF is in the PS orientation (Russell et al., 1997). Furthermore there were more observed crossings per pass at the dayside dawn-flank under PS IMF (Russell et al., 1997), which could be due to a higher occurrence rate of processes like KHI or FTEs at the dawn-flank.

KHI

It has been proposed that asymmetries in the MSH may lead to a dawn flank preference for wave-particle interactions such as KHI and KAW activity that could explain the temperature asymmetry of the cold-component ions in the plasma sheet (Nykyri, 2013). In fact, recent BATS-R-US global MHD simulations have shown that the magnetosheath plasma downstream of the quasi-parallel shock has less tangential magnetic field along the magnetosheath flow, allowing for faster KH growth times (Nykyri, 2013). Because the IMF is statistically more often in PS orientation, faster onset times at the dawn flank suggests that KHI might favor the dawn-flank (Nykyri, 2013). Furthermore stronger tangential magnetic field along magnetosheath flow downstream of the quasi-perpendicular shock may stabilize KHI under PS at the dusk-flank. Indeed stronger magnetic field strengths have been shown to favor the dusk-flank magnetosheath under PS IMF – a result from a recent statistical study spanning 5 years of THEMIS magnetosheath and OMNI solar wind data (Dimmock & Nykyri, 2013); these results are consistent with global BATS-R-US and local simulations under similar solar wind conditions (Dimmock & Nykyri, 2013). Additionally, in a statistical study of ultra low frequency (ULF) Pc3 velocity fluctuations

from 6 years of THEMIS data, enhancements in the power spectral density have been shown to favor the magnetosheath downstream of the quasi-parallel shock. The source of which these fluctuations differed close to the magnetopause compared to the central magnetosheath and the region directly downstream of the shock (Dimmock, Nykyri, et al., 2016). Work by Nykyri (2017) has shown that magnetosheath velocity fluctuations can be 40-80 km/s and have a strong dawn-dusk asymmetry (favoring the quasi-parallel shock side) which can impact KH growth rates and the initiation of reconnection at the magnetopause. Dimmock, Nykyri, et al. (2016) suggest that the Pc3 velocity fluctuations near the magnetopause are caused by a velocity shear and velocity shear driven processes such as KHI drive. Furthermore Dimmock, Nykyri, et al. (2016) reported that these Pc3 velocity fluctuations are significantly enhanced during fast solar wind intervals. KHI has long been associated with continuous field line resonances in the Pc3 - Pc5 range (Miura, 1987; Lessard et al., 1999).

In a followup statistical study of Pc4 - Pc5 field fluctuations Nykyri et al. (2016) reported the magnetic field fluctuations – a feature associated with KHI – near the magnetopause to be strongest at the dawn flank. Furthermore from the tailward velocity profile, the dawn flank LLBL was shown to be thicker than at the dusk flank.

Recent work by Walsh (2014) suggests that KHI can be initiated on the dusk-side dayside magnetopause when the plasmaspheric plume is in contact with the magnetopause by lowering the threshold for the KHI initiation. Future studies, with equal amount of dawn and dusk-flank crossings with similar solar wind conditions may shed light on which flank KHI is observed more frequently. Recently, Henry et al. (2017) sorted the list of KH events from Kavosi & Raeder (2015) and showed that the normalized occurrence rates of KHI favor the dawn-flank during PS IMF.

Wave Heating

A statistical study by Yao et al. (2011) showed a dawn-dusk asymmetry in the spectral energy densities of ion gyro-radii scale electromagnetic waves that favored the dawnside over the duskside magnetopause. Without detailed wave mode identification they suggested the waves were likely KAWs, which have been attributed to ion heating and plasma transport across the magnetopause (A. Hasegawa & Mima, 1978; Rezeau et al., 1989; Lee et al., 1994; Johnson & Cheng, 1997, 2001; Chaston et al., 2007).

1.6 Motivation

There exists a strong dawn-dusk asymmetry in the cold-dense plasma sheet under northward IMF conditions (H. Hasegawa et al., 2003; Wing et al., 2005). The plasma sheet hosts two distinct ion populations during northward IMF conditions: the cold component ions (magnetosheath origin) and the hot component ions of (magnetospheric origin) (Fujimoto et al., 1998; H. Hasegawa et al., 2003; H. Hasegawa, Fujimoto, Saito, & Mukai, 2004; Wing et al., 2005). The cold component ions are 30% - 40% hotter on the dawn-side plasma sheet compared to the dusk side (see Figure 1.13). The origins of this asymmetry are not currently understood. A more recent statistical study of magnetosheath temperatures (Dimmock et al., 2014) shows that the magnetosheath temperatures are only about 10% - 15% higher at the dawn-flank compared to the dusk-flank. Therefore, additional mechanisms at the magnetopause must be at play to explain the temperature asymmetry in the plasma sheet: (1) the entry mechanism generating the cold-dense plasma sheet; (2) an asymmetry in the source magnetosheath plasma; or (3) a combination of the two.

Furthermore the specific entropy in the magnetosphere is several orders of magnitude higher than in the magnetosheath (Borovsky & Cayton, 2011), a signature of strong non-adiabatic heating. This phenomena is, at present, not well understood. It is the motivation

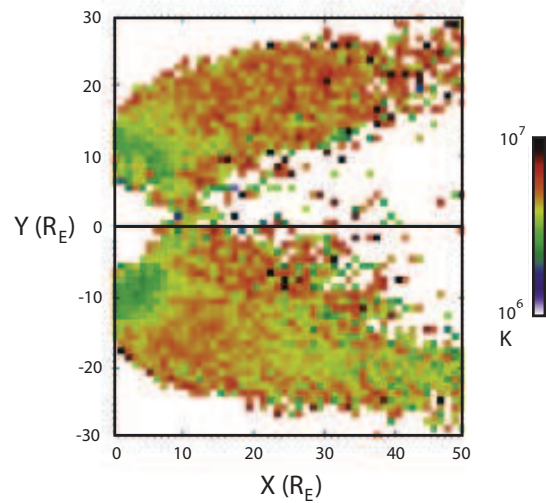


Figure 1.13: The cold component temperature profile of the two-component Maxwellian distribution function of the plasma sheet ions are calculated using data from the Defense Meteorological Satellite Program (DMSP) (Wing et al., 2005). The cold component ions tailward of $\approx -20 R_E$ on the dawn flank are hotter compared to the dusk flank.

of this thesis to explore the the possible mechanisms at play that may be responsible for non-adiabatic heating across the magnetopause and the plasma sheet temperature asymmetry.

Chapter 2

Methodology

In this thesis, we analyze boundary crossings for ion-scale wave activity during periods when KHI are active and inactive. In this section, methodologies and pertinent theories are introduced related to KHI identification, the identification and dispersion analysis of ion-scale wave activity and statistics. Identification of KHI activity is two fold, involving observations and validation through modeling. The analysis of ion-scale wave activity includes the identification of wave activity through wavelet and Fourier analysis, multi-spacecraft determination of the full dispersion relation, determination of ion-scale wave properties and kinetic modeling.

2.1 Identifying KH Signatures in the LLBL

In order to efficiently identify intervals for KH waves in the LLBL, a search of the Cluster Science Archive is performed over the dates when the Cluster spacecraft formation orbit is in the vicinity of the low-latitude magnetospheric flanks. Plasma parameters including ion number density, temperature, and total pressure along with the magnetic field properties are analyzed for specific signatures consistent with KHI observations from the literature.

These typical signatures of KHI are as follows:

- Quasi-periodic variation of anti-correlated ion number density and temperature, between cold dense plasma (of magnetosheath origin) and hot tenuous plasma (of magnetospheric origin).
- Significant total pressure variation – a maximum observed at the edge of the vortex followed by a minimum at the vortex center.
- Faster than sheath flow, a unique feature observed in simulation results (H. Hasegawa, Fujimoto, Phan, et al., 2004). In order for the force balance in the radial direction to be maintained, the hot tenuous plasma must rotate faster than the cold dense plasma (Nakamura et al., 2004).
- Bipolar variation in the component of the magnetic field normal to the magnetopause current layer B_N . The growing KH wave twists the magnetic field inside of its vortices as it propagates along the magnetopause. This twisting motion causes the unit vector normal to the magnetopause surface to change polarity as the magnetopause folds in on itself resulting in the bipolar variation in B_N .

These observations are depicted in an overview plot of the KHI event from June 6th 2002 (Moore, 2012; Moore et al., 2016), shown in Figure 2.1. From Panel (a) of Figure 2.1, there is quasi-periodic variation between high energy ion (of magnetospheric origin) and low energy ions (of magnetosheath origin); anti-correlated variation in the ion number density and temperature are shown to be quasi-periodic in Panels (b) and (c) respectively; quasi-periodic bi-polar variation in the magnetic field component normal to the magnetopause is shown in Panel (d); and the total pressure variation plotted in Panel (e) is quasi-periodic – minimums are encountered as the Cluster spacecraft encounters KH vortices. Observations of faster than sheath flow are depicted in Panel (c) of Figure 2.2 – the collection of low

density and high tailward velocity ($V_x < 0$) in the lower left quadrant denote this faster than sheath flow..

2.2 Boundary Normal Coordinate System and Variance Analysis

In order to locate intervals with bipolar variation in the component of the magnetic field that is most normal to the magnetopause boundary, it is often convenient to rotate the field data into the Boundary Normal Coordinate System (BNC) denoted by the unit vectors \mathbf{LMN} . In the standard notation, \mathbf{N} points normal to the magnetopause surface, \mathbf{L} points locally northward and \mathbf{M} completes the system. These orthogonal unit vectors can be obtained from the variance directions through minimum variance analysis of the magnetic field (MVAB) or maximum variance analysis of the $-\mathbf{v} \times \mathbf{B}$ electric field (MVAE) (Khrabrov & Sonnerup, 1998; B. U. Ö. Sonnerup & Scheible, 1998). This method was developed in the context of a spacecraft traversal across a transition layer such as a current sheet or a wave front. Therefore this is an invaluable technique in space physics for finding the unit vector normal to the magnetopause and propagation direction of plasma waves.

MVAB is based on an ideal 1D approximation of a transition layer, such that $\partial/\partial x = 0$ and $\partial/\partial y = 0$ (B. U. Ö. Sonnerup & Scheible, 1998). From the divergence of the magnetic field ($\nabla \cdot \mathbf{B} = 0$), the 1D approximation is $\partial B_z/\partial z = 0$; and from Faraday's Law, the 1D approximation reduces to $\partial B_z/\partial t = 0$. With these approximations it follows that the z -component of the transition layer magnetic field is constant in space and time. Suppose a spacecraft takes 3 distinct magnetic field measurements across a transition layer can be written as $\mathbf{B}^{(1)} \cdot \hat{\mathbf{n}} = \mathbf{B}^{(2)} \cdot \hat{\mathbf{n}} = \mathbf{B}^{(3)} \cdot \hat{\mathbf{n}}$, such that $(\mathbf{B}^{(1)} - \mathbf{B}^{(2)})$ and $(\mathbf{B}^{(2)} - \mathbf{B}^{(3)})$ are not co-linear (B. U. Ö. Sonnerup & Scheible, 1998). It follows that their cross product is

2.2. BOUNDARY NORMAL COORDINATE SYSTEM AND VARIANCE ANALYSIS

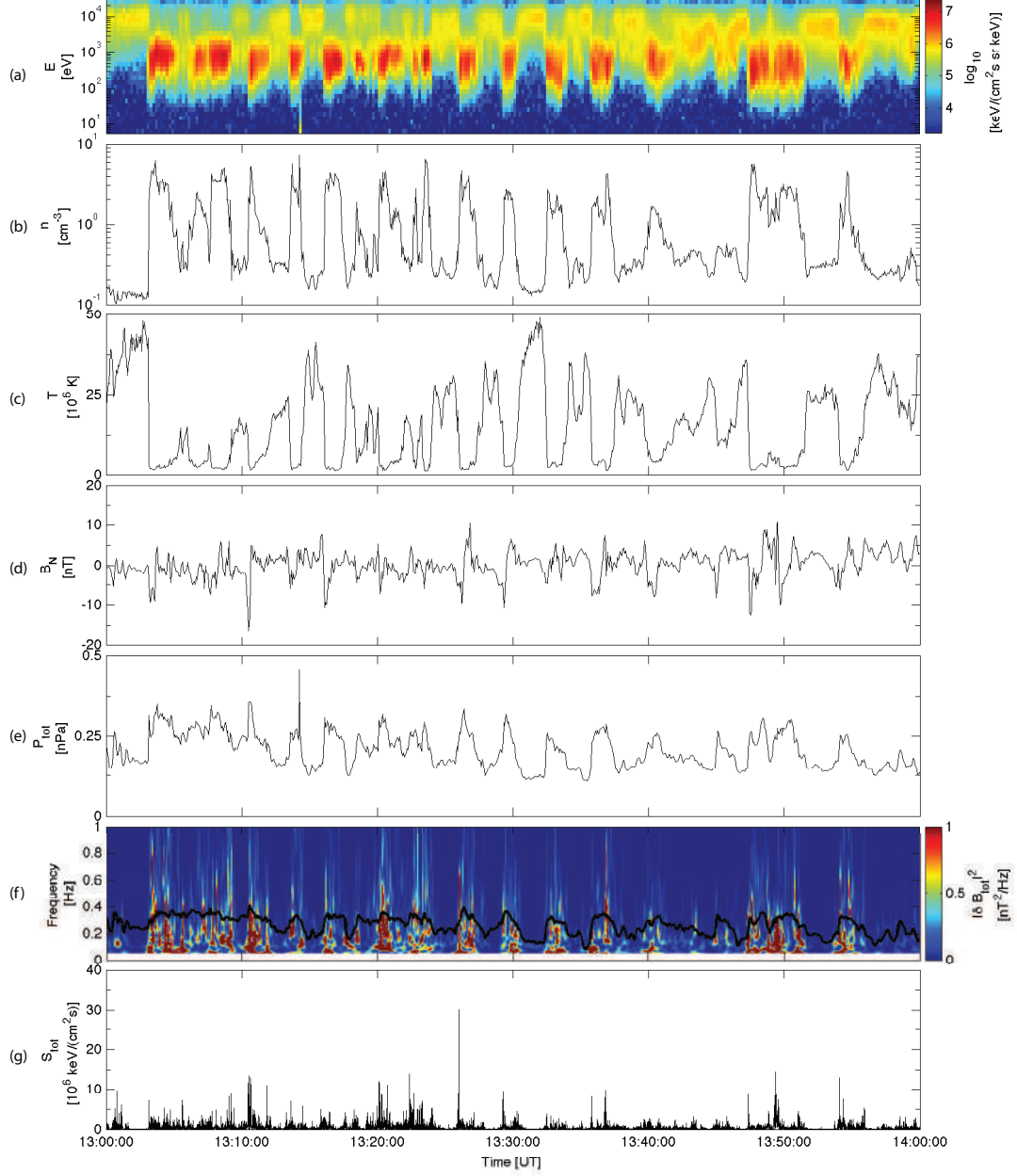


Figure 2.1: Overview plot of the June 6th 2002 KHI event during PS IMF including the omni-directional ion energy spectrogram (a), ion number density n (b), ion temperature T (c), normal component of the magnetic field B_N (d), total pressure (e), total magnetic wave power $|\delta B_{tot}|^2$ (f) and total Poynting flux S_{tot} (g).

2.2. BOUNDARY NORMAL COORDINATE SYSTEM AND VARIANCE ANALYSIS

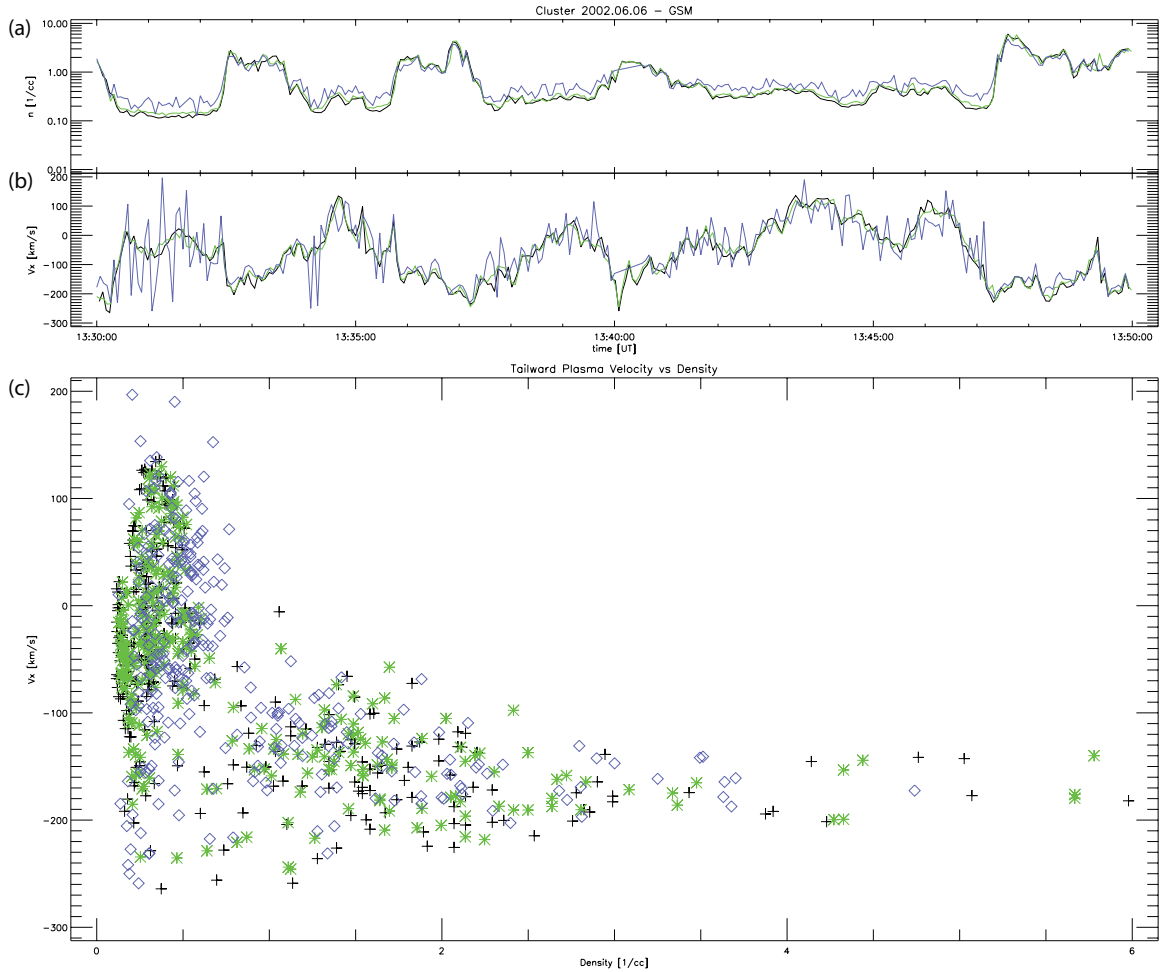


Figure 2.2: Cluster C_1 , C_2 and C_3 observations of the ion number density (a); ion velocity (b); and faster than sheath flow (c) depicted by the fast tailward ($-V_x$) low density plasma in the lower left quadrant of (c).

perpendicular to the transition layer. Ideally $\mathbf{B}^{(2)}$ would be measured nearest the transition layer, while $\mathbf{B}^{(1)}$ and $\mathbf{B}^{(3)}$ would be measured on either side (B. U. Ö. Sonnerup & Scheible, 1998).

In the real system, the direction normal to a transition layer is not zero and instead, $\hat{\mathbf{n}}$ is determined from the minimum variance of the difference magnetic field vectors across the transition layer (B. U. Ö. Sonnerup & Scheible, 1998). This minimum variance is shown in Equation 2.1, where $\langle \mathbf{B} \rangle$ is the time-averaged magnetic field for all $m = 1 : M$ measurements.

$$\sigma^2 = \frac{1}{M} \sum_{m=1}^M |(\mathbf{B}^{(m)} - \langle \mathbf{B} \rangle) \cdot \hat{\mathbf{n}}|^2 \quad (2.1)$$

This minimization is achieved using the method of Lagrange multipliers λ with the constraint $|\hat{\mathbf{n}}|^2 = 1$, such that

$$\frac{\partial}{\partial n_x} (\sigma^2 - \lambda(|\hat{\mathbf{n}}|^2 - 1)) = 0 \quad (2.2)$$

$$\frac{\partial}{\partial n_y} (\sigma^2 - \lambda(|\hat{\mathbf{n}}|^2 - 1)) = 0 \quad (2.3)$$

$$\frac{\partial}{\partial n_z} (\sigma^2 - \lambda(|\hat{\mathbf{n}}|^2 - 1)) = 0 \quad (2.4)$$

which yields the following:

$$\sum_{\nu=1}^3 M_{\mu\nu}^B n_\nu = \lambda n_\mu \quad (2.5)$$

$M_{\mu\nu}^B$ is the magnetic variance matrix such that $M_{\mu\nu}^B := \langle B_\mu B_\nu \rangle - \langle B_\mu \rangle \langle B_\nu \rangle$, where $\mu, \nu = 1, 2, 3$ represents the components x, y, z in Cartesian coordinates from the

original system geometry (B. U. Ö. Sonnerup & Scheible, 1998). The eigenvectors $\hat{\mathbf{n}}$ form the orthonormal set of variance directions: maximum, intermediate and minimum corresponding to the maximum, intermediate and minimum eigenvalues. The minimum variance corresponds to the unit vector normal to the transition layer, while the intermediate and maximum variance directions are co-planar to the transition layer.

In this research variance analysis is also used to determine the wave propagation direction (i.e. the unit wave vector $\hat{\mathbf{k}}$) and the unit vector normal to the magnetopause \mathbf{N} . For the determination of the propagation direction of a plane wave, the minimum variance direction corresponds to $\hat{\mathbf{k}}$, while the intermediate and maximum variance directions are co-planar to the wave fronts. And for the determination of \mathbf{N} , the minimum variance direction corresponds to \mathbf{N} while the intermediate and maximum variance directions correspond to \mathbf{L} and \mathbf{M} respectively as depicted in Figure 2.3.

One limitation of the variance analysis is that it has an 180° ambiguity and thus further information of the system is required in order to resolve this ambiguity. For example, multiple spacecraft measurements of the same wave signal along with Doppler shift information may help to resolve the 180° ambiguity.

2.3 Kinetic Theory

To this point, we have discussed ideal and resistive MHD plasmas because it is generally an adequate approximation for a broad range of space plasma systems. However, kinetic theory offers a much more accurate description of a plasma, including individual particle motion and it is the foundation for deriving the MHD model. In this section, we will discuss the full kinetic theory and how it leads into the multi-fluid and single fluid (MHD) approximations.

Kinetic theory treats the plasma as species-specific distributions in the six-dimensional \mathbf{v} - \mathbf{x} phase space, defined by the independent, three-dimensional velocity and position vectors

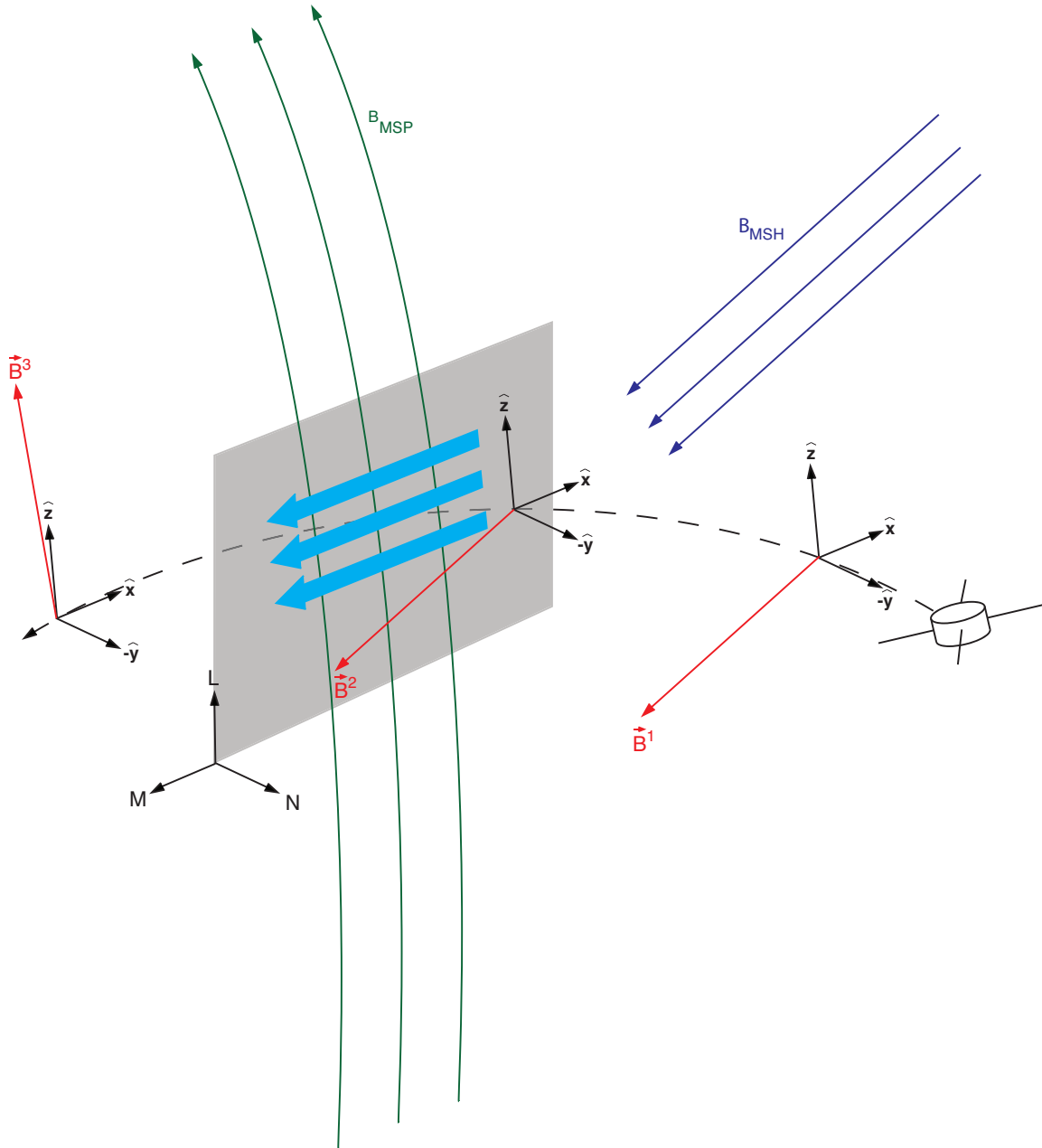


Figure 2.3: Illustration of three-point measurement MVAB to determine LMN coordinate system.

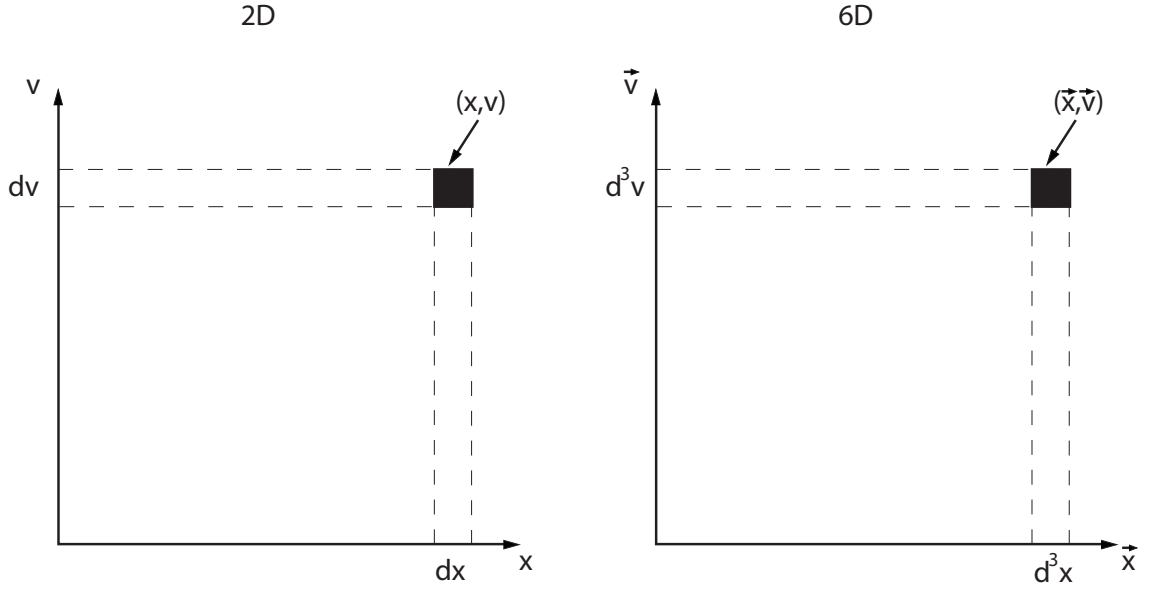


Figure 2.4: .

(see Figure 2.4). Consider a collection of plasma such that the number of particles of species s , N_s , is attained by integrating over its distribution function, $f_s(\mathbf{x}, \mathbf{v}, t)$.

$$N_s = \int_V f_s(\mathbf{x}, \mathbf{v}, t) d^3x d^3v \quad (2.6)$$

Where \mathbf{v} and \mathbf{x} are independent variables. The conservation of particles moving with volume V is conserved and therefore the $\frac{dN_s}{dt} = 0$. Differentiating Equation 2.6 with respect to time gives the following

$$\frac{d}{dt} \int_V f_s(\mathbf{x}, \mathbf{v}, t) d^3x d^3v = \int_V \left[\frac{\partial f_s}{\partial t}(\mathbf{x}, \mathbf{v}, t) + \mathbf{v} \cdot (\nabla_{\mathbf{x}} f_s) + \frac{\mathbf{F}}{m} \cdot (\nabla_{\mathbf{v}} f_s) \right] d^3x d^3v = 0 \quad (2.7)$$

Taking the force to be the full Lorentz Force, $F = q_s(\mathbf{E} + \mathbf{v} \times \mathbf{B})$, Equation 2.7 reduces to the Vlasov equation.

$$\frac{\partial f_s}{\partial t}(\mathbf{x}, \mathbf{v}, t) + \mathbf{v} \cdot \nabla_x f_s + \frac{q_s}{m}(\mathbf{E} + \mathbf{v} \times \mathbf{B}) \cdot \nabla_v f_s = 0 \quad (2.8)$$

Equation 2.8 is often referred to as the collisionless Boltzmann equation. For a magnetized plasma, solving the non-linear Vlasov equation coupled with Maxwell's equations is a daunting task at best. Landau offered a solution for a homogenous Maxwellian plasma in the electrostatic limit using linear perturbation theory and residue calculus. Landau's solution provided a real and imaginary component, or dispersion relations; the real part is the dispersion relation for the electrostatic Langmuir wave, while the imaginary part represents the growth rate for Landau damping. As noted earlier the dispersion relation of a wave relates the frequency to its wavevector \mathbf{k} . Dispersion relations are unique to each wave mode and thus can serve as an invaluable tool in wave mode identification in plasma physics. In general, the approximations placed on a plasma restrict the resultant solution to a particular behavior.

Case in point is the Langmuir wave, which is the description of an electron-scale wave which propagates parallel to the magnetic field. In order to find the dispersion relation of such a wave Landau assumed that no ambient fields were present, forced the magnetic fluctuations to zero, and neglected ion effects. The electrostatic limit with zero magnetic fluctuations reduces the field equations to Poisson's equation $\mathbf{E} = -\nabla\psi$. Furthermore, Landau placed a limitation on the plasma such that the plasma response was dependent on small time scales, thus neglecting ion motion and its subsequent effects. Using Maxwellian distributed electrons forces damping, as there isn't available energy to generate positive growth rate.

For magnetized plasmas, a general dispersion relation can be obtained from combining Ampere's Law ($\nabla \times \mathbf{B} = \mu_0 \mathbf{j}$) and the Faraday's Equation ($\nabla \times \mathbf{E} = -\delta \mathbf{B} / \delta t$) to obtain the following expression:

$$\nabla \times \nabla \times \mathbf{E} = -\mu_0 \frac{\delta}{\delta t} \mathbf{j} \quad (2.9)$$

Linearization of Equation 2.9 and the plane wave approximation yields the following:

$$\left[\left(k^2 - \frac{\omega^2}{c^2} \right) \underline{\underline{\mathbf{I}}} - \mathbf{k}\mathbf{k} \right] |\delta \mathbf{E}(\omega, \mathbf{k})| = i\omega\mu_0 |\delta \mathbf{j}(\omega, \mathbf{k})| \quad (2.10)$$

And using the plane wave approximation of the linearized Ohm's Law $\underline{\underline{\boldsymbol{\sigma}}}(\omega, \mathbf{k}) |\delta \mathbf{E}(\omega, \mathbf{k})| = |\delta \mathbf{j}(\omega, \mathbf{k})|$, Equation 2.10 reduces to

$$\det \left[\frac{k^2 c^2}{\omega^2} \left(\frac{\mathbf{k}\mathbf{k}}{k^2} - \underline{\underline{\mathbf{I}}} \right) + \underline{\underline{\boldsymbol{\epsilon}}}(\omega, \mathbf{k}) \right] = 0 \quad (2.11)$$

Where $\underline{\underline{\boldsymbol{\epsilon}}}$ is the dielectric tensor, and is defined by the following:

$$\underline{\underline{\boldsymbol{\epsilon}}}(\omega, \mathbf{k}) = \underline{\underline{\mathbf{I}}} + \frac{i}{\omega\epsilon_0} \underline{\underline{\boldsymbol{\sigma}}}(\omega, \mathbf{k}) \quad (2.12)$$

The species specific distribution functions are included in the dielectric tensor. The dielectric tensor is dependent to type of plasma being described (e.g. a cold magnetized plasma) Dispersion surfaces are obtained from the non-trivial solutions to Equation 2.11; these dispersion surfaces describe linear wave propagation in an anisotropic magnetized plasma.

2.3.1 WHAMP

In this research, the Waves in an Homogeneous Anisotropic, Multicomponent Plasma (WHAMP) solver is used to solve the general dispersion relation from Equation 2.10 in §2.3. WHAMP uses a linearized derivation of the dielectric term from Equation 2.10 given by the following:

Table 2.1: **WHAMP input parameters.**

Parameter	Description	Unit
B	background magnetic field	nT
m	mass to proton mass ratio	-
n	density	cm^{-3}
T	temperature	eV
T_{\perp}/T_{\parallel}	anisotropy	-
Δ	depth of loss cone	-
α	size of loss cone	-
v_d/v_{th}	$V_{drift}/V_{thermal}$	-

$$\underline{\underline{\epsilon}} = \underline{\underline{\mathbf{I}}} - \sum_j \frac{\omega_{pj}^2}{\omega^2} \left[\underline{\underline{\mathbf{I}}} - \sum_{j=-\infty}^{\infty} \int d\vec{v} \underline{\underline{\mathbf{\Pi}}} \frac{\frac{n\omega_{cj}}{v_{\perp}} \frac{\partial}{\partial v_{\perp}} + k_{\parallel} \frac{\partial}{\partial v_{\parallel}}}{\omega - k_{\parallel} v_{\parallel} + n\omega_{cj}} f_j \right] \quad (2.13)$$

Where ω_{pj} is the plasma frequency, ω_{cj} if the gyro-frequency (or cyclotron frequency) and f_j is the distribution function for the j^{th} species. The matrix $\underline{\underline{\mathbf{\Pi}}}$ contains n^{th} order square Bessel functions of argument $k_{\perp} v_{\perp} / \omega_j$. WHAMP assumes the background magnetic field is in the z -direction and uses a coordinate system defined by orthogonal unit vectors $\hat{\mathbf{e}}_1$, $\hat{\mathbf{e}}_2$ and $\hat{\mathbf{e}}_3$ such that $\mathbf{B} = B\hat{\mathbf{e}}_3$, $\mathbf{v} = v_{\perp}^1 \hat{\mathbf{e}}_1 + v_{\perp}^2 \hat{\mathbf{e}}_2 + v_{\parallel} \hat{\mathbf{e}}_3$ and $\mathbf{k} = k_{\perp} \hat{\mathbf{e}}_1 + k_{\parallel} \hat{\mathbf{e}}_3$. WHAMP is capable of handling up to 10 species at once each with it's own unique distribution function. Furthermore, the input parameters can be adjusted to form non-Maxwellian distributions. Apart from the background magnetic field, each species has its own set of input parameters that directly effect its distribution function. Table 3.3 lists the set of input parameters for species j .

For species with a default Maxwellian distribution, the input parameters are listed in Table 2.2.

Along with the input parameters for each species listed in Table 3.3, a starting frequency and wavenumber range are required. The starting frequency is unit-less parameter, scaled by $1/\omega_c$ of the first species provided. The wavenumber range is unit-less vector array of the

Table 2.2: **WHAMP Maxwellian (default) parameters.**

Parameter	Default
T_{\perp}/T_{\parallel}	1
Δ	1
α	0
v_{\parallel}/v_{\perp}	0

form $[k_{\perp, start}, \delta k_{\perp}, k_{\perp, stop}]$ and $[k_{\parallel, start}, \delta k_{\parallel}, k_{\parallel, stop}]$; this parameter is scaled by ω_c/v_{th} of the first species provided.

If a solution exists for the specified input parameters in the given frequency and wavenumber range, WHAMP returns a unit-less complex-valued frequency matrix $Dim(\omega_{output}) = [length(k_{\parallel}), length(k_{\perp})]$ scaled by $1/\omega_c$; $\Re\{\omega_{output}\}$ is the dispersion surface and $\Im\{\omega_{output}\}$ is the growth rate surface. Positive growth rates suggest that energy is available from the plasma system to generate the wave, whereas negative growth rates suggests wave damping, where the wave energy is absorbed by the plasma. Non-Maxwellian particle distributions can provide energy required to generate wave modes, resulting in a positive wave growth. WHAMP outputs also include the wave electric and magnetic fields, that can be used to calculate ellipticity (please refer to §2.8).

To illustrate the abilities of WHAMP, let us model a plasma in the cusp region (Dombrowski et al., 2012), by making similar assumptions to Landau’s solution – a homogenous Maxwellian plasma with electron (temporal) scale plasma response – with the addition of an ambient magnetic field. This system can be modeled as a Maxwellian electron plasma in WHAMP, with input parameters defined by the following MATLAB script:

```
T = 2; % eV
n = 2149; % cm-3
m = 0; % electron/proton mass
PlasmaModel.B = 36.850e3; % nT
```

```

a = 1; % anisotropy
b = 0; % size of loss cone
d = 1; % depth of loss cone
vd = 0; % V_drift/V_thermal
PlasmaModel.Species = {...
struct('m',m,'n',n,'t',T,'a',a,'b',b,'d',d,'vd',vd)...
};
fstart = 2*pi*10e3/w_ce;
kperp = [-4 .08 0];
kpar = [-4 .03 0];
varyKzFirst = 1;
useLog = 1; % 1 input log10(kpar) and log10(kperp)
           % 0 input given as kpar and kperp
maxIterations = 100;
InputParameters = {...
struct('fstart',fstart,'kperp',kperp,'kpar',kpar,...
'varyKzFirst',varyKzFirst,'useLog',useLog,...
'maxIterations',maxIterations)...
};

```

The $\Re\{\omega_{output}\}-\vec{k}$ dispersion surface is shown in Figure 2.5. The surface color represents the ellipticity of the wave mode; an ellipticity of "-1" (dark blue) represents a left-hand circular polarization, "0" (white) represents a linear polarisation and "+1" represents a right-hand circular polarization. This dispersion surface describes the Langmuir-Whistler modes (Dombrowski et al., 2012). The Whistler modes are represented by the strong right hand polarization (bright red spot in Figure 2.5) whereas the Langmuir waves are more

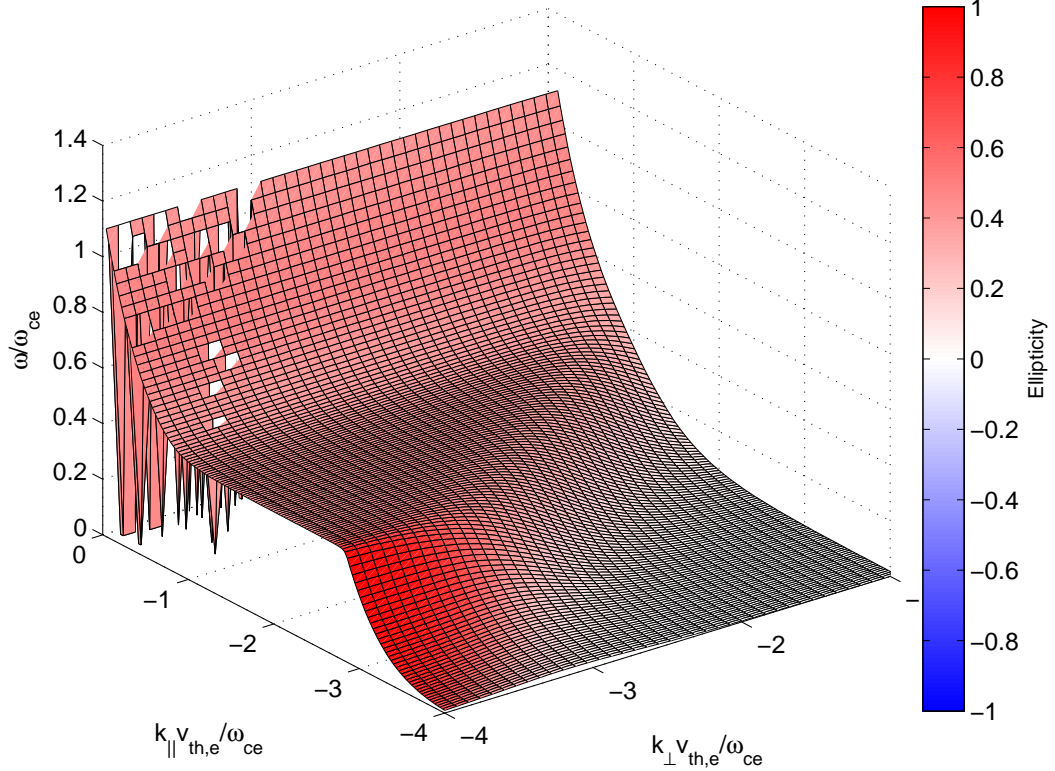


Figure 2.5: WHAMP dispersion surface for Langmuir-Whistler Modes. Shading represents wave ellipticity from left-handed circular polarized (strong blue) to linear polarized (white) to right-hand circular polarized (strong red).

linearly polarized. One of the limitations of WHAMP, is that it is only able to form a single solution for each $\omega_{output}(k_{\parallel}, k_{\perp})$, when in fact many solutions may exist in the "full" solution to the general dispersion relation. In the context of our example, the dispersion surface shows two distinct wave modes as a single dispersion surface instead of multiple distinct surfaces.

The theoretical dispersion relation for the electrostatic Langmuir wave mode is compared to a cut from the WHAMP solution by Figure 2.6. The cut taken from the 2-D dispersion surface is obtained for approximately $k_{\parallel} v_{th,e} / \omega_{ce} > -3$ and $k_{\perp} v_{th,e} / \omega_{ce} \approx -4$. Slight

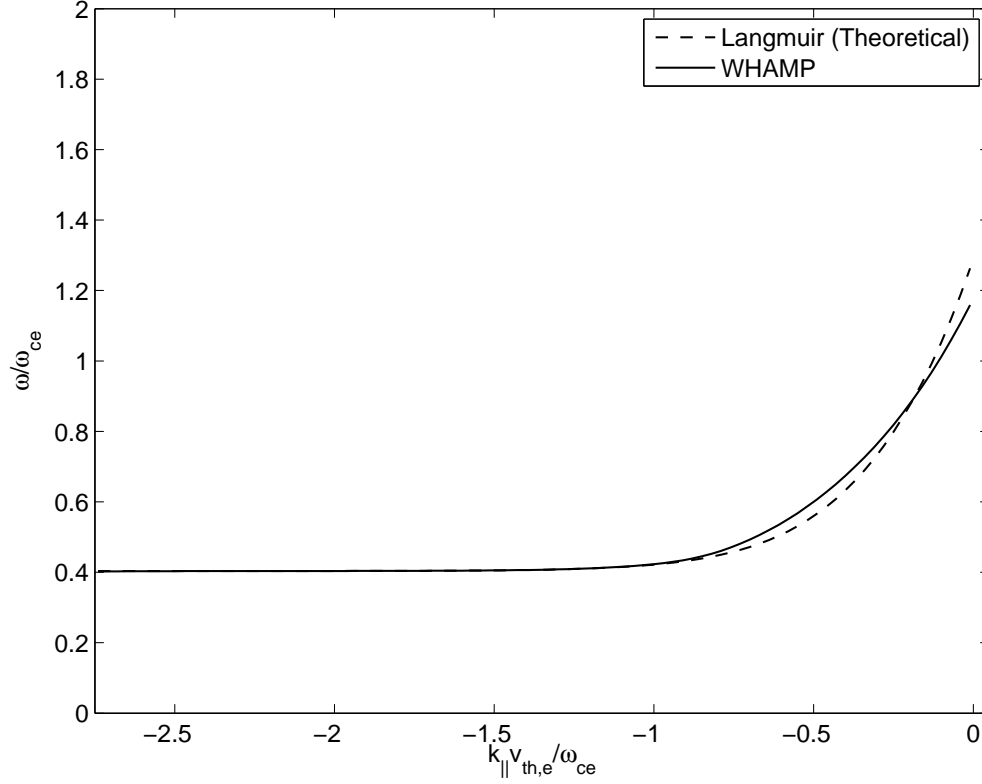


Figure 2.6: Comparison of theoretical dispersion relation to slice from WHAMP dispersion surface for $k_{\parallel} \gg k_{\perp}$.

discrepancies between the WHAMP cut and the theoretical dispersion for $k_{\parallel}v_{th,e}/\omega_{ce} > -1$ depicted in Figure 2.6 can most likely be attributed to taking a cut with a varying k_{\parallel} and constant k_{\perp} , such that $k \neq k_{\parallel}^2 + k_{\perp}^2$. In practice, a cut would be taken at a constant propagation angle θ_{kB} , ensuring that $k \approx k_{\parallel}^2 + k_{\perp}^2$.

2.3.2 MHD Physics

As mentioned throughout the text, there are much more simplistic descriptions of a plasma system, with the caveat of sacrificing some of the “less important” physics. Plasma proper-

ties such as velocity, number density and etc. for species s are derived by taking moments of the distribution function $f_s(\mathbf{x}, \mathbf{v}, t)$ (e.g. integrating the distribution function over velocity space). For example the number density n_s is the zeroth moment of the distribution function.

$$n_s(\mathbf{x}, t) = \int_V f_s(\mathbf{x}, \mathbf{v}, t) d^3v \quad (2.14)$$

The first and second moments of the distribution function are the bulk velocity and energy shown in Equations 2.15 and 2.16 respectively.

$$\mathbf{V}_s(\mathbf{x}, t) = \frac{1}{n_s} \int_V \mathbf{v} f_s(\mathbf{x}, \mathbf{v}, t) d^3v \quad (2.15)$$

$$E_s(\mathbf{x}, t) = \frac{1}{n_s} \int_V \frac{1}{2} m_s v^2 f_s(\mathbf{x}, \mathbf{v}, t) d^3v \quad (2.16)$$

Taking moments of the Vlasov equation leads to a fluid description of the plasma. In doing so, the velocity distribution of the plasma is lost in fluid theory, replaced with a value averaged over velocity space. The zeroth moment of the Vlasov equation is given by the following equation:

$$\int_V \left[\frac{\partial f_s}{\partial t}(\mathbf{x}, \mathbf{v}, t) + \mathbf{v} \cdot \nabla_x f_s + \frac{q_s}{m} (\mathbf{E} + \mathbf{v} \times \mathbf{B}) \cdot \nabla_v f_s \right] d^3v = 0 \quad (2.17)$$

which reduces to the fluid continuity equation for a collisionless plasma shown in Equation 2.18.

Continuity (Fluid)

$$\frac{\partial n_s}{\partial t} + \nabla \cdot (n_s \mathbf{V}_s) = 0 \quad (2.18)$$

Similarly the first and second moments of the Vlasov equation reduce to the Momentum

Equation (Equation 2.19) and the Energy Equation (Equation 2.20) respectively.

Momentum (Fluid)

$$\frac{\partial}{\partial t}(\rho_s \mathbf{V}_s) + \nabla \cdot (\rho_s \mathbf{V}_s \mathbf{V}_s) = \frac{q_s}{n_s}(\mathbf{E} + \mathbf{V}_s \times \mathbf{B}) - \nabla \cdot \underline{\underline{\mathbf{P}_s}} \quad (2.19)$$

$\underline{\underline{\mathbf{P}_s}}$ is the second-order pressure tensor defined by $m_s \int_V (\mathbf{v} - \mathbf{V}_s)^2 f_s d^3v$.

Energy (Fluid)

$$\frac{1}{\gamma - 1} \left(\frac{\partial}{\partial t} p_s + \nabla \cdot (p_s \mathbf{V}_s) \right) = -(\underline{\underline{\mathbf{P}_s}} \cdot \nabla) \cdot \mathbf{V}_s - \nabla \cdot \mathcal{L} \quad (2.20)$$

Where p_s is the scalar pressure, \mathcal{L} is the heat flux defined by $\frac{1}{2} m_s \int_V (\mathbf{v} - \mathbf{V}_s)^3 f_s d^3v$, and γ is the ratio of specific heats ($\gamma = 5/3$ for an adiabatic equation of state).

The two-fluid approximation treats the plasma as electron and ion fluids. To simplify a plasma system even further, one can reduce the two-fluid approximation into a single fluid approximation – this is the MHD approximation. This single fluid description of the plasma is derived from the two-fluid approximation by combining the electron and ion fluid equations separately and defining the current density, total mass density and combined momentum as follows:

Current Density

$$\mathbf{j} = e(\mathbf{V}_i - \mathbf{V}_e) \quad (2.21)$$

Total Mass Density

$$\rho = n(m_i + m_e) \quad (2.22)$$

Combined Momentum

$$\rho \mathbf{u} = n(m_i \mathbf{u}_i + m_e \mathbf{u}_e) \quad (2.23)$$

Thus the MHD equations of motion are as follows:

Continuity (MHD)

$$\frac{\partial \rho}{\partial t} + \nabla \cdot (\rho \mathbf{u}) = 0 \quad (2.24)$$

Momentum (MHD)

$$\frac{\partial \rho \mathbf{u}}{\partial t} + \nabla \cdot (\rho \mathbf{u} \mathbf{u}) = -\nabla p + \mathbf{j} \times \mathbf{B} \quad (2.25)$$

Generalized Ohm's Law (MHD)

$$\mathbf{E} + \mathbf{u} \times \mathbf{B} = \frac{m_e m_i}{e^2 \rho} \left[\frac{\partial \mathbf{j}}{\partial t} + \nabla \cdot (\mathbf{u} \mathbf{j} + \mathbf{j} \mathbf{u}) \right] - \frac{M}{\epsilon \rho} \nabla p_e + \frac{m_i}{e \rho} \mathbf{j} \times \mathbf{B} + \eta \mathbf{j} \quad (2.26)$$

Equations 2.24, 2.25, 2.26 and the Energy Equation (not shown) define a single fluid plasma that is isotropic (thermal scalar pressure) and neutral ($n = n_i = n_e$). Maxwell's equations combined with the single fluid equations (including the single fluid energy equation) comprise the MHD description of a plasma. Equation 2.26 is called the Generalized Ohm's Law. From the right hand side of Equation 2.26, the first term is the electron inertial term, the second term is the electron pressure term, the third term is the Hall term and the fourth term is the resistivity. The resistivity η from the resistivity term is produced by particle-wave interactions in the real system. In the resistive MHD approximation the numerical resistivity parameter is set to zero and is switched on when the critical current density reaches a critical threshold. At certain length scales, it is often sufficient sufficient to drop most of the terms on the right hand side of the Generalized Ohm's Law. For ideal MHD all of the terms on the right hand side are dropped so that Equation 2.26 reduces to $\mathbf{E} + \mathbf{u} \times \mathbf{B} = 0$. Taking $\underline{\underline{\mathbf{P}}} = p \underline{\underline{\mathbf{I}}}$ and assuming zero heat flux ($\nabla \cdot \mathcal{L}$), the Energy Equation reduces to:

Energy (Ideal MHD)

$$\frac{\partial p}{\partial t} = -\mathbf{u} \cdot p - \gamma p \nabla \cdot \mathbf{u} \quad (2.27)$$

The ideal MHD approximation is sufficient for most astrophysical plasmas, however it

does not retain the physics necessary for small scale processes such as diffusion and magnetic reconnection. As discussed in §1.3.1, magnetic reconnection violates the frozen-in condition given by the $\mathbf{u} \times \mathbf{B}$ term. In order to describe a system in which magnetic reconnection occurs, at the very least the resistive term must be included, thus a resistive MHD approximation of the plasma becomes necessary. The resistive Ohm's Law is $\mathbf{E} + \mathbf{u} \times \mathbf{B} = \eta \mathbf{j}$. From the resistive MHD approximation (resistive Ohm's law), the resistive form of the energy equation can be written as shown in Equation 2.28.

Energy (Resistive MHD)

$$\frac{1}{\gamma - 1} \left(\frac{\partial}{\partial t} p + \nabla \cdot (p\mathbf{u}) \right) = -\nabla p \cdot \mathbf{u} - \eta \mathbf{j}^2 \quad (2.28)$$

2.4 Local 2-D MHD Simulations

In-situ satellite observations coupled with physical models are at the foundation of many published KHI studies. Observations alone are not always sufficient for identifying KHI at the magnetopause; signatures such as bipolar variation in the normal (to the magnetopause) component of the magnetic field and faster than sheath flow are good indications of KH waves, however flux transfer events (FTEs) have been known to produce similar signatures (Russell & Elphic, 1979). FTE observations have shown bipolar variation in B_N (Paschmann et al., 1982) as well as faster than sheath flow for the magnetosphere plasma (Korotova et al., 2009). Additionally, trains of flux transfer events can even produce quasi-periodic structures with periods similar to KH waves. A study of International Sun-Earth Explorer (ISEE) magnetopause crossings on the dayside magnetosphere showed that the observed FTEs had a mean periodicity of 3 minutes and a mode of just 3 minutes (Lockwood & Wild, 1993).

Simulating the magnetopause boundary with a physical model can be an invaluable

application to test whether or not the interface separating the magnetospheric and magnetosheath plasma is unstable to KHI. Ideally a global, fully-kinetic model encompassing the dynamic solar wind, bow shock, magnetosheath and entire magnetosphere would be the ultimate simulation, however is infeasible due to computational restrictions. A more computationally reasonable approach is to use a local 2-D MHD model (Otto & Fairfield, 2000; Nykyri & Otto, 2001; Nykyri et al., 2006). Although MHD has its limitations, it is a powerful tool when applied within its limiting boundaries. In this research a well accepted local 2-D MHD local model (Otto & Fairfield, 2000; Nykyri & Otto, 2001; Nykyri et al., 2006) is used to validate Cluster observations of KHI in the LLBL.

The 2D simulation window is comprised of a boundary separating 2 plasma (and magnetic field) regions. For the purpose of this work, these 2 plasma regions and the boundary which separates them represent the magnetospheric and magnetosheath plasmas and the magnetopause, respectively. The simulation box corresponds to the low-latitude magnetospheric flanks. The initial conditions for defining the simulation plane are assembled via careful analysis of the shear flow geometry in the region where the instability is observed. For each side of the boundary, the magnetic field initial conditions are given by $B_{x0} = B \sin \psi$, $B_{y0} = 0$, $B_{z0} = B \cos \psi$, where ψ is the angle between the unperturbed magnetic field and the direction normal to the shear flow plane (Nykyri, 2013) (see Figure 2.7). The direction of the shear flow is in the direction of the MSH plasma velocity, as this is where the dominant flow exists; the magnitude of the shear flow is calculated by taking the difference in the magnitudes of the observed MSH plasma velocity and the MSP plasma velocity projected along the direction of the MSH plasma velocity. Distribution of the initial density, pressure, velocity and magnetic field magnitudes across the simulation grid are defined by hyperbolic tangent profiles (Otto & Fairfield, 2000) as depicted in Equations 2.29, 2.30, 2.31 and 2.32 respectively. The simulation is seeded by initial velocity perturbations perpendicular to the boundary separating the MSP and MSH plasmas.

$$\rho_0(x) = \frac{1}{2}(\rho_{msh} + \rho_{msp}) + \frac{1}{2}(\rho_{msh} - \rho_{msp})\tanh\left(\frac{y}{L_0}\right) \quad (2.29)$$

$$p_0(x) = \frac{1}{2}(p_{msh} + p_{msp}) + \frac{1}{2}(p_{msh} - p_{msp})\tanh\left(\frac{y}{L_0}\right) \quad (2.30)$$

$$v_0(x) = \frac{1}{2}(v_{msh} + v_{msp}) + \frac{1}{2}(v_{msh} - v_{msp})\tanh\left(\frac{y}{L_0}\right) \quad (2.31)$$

$$b_0(x) = \frac{1}{2}(b_{msh} + b_{msp}) + \frac{1}{2}(b_{msh} - b_{msp})\tanh\left(\frac{y}{L_0}\right) \quad (2.32)$$

The subscripts *msp* and *msh* correspond to the magnetospheric and magnetosheath sides of the simulation boundary respectively and L_0 is the length scale which corresponds to the width of the boundary layer (Otto & Fairfield, 2000; Nykyri & Otto, 2001). The KH wave length of the fastest growing mode is proportional to the boundary layer thickness, L ($\lambda (2-4)\pi L$) (Miura & Pritchett, 1982). The vortex size of the each mode is approximately 1/4 of the wave length of the mode.

In the 3D system, KH waves are not bound to the equatorial plane and may propagate wherever the onset condition is satisfied. Propagation of KH waves outside of the shear flow plane is accomplished in the 2D model by tilting the simulation window by an angle of ϕ , such that ϕ is the angle between the KH wave vector \mathbf{k}_{KHI} and the shear flow plane (see Figure 2.7).

The model is defined by a set of resistive MHD equations (Otto, 1990) which are discretized using a finite difference leap frog technique (Potter, 1973) over a non-uniform Cartesian grid with the highest resolution at the boundary layer. Selection of the time step and spatial grid resolution used in the numerical differentiation is restricted by the Courant-Friedrichs-Lewy condition to ensure that the numerical solution is physically valid. The

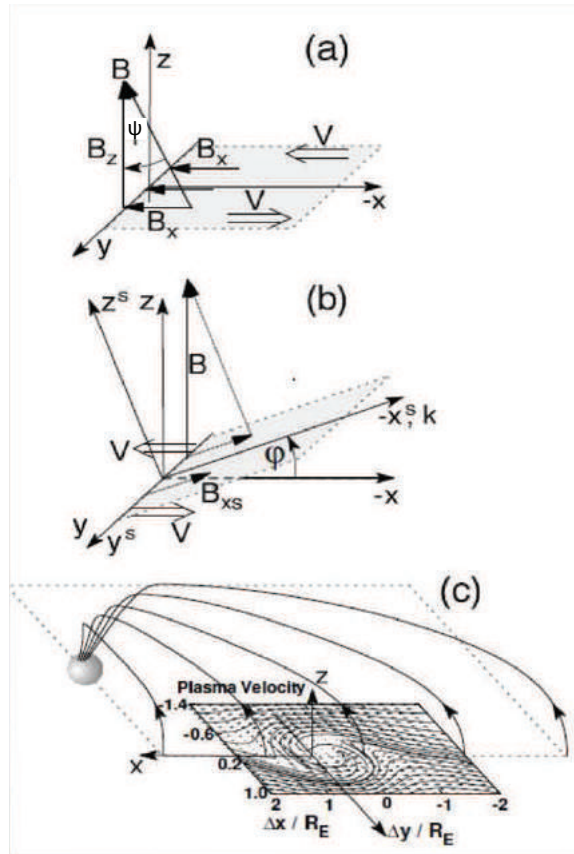


Figure 2.7: Schematic of the simulation plane (Otto & Nykyri, 2003); (Panel a) angle between the ambient magnetic field and direction normal to the shear flow plane, ψ ; (Panel b) the angle between \mathbf{k}_{KHI} , ϕ .

Courant-Friedrichs-Lewy condition states that the speed of information must not surpass a single grid cell in a single time step (Fletcher, 1988). To satisfy the Courant-Friedrichs-Lewy condition, the temporal δt and spatial δx , δy resolutions must be chosen such that following inequality is satisfied

$$v \frac{\delta t}{\delta x} + v \frac{\delta t}{\delta y} \leq C_{MAX} \quad (2.33)$$

where $v = \sqrt{v_A^2 + v_s^2}$. For an explicit finite difference method, $C_{MAX} = 1$.

2.5 Identifying High-Frequency Waves

Identifying intervals of high-frequency wave activity relative to the KH wave frequency is accomplished through analyzing (temporal) wavelet spectrograms performed on the high-resolution magnetic field data in the desired frequency range. The 22.4 Hz data capture rate of the Flux Gate Magnetometer (FGM) instrument onboard Cluster allows for spectrogram analysis of up to ≈ 11.2 Hz.

In order to capitalize on the most ion heating rich regions, the ion mixing regions are identified in order to conduct a search for high-frequency wave activity. H. Hasegawa et al. (2009) has shown evidence of three distinct ion energy populations during an extended interval when the magnetopause boundary was under KHI: (1) low-energy MSH-like ion centered about 1 keV, (2) high-energy MSP-like ions centered about 10 keV and (3) a population with an energy range of $\approx 1 - 10$ keV. It is in the mixed plasma region that we focus our search for enhanced wave activity because we hypothesize this to be the source region of ion-heating and the heating mechanism. Various filtering techniques (i.e. low-pass, high-pass and band-pass filtering) are applied to the high-resolution magnetic field data in the regions of enhanced wave activity inside the ion mixing regions. Filtering out

the lower amplitudes and waves with frequencies outside the desired range from the signal makes for easier identification of wave packets, under the assumption that the signal is a linear superposition of the waves present in the data. One must take precaution when using frequency filtering, as artifacts due to bleeding across spectral peaks and instrument induced effects due to spacecraft spin and data capture rate frequencies can present themselves in the data.

2.6 Experimental Dispersion Relation

The wave vector magnitude of an electromagnetic wave can be determined experimentally by the observed phase shift between two spacecraft with the limitation that the spacecraft separation is on the order of the observed wavelength (Balikhin et al., 1997; Dimmock et al., 2013). The phase shift of an electromagnetic wave passing through two spatially separated spacecraft is given by the following relation:

$$\Psi(\omega_1) = \vec{\mathbf{k}}(\omega_1) \cdot \vec{\mathbf{R}} = |\vec{\mathbf{k}}(\omega_1)| |\vec{\mathbf{R}}| \cos(\theta_{kR}) \quad (2.34)$$

Where $\Psi(\omega_1)$ is the phase shift and θ_{kR} is the angle between wave vector $\vec{\mathbf{k}}(\omega_1)$ and the separation vector $\vec{\mathbf{R}}$. The phase shift is estimated by taking the (spatial) wavelet transform of the magnetic field and $\hat{\mathbf{k}}$ is determined via MVAB B. U. O. Sonnerup & Cahill (1967) and the corresponding multi-spacecraft geometry (e.g which spacecraft observes the wave first).

For each frequency bin, the full wave vector can be reconstructed and thus the dispersion relation can be resolved in the spacecraft frame. Applying a Doppler shift transform to the frequencies in the spacecraft frame ω , yields the plasma rest frame frequencies ω_1 (see

Equation 2.35).

$$\omega_1 = \omega + \vec{\mathbf{k}}(\omega_1) \cdot \vec{\mathbf{V}} \quad (2.35)$$

Where $\vec{\mathbf{V}}$ is the measured plasma velocity. This experimentally determined dispersion relation can be compared with a theoretical dispersion relation and in combination with other wave properties such as the polarization, polarity and propagation angle, the plasma wave mode can be identified.

2.7 Statistical Study

2.7.1 Data Binning Process

Events Selection

The KHI database was populated from a list of previously published KH events, validated with simulations (based on observational data) leading to the onset of KHI, with varying IMF configurations. This database contains five dawn-flank events – one mixed PS-OPS IMF event (Nykyri et al., 2006), two PS IMF events (Moore, 2012; Moore et al., 2016) and two OPS IMF events (Moore, 2012; Moore et al., 2016) – and one dusk flank event under northward IMF (H. Hasegawa, Fujimoto, Phan, et al., 2004). Observations consistent with KHI are quasi-periodic variations in the plasma and field parameters including anti-correlated density and temperature, bipolar variation of the magnetic field component normal to the magnetopause, total pressure variations, with strong pressure minimums at the center of the vortex.

For the non-KHI database, the Cluster Science Archive was searched for boundary crossing which did not exhibit observations commonly associated with KHI. It is worth noting that although the non-KHI database consists of events which lack observations consistent

KHI, there is currently no way to exclude the possibility that KHI was previously acting on the magnetopause boundary.

The total time duration of observations is about ≈ 12.5 hrs for KH events and ≈ 13 hrs for non-KH events. The discrepancy in times is taken into account in various statistics by including a weighting factor.

Data Binning

In order to perform statistics on boundary crossings during KHI activity, the data is binned with respect to ion energy level. Fluctuations in ion energies between cold-component and hot-component ions of magnetosheath and magnetospheric origin respectively as well as a mixed population of moderate energies has been observed during periods of KHI (H. Hasegawa, Fujimoto, Phan, et al., 2004). Thus, ion energies are separated into three levels – magnetosphere (MSP), magnetosheath (MSH) and mixed (MIX) levels – representative of their corresponding plasma regions. Determination of these energy level values (and subsequent plasma region bin) is based on statistical analysis of the ion distribution in flux-energy space over the event interval. This is performed systematically for each event. The ion energy spectrogram data from the Hot Ion Analyzer (HIA) on board Cluster Spacecrafts 1 and 3 have been obtained from the Cluster Science Archive.

Peaks in the flux-energy distribution are stored for each time stamp and used to construct a frequency (occurrence) distribution of observed ion energies. By careful examination of the peaks in the ion energy frequency distributions along with associated temperature, number density and total pressure profiles, two thresholds are determined corresponding to two out of the three MSP, MIX and MSH plasma profiles. The third threshold is calculated, such that $E_{MIX}^{bin} = AVG_{\log_{10}}(E_{MSH}^{bin}, E_{MSP}^{bin})$.

A pictogram illustrating how the binning algorithm is implemented to select the energy levels for the MSH, MIX and MSP bins is shown for the June, 6th 2002 event in Figure 2.8.

The top panel of Figure 2.8 shows an overlay of the flux-energy distributions for the entire hour interval from the June 6th 2002 event. From the middle panel of Figure 2.8, it is apparent that E_{MSH}^{bin} and E_{MSP}^{bin} are statistically determined to be 722 eV and 9.90×10^3 eV respectively. Therefore E_{MIX}^{bin} is calculated to be the \log_{10} -average of the MSP and MSH energy levels, 2.67×10^3 eV.

For data to be sorted into its appropriate plasma region (energy level bin), the corresponding ion energy needs to be assessed for each time stamp; this is accomplished systematically. For each time stamp, the ion energy weighted average is calculated in \log_{10} -space, such that $AVG_{\log_{10}}(KE) = \frac{\sum_{i=1}^N KE_i * KE_{flux,i}}{\sum_{j=1}^N KE_{flux,j}}$. The $AVG_{\log_{10}}(KE)$ from each time stamp from the June 6th 2002 event are plotted in the bottom panel of Figure 2.8 along with the energy bin thresholds. The resulting weighted average is then sorted into its appropriate energy bin by taking the minimum (absolute) difference between the three thresholds; e.g. for time stamp τ , its corresponding energy bin is determined by the minimum difference of the ion energy thresholds $\min(|AVG_{\log_{10}}(KE^\tau) - \log_{10}([E_{MSH}^{bin} E_{MIX}^{bin} E_{MSP}^{bin}]|)|)$. Figure 2.9 shows qualitatively how the binning algorithm sorts into the three plasma region bins.

2.7.2 Ion-scale MVAB Wave Intervals

In order to collect information on the propagation angle θ_{kB} between the wave (unit) vector \hat{k} and the background magnetic field \mathbf{B} , a sliding window minimum variance analysis on the high-pass filtered 22.4 Hz magnetic field (MVAB) is performed. The (temporal) length of the window Δt is proportional to the desired frequency such that $\Delta t = 1/(2f_j)$ where j is the j^{th} -index of the frequency array. A step size equal to 50% of Δt is used allowing for some overlap. The frequency array is a power of two distribution of frequencies ranging from 0.05 Hz to 2.7 Hz.

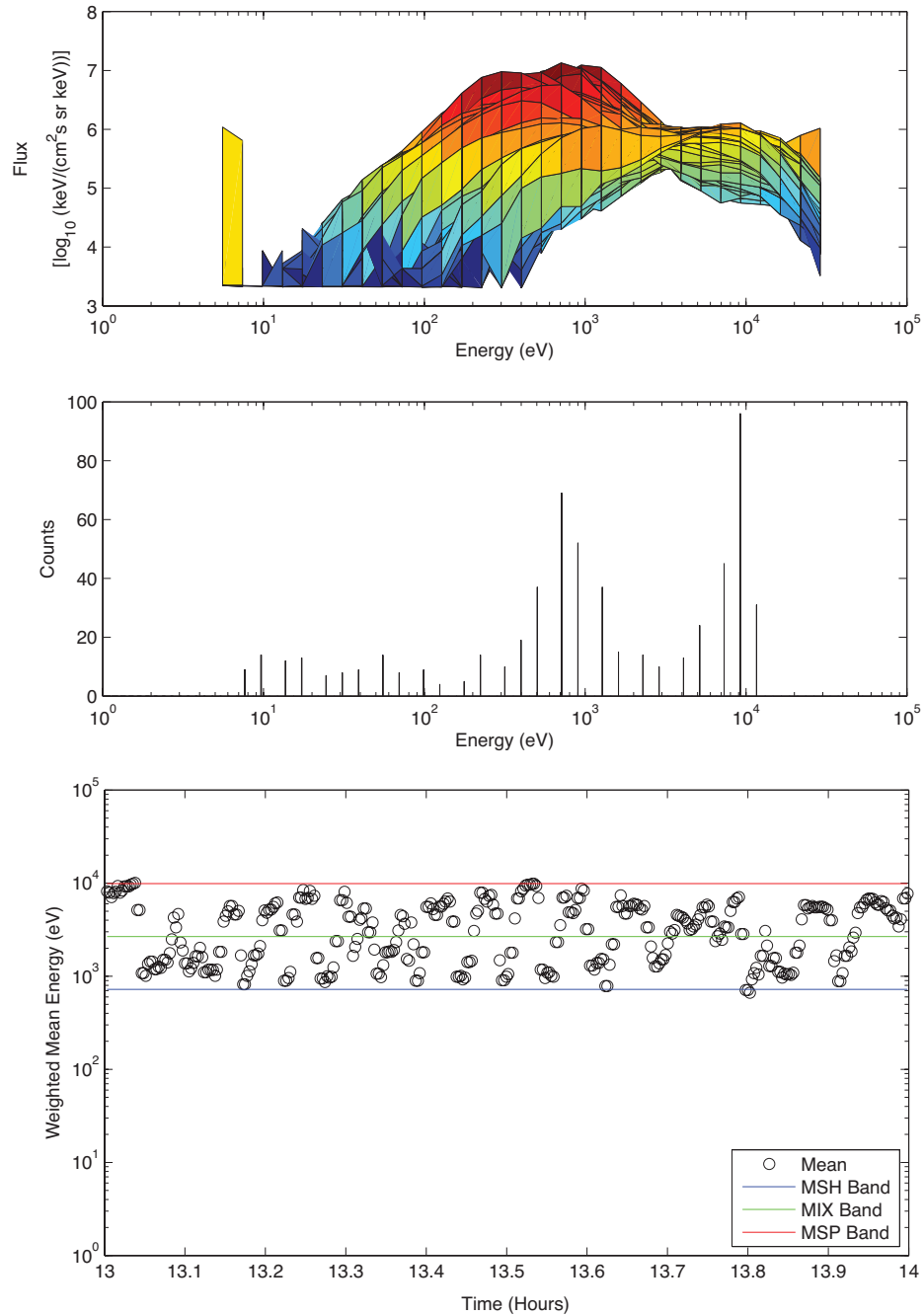


Figure 2.8: Statistical Determination of Energy Levels. Overlay of ion flux-energy distributions of from all time stamps (top panel); ion energy frequency distribution (middle panel); and weighted mean energy for each time stamp (bottom panel).

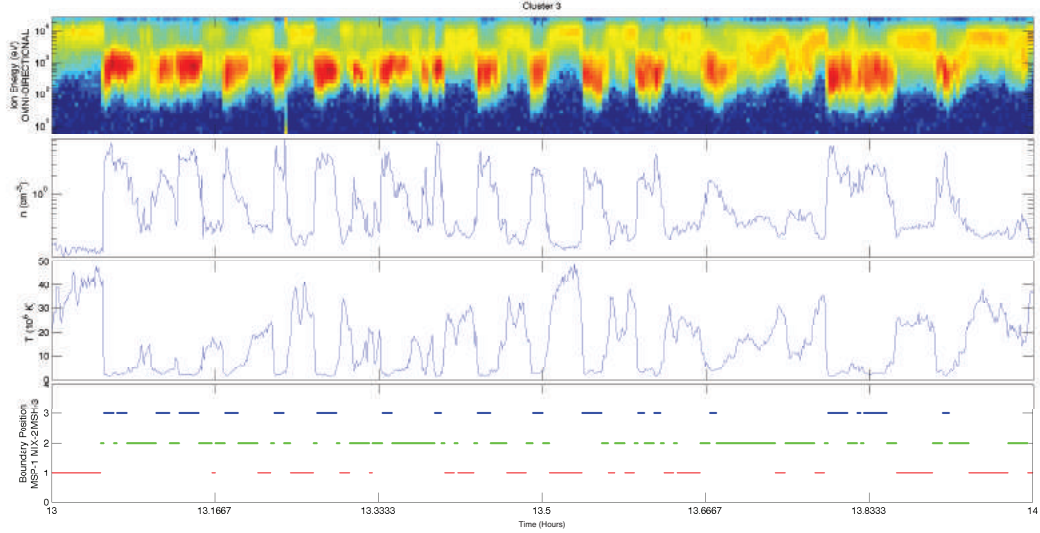


Figure 2.9: Binning algorithm output. A plot of the plasma parameters relative to its plasma region sorting (bottom panel) by the binning algorithm for the June 6th 2002 event.

For data integrity only MVAB wave intervals with an eigenvalue ratio $\lambda_{int}/\lambda_{min} > 5$ are retained. Furthermore, only well polarized MVAB wave intervals ($\sqrt{\lambda_{int}/\lambda_{max}} > 0.5$) are retained for computing statistics.

2.8 Ellipticity Calculation

Almost as important to wave identification as a dispersion relation is a plasma waves' ellipticity. For electromagnetic waves, the ellipticity describes the polarity and handedness of a wave with respect to its propagation direction \mathbf{k} . Together they define how the wave fields (e.g. $\delta\mathbf{B}(\mathbf{x}, t)$) oscillate in time with respect to \mathbf{k} . For a plane wave, the handedness describes the direction in which the field vectors "rotate" about \mathbf{k} in the plane perpendicular to \mathbf{k} ; in other words right-hand and left-hand waves follow the right-hand and left-hand rules respectively, where the thumb points in the direction of \mathbf{k} .

Suppose an electromagnetic wave is propagating in the positive z -direction, with magnetic field oscillations bound to the xy -plane such that $\mathbf{k} = k\hat{z}$, $\mathbf{B} = B_0\hat{z}$ and

$$\delta\vec{B} \approx B_0[\cos(\omega t)\hat{x} + \sin(\omega t)\hat{y}] \quad (2.36)$$

The trace of the magnetic field vector about \mathbf{k} is shown in the left panel of Figure 2.10. However, in plasma physics and in the context of this thesis, we are more concerned with the polarization relative to the ambient magnetic field. In this case, the trace of the magnetic field about the background (ambient) magnetic field \mathbf{B} can be determined by rotating the wave magnetic field $\delta\mathbf{B}$ into the variance directions determined by MVAB. Thus the wave described in Equation 2.36 follows the right-hand rule with respect to the ambient magnetic field (pointing out of the page) as seen in the right panel of Figure 2.10. Although it might be tempting to use descriptors such as "clockwise" and "counter-clockwise", doing so will only lead to confusion. Descriptors like "clockwise" and "counter-clockwise" are frame dependent (e.g. source vs observer) and not particularly useful after rotating into the MVAB coordinates, especially when considering the angle between the wavevector and the ambient magnetic field θ_{kB} .

Wave polarity is analogous to eccentricity from Algebra, except a polarization of 1 represents circular polarization, 0 represents linear polarization and $polarity \in (0, 1)$ represents an elliptical polarization. Thus, the circular polarized electromagnetic wave from Equation 2.36 and Figure 2.10 has a polarity of 1.

The ellipticity can be extracted from satellite field measurements such as Cluster's FGM instrument. Although the ellipticity can be calculated from electric field measurements, Cluster's EFW instrument can only resolve the two-dimensional electric field in the spin plane. Subsequently the electric field component along the spin axis is derived from the ideal MHD approximation ($\mathbf{E} = -\mathbf{v} \times \mathbf{B}$) and thus some important physics in regions deviating

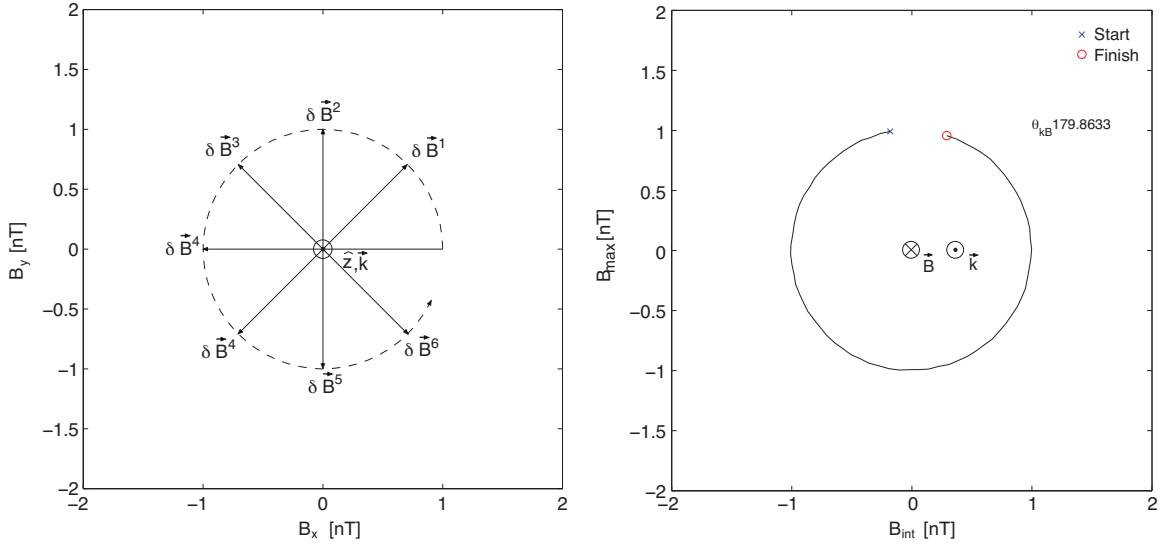


Figure 2.10: Trace of the wave magnetic field vector $\delta \mathbf{B}$ of an electromagnetic wave propagating with respect to the propagation direction \mathbf{k} (left panel) and trace of $\delta \mathbf{B}$ rotated into MVAB coordinates with respect to the ambient field \mathbf{B} .

from ideal MHD are lost. In this thesis, the ellipticity is calculated using the high resolution magnetic field data from Cluster's FGM instrument.

In this research, two methods are used to calculate the ellipticity: (1) *ellipticity*, ϵ described by Krauss-Varban et al. (1994) and (2) the *degree of ellipticity*, \mathcal{V}_p described by Carozzi et al. (2001). Both methods are dependent upon the wave fields (wavelet transform of the high resolution magnetic field) that have been rotated into a field-aligned (\mathbf{B}_{avg}) coordinate system. The \mathbf{B}_{avg} -aligned coordinate system is defined by a set of three orthonormal vectors, $\hat{\mathbf{e}}_{\parallel}$, $\hat{\mathbf{e}}_{\perp 1}$, $\hat{\mathbf{e}}_{\perp 2}$ such that $\hat{\mathbf{e}}_{\parallel}$ is parallel to \mathbf{B}_{avg} and $\hat{\mathbf{e}}_{\perp 1}$, $\hat{\mathbf{e}}_{\perp 2}$ are coplanar, perpendicular to \mathbf{B}_{avg} as illustrated in Figure 2.11. It turns out that the specific directions of the coplanar vectors $\hat{\mathbf{e}}_{\perp 1}$, $\hat{\mathbf{e}}_{\perp 2}$ in relation to the original coordinate system are arbitrary as long as $\hat{\mathbf{e}}_{\parallel}$ is parallel to \mathbf{B}_{avg} and together form a right handed coordinate system such that $\hat{\mathbf{e}}_{\parallel} \times \hat{\mathbf{e}}_{\perp 1} = \hat{\mathbf{e}}_{\perp 2}$.

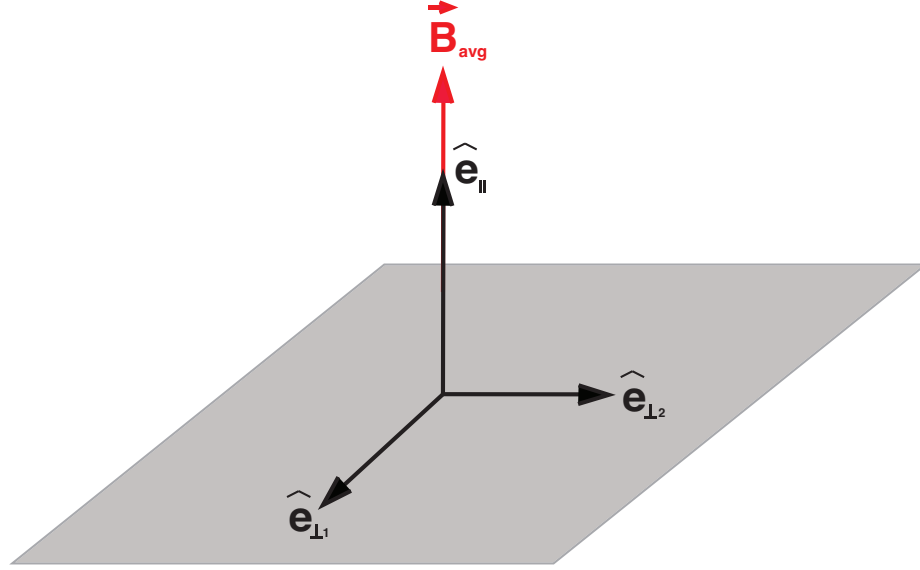


Figure 2.11: Orientation of the field-aligned coordinate system defined by the orthonormal vectors \hat{e}_{\parallel} , $\hat{e}_{\perp 1}$, $\hat{e}_{\perp 2}$.

Ellipticity ϵ

The ellipticity as defined by Krauss-Varban et al. (1994) essentially calculates the difference between the in right-hand circularly polarized and left-hand circularly polarized field powers, E_R and E_L respectively. E_R and E_L are defined by Equations 2.37 and 2.38 respectively, and the ellipticity is defined in Equation 2.39.

$$E_R = \frac{1}{\sqrt{2}}[\delta E_{\perp 1} + i\delta E_{\perp 2}] \quad (2.37)$$

$$E_L = \frac{1}{\sqrt{2}}[\delta E_{\perp 1} - i\delta E_{\perp 2}] \quad (2.38)$$

$$\epsilon = \Re\left\{\frac{E_R - iE_L}{E_R + iE_L}\right\} \quad (2.39)$$

Degree of Ellipticity \mathcal{V}_p

The Stoke's Parameters $[I \ Q \ U \ V]^T$ are quantities that describe the behavior of the oscillating field associated with an electromagnetic wave. I is the total (polarized and unpolarized) intensity; Q is the difference between horizontal linear and vertical linear polarized intensities; U is the difference between $+45^\circ$ and -45° linear polarized intensities; and V is the difference between right hand circular and left hand circular polarized intensities. Carozzi et al. (2001) formulated a set of Stoke's Parameters based on the wave fields for wide band polarimetry.

$$\begin{bmatrix} \mathcal{I} \\ \mathcal{Q} \\ \mathcal{U} \\ \mathcal{V} \end{bmatrix} = \begin{bmatrix} \delta E_{\perp 1}^2 + \delta E_{\perp 2}^2 \\ \delta E_{\perp 1}^2 - \delta E_{\perp 2}^2 \\ 2 \Re\{\delta E_{\perp 1} \delta E_{\perp 2}^*\} \\ 2 \Im\{\delta E_{\perp 1} \delta E_{\perp 2}^*\} \end{bmatrix} \quad (2.40)$$

The Stoke's Parameters from Equation 2.40 are used in this research to resolve the behavior of the wide band wave magnetic field ($\delta \mathbf{B} \in (0, 22.4/2 \text{ Hz}]$). More specifically the degree of ellipticity \mathcal{V}_p shown in Equation 2.41 is used to determine the handedness and polarity of the wave magnetic field with respect to \mathbf{B}_{avg} .

$$\mathcal{V}_p = \frac{\mathcal{V}}{\sqrt{\mathcal{Q}^2 + \mathcal{U}^2 + \mathcal{V}^2}} \quad (2.41)$$

Table 2.3 details how the ellipticity ϵ (Krauss-Varban et al., 1994) and degree of ellipticity \mathcal{V}_p (Carozzi et al., 2001) describe the motion of the wave field associated with a propagating wave.

Table 2.3: Ellipticity ϵ and degree of ellipticity \mathcal{V}_p ranges.

$\epsilon, \mathcal{V}_p \in$	Handedness	Polarity
-1	left	circular
(-1, 0)	left	elliptical
0	-	linear
(0, 1)	right	elliptical
1	right	circular

Field-Aligned Coordinate System

Because the ellipticity calculations are dependent upon the perpendicular wave-field components, the high-resolution wave magnetic field must first be rotated into a field aligned coordinate system (see Figure 2.11). A set of orthonormal basis vectors $\hat{\mathbf{e}}_{\parallel}$, $\hat{\mathbf{e}}_{\perp 1}$, $\hat{\mathbf{e}}_{\perp 2}$ that make up this field-aligned coordinate system are determined using the Gram-Schmidt Process. $\hat{\mathbf{e}}_{\parallel}$ is first established by calculating the unit-vector parallel to the ambient magnetic field from the smoothed low-resolution magnetic field data. Then an arbitrary vector is chosen such that it is not parallel to $\hat{\mathbf{e}}_{\parallel}$; this second vector is selected in practice by using the minimum (maximum) variance direction \mathbf{N} determined using MVAB (MVAE) to ensure a non-parallel vector to $\hat{\mathbf{e}}_{\parallel}$. The following algorithm shows how $\hat{\mathbf{e}}_{\perp 1}$ and $\hat{\mathbf{e}}_{\perp 2}$ are determined using the Gram-Schmidt process:

$$\begin{aligned} \mathbf{v}_2 &= \mathbf{N} \\ \hat{\mathbf{e}}_{\perp 1} &= \frac{\mathbf{v}_2 - \hat{\mathbf{e}}_{\parallel} \cdot \mathbf{v}_2}{\|\mathbf{v}_2 - \hat{\mathbf{e}}_{\parallel} \cdot \mathbf{v}_2\|} \\ \hat{\mathbf{e}}_{\perp 2} &= \hat{\mathbf{e}}_{\parallel} \times \hat{\mathbf{e}}_{\perp 1} \end{aligned}$$

Validation

Suppose a right-hand circular polarized with wave magnetic field $\delta\mathbf{B} \approx B_0[\cos(\omega t)\hat{\mathbf{e}}_{\perp 1} + \sin(\omega t)\hat{\mathbf{e}}_{\perp 2}]$ propagates along $\mathbf{k} = k\hat{\mathbf{e}}_{\parallel}$ in an ambient field $\mathbf{B} = B_0\hat{\mathbf{e}}_{\parallel}$. Figure 2.12a shows that $\delta B_{\perp 2}$ leads $\delta B_{\perp 1}$ in phase by $\pi/2$. From Figures 2.12b and 2.12c, the ellipticity ϵ and degree of ellipticity \mathcal{V}_p are in good agreement, depicting a right-hand circular polarized wave.

Similarly suppose a left-hand circular polarized with wave magnetic field $\delta\mathbf{B} \approx B_0[\cos(\omega t)\hat{\mathbf{e}}_{\perp 1} - \sin(\omega t)\hat{\mathbf{e}}_{\perp 2}]$ propagates along $\mathbf{k} = k\hat{\mathbf{e}}_{\parallel}$ in an ambient field $\mathbf{B} = B_0\hat{\mathbf{e}}_{\parallel}$. Figure 2.12a shows that $\delta B_{\perp 1}$ leads $\delta B_{\perp 2}$ in phase by $\pi/2$. Figures 2.13b and 2.13c the ellipticity ϵ and degree of ellipticity \mathcal{V}_p both depict a left-hand circular polarized wave.

Finally, Figure 2.14 shows a comparison of \mathcal{V}_p from Nykyri et al. (2011) (top panel) and the algorithm used in this research (bottom panel). In order to determine the perpendicular wave components of the magnetic field, both panels from Figure 2.14 are obtained by rotating the magnetic wave-field data into a (magnetic) field aligned coordinate system.

2.8. ELLIPTICITY CALCULATION

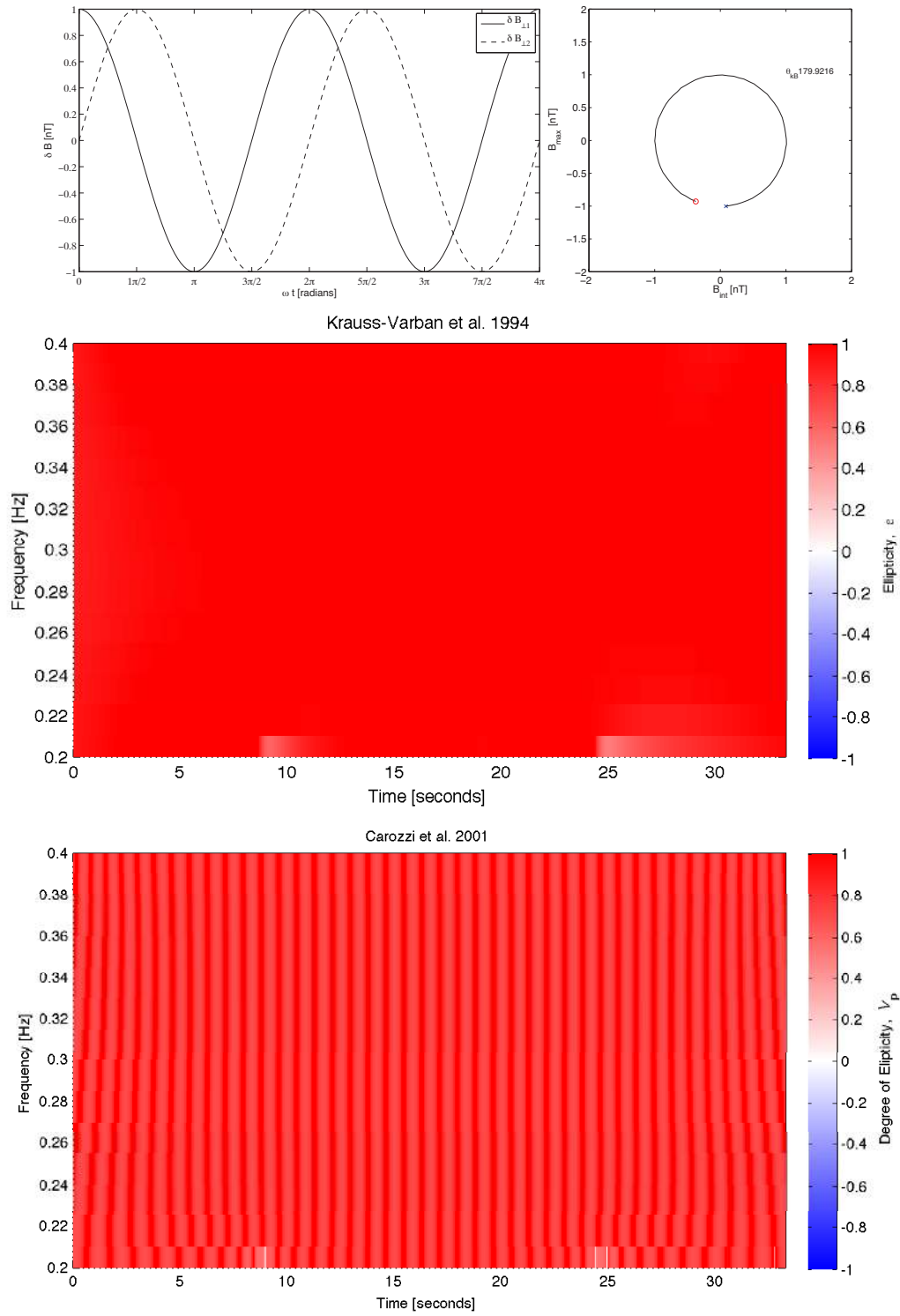


Figure 2.12: (a) Right-hand wave signal, (b) the ellipticity ϵ and (c) degree of ellipticity V_p .

2.8. ELLIPTICITY CALCULATION

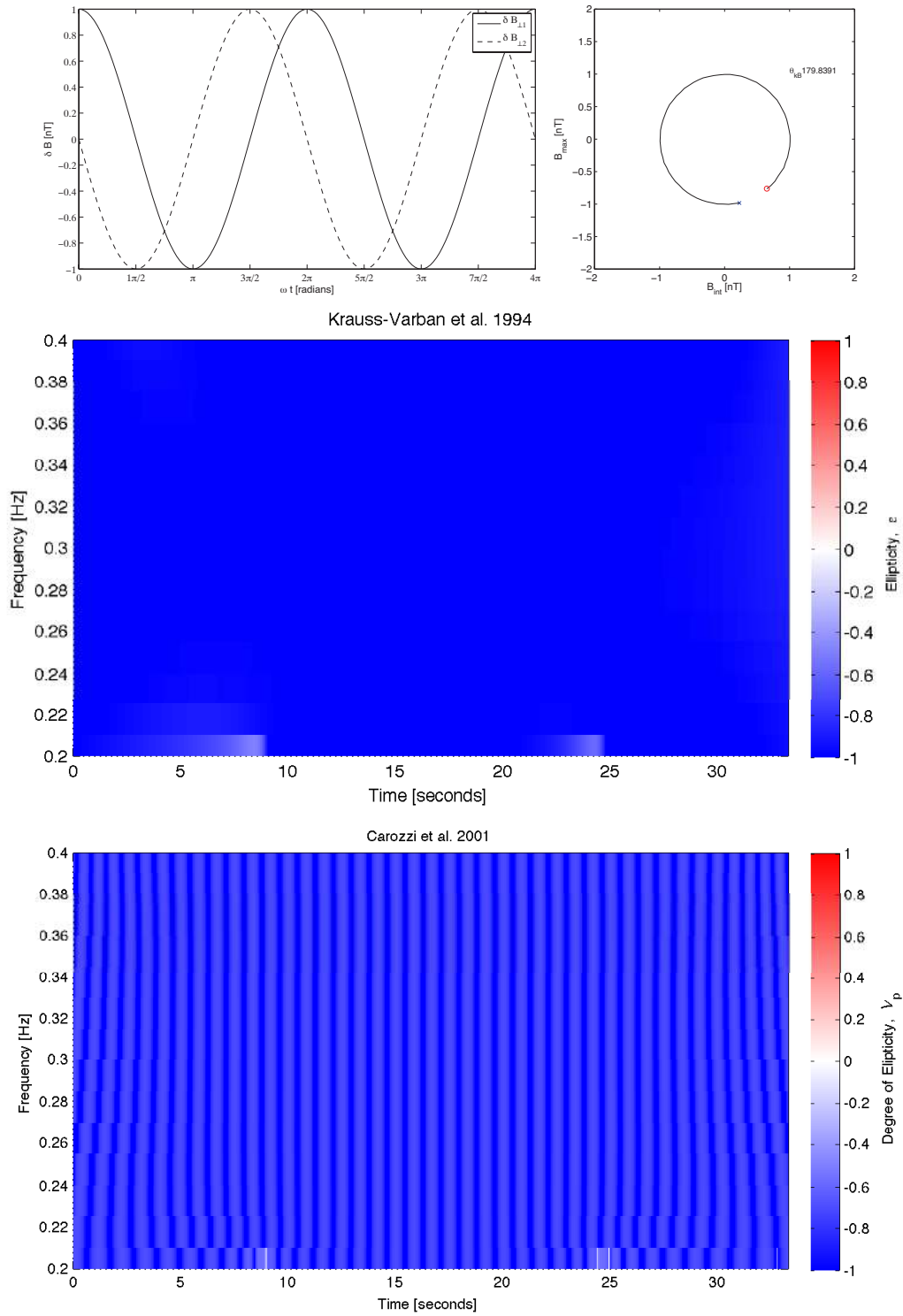


Figure 2.13: (a) Left-hand wave signal, (b) the ellipticity ϵ and (c) degree of ellipticity \mathcal{V}_p .

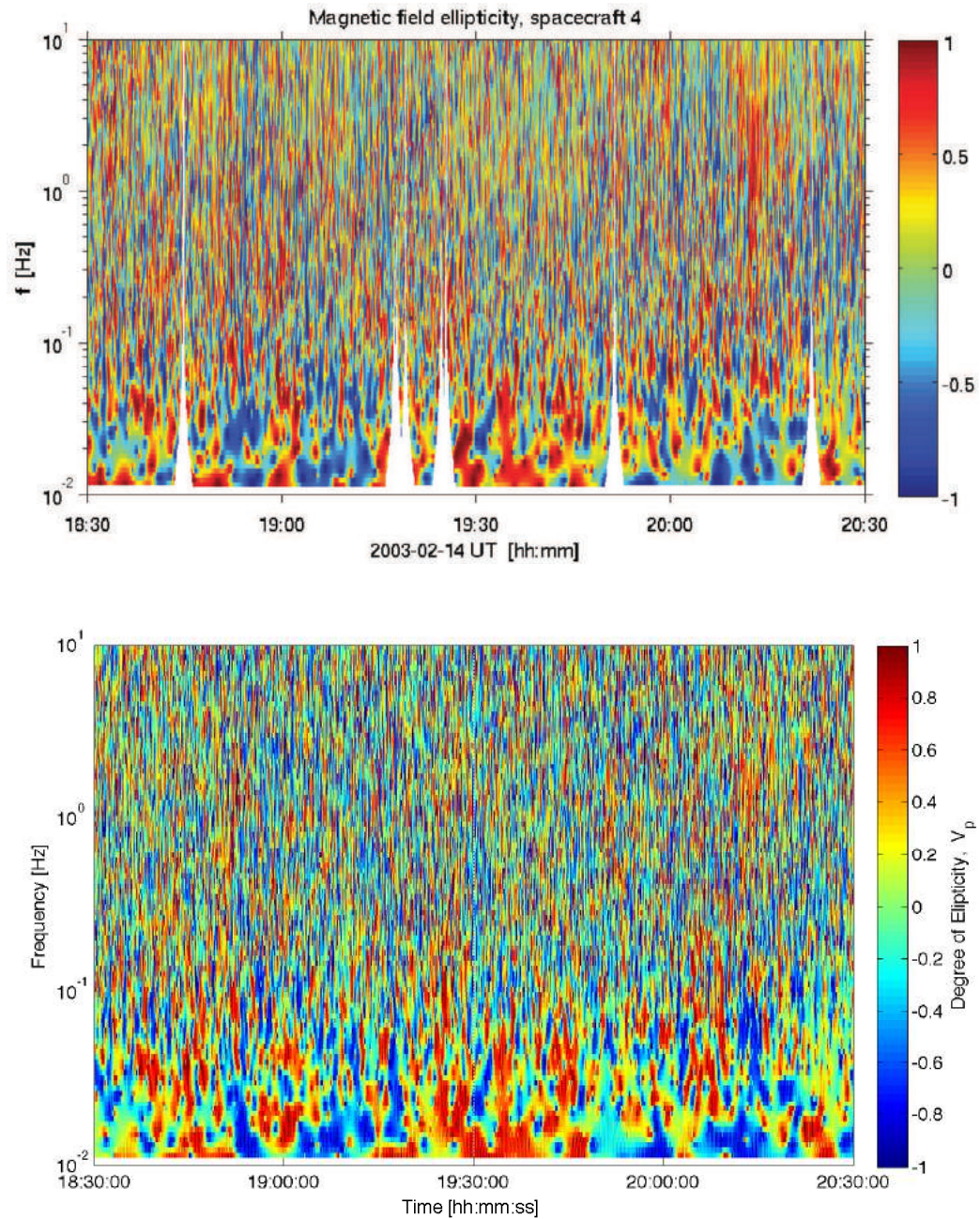


Figure 2.14: Ellipticity from (a) Nykyri et al. 2011 and (b) algorithm developed in this thesis.

Chapter 3

Case Study

The work within this Section has been published and first appeared in *Nature Physics* in September 2016 (Moore et al., 2016).

3.1 Introduction

Understanding the transport and heating of plasma across different spatial and temporal scales is particularly important in laboratory and space plasmas. The specific entropy, $S_i = T_i/n^{2/3}$ (where T_i is the ion temperature in eV/cm and n is the ion number density) increases by two orders of magnitude from 2.5 -70 eV cm² in the magnetosheath to 700 -16000 eV cm² in the magnetosphere (Borovsky & Cayton, 2011). Theoretical work suggests that stochastic ion heating (perpendicular to the magnetic field) via kinetic Alfvén wave (KAW) turbulence may to some extent be responsible (Johnson & Cheng, 2001). Amplification of perpendicular wave power at the Earth's magnetopause can be explained by the theory of mode conversion of compressional magnetohydrodynamic (MHD) waves into KAWs (Johnson et al., 2001). Observations of mode conversion from surface waves to KAWs including the transport of both electromagnetic energy and plasma at the Alfvén resonance

location have been made (Chaston et al., 2007). Furthermore, in a recent statistical study, it has indeed been shown that the spectral energy densities of ion-gyro radii scale waves are stronger on the dawn flank (Yao et al., 2011). However, these studies have not determined experimentally the wave vector (\mathbf{k}) of the observed waves which is required for a robust wave mode identification.

At the magnetopause, a strong velocity shear takes place between the magnetosheath and magnetospheric plasma and as a result, ultra-low frequency Kelvin-Helmholtz Waves (KHW) are generated by Kelvin-Helmholtz Instability (KHI). The fastest growing KHWs typically have wavelengths of the order $(2-4\pi\Delta)$, where Δ is the width of the velocity shear layer (Miura & Pritchett, 1982). Assuming that a velocity shear layer has a width of approximately 4800 km in the source region of the wave, then the fastest growing KH mode has a wavelength of about 30,160 - 60,320 km which is well above the ion inertial and gyro radius scales. Mass transport across the magnetopause associated with KHI has been quantified in simulations and shown to be efficient in generating a cold-dense plasma sheet in the time scale of about 2 hours (Nykyri & Otto, 2001, 2004). Due to smaller magnetic field tension at the dawn-flank during Parker-Spiral IMF (which is the most frequent IMF orientation), the simulations have shown that KH is more unstable at the dawn-flank past the terminator (Nykyri, 2013). It has therefore been suggested that KHI and associated processes may be responsible for the dawn-favored plasma sheet density and temperature asymmetry (Nykyri, 2013).

Prior theoretical work has shown that MHD FMWs can be excited by magnetosheath flows in a presence of total pressure perturbations (Mann et al., 1999). The fast magnetosonic modes are the kinetic counterpart of the MHD FMWs. Previous simulations also suggest that perpendicular propagating, large amplitude magnetosonic waves, with frequencies $\omega_{ci} < \omega < \omega_{LH}$, can accelerate ions via the $\vec{v} \times \vec{B}$ -force parallel to the wave fronts sufficiently damping the wave (Lembege et al., 1983). Investigation of the subharmonic-

resonant interaction between ions and perpendicular propagating MHD waves has shown that ions can be effectively perpendicularly heated for increasing wave magnetic field $\delta|\mathbf{B}|$, but are limited to their source region as they are short lived (Terasawa & Nambu, 1989a).

Here, we present the first observations of a short lived (ion-scale) Fast Magnetosonic Wave (FMW) that originates inside of an MHD-scale Kelvin-Helmholtz (KH) vortex, characterized by a strong total pressure minimum (see Figure 3.1). KH waves are created by a velocity shear and have been frequently observed at the magnetopause of Earth (Fairfield et al., 2000; H. Hasegawa, Fujimoto, Phan, et al., 2004; Nykyri et al., 2006; Taylor et al., 2012; Hwang et al., 2011; Yan et al., 2014; Kavosi & Raeder, 2015) and other planets (Pope et al., 2009; Masters et al., 2010; Boardsen et al., 2010; Sundberg et al., 2012). The observed magnetosonic wave has adequate energy to provide ≈ 2 keV energy increase for the cold-component ions of magnetosheath origin.

It is well known that macroscopic velocity shears can lead to the formation and excitation of KH instabilities (H. Hasegawa, Fujimoto, Phan, et al., 2004) and ion-scale waves (Ganguli et al., 2002; Nykyri et al., 2003). In addition, the inclusion of smaller length-scale terms in the generalised Ohms law produces multi-scale effects in the simulations of the Kelvin-Helmholtz Instability (KHI). For example, it has been shown that including the Hall term produces ion-inertial-scale structures within large MHD scale vortices (Nykyri & Otto, 2004). Similarly, the addition of the electron inertial term allows for the formation of electron-scale vortices inside an MHD-scale KH vortex (Nakamura et al., 2004). Despite this, these multi-scale KH waves have not yet been verified with observations, and while they may contribute to plasma transport, they are currently not linked to ion or electron heating.

Simulations (Nykyri & Otto, 2001, 2004) and observations (Nykyri et al., 2006; H. Hasegawa et al., 2009) also have shown that the KHI can generate magnetic reconnection as a secondary mechanism. In these cases, isolated ion beams accelerated anti-parallel

with respect to background magnetic field were observed during brief intervals which satisfied the reconnection criteria within the KHW (Nykyri et al., 2006). In a previous study (H. Hasegawa et al., 2009), clear experimental evidence of ion-scale current sheets forming near an MHD-scale KH vortex were reported. However, in this case, the circumstances did not allow the authors to resolve particle heating on ion-scales like the present study. It is also noteworthy that the formation of ion-scale current sheets inside MHD-scale vortices have been generated in a simulated environment Rossi et al. (2015), thus strengthening the interpretation of in-situ measurements.

Yet to be shown in observations, recent two fluid simulations show the formation of shock structures inside KH vortices (Palermo et al., 2011). In the magnetotail, it has been shown that fast Earthward plasma flows can lead to an ion temperature asymmetry that can generate ion-scale mirror-mode structures (Zieger et al., 2011). The present manuscript describes the first unambiguous experimental determination of an obliquely propagating kinetic magnetosonic wave located inside of an MHD-scale KH vortex in which ions were heated during the wave interval. In the magnetosheath side of the vortex, we observed nearly parallel propagating left-handed waves (LH interval) that likely belong to the ion cyclotron or kinetic Alfvén branch. We also analyse an upstream interval with considerable wave power containing right-hand polarized waves that propagate above and below ω_{ci} (RH interval). The coupling of the MHD - scale KH instability and the ion scale wave activity seems to be responsible for the observed ion heating. What is noteworthy is that this heating may explain the origin of the ion temperature asymmetry reported in the plasma sheet. Since this mechanism leads to non-adiabatic cross-scale heating, it may be also important elsewhere in the universe where velocity shears are present.

3.2 Cross-Scale Observations

On June 6th 2002, the four Cluster spacecraft (≈ 100 km from each other) traversed the dawnside flank of the Earth's magnetosphere under a Parker Spiral oriented IMF (see Figure 3.1). Observations show periodic ($\tau \approx 3$ min) encounters both with magnetosheath-like and magnetospheric-like plasma regions and bipolar variations of the normal component (B_N) of the magnetic field (see Figure 3.2). Fluctuations in the total pressure (P_T) range from 0.1 to 0.33 nPa and brief intervals of 'faster than sheath flow'-plasma (H. Hasegawa et al., 2006) are observed in the tenuous magnetospheric-like regions. The magnetopause boundary was determined to be KH unstable (please refer to the § 3.4 for a detailed analysis of the KH observations and simulations). We estimate that the observed KHW has a wavelength $\approx 36,000$ km.

A high frequency magnetosonic wave was detected between 13:27:36 - 13:27:54 UT inside a vortex of the KHW characterized by the total pressure minimum (see Figures 3.1 and 3.2). Plotted in Figure 3.3 is the experimental dispersion relation compared to cuts from the kinetic dispersion surface and theoretical dispersion relations for an MHD FMW, kinetic Alfvén wave (KAW) (Stasiewicz et al., 2000) and an Ion-Cyclotron (IC) wave (Stix, 1992). The MHD FMW dispersion relation is defined by the following expression:

$$\omega^2 = \frac{k^2}{2} \left(c_{ms}^2 + \left[(v_A^2 - c_s^2)^2 + 4v_A^2 c_s^2 \frac{k_{\perp}^2}{k^2} \right]^{1/2} \right) \quad (3.1)$$

where $c_{ms}^2 = c_s^2 + v_A^2$. The plasma parameters in Equation 3.1 taken from the magnetosheath-like plasma interval just outside of the FMW interval are as follows: Alfvén speed $V_A = 2.47 \times 10^5$ m/s, sound speed $c_s = 2.34 \times 10^5$ m/s, and the magnetosonic speed $c_{ms} = 3.40 \times 10^5$ m/s. The closeness between the experimental, and theoretical MHD FMW dispersion in Figure 3.3 is striking. This agreement is strongly suggestive that the electromagnetic wave packet consists of FMWs with wavelengths of 200-2,000 km. Al-

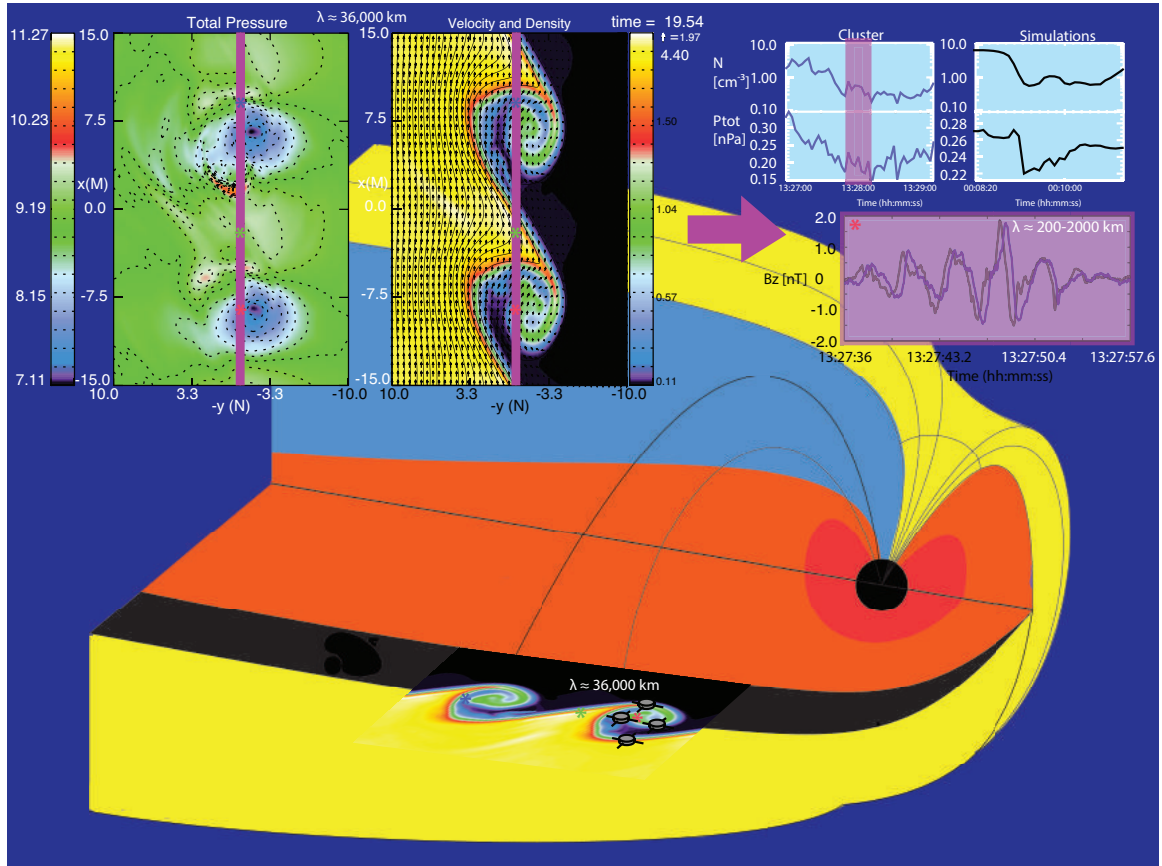


Figure 3.1: An illustration depicting the Cluster spacecraft location with respect to the large scale KH wave with $\lambda_{KH} \approx 36,000$ km and $\tau \approx 3$ minutes, and small scale (200 -2000 km) Fast Magnetosonic Mode wave packet. Total pressure and density from simulation and Cluster data is shown. The blue, green and pink asterisks represent the approximate locations of the observed RH, LH and FMW intervals respectively.

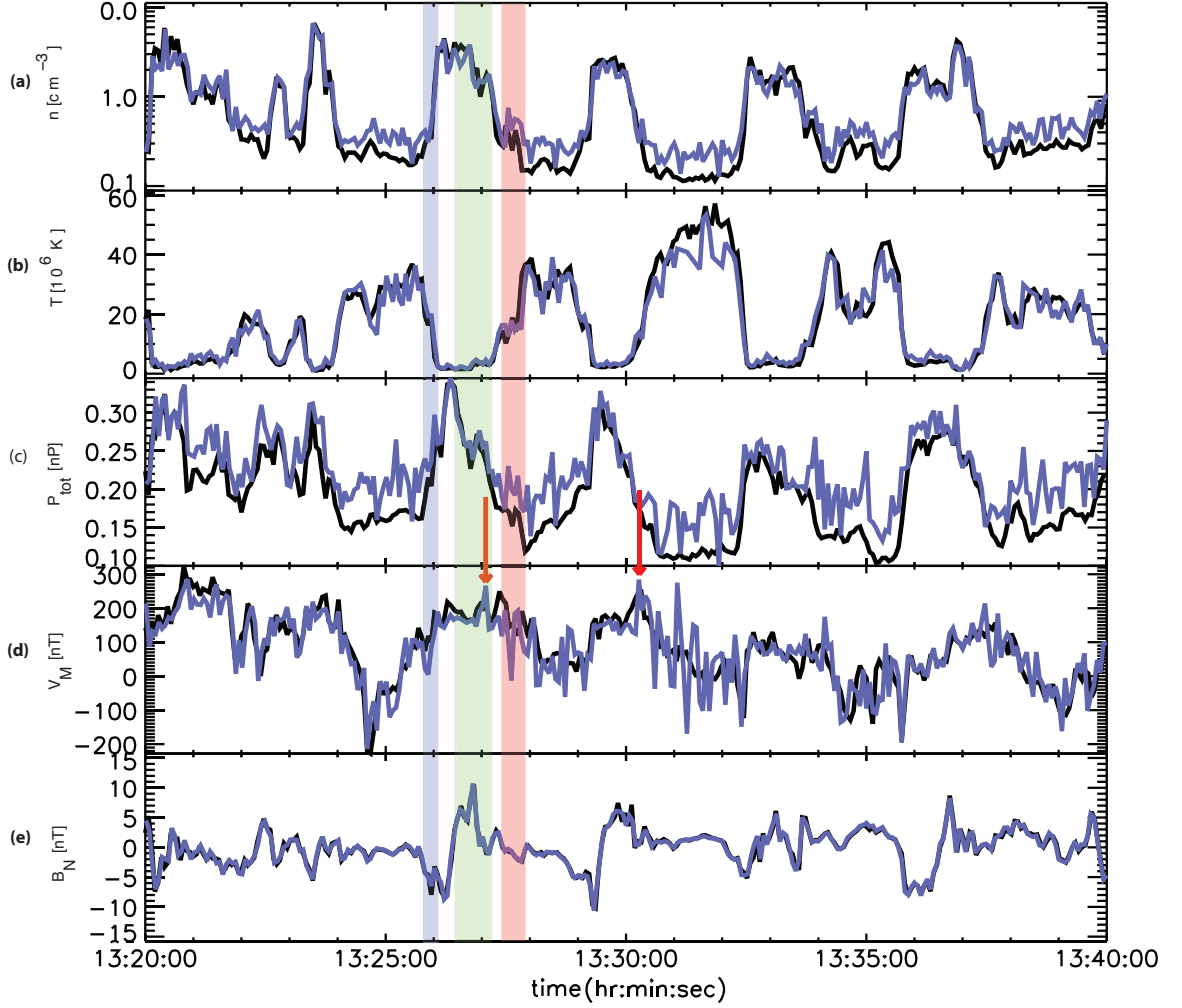


Figure 3.2: Overview plot showing time series data collected by the Cluster spacecraft for the boundary crossing on June 6th 2002. Cluster 1 (black trace) and 4 (blue trace) field data is represented in boundary normal coordinates using maximum variance analysis (MVAE) of the $-(\mathbf{V} \times \mathbf{B})$ electric field (Paschmann & Daly, 1998) Density (Panel a), Temperature (Panel b), Total Pressure (Panel c), V_M (Panel d) and B_N (Panel e). The red arrows represent faster than sheath flows and the shaded blue, green and pink regions represent the RH, LH and high frequency FMW intervals respectively.

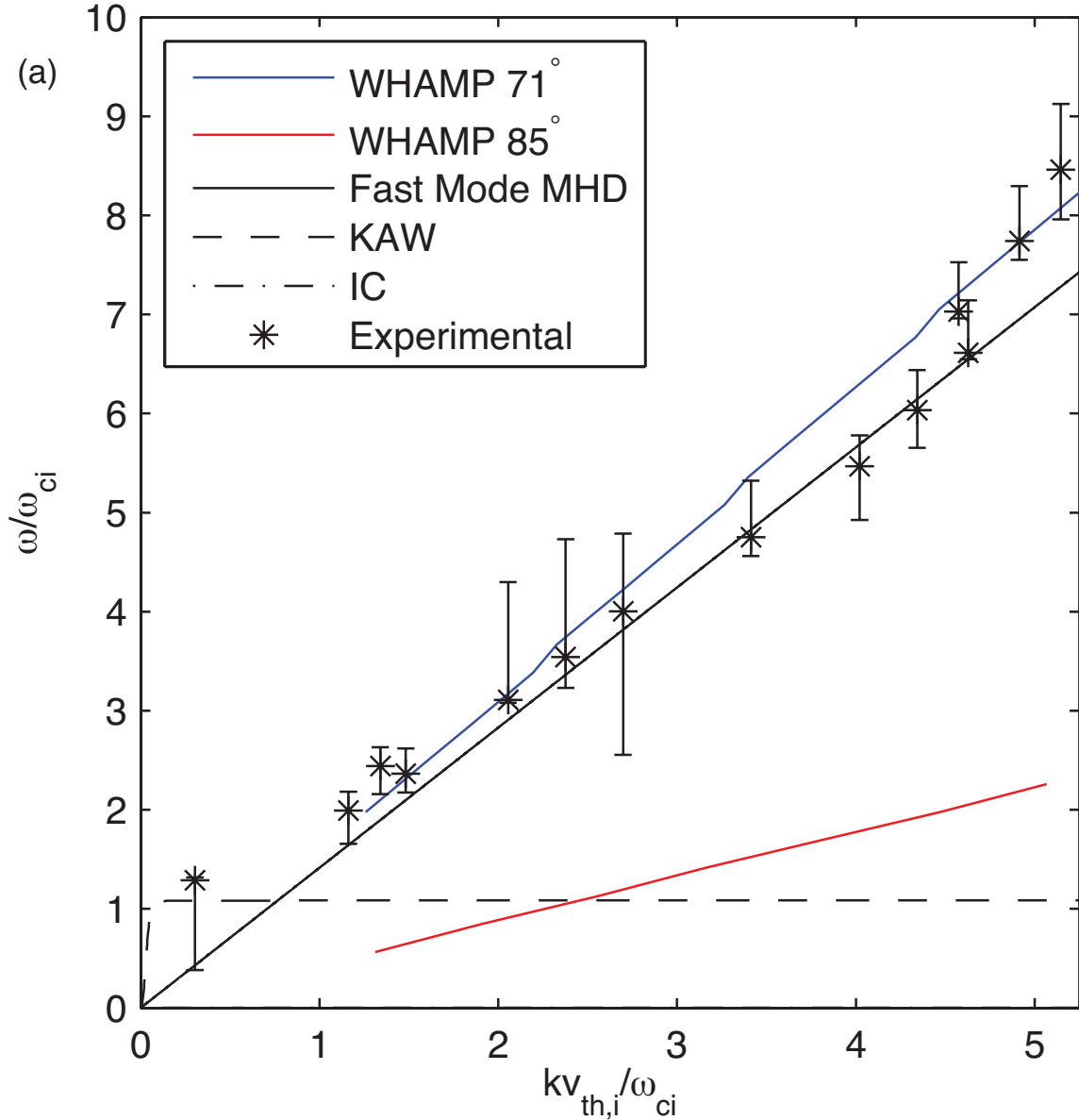


Figure 3.3: Experimental and theoretical dispersion relations used for wave mode identification of the FMW interval: experimentally determined dispersion relation (*) plotted against the 71° (blue line) and 85° (red line) cuts from the WHAMP dispersion surface and theoretical dispersion relations for an MHD FMW (solid black line), KAW (dashed black line) and IC wave (dot dashed black line).

though the observed wave packet satisfies the MHD fast mode dispersion relation, it likely belongs to the kinetic magnetosonic branch (Krauss-Varban et al., 1994) because its frequency is in the vicinity of the local proton cyclotron frequency. The kinetic dispersion is determined by using a hot plasma dispersion solver – waves in a homogeneous, anisotropic multicomponent plasma (WHAMP (Roennmark, 1982)). Shell-like distribution functions were observed for the ion and electron species (see Figure 3.4) and are used as an input for the WHAMP solver (Colpitts et al., 2012) (see Table 3.3); magnetosonic wave observations have been associated with shell-like ion distributions through observations (Perraut et al., 1982; Boardsen et al., 1992; Meredith et al., 2008; Balikhin et al., 2015; Walker et al., 2015) and simulations (Min & Liu, 2015). The kinetic solution is depicted in Figure 3.5. Cuts at varying propagation angles are taken from the WHAMP dispersion surface to be compared with the experimental dispersion; the cut corresponding to the 71° propagation angle with respect to the ambient field is in best agreement with the experimental dispersion (Figure 3.3). Furthermore, a positive wave growth (evidenced by the positive imaginary part in Figure 3.6) suggests that there is sufficient energy supplied by the observed shell-like distributions to generate this wave mode. From Figure 3.3, the theoretical KAW and IC dispersion relations are not in agreement with the experimental results.

Stronger emissions in the B_z spectrum from Figure 3.9 occur slightly upstream of the FMW interval. The RH and LH intervals occur during 13:25:52 - 13:26:07 UT and 13:26:28 - 13:27:09 UT respectively. Over the RH interval, the B_z spectrum depicts separate emissions above and below ω_{ci} . Further analysis shows (see § 3.5) that the right-handed wave which propagates above the ω_{ci} most likely belongs to the magnetosonic branch. The right-handed wave mode (RH interval) that propagates below ω_{ci} most likely belongs to the KAW branch (see Figure 3.8 (LH interval) most likely belongs to the KAW or ion-cyclotron branch (see Figure 3.8). It has been suggested that KAW activity is linked to KHI via mode conversion (Johnson et al., 2001; Chaston et al., 2007) and that KAW can heat ions stochastically

3.2. CROSS-SCALE OBSERVATIONS

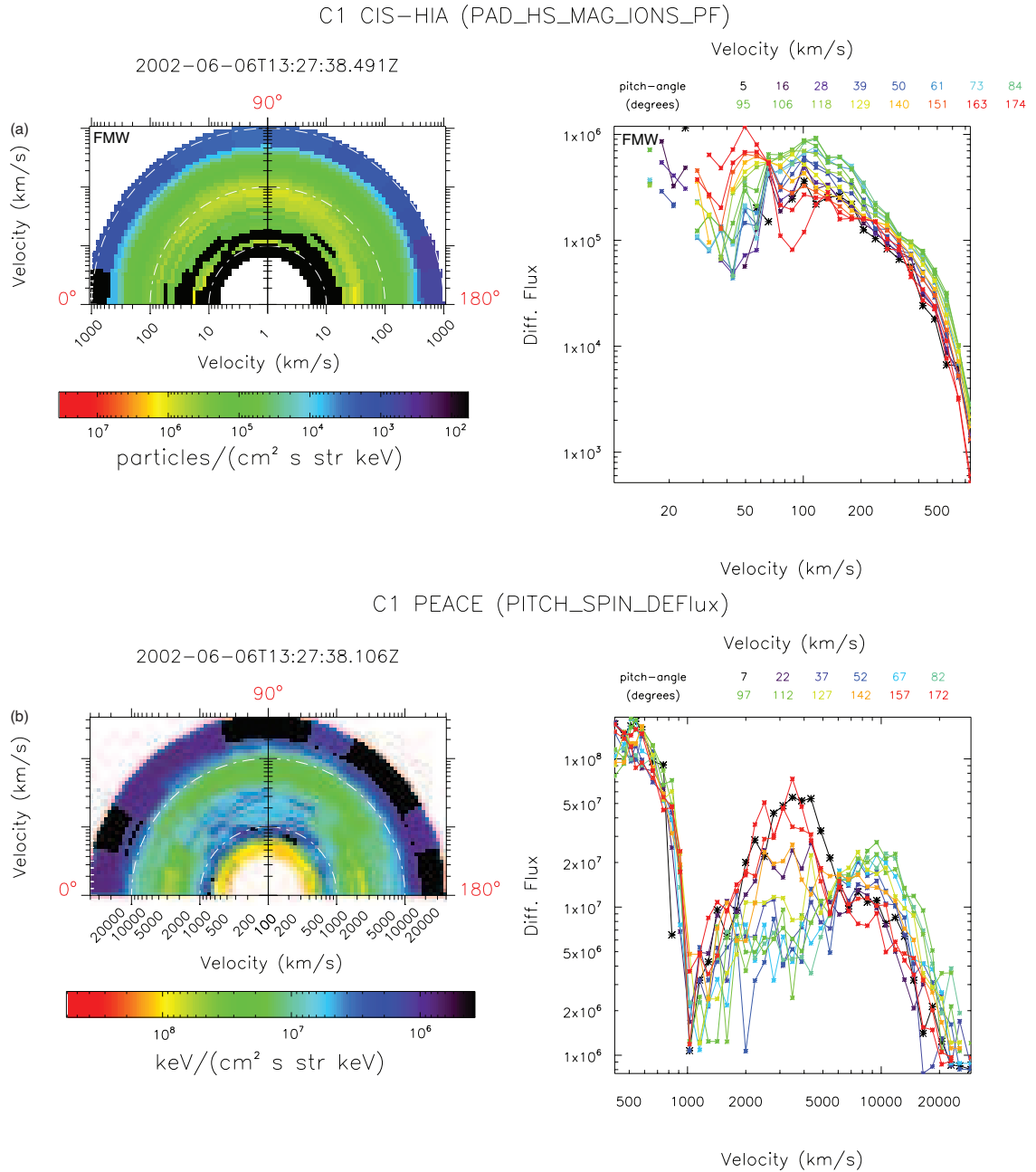


Figure 3.4: Observed distribution ion and electron distribution functions observed by C_1 during the FMW wave interval.

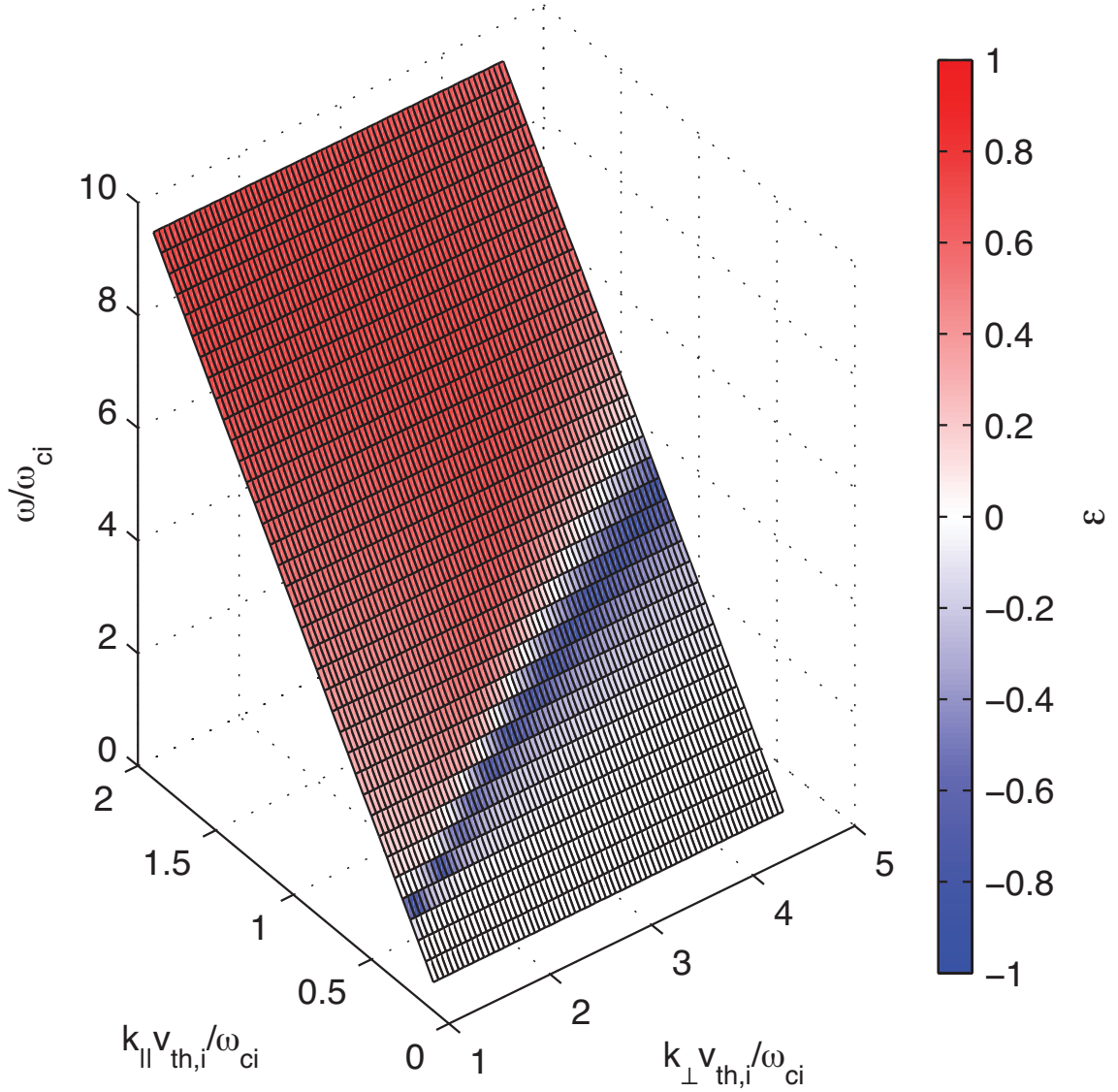


Figure 3.5: Dispersion surfaces determined by WHAMP using inputs parameters described in Table 3.3 for the FMW wave interval. The color bar represents the ellipticity ϵ , where red represents a right-handed wave, blue represents a left-handed wave and white represents a linear polarisation.

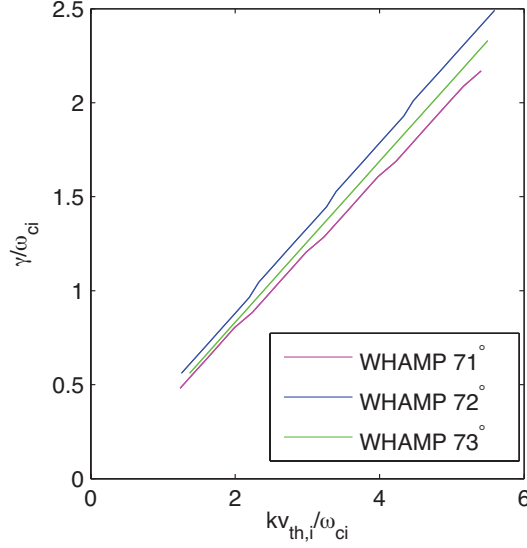


Figure 3.6: Growth rates calculated for the FMW interval: imaginary part of the dispersion surface generated by WHAMP at varying propagation angles.

(Johnson & Cheng, 2001) at the magnetopause. The right-handed mode from the RH interval that propagates above ω_{ci} might very well belong to the magnetosonic branch. Please refer to § 3.5 for a more detailed analysis on the RH, LH and FMW intervals.

Table 3.1: **Table of wave profiles for right hand, left hand and fast magnetosonic wave modes.** Wave properties and local plasma parameters for the observed RH, LH and FMW intervals. The $< \omega_{ic}$ and $> \omega_{ic}$ subscripts denote propagation angles from MVAB for frequency ranges below and above ω_{ic} respectively.

	RH	LH	FMW
Polarisation	right-handed	left-handed	right-handed
$\theta_{kB,1}$	$88^{\circ}_{<\omega_{ic}}$	4°	95°
$\theta_{kB,4}$	$89^{\circ}_{>\omega_{ic}}$		92°
β	0.79	0.42	1.0

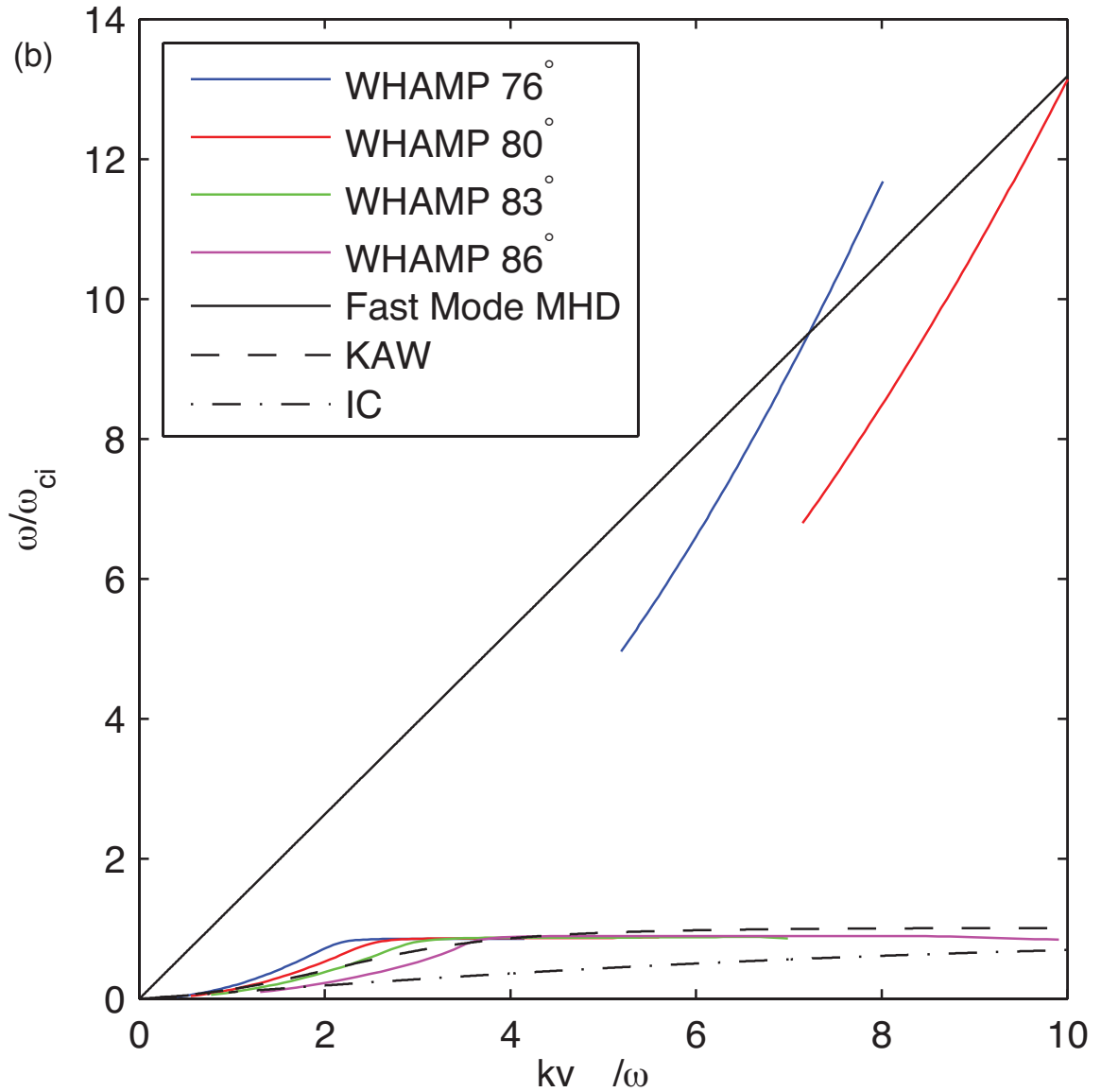


Figure 3.7: Theoretical dispersion relations used for wave mode identification of the RH interval: 76° (blue line), 80° (red line), 83° (green line) and 80° (magenta line) cuts from the WHAMP dispersion surface plotted against theoretical dispersion relations for an MHD FMW (solid black line), KAW (dashed black line) and IC wave (dot dashed black line).

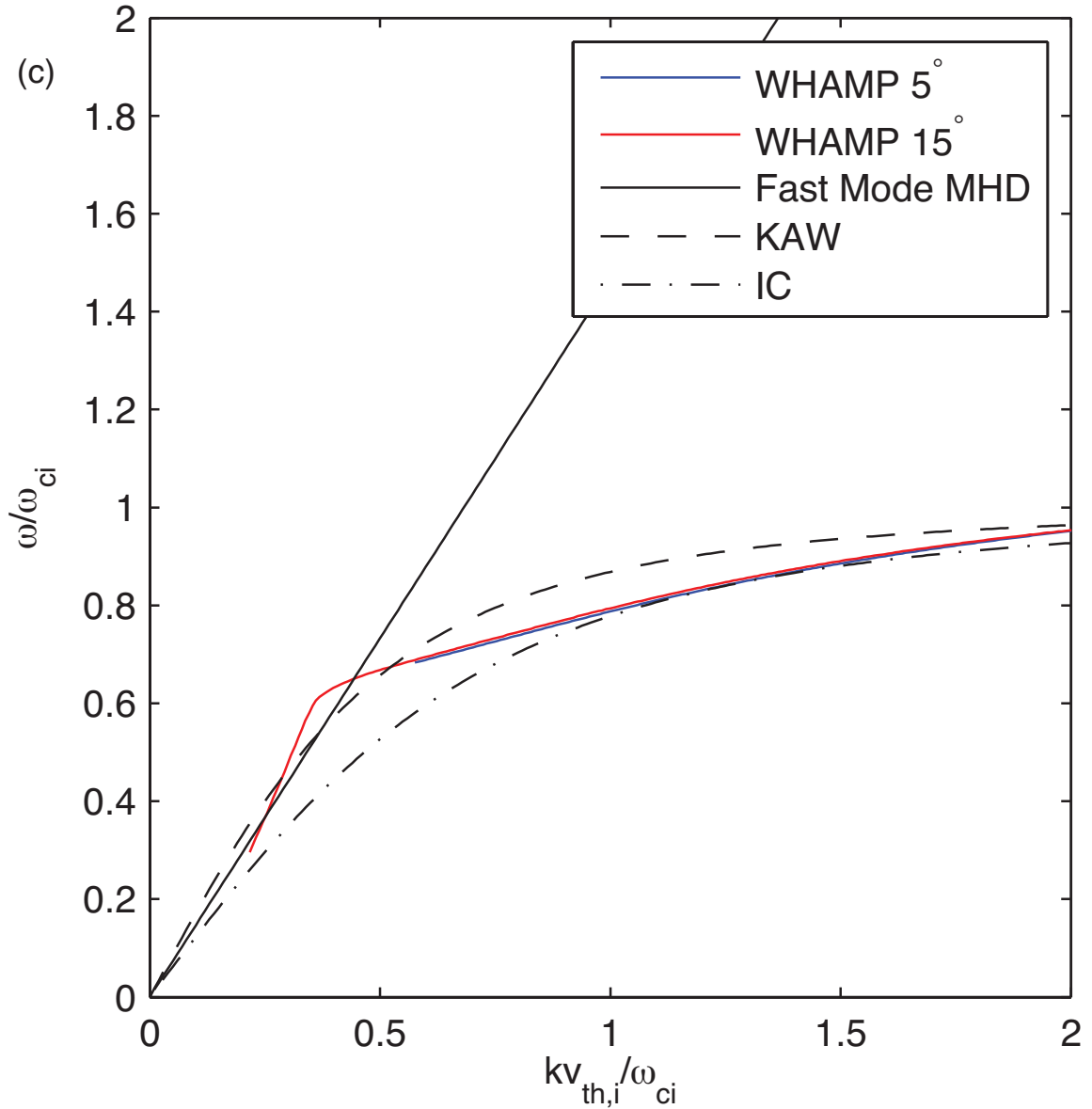


Figure 3.8: Theoretical dispersion relations used for wave mode identification of the LH interval: 76° (blue line), 80° (red line), 83° (green line) and 80° (magenta line) cuts from the WHAMP dispersion surface plotted against theoretical dispersion relations for an MHD FMW (solid black line), KAW (dashed black line) and IC wave (dot dashed black line).

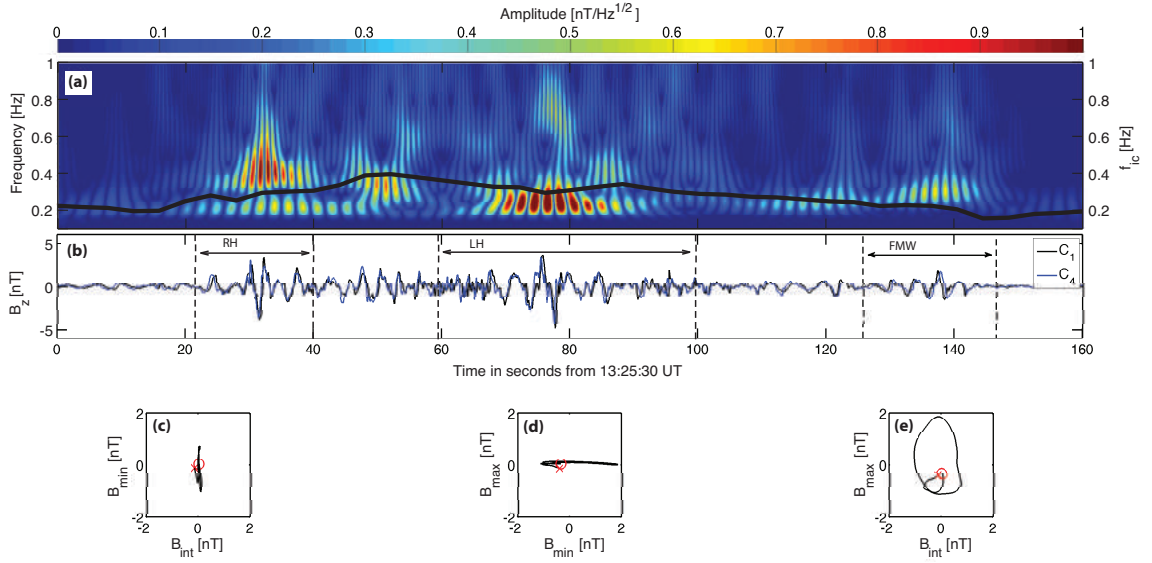


Figure 3.9: **Observations of the high frequency wave packet and associated hodograms.** Magnetic (B_Z) spectrogram (Panel a) with ion cyclotron frequency f_{ic} (black line, Panel a) in the foreground and the high-pass filtered magnetic field B_Z component (Panel b). Hodograms from the FMW interval are shown in Panels c-e: B_{int} vs B_{min} (Panel c), B_{min} vs B_{max} (Panel d), B_{int} vs B_{max} (Panel e).

3.3 Cold Component Ion Heating

The ion spectrogram in Figure 3.10b shows clearly a 1.39 keV ion population at $\approx 13:27:32.4$ followed by 2.6 keV and 3.4 keV ion populations with the same flux magnitudes of $\approx 3.8 \times 10^5$ keVcm $^{-2}$ s $^{-1}$ sr $^{-1}$ keV $^{-1}$ (light orange color). The net increase in the kinetic energy flux, ΔKE_{flux} , is estimated by integrating the instantaneous change in KE over the wave interval to get $\approx 7.0 \times 10^6$ keVcm $^{-2}$ sr $^{-1}$; the solid angle is assumed to be unit-less. The total Poynting flux of the FMW, S_{tot} , is plotted over the shaded pink wave interval in Figure 3.10b, where $S_{tot}^{max} \approx 2.5 \times 10^6$ keVcm $^{-2}$ s $^{-1}$. Similarly by integrating the instantaneous S_{tot} over the wave interval, we arrive at a total integrated Poynting Flux of $\approx 4.4 \times 10^6$ keVcm $^{-2}$. The total integrated Poynting Flux and the integrated ΔKE_{flux} have values that are of the same order of magnitude; discrepancies are most likely owed to the fact that the Poynting Flux is calculated using Cluster 4 whereas the ΔKE_{flux} is calculated using Cluster 1; this is because the 3D particle energy flux data is only available for Cluster 1 and Cluster 3, whereas the electric field data use for the Poynting Flux calculation is corrupted for Cluster 1 during for the wave interval. Assuming that the FMW is completely damped, its wave energy is sufficient to cause a ≈ 2 keV increase in the ion energy when assuming an integrated flux magnitude of $\approx 7.0 \times 10^6$ keVcm $^{-2}$ sr $^{-1}$.

The condition for cyclotron resonance (Terasawa & Nambu, 1989b) $\omega - k_{\parallel}V_{\parallel} = n\omega_{ci}$ ($n = \pm 1, \pm 2, \pm 3,$) is met for the fourth harmonic and is consistent with the parallel velocity bands observed in the ion distribution functions during the wave interval. The experimental dispersion relation shows that the FMW packet consists of waves with frequencies $\approx 1-9$ times the ω_{ci} . We expect this to be a possible mechanism responsible for the ion heating.

It has been shown that velocity shears (including those generated by KHI) can generate a broad spectra of electromagnetic waves (Peñano & Ganguli, 1999, 2000, 2002; Tejero et al., 2011; Ganguli et al., 2014). The macroscopic velocity shear originating from the interaction

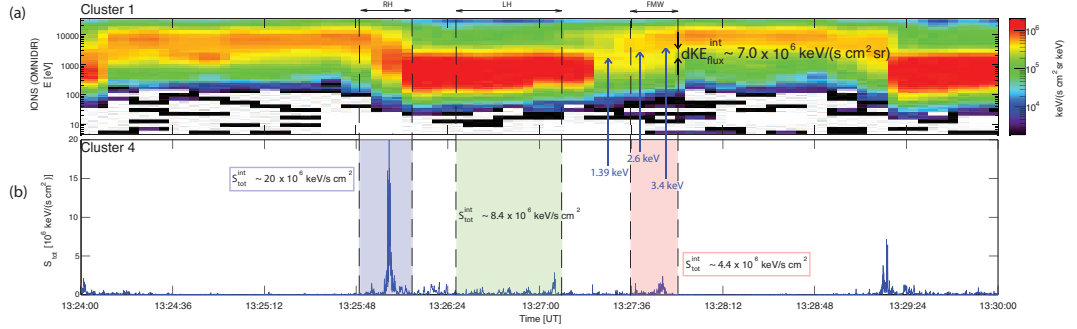


Figure 3.10: **Cluster data showing the mixing region where cross-scale energy transport takes place.** Omni-directional Ion Energy Spectrogram (Panel a) and the total Poynting flux S_{tot} calculated with the high pass filtered electric and magnetic fields with a cutoff frequency of 0.2 Hz (Panel b). The total integrated Poynting flux is provided for the RH, LH and FMW intervals denoted by the blue, green and pink shaded regions respectively. Please note that the total Poynting flux is calculated from C_4 data because the electric field and wave (EFW) data from C_1 is corrupted for the interval 13:00:00 - 14:00:00 UT. The three blue arrows (Panel a) represent the 1.39 keV, 2.6 keV and 3.4 keV ion energies.

between the solar wind and the Earth's magnetosphere provides free energy which generates KHI on MHD scales. We have estimated that the kinetic energy per unit area contained in the velocity shear is about 840 keV cm^{-2} . Twisting and compression of the magnetic field and plasma by the KHI is estimated to use about 820 keV cm^{-2} leaving a surplus of about 20 keV cm^{-2} . The wave energy given by the integrated Poynting flux is $\approx 22\%$ of the available energy surplus. It is well possible that other similar wave packages have been excited in other regions not observed in-situ by the spacecraft. We would like to note that 22% is an estimate based on a single wave packet, and does not include any contributions from the additional structures we observed during this interval. As a result, 22% can be interpreted as a conservative estimate which would likely increase if all wave packet contributions could be included. The calculation of the global impact from cross-scale coupling mechanisms are better suited to studies of a statistical nature, and for this, more events are required. However, we should stress that suitable observations of such a phenomena are very rare due

to the requirement of numerous strict criteria such as: 1) the occurrence of MHD-scale KHI during its non-linear phase, 2) simultaneous measurement of clear and coherent ion-scale wave structures coinciding with a KH vortex, 3) spacecraft separation distances within a fraction of the wave length and 4) non-perpendicular k vector relative to the spacecraft separation vector. It is also worth noting that associated with conditions 1-4 are additional sub-criteria and the satisfaction of 1-4 does not necessarily guarantee a suitable event. In our case, the circumstances arose such that each one was satisfied, making these set of observations particularly rare.

The total integrated Poynting flux is shown to be larger for the RH and LH intervals when compared to the FMW interval. Because the RH and LH intervals are located in higher density regions, the level of energization in the ion spectrograms is not as clear as during the FMW interval which was observed in the more tenuous plasma. However, it has been shown that the ion energization process is indeed more effective in the vicinity of the dawn-flank magnetopause compared to the dusk-flank (H. Hasegawa et al., 2003), so the presence of these high-frequency waves adjacent to KH vortex can be the explanation to this dawn-dusk asymmetry. Simulations show that for variety of Solar Wind plasma conditions, the KHI typically grows more efficiently at the dawn-flank (Nykyri, 2013) magnetopause due to the smaller magnetic field tension during the most typical IMF orientation (the Parker-Spiral IMF). Also, a recent statistical study has confirmed that PC_4 - PC_5 ULF fluctuation power, which characterizes the fluctuations generated by the KHI, is more enhanced in the region of the magnetopause downstream of a quasi-parallel shock, which coincides with the dawn-flank for the Parker-Spiral IMF (Nykyri & Dimmock, 2016). Furthermore, a statistical study shows that the spectral energy densities on the order of the ion gyro-radius are larger on the dawn flank (Yao et al., 2011).

3.4 KHI Observations and Simulations

Presented in Figure 3.11 are measurements made by the Cluster spacecraft over the time interval between 13:00:00 and 14:00:00 UT on June 6th during Parker-Spiral IMF. The solar wind conditions and IMF orientation were determined using the OMNI database (King & Papitashvili, 2005). Each quantity has been rotated from GSE, to boundary normal co-ordinates (Paschmann & Daly, 1998) to better highlight the structures, where N is in the direction normal to the magnetopause, M runs along the magnetopause and is most aligned with the tailward plasma flow and L completes the system. Observations show periodic ($\tau \approx 3$ min) encounters both with magnetosheath-like and magnetospheric-like plasma regions and bipolar variations of the normal component (B_N) of the magnetic field. Magnetosheath-like plasma typically has a high density, low temperature but high tailward velocities, whereas magnetospheric plasma is hotter, with predominantly low tailward velocities. Fluctuations in the total pressure (P_T) range from 0.1 to 0.33 nPa where the total pressure is defined by the sum of the thermal and magnetic pressures i.e.

$$P_T = nkT + \frac{B^2}{2\mu_0} \quad (3.2)$$

About mid-way through the hour interval, B_N rapidly rises then falls off gradually; this signature has been observed previously at the dawn-flank magnetopause, also under Parker Spiral IMF orientation, and was identified as KHI (Nykyri et al., 2006). Figure 3.12 shows a 2.5-D MHD simulation of the KHI created using plasma and field parameters from this event (see Table 3.2). A strong total pressure minimum is created inside the vortex of a non-linear KH wave with a wavelength of $\approx 36,000$ km. The plasma density has an intermediate value between high-density magnetosheath-like and low-density magnetospheric-like plasma in the vortex. In Figure 3.12, plasma parameters and field values from Cluster are compared with corresponding quantities from the 2.5-D Local MHD simulation – the results have a

Table 3.2: The normalisation constants are $n_{norm} = 3.5 \text{ cm}^{-3}$, $B_{norm} = 8.5 \text{ nT}$, $V_{norm} = 100.7 \text{ km/s}$, $P_{norm} = 0.036 \text{ nPa}$, $l_{norm} = 2400 \text{ km}$ and $t_{norm} = 21.68 \text{ s}$. The shear layer thickness was set to 4800 km.

Initial conditions	MSP	MSH
B_L	0.886	2.537
B_M	-0.156	0.923
V_L	0.836	-2.507
V_M	-0.996	2.988
n	0.11	1.89
P	8.18	1.7
β	10.1	0.23
V_A	2.71	1.96

striking qualitative agreement. The red highlighted column in Figure 3.1 indicates how the KH wave might pass by the spacecraft in order to produce the observed signatures. The FMW interval was observed inside the total pressure minimum (signifying the center of the KHI vortex) and at the gradient between intermediate density and low-density plasma. A total pressure minimum is observed when B_N polarity switches, due to twisting of the magnetic field in the N, M -plane by the KHI. The simulations qualitatively reproduce the polarity and structure of the observed B_N . Other key signatures of non-linear vortices are the hot, magnetospheric-like plasma in the region of a total pressure minimum, and faster than the magnetosheath flow in magnetospheric-side of the non-linear vortex. These signatures are consistent with the previously published KH observations and simulations (Fairfield et al., 2000; Otto & Fairfield, 2000; Nykyri et al., 2006; H. Hasegawa et al., 2005; Nykyri & Foullon, 2013; Kavosi & Raeder, 2015).

For example, this faster than sheath flow in the V_M -component is first observed by C_4 at $\approx 13:27:06$ UT and later at $\approx 13:30:15$ UT. Similarly, the virtual spacecraft measures the faster than sheath flow in the V_M -component first at $t = 00:06:58$ and later, during the 2nd encounter of the vortex at $t = 00:09:24$.

3.4. KHI OBSERVATIONS AND SIMULATIONS

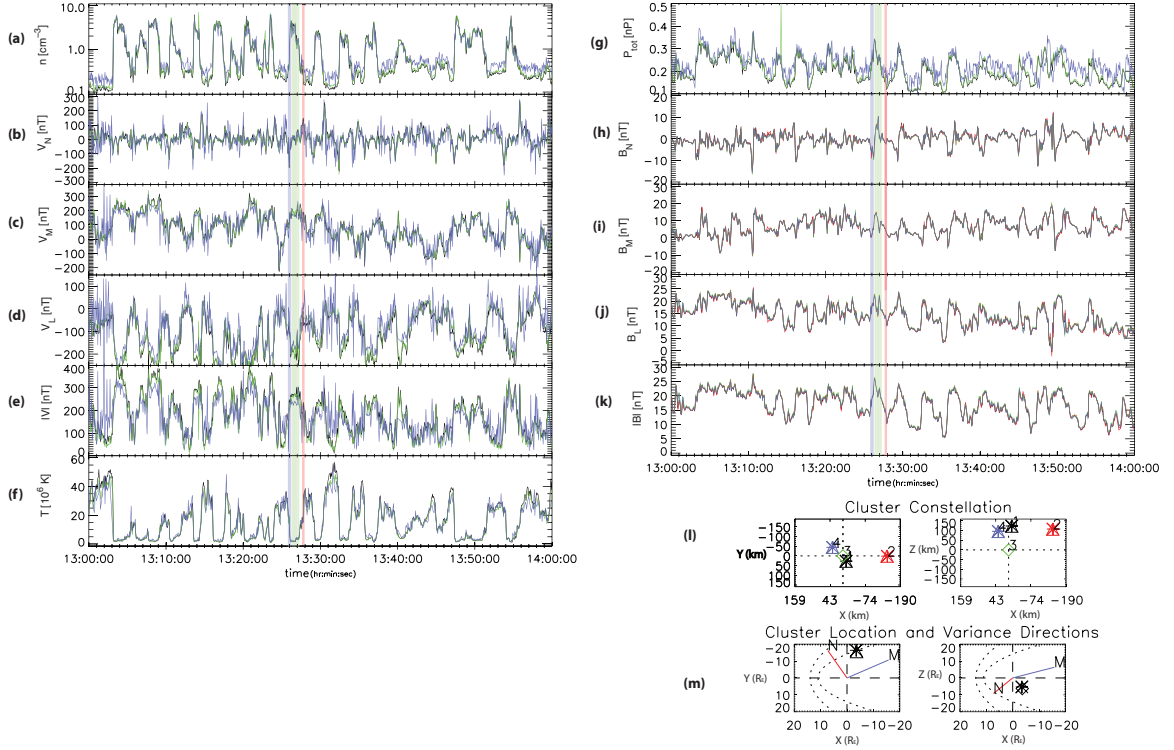


Figure 3.11: An overview of processed time series data collected by the Cluster spacecraft during the KH interval: C_1 (black), C_2 (red), C_3 (green), and C_4 (blue) field data is represented in boundary normal coordinates using maximum variance analysis (MVAE) of the $-(\mathbf{V} \times \mathbf{B})$ electric field. No plasma data exists for C_2 . Density (Panel a), V_N (Panel b), V_M (Panel c), V_L (Panel d), V_T (Panel e), Temperature (Panel f), Pressure (Panel g), B_N (Panel h), B_M (Panel i), B_L (Panel j), B_T (Panel k), Satellite Constellation Positions in km from C_3 (Panels l), and Cluster location in R_E and variance directions (Panels m). The shaded blue, green and pink regions represent the RH, LH and high frequency FMW intervals respectively.

3.4. KHI OBSERVATIONS AND SIMULATIONS

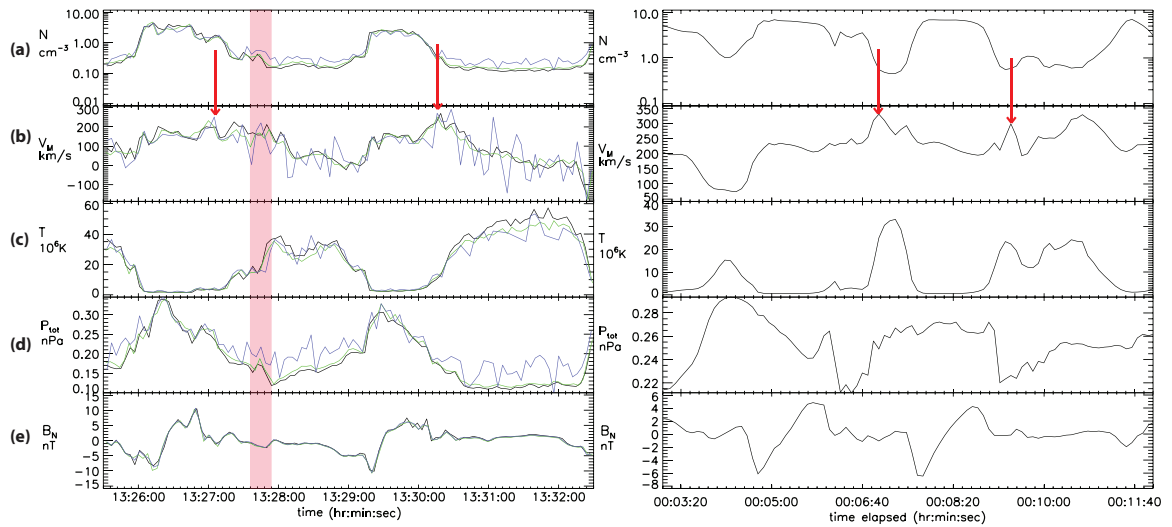


Figure 3.12: Comparison of observed and simulated plasma and magnetic field properties. The left most panel depicts the observed data (C_1 , C_3 and C_4 are the black, green and blue trace, respectively) and the right most panel depicts the time series simulation data. Density (Panel a), Temperature (Panel b), Total Pressure (Panel c), B_N (Panel d) and V_M . The red arrows show the ‘faster than sheath flow’-signature for C_4 .

3.5 Wave Analysis

Ion energy spectrograms measured during extended periods of KH activity at the LLBL have shown quasi-periodic fluctuations between hot and cold ion populations of magnetosphere and magnetosheath origin, respectively. These observations include regions where these ion populations become mixed which may be indicative of plasma transport and heating (H. Hasegawa et al., 2003). Figure 3.13 depicts three distinct ion populations: (1) magnetosphere typical, (2) magnetosheath typical and (3) mixed. Typical magnetospheric ion energies are centered around 10 keV, typical magnetosheath ion energies are centered about 1 keV, whereas the mixed ion energies range from about 1 keV to 10 keV. The FMW was observed inside one of the aforementioned mixing regions. The z -component magnetic wave power, and the high pass filtered B_z are presented in Supplementary Figure 3.9, respectively. From Supplementary Figure 3.9 the wave power decreases instantaneously after the wave pulse ends (denoted by the second dotted line in Supplementary Figure 3.9). The highest power is mainly in the lower frequency range centred at approximately 0.3 Hz, however there is an obvious amplification in the magnetic wave power in the higher frequency range (up to nearly 1 Hz) which occurs towards the end of the wave packet. The frequency of the highest amplitude oscillation is roughly 0.28 Hz and is remarkably close to f_{cp} which is around 0.3 Hz.

MVAB performed on the high-pass filtered, and smoothed (using a box car moving average) 22 Hz magnetic field data from Cluster 1 and 4, yielded propagation angles of 95° , and 98° with respect to the ambient magnetic field direction, respectively. The quasi-perpendicular propagating wave is first encountered by Cluster 1 then closely followed by Cluster 4. Hodograms were computed based on the MVAB directions and suggest the wave packet is elliptically and right handed polarized in the spacecraft frame (please refer Supplementary Figure 3.9). The ratio of the maximum and minimum eigenvalues (max/min)

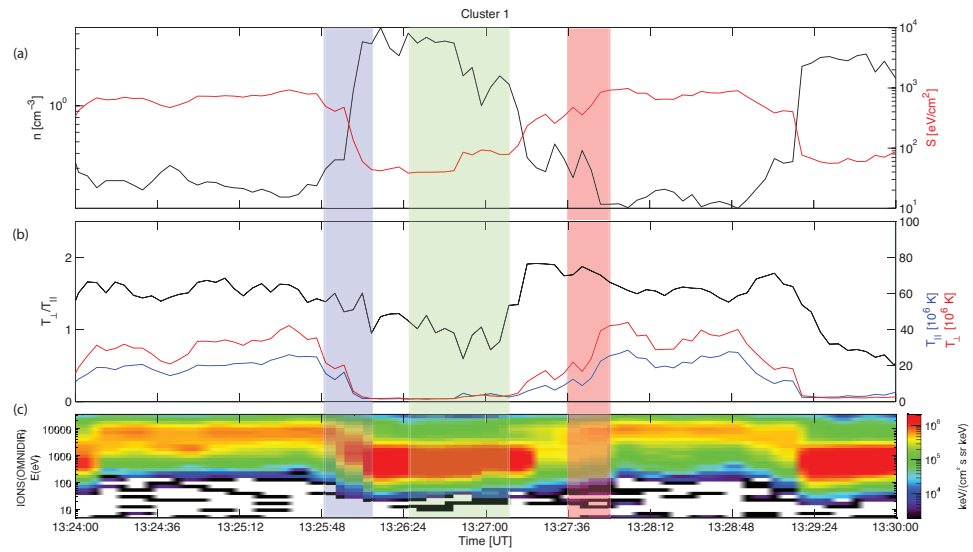


Figure 3.13: **A plot of temperature and specific entropy highlighting the increase during the wave interval.** Density (black line, Panel a) and Specific Entropy (red line, Top Panel a), T_{\perp}/T_{\parallel} (black line, Panel b), T_{\perp} (red line, Panel b), T_{\parallel} (blue line, Panel b) and Omni-directional Ion Energy Spectrogram (Panel c). The shaded blue, green and pink region represent the RH, LH and FMW intervals respectively.

is approximately 3.13 and 2.31 for C_1 and C_4 respectively, whereas the intermediate to minimum (int/min) eigenvalue ratios were approximately 525 and 116 for C_1 and C_4 , respectively. The large magnitude of int/min indicates clearly defined MVAB directions, whereas the square root of the intermediate to maximum eigenvalue ratio defines the ellipticities (e) which are $e_1 \approx 0.57$ and $e_4 \approx 0.66$. Figure 3.9 shows that the wave activity lasted over 110 seconds, but we were able to utilize the 2-spacecraft technique only for the latter 20 second interval. It is evident that over this longer wave interval, the specific entropy increases nearly an order of a magnitude. During the 20 second interval that was identified as a FMW, the specific entropy increases by factor of ≈ 3 and both the parallel and perpendicular temperature increase by a factor of ≈ 2 (see Supplementary Figure 3.9).

Analysis of RH, LH and WHAMP The upstream wave activity corresponds to larger emissions in the B_z -spectrum (Supplemental Figure 4a) and consequently more wave energy (see Figure 5b). The B_z -spectrum shows two emissions over the RH interval (13:25:52 - 13:26:07 UT) that are separated in frequency space at ω_{ci} ; MVAB reveals right-hand polarized waves with a quasi-perpendicular propagation to the ambient magnetic field above and below ω_{ci} . Similarly, MVAB reveals a left-hand polarized wave with a quasi-parallel propagation angle to the ambient magnetic field over the LH interval from Supplemental Figure 4 (13:26:28 - 13:27:09 UT). However, by resolving the 180° ambiguity of $\hat{\mathbf{k}}$ with two-point spacecraft measurements and considering the plasma flow one can determine the polarisation in the plasma frame. The (filtered) magnetic field data suggested that C_4 encounters the wave first followed by C_1 (Figure 3.9). Due to the 180° ambiguity of $\hat{\mathbf{k}}$'s direction, there are two possibilities: (1) $\hat{\mathbf{k}} = \langle -0.00691, 0.668, -0.744 \rangle$ or (2) $\hat{\mathbf{k}} = - \langle -0.00691, 0.668, -0.744 \rangle$. By taking $\hat{\mathbf{k}}$ and projecting it onto the separation vector R_{41} , it becomes apparent that (2) is the more appropriate representation of the wave vector direction (see Figure 3.14). Taking the resolved $\hat{\mathbf{k}} = \langle 0.00691, -0.668, 0.744 \rangle$, we then calculate the frequency in the plasma frame, ω_{plasma} , based on the Doppler Effect

Table 3.3: WHAMP Inputs. Mass m is scaled by the proton mass (m_s/m_p), the density n is given in cm^{-3} and the parallel temperature $T_{||}$ is given in eV .

Interval	Species	Distribution	m	n	$T_{ }$	$T_{\perp}/T_{ }$
RH	H^+	Shell	1	0.910	10.5	0.736
			1	-0.910	2.09	1
	e^-	Maxwellian	0	2.64	0.35	1
LH	H^+	Maxwellian	1	2.54	209	0.92
	e^-	Maxwellian	0	2.64	0.35	1
	e^-	Shell	0	2.64	2.84	1
			0	-2.64	1.02	1
FMW	H^+	Maxwellian	1	0.25	0.522	1
	H^+	Shell	1	0.25	4.70	8.60
			1	-0.25	2.01	1
			0	0.95	0.455	1
	e^-	Shell	0	0.95	11.4	1
			0	-0.95	1.02	1

on the the observed frequency in the spacecraft frame $\omega_{spacecraft}$. The equation for the Doppler shift is given by $\omega_{plasma} = \omega_{spacecraft} + \vec{k} \cdot \vec{v}_{bulk}$ where $\vec{k} = |\vec{k}| \hat{\mathbf{k}}$. $|\vec{k}|$ is given a range of $2\pi/2000km < |\vec{k}| < 2\pi/200km$. Figure 3.15 shows that the wave in the spacecraft frame has a right-handed polarization for wavelengths less than $\approx 272 km$ which is on the order of the satellite separation between C_4 and C_1 ($R_{41} = 188 km$). Therefore it is possible that the LH wave is either left-handed or right-handed in the plasma frame depending on its wavelength. This procedure is duplicated for the RH and FMW intervals, and it is determined that the polarization remains right-handed in the plasma frame.

Similar to the FMW interval, a theoretical kinetic dispersion is found using WHAMP for the RH and LH intervals. Hollow shell-like distributions are observed for the ion species (see Figure 3.16) during the RH interval and used as an input for WHAMP. For the LH interval, shell-like distribution functions were observed for the electron species (see Figure 3.17) and are used as an input for the WHAMP solver. Table 3.3 depicts the WHAMP input parameters used for all three intervals.

The kinetic solutions produced by WHAMP for the RH and LH wave intervals are

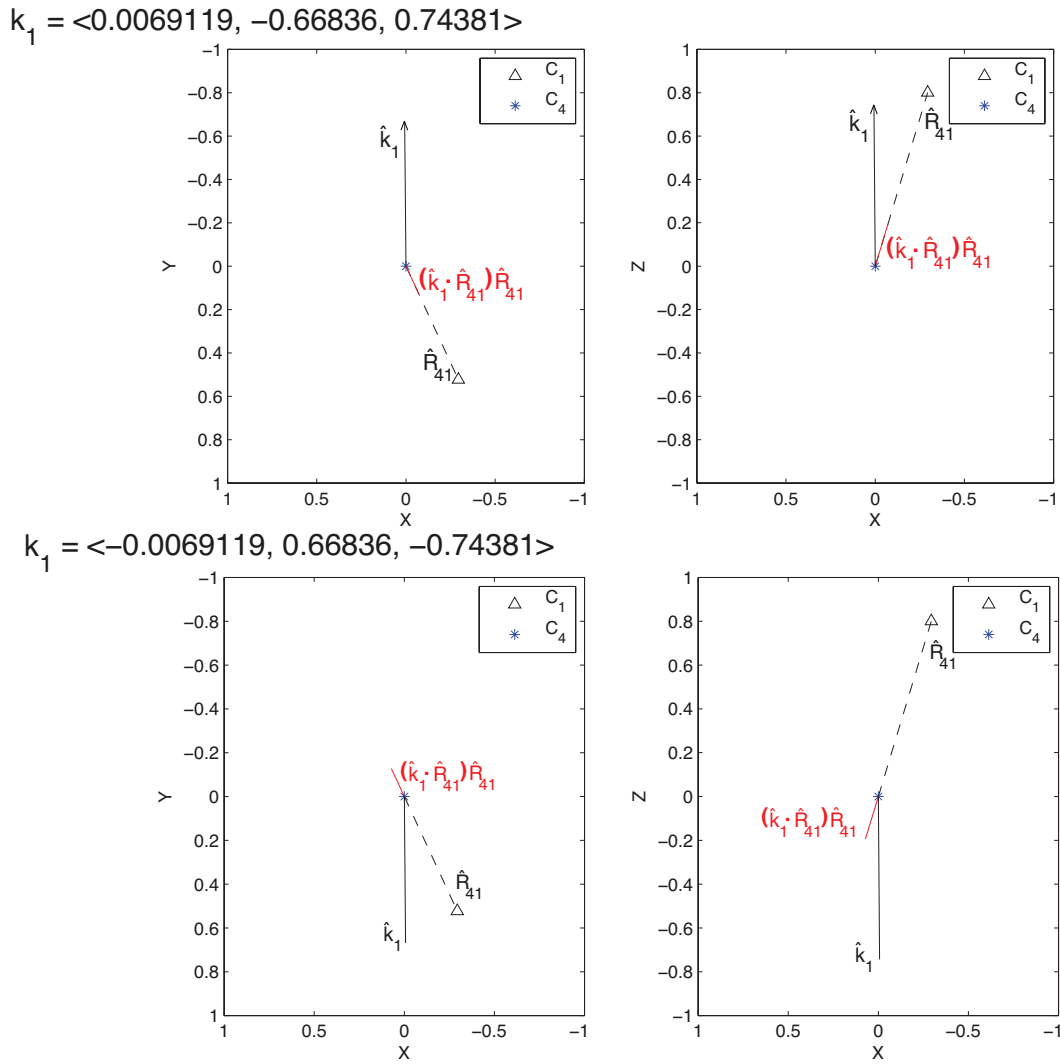


Figure 3.14: Resolving the 180° ambiguity of $\hat{\mathbf{k}}$. Projections of $\hat{\mathbf{k}}$ onto \vec{R}_{14} for cases (1) and (2) discussed in the text.

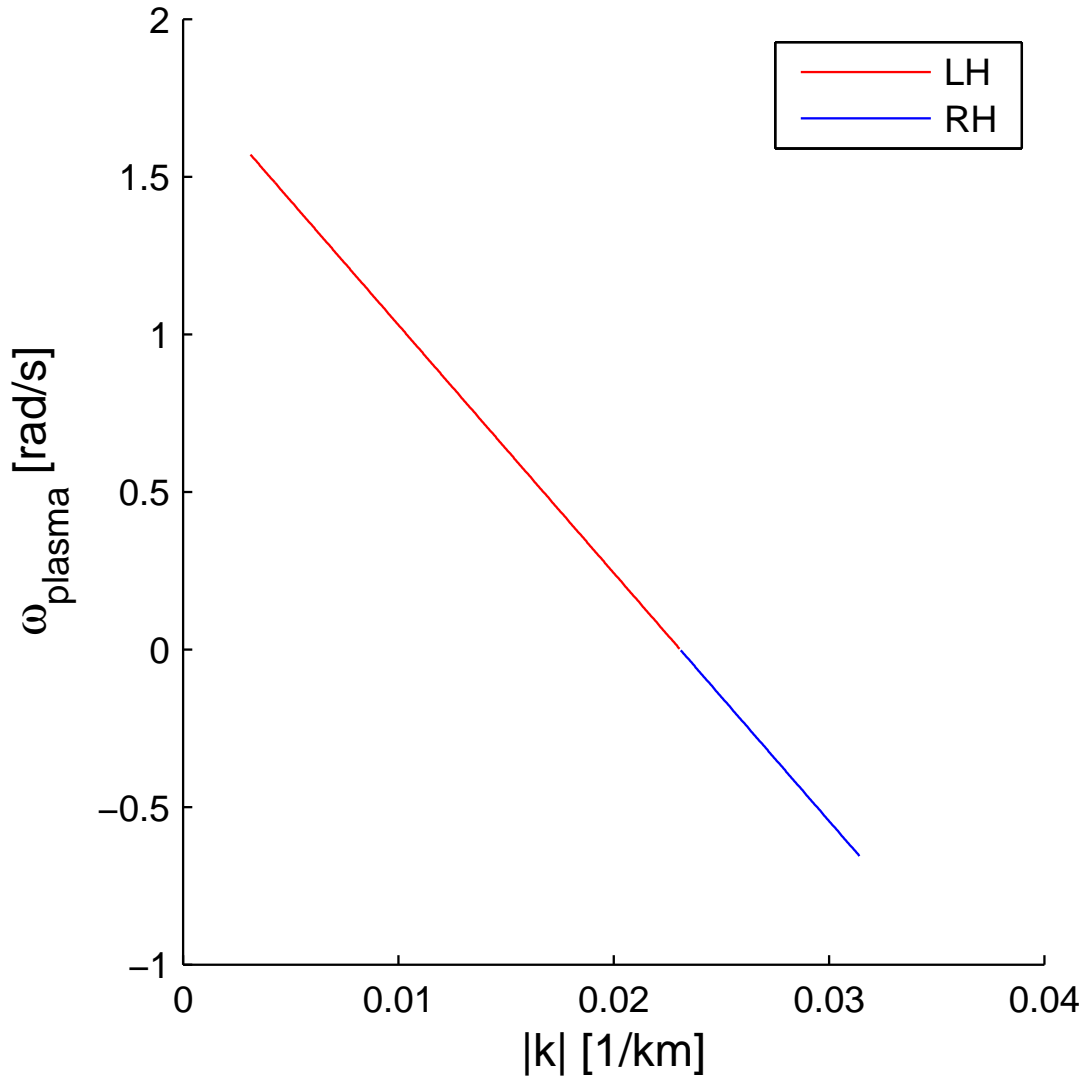


Figure 3.15: Demonstration of the Doppler effect for the LH wave interval. The red curve represents the $|k|$ -range associated with a right-handed polarization in the plasma frame and the blue curve represents the $|k|$ -range associated with a left-handed polarization in the plasma frame due to Doppler shifting. The cutoff wavelength of ≈ 273 km represents the point where the Doppler shift causes a shift in polarization in the plasma frame.

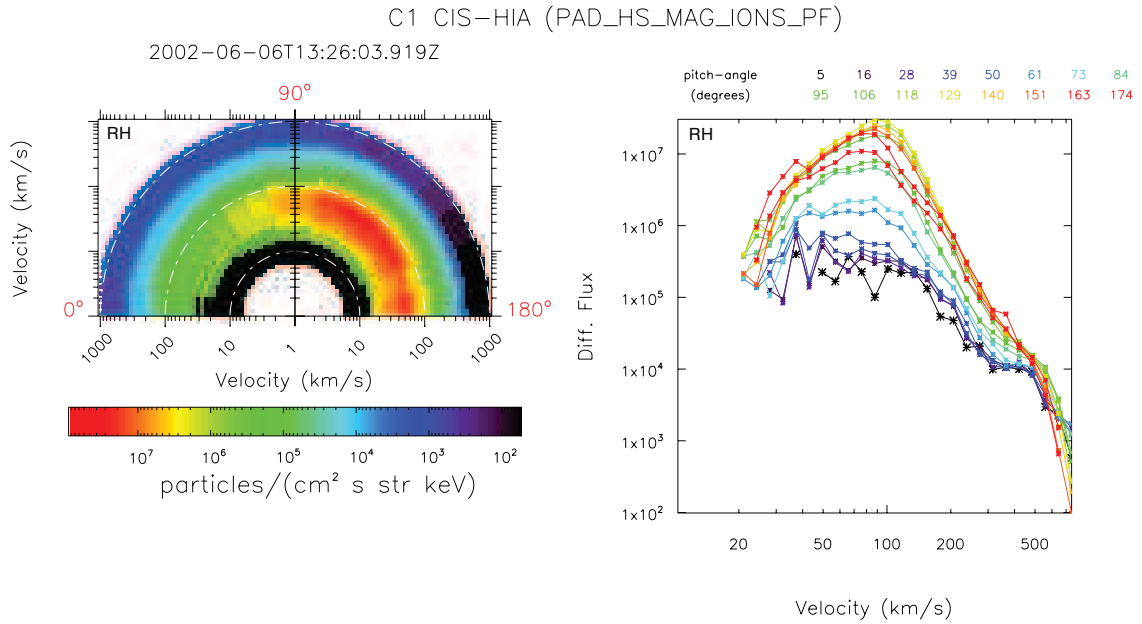


Figure 3.16: Observed distribution ion distribution functions observed by C_1 during the RH wave interval.

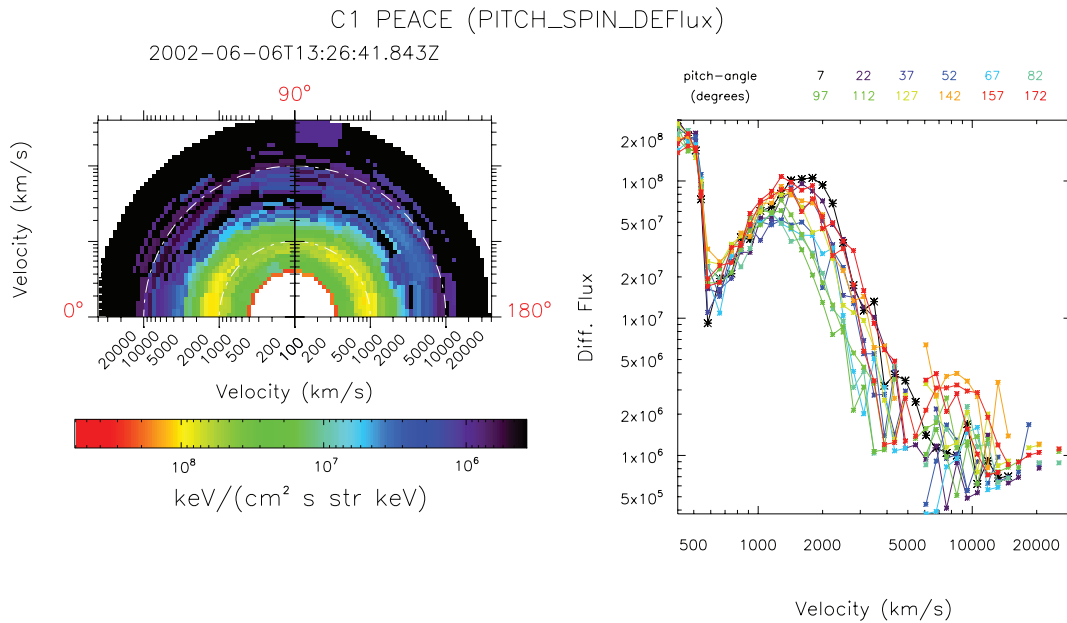


Figure 3.17: Observed electron distribution functions observed by C_1 during the LH wave interval.

depicted in Figures 3.18 and 3.19 respectively. From Figure 3.18, two distinct wave modes are shown: a right-hand mode that propagates under ω_{ci} and a right-hand mode that propagates above ω_{ci} . From Figure 3.19, a left-hand wave mode is shown that propagates under ω_{ci} and becomes slightly right-handed for very small values of k_{\parallel} . Figure 3.5, a wave mode extending over many times the ω_{ci} is right-handed for oblique propagation angles and becomes left-handed and then linearly polarized as the propagation angle approaches 90° . Cuts at varying propagation angles are taken from each dispersion surface (from Figures 3.18, 3.19 and 3.5) corresponding to the appropriate observed propagation angles listed in Table 3.1 for the RH, LH and FMW intervals, respectively; the best match to a known theoretical dispersion (and experimentally determined dispersion relation for the FMW interval) is chosen and shown in Figures 3.7, 3.8 and 3.3. From Figure 3.7, the quasi-perpendicular right-hand modes – corresponding to the 83° and 86° cuts – propagating under ω_{ci} are a close match to the theoretical dispersion for a KAW; the oblique right-hand (76° and 80° cuts) modes propagating above ω_{ci} might belong to the magnetosonic branch. From Figure 3.8, the quasi-parallel left-hand wave modes are close to the theoretical KAW and IC dispersions.

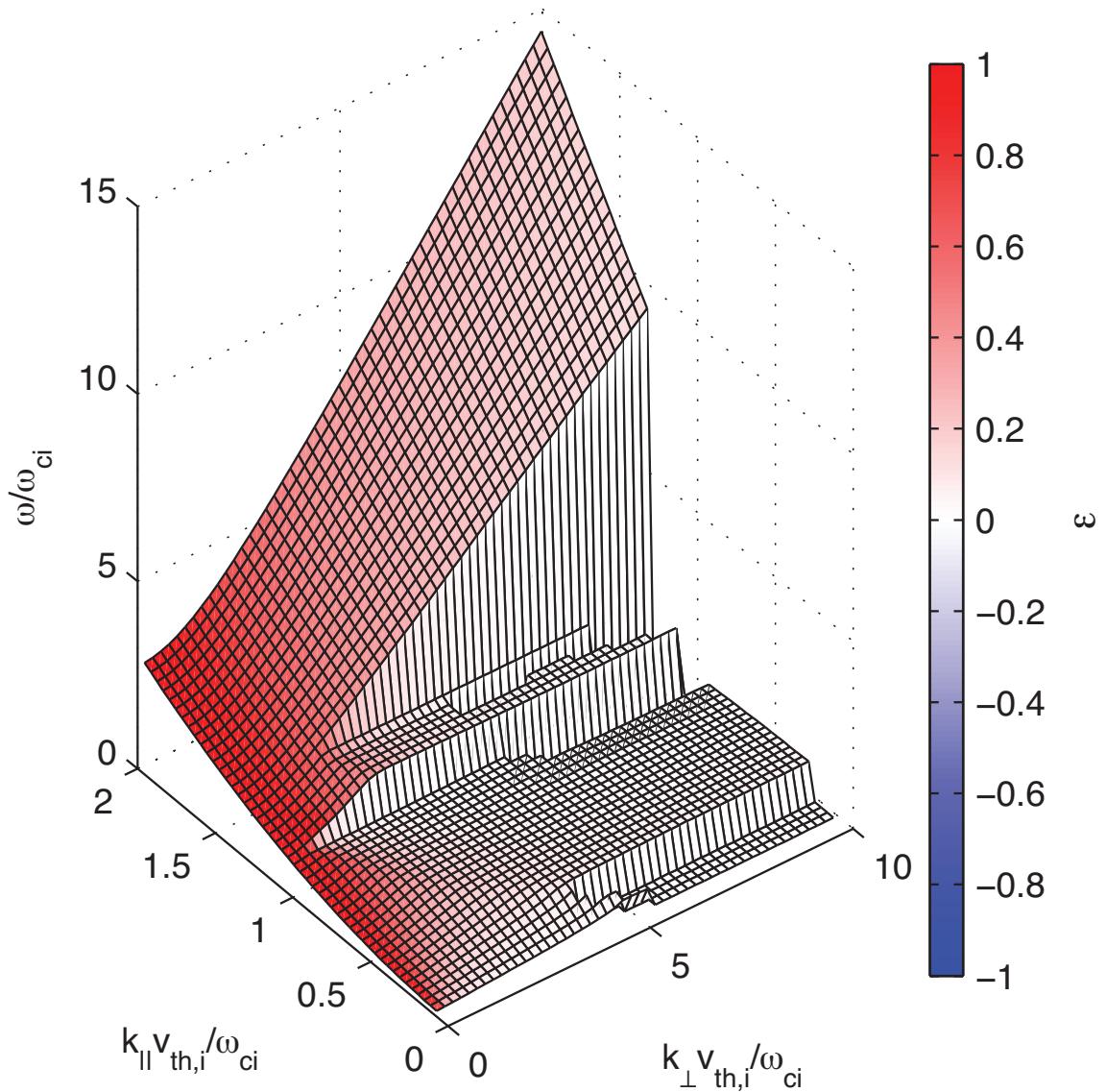


Figure 3.18: Dispersion surfaces determined by WHAMP using inputs parameters described in Table 3.3 for the RH wave interval. The color bar represents the ellipticity ϵ , where red represents a right-handed wave, blue represents a left-handed wave and white represents a linear polarisation.

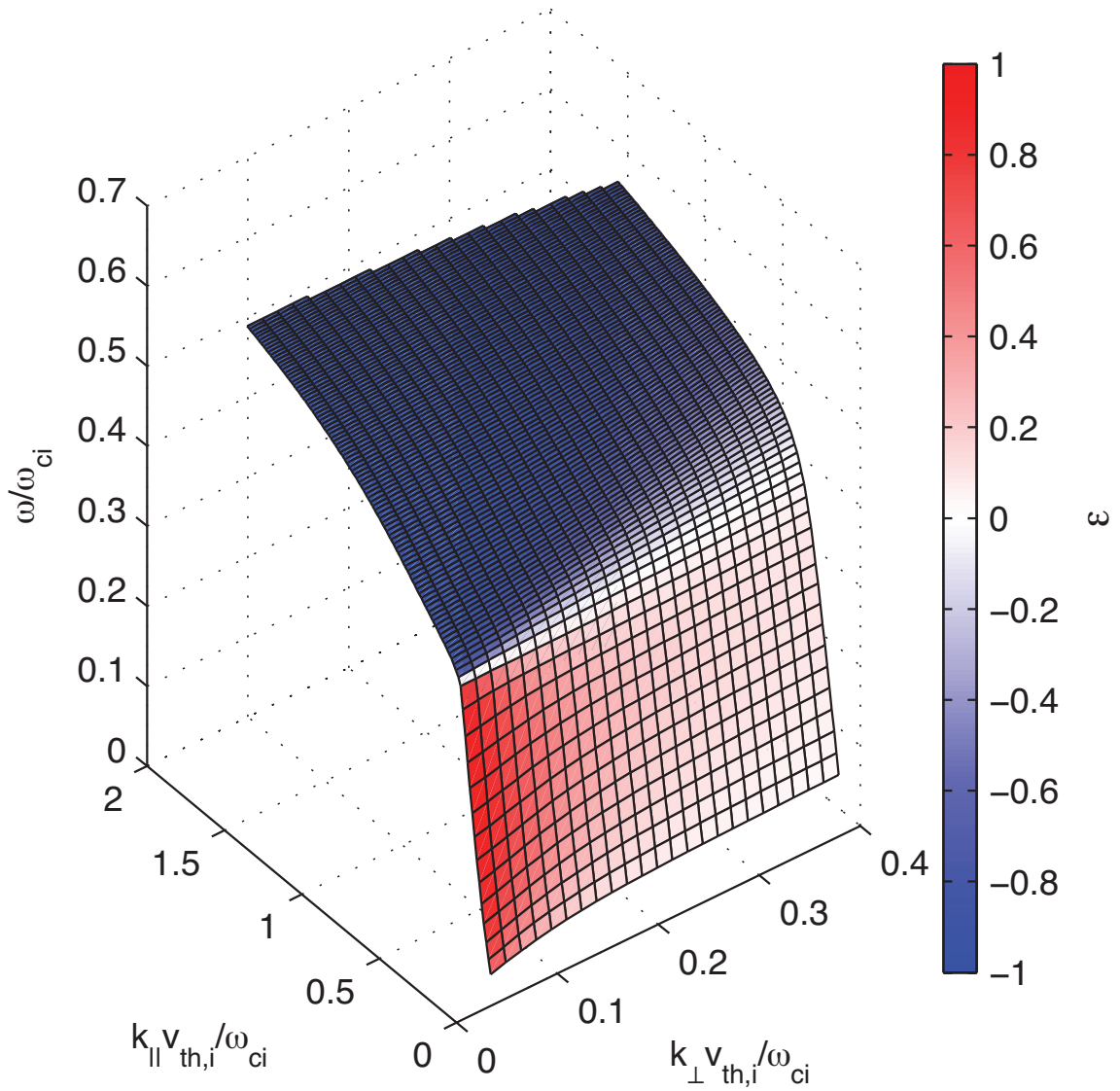


Figure 3.19: Dispersion surfaces determined by WHAMP using inputs parameters described in Table 3.3 for the LH wave interval. The color bar represents the ellipticity ϵ , where red represents a right-handed wave, blue represents a left-handed wave and white represents a linear polarisation.

Chapter 4

Statistical Study

The work within this Section was submitted to *Journal of Geophysical Research: Space Physics* in March 2017.

4.1 Introduction

The origin of the properties of our near-Earth plasma is still not well understood – for instance the specific entropy ($\mathcal{S} = T/n^{2/3}$) increases by 1-2 orders of magnitude across the magnetopause which is indicative of strong non-adiabatic heating (Borovsky & Cayton, 2011). Furthermore, the magnetospheric ions are about 50 times hotter than those in the magnetosheath. There also exists a temperature and density asymmetry among the cold component ions in the magnetotail plasma sheet favoring the dawn flank – cold component ions are 30 - 40% hotter and more abundant on the dawn flank (H. Hasegawa et al., 2003; Wing et al., 2005).]

There are three possible sources for these plasma sheet asymmetries: a) seed asymmetry of the magnetosheath plasma temperature and density, b) asymmetry of magnetopause processes favoring the dawn flank, c) asymmetry of some plasma sheet/magnetotail processes:

Walsh et al. (2012) have shown dawn favored asymmetries in the proton densities and temperatures, as well as dusk favored asymmetries of the plasma flow speed and magnetic field strengths in the dayside magnetosheath near the magnetopause. In studies considering the entire dayside magnetosheath, the dawn flank, which is downstream of the quasi-parallel bow shock, has been shown to host a hotter and denser plasma (Dimmock et al., 2015; Dimmock, Pulkkinen, et al., 2016). However, the level of this dayside asymmetry (15 %) is insufficient to account for the observed plasma sheet asymmetry (30-40 %) in the magnetotail, in particular because magnetosheath plasma becomes cooler with increasing tailward distance. The dawn flank magnetosheath is also more prone to higher amplitude magnetic field fluctuations which are further enhanced during faster solar wind velocities (Dimmock et al., 2014), which may affect the growth of the physical mechanisms at the magnetopause.]

The two main mechanisms that can facilitate plasma transport and heating at the Low Latitude Boundary Layer (LLBL) are magnetic reconnection and Kelvin-Helmholtz Instability. Recently, Ma & Otto (2014) showed, using Hall-MHD simulations, that significant specific entropy increase in magnetic reconnection at the Earth's magnetopause is possible only if magnetosheath plasma beta is low ($\beta \ll 1$). Because magnetosheath beta typically is of the order of unity close to magnetopause (see Appendix A), other physical mechanisms must also be at work that contribute to the strong non-adiabatic ion heating in this region. The other possible mechanism is the Kelvin-Helmholtz Instability, which has been observed during northward (H. Hasegawa, Fujimoto, Phan, et al., 2004), southward (Hwang et al., 2011; Yan et al., 2014) and Parker Spiral (PS) (Nykyri et al., 2006; Moore et al., 2016) interplanetary magnetic field (IMF) orientations. A recent survey of 6 years of in situ data from NASA's Time History of Events and Macroscale Interactions during Substorms (THEMIS) mission has shown that Kelvin-Helmholtz (KH) waves are frequent at the magnetopause, providing strong observational evidence as to their importance for magnetopause

dynamics (Kavosi & Raeder, 2015). The spatial distribution of these KH waves observed between 2007-2013 using the list by (Kavosi & Raeder, 2015) favors the dawn flank magnetopause during the Parker-Spiral (PS) IMF orientation (in preparation (Henry et al., 2017)). Also, MHD simulations demonstrate that for variety of Solar Wind plasma conditions and during PS IMF orientation, the KHI growth shows a slight preference for dawn flank due to the smaller magnetic field tension when compared to the dusk flank (Nykyri, 2013). Furthermore, Nykyri (2017) showed that the seed velocity fluctuations in the magnetosheath have a strong dawn favored asymmetry and can contribute to faster KHI growth times at the dawn magnetopause. Recent statistical studies using 6 years of THEMIS data illustrate that the fluctuations in ULF Pc4-Pc5 and Pc3 range, which characterize the frequency range of fluctuations generated by the KHI (Miura & Pritchett, 1982), are indeed more enhanced in the dawn flank (Nykyri & Dimmock, 2016; Dimmock, Nykyri, et al., 2016).

There are many secondary mechanisms associated with the KHI that can make plasma heating and transport more efficient on the dawn-side magnetopause flank: Magnetic reconnection inside KH vortices has been proposed as a mechanism for transporting mass across the magnetopause and generating the cold-dense plasma sheet (Nykyri & Otto, 2001, 2004; Nykyri et al., 2006; Taylor & Lavraud, 2008; H. Hasegawa et al., 2009). KH associated ion-beams observed during a reconnection interval may act as a driver for ion-scale waves (Nykyri et al., 2006), which may in turn heat the plasma.

KHI may also lead to the formation of kinetic Alfvén waves (KAWs) at the magnetopause via mode conversion from ultra low frequency MHD surface waves (Johnson & Cheng, 1997; Johnson et al., 2001). KAWs have been attributed to ion heating and plasma transport across the magnetopause (A. Hasegawa & Mima, 1978; Rezeau et al., 1989; Lee et al., 1994; Johnson & Cheng, 1997; Johnson et al., 2001). Observations consistent with this phenomenon have been shown to transport significant energy into the magnetosphere at the Alfvén resonance (Chaston et al., 2007). A statistical study by Yao et al. (2011) showed a

dawn-dusk asymmetry in the spectral energy densities of ion gyro-radii scale electromagnetic waves that favored the dawnside over the duskside magnetopause.

Using measurements from two Cluster spacecraft ≈ 80 km apart, Moore et al. (2016) recently unambiguously identified, in terms of an observational dispersion relation, a fast magnetosonic (FMW) wave packet in the vicinity of a KH vortex. The wave energy associated with the FMW interval accounted for a substantial amount of energy transport to the cold-component ion population. It was suggested that velocity shears at the flank magnetopause generate KHI at the MHD scale, which contained sufficient kinetic energy to power ion-scale FMW generation in the vicinity of a rolled-up KH vortex. Shell-like ion distributions observed inside the KH vortex were suggested as a likely driving source of the observed FMW. During this event, also other wave packets were observed with properties consistent with KAWs in magnetosheath side of the vortex, as well as another wave packet in mixed region that had properties consistent with FMW. The ion scale wave observations and associated heating during this event are consistent with cross-scale energy transport from fluid-scale KHI, into ion-scale waves, allowing the kinetic energy of the velocity shear to be transferred into heat energy of ions. We have calculated various wave properties such as ellipticity, Poynting flux, wave power and wave propagation angle with respect to the magnetic field, during this event, which can be used as a bench-mark for the interpretation of the results of a statistical study of the wave properties.

In the present study our motivation is to study a) whether ion-scale waves are more abundant when KHI is present and b) whether ion heating is more abundant during ion-scale wave observations when KHI is present compared to crossings without KHI. We compare the statistics of ion scale wave properties and plasma parameters between boundary crossings during ≈ 12 hrs of KHI to crossings where signatures of active KHI are absent. Summary along with binning statistics plots for each of the KH and non-KH events are shown in Appendix A.1.1.

4.2 Broad Band Statistics

The following broad band statistics are taken over a relatively large band of frequencies $0.05 Hz \leq f \leq 2.7 Hz$ to offer a general account for the degree of polarization and magnetic compressibility over the three plasma regimes during KHI and non-KHI boundary crossings.

4.2.1 Degree of Polarization

The degree of polarization ϵ , plotted in Figure 4.1, is calculated from the Stokes' parameters compiled from the magnetic wave fields described by Carozzi et al. (2001). Probability distributions in ϵ are non-zero between approximately ± 0.9 for frequency ranges above (Top Panels of Figure 4.1) and below (Bottom Panels of Figure 4.1) the local f_{ic} . These distributions form a trident distribution containing three distinct peaks at approximately ± 0.675 and at 0 for all plasma regimes at all frequencies. Overall there is little distinction in the observed ϵ between KHI and non-KHI events. Furthermore, due to possible Doppler effects, an accurate weight of handedness (right-hand vs left-hand) in the plasma frame is not attainable.

4.2.2 Magnetic Compressibility

One dimensional probability distribution functions depicting the magnetic compressibility $|\delta B_{||}|^2/|\delta B_{\perp}|^2$ are shown for the MSP, MIX and MSH plasma regimes in Figure 4.2 for both KHI events (left panels) and non-KHI events (right panels). Although statistically transverse ($|\delta B_{||}|^2/|\delta B_{\perp}|^2 < 1$ for most intervals), there are less observed transverse waves in the MSP plasma regime relative to the MIX and MSH regimes during KHI events when compared to non-KHI events – please refer to the top left and top right panels of Figure 4.2. However, when considering only the significant wave power ($|\delta B_{tot}|^2 > 33\% \overline{|\delta B_{tot}|^2}$), an amplification in the transverse wave power occurs (statistically) in the MIX plasma regime

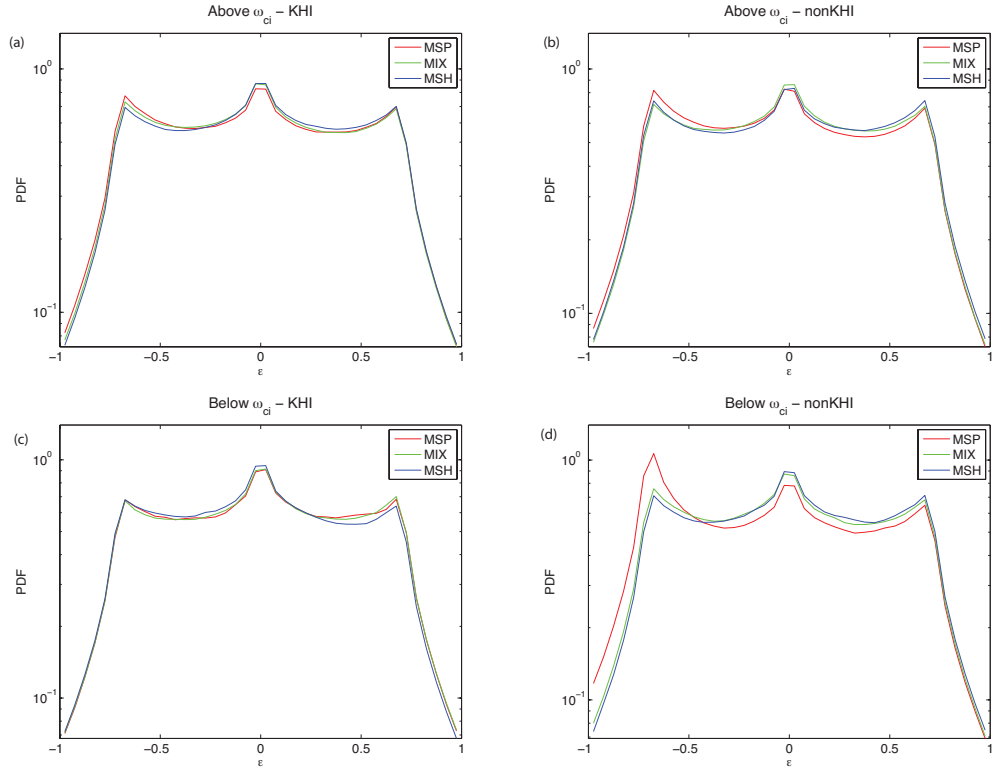


Figure 4.1: Degree of polarization ϵ calculated in the MSP (red), MIX (green) and MSH (blue) plasma above (Top Panels) and below (Bottom Panels) the local ion cyclotron frequency f_{ic} during KHI (Left Panel) and non-KHI events (Right Panel).

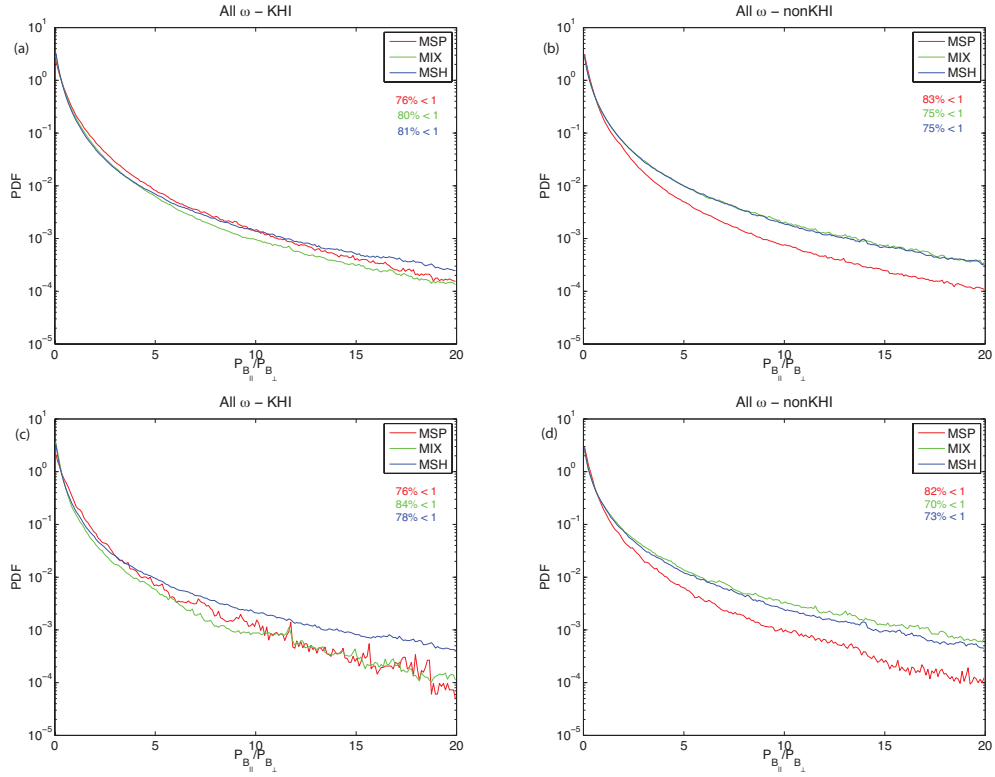


Figure 4.2: Magnetic compressibility $|\delta B_{\parallel}|^2/|\delta B_{\perp}|^2$ calculated in the MSP (red), MIX (green) and MSH (blue) plasma for all frequencies ($0.05 \text{ Hz} \leq f \leq 2.7 \text{ Hz}$) during KHI (Left Panel) and non-KHI events (Right Panel). PDFs depicted in the Bottom Panels result from filtering out wave intervals with $|\delta B_{tot}|^2 < 33\% |\overline{\delta B_{tot}}|^2$.

for the KHI events.

4.3 Ion-scale Wave Intervals

The statistics for the ion scale wave intervals are obtained by considering frequency bins near the local f_{ic} , including the range $[f_{(j_{ic}-10)}, f_{(j_{ic}+10)}]$, where j_{ic} is the index of the frequency bin corresponding to the local f_{ic} . The 2-d histograms consisting of θ_{kB} and kinetic wave properties are compiled by tallying counts accrued in each parameters' overlapping bins.

All of the ion-scale wave properties are calculated in the spacecraft frame. Because it

is not possible to account for the actual Doppler shift for each of the MVAB wave intervals on a statistical basis, we approximate the possible effects by accounting for the maximum effects. For a brief analysis on the Doppler shift effects, please refer to Appendix B.

4.3.1 Mean Total Magnetic Wave Power, P_{tot}

The mean total magnetic wave power, $P_{tot} = \overline{|\delta B_{tot}|^2}$, is determined by taking the mean of the total magnetic wave power over each MVAB wave interval. The 2-d distribution of P_{tot} versus wave propagation angle, θ_{kB} , for the MSP plasma regime are shown in the left (KHI events) and right (non-KHI events) panels of Figure 4.3. From the left panel in Figure 4.3, a higher count density (\log_{10} -counts per cell) during KHI events is observed for obliquely propagating waves with relatively low power (P_{tot}), with the highest count density accounted for in the $80^\circ - 90^\circ$ bin. A more moderate count density is observed for oblique waves ($60^\circ - 90^\circ$) with significantly higher power for KH events than for non-KHI events. In contrast, during non-KHI events the highest count density is observed for $40^\circ - 50^\circ$, low power waves (see Figure 4.3 (b)). High power ion scale waves are rarely observed during the non-KHI events in MSP region.

To offer a better comparative analysis between statistics gathered during KHI and non-KHI events, a \log_{10} count difference between the KHI and non-KHI events is calculated for each of the kinetic wave properties and plotted in the following 2-d distributions. Difference distributions in which observations taken from KHI events dominate are designated by red whereas those dominated by observations taken from non-KHI events are designated by blue, and a zero \log_{10} count difference is designated by white. Please note that an actual count difference of 0 or 1 is assigned a \log_{10} count difference of 0.

The 2-d comparative distributions of the mean total wave power versus propagation angle (P_{tot} vs θ_{kB}) depicting the \log_{10} count difference between observations made during

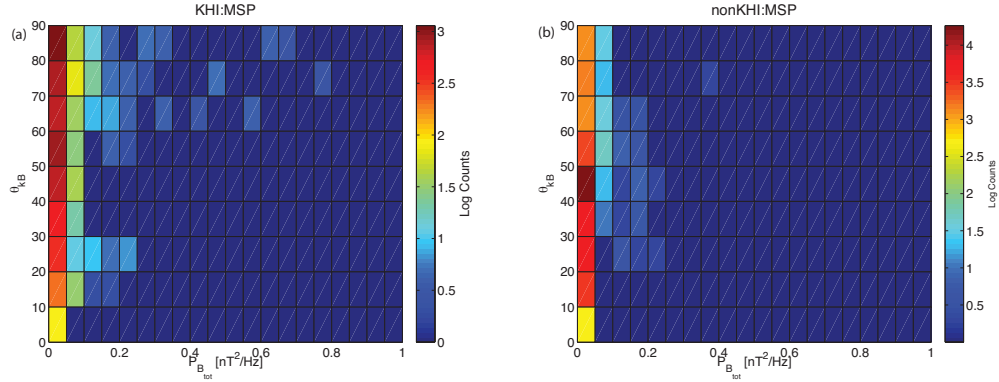


Figure 4.3: The 2-d distributions of mean total magnetic wave power versus wave propagation angle (P_{tot} vs θ_{kB}) between KHI (left panel) and non-KHI (right panel) events in the MSP plasma regime.

KHI and non-KHI events are shown in Figure 4.4 for the MSP, MIX and MSH plasma regimes respectively. In the MSP plasma regime (Figure 4.4 (a)), more obliquely propagating waves between $50^\circ - 90^\circ$ are observed during KHI events for a broad range of power ($P_{tot} \approx 0 - 0.9 nT^2/Hz$), whereas during non-KHI events more waves with low power ($P_{tot} \approx 0 - 0.05 nT^2/Hz$) and lower propagation angle ($\theta_{kB} \approx 10^\circ - 50^\circ$) are observed.

A similar trend is seen for waves with low power ($P_{tot} \approx 0 - 0.1 nT^2/Hz$) in the MIX plasma regime, where observations of obliquely propagating waves ($\theta_{kB} \approx 40^\circ - 90^\circ$) are dominant during KHI events and waves with lower propagation angle ($\theta_{kB} \approx 0^\circ - 40^\circ$) are dominant during non-KHI events (Figure 4.4 (b)).

There is a larger disparity between high power waves in the MIX plasma regime when compared to the MSP, with a slight preference of KHI event observations between $\theta_{kB} = 40^\circ - 80^\circ$. The quasi-perpendicular propagating ($\theta_{kB} = 80^\circ - 90^\circ$) observations tend to be more non-KHI dominant.

In the MSH plasma regime (Figure 4.4 (c)), the low power wave observations are non-KHI dominant for all propagation angles. There is a slight asymmetry for waves contributing to the higher power with a clear dominance of KHI events for low propagation angles

($\theta_{kB} \approx 0^\circ - 30^\circ$).

4.3.2 Total Integrated Poynting Flux

The total integrated Poynting flux, $S_{int} = \int S_{tot} dt$, associated with the FMW interval from Moore et al. (2016) is approximately $4.4 \times 10^6 \text{ keV cm}^{-2}$. For statistics the S_{int} is computed by integrating the wave Poynting flux over each MVAB wave interval. The 2-d distributions of S_{int} vs θ_{kB} are displayed in Figure 4.5. In the Figure 4.5 (a), observations made in the MSP plasma regime show a broad distribution of KHI dominant S_{int} for obliquely propagating waves ($\theta_{kB} = 50^\circ - 90^\circ$) and non-KHI dominant (narrowly distributed S_{int}) wave observations for lower propagation angles ($\theta_{kB} = 10^\circ - 50^\circ$).

In the MIX plasma regime (Figure 4.5 (b)), however, the KHI dominant observations are subdued to a narrow band of low S_{int} for $\theta_{kB} \approx 40^\circ - 90^\circ$. The non-KHI dominant wave observations comprise a narrow band of S_{int} for lower propagating angles ($\theta_{kB} \approx 0^\circ - 40^\circ$). The trend for higher S_{int} values is not well discernible, however there is a band of KHI dominant quasi-perpendicular wave observations for $S_{int} \approx 0.5 - 2 \text{ keV cm}^{-2}$.

There is a transition to non-KHI dominant wave observations in MSH plasma regime (Figure 4.5 (c)) for the low S_{int} across most propagation angles ($\theta_{kB} = 0^\circ - 50^\circ, 60^\circ - 90^\circ$). There is a slight asymmetry for moderate integrated Poynting flux ($S_{int} \approx 0.25 - 1.75 \times 10^6 \text{ keV cm}^{-2}$) where obliquely propagating waves ($\theta_{kB} = 60^\circ - 90^\circ$) are non-KHI dominant and waves with smaller propagation angles ($\theta_{kB} = 0^\circ - 40^\circ$) are dominant during KH events.

4.3.3 Polarization Dispersion: FMW

Moore et al. (2016) showed unambiguous observations of a quasi-perpendicular propagating ($\theta_{kB} \approx 85^\circ, 88^\circ$) FMWs observed close to center of a KH vortex (evidenced by a total pressure minimum) with sufficient energy to account for observed ion heating. The wave

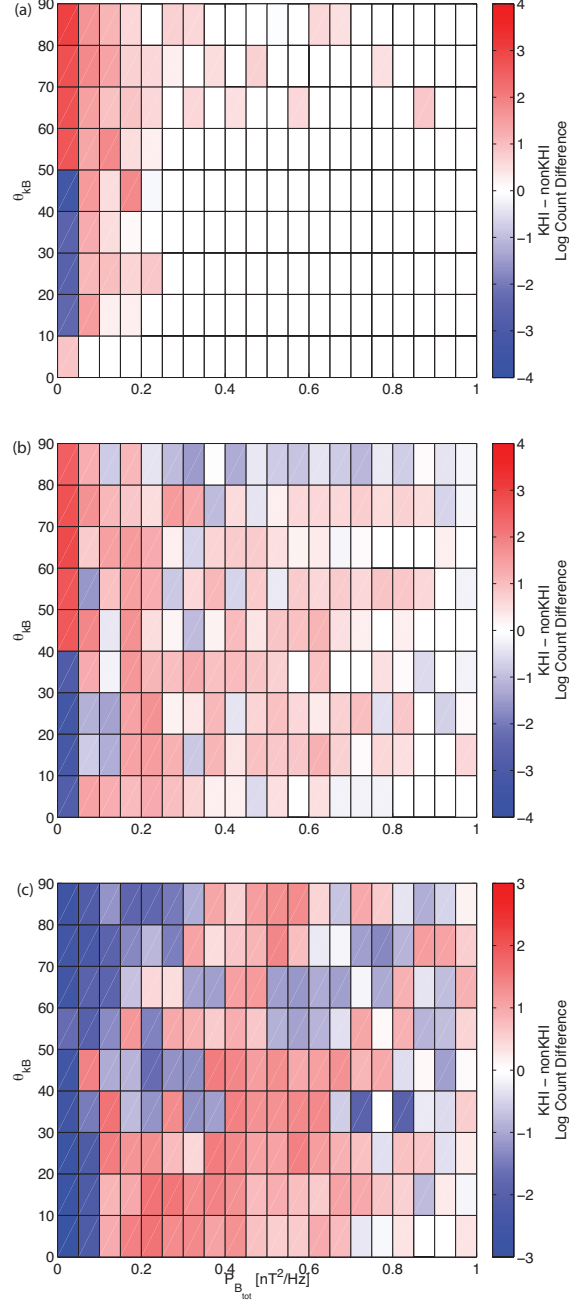


Figure 4.4: The 2-d comparative distributions of mean total power (P_{tot}) versus propagation angle (θ_{kB}) between KHI and non-KHI events. The panels from top to bottom represent the MSP, MIX and MSH plasma regimes, respectively.

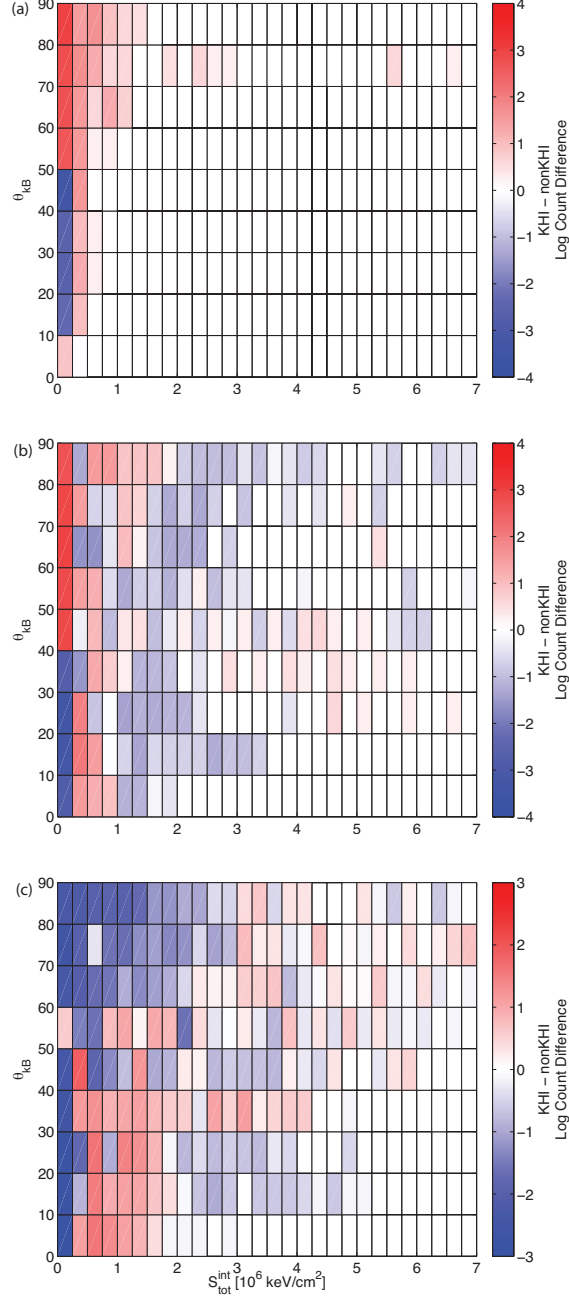


Figure 4.5: The 2-d comparative distribution of the integrated Poynting flux versus propagation angle (S_{int} versus θ_{kB}). The panels from top to bottom represent the MSP, MIX and MSH plasma regimes, respectively.

$\delta E/\delta B$ -polarization (scaled by the local Alfvén speed), $(|\delta E_{\perp}|/|\delta B_{\perp}|)/v_A$ versus the wave frequency calculated during this FMW interval is plotted in Figure 4.6. For $f < f_{ic}$, where $f_{ic} \approx 0.3 \text{ Hz}$, there is a strong count density between approximately 0 – 4, indicating the waves are mostly electromagnetic. This distribution broadens (becomes more electrostatic) for $f > f_{ic}$, but the strongest count densities are still in electromagnetic regime 0 – 10.

Because the local f_{ic} for the FMW interval is approximately 0.3 Hz , the frequency range of interest in context to the MVAB wave interval statistics is approximately $0.20 - 0.45 \text{ Hz}$. In Figure 4.6 the scaled $\delta E/\delta B$ -polarization is approximately 0 – 4 for the strongest count densities and up to 8 for the lower count densities.

4.3.4 Mean $\delta E/\delta B$ Polarization Dispersion

The 2-d distributions of the mean scaled $\delta E/\delta B$ polarization, \mathcal{P} , versus propagation angle are plotted in Figures 4.7 (a)-(c). \mathcal{P} is calculated by taking the mean $(|\delta E_{\perp}|/|\delta B_{\perp}|)/v_A$ over each MVAB wave interval. In the MSP plasma regime (Figure 4.7 (a)), the distributions of \mathcal{P} vs θ_{kB} show a dominance for KHI events across all values of \mathcal{P} for the strongly obliquely propagating waves ($\theta_{kB} = 50^{\circ} - 90^{\circ}$). This KHI dominant distribution is much narrower ($\approx 0.125 - 4$) for smaller propagation angles ($\theta_{kB} = 0^{\circ} - 40^{\circ}$). This trend is qualitatively similar in the MIX plasma regime (Figure 4.7 (b)).

Observations in the MSH plasma regime (Figure 4.7 (c)) show a narrow KHI dominant distribution in \mathcal{P} ($\approx 0.125 - 2$) for all θ_{kB} , whereas observations at higher values of \mathcal{P} (> 2.125) are non-KHI dominant for all θ_{kB} .

4.3.5 Plasma Parameters

In this section, plasma parameters are shown for both the ion-scale wave intervals and from a global perspective. Please refer to Appendix A for an analysis on possible solar wind

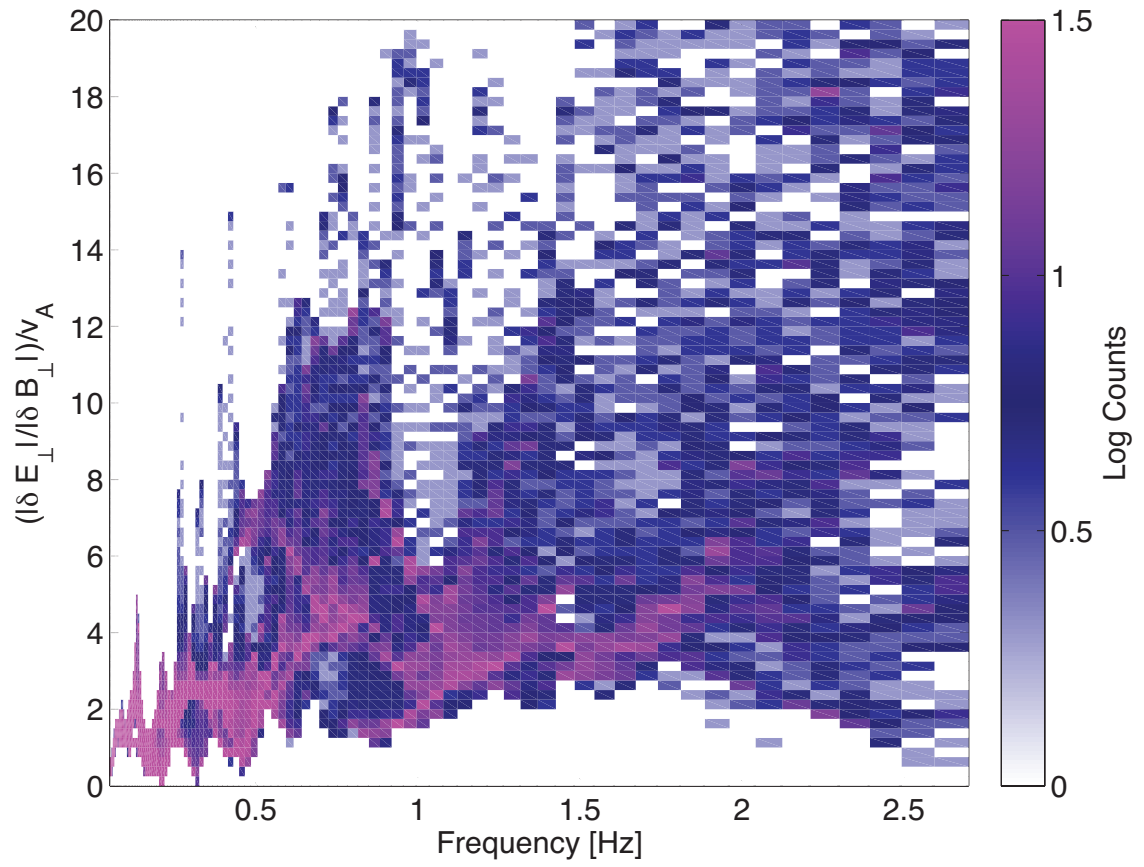


Figure 4.6: Polarization dispersion $(|\delta E_{\perp}|/|\delta B_{\perp}|)/v_A$ from the June 6th 2002 FMW interval.

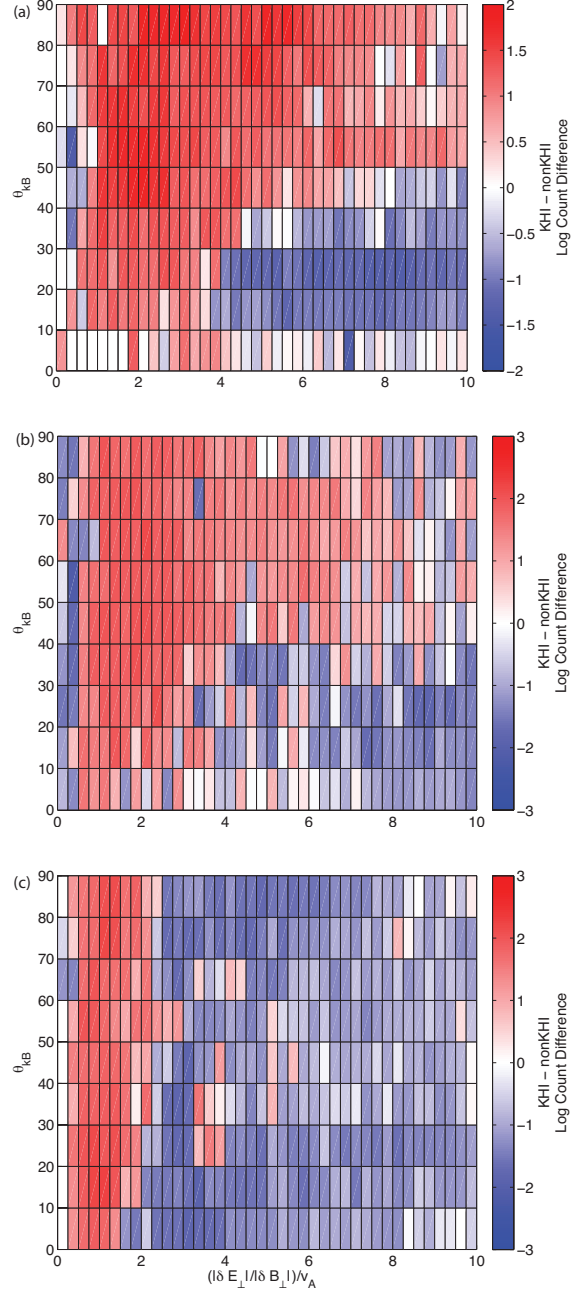


Figure 4.7: The 2-d comparative distributions of scaled mean $\delta E/\delta B$ polarization versus propagation angle. The panels from top to bottom represent the MSP, MIX and MSH plasma regimes, respectively.

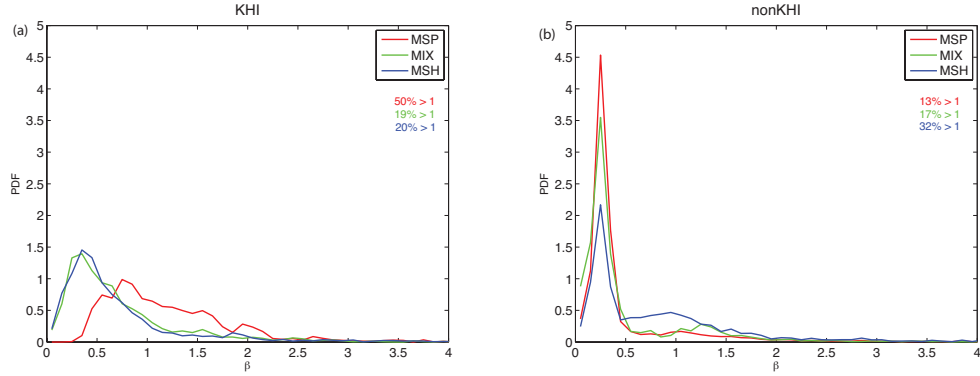


Figure 4.8: Plasma beta calculated during the ion-scale MVAB wave intervals for the MSP (red), MIX (green) and MSH (blue) plasma for the KH (left panel) and non-KH (right panel) events.

effects on magnetosheath plasma parameters.

The plasma beta β calculated over the MVAB wave intervals is plotted in Figures 4.8 (a)-(b). During the KHI events the β probability distributions are much narrower in the MIX and MSH plasma regimes with peaks < 1 and are much broader in the MSP plasma (Figure 4.8 (a)). When integrating the tails of the distributions in the MIX and MSH plasma, only $\approx 20\%$ of all the wave intervals have $\beta > 1$. For KHI events $\approx 50\%$ of all wave intervals in MSP plasma regime have $\beta > 1$. During the non-KHI events, the distributions in all three plasma regimes share similar peaks, with the broadest distribution in the MSH plasma (right panel of Figure 4.8). Integrating the tails of the distributions reveals that the β steadily increases from the MSP ($\approx 13\% > 1$) to the MIX ($\approx 17\% > 1$) to the MSH ($\approx 32\% > 1$) plasma regime.

Although the PDFs from the Figures 4.8 (a)-(b) depict ion-scale waves propagating through lower beta MSH plasmas during KH events compared to the non-KH events, it is worthwhile to inspect the global plasma beta β_{global}^{MSH} observed in the MSH plasma regime. Figures 4.9 (a)-(b) show the 1-d distributions of the global MSH plasma beta calculated over the range $0 < \beta \leq 10$ for the KH and non-KH events respectively. It should be noted

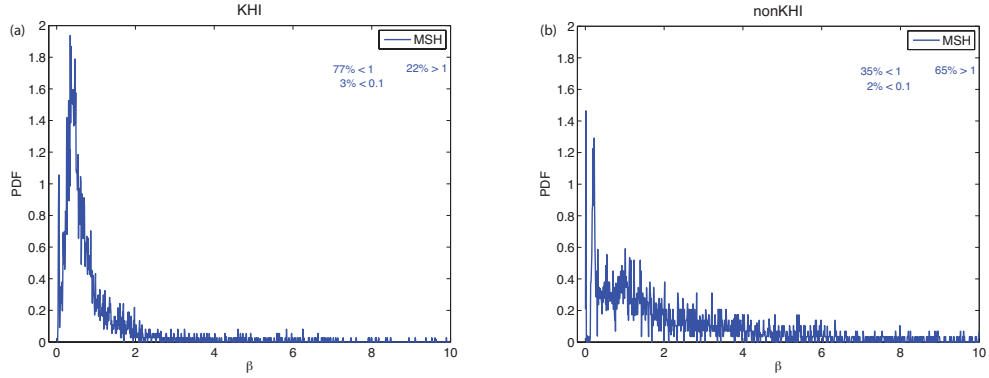


Figure 4.9: Plasma beta calculated globally for the MSP (red), MIX (green) and MSH (blue) plasma for the KH (left panel) and non-KH (right panel) events.

that the global MSH data value range extends beyond β_{global}^{MSH} , however the low MSH β (relative to 1) is of special interest.

In general, β_{global}^{MSH} is lower during the KH events compared to the non-KH events – $\approx 77\% < 1$ and $\approx 35\% < 1$ for the KH and non-KH events respectively. Hall MHD simulations of the dayside magnetopause have shown a significant specific entropy increase from the inflow to outflow region, associated with magnetic reconnection, is only possible for sufficiently low plasma beta ($\beta \ll 1$) in the inflow region (Ma & Otto, 2014). Although there exists components of the β_{global}^{MSH} PDFs from both the KH and non-KH events that are much lower than one, they are statistically insignificant – $\approx 3\%$ and 2% of the PDFs have a global MSH plasma beta less than 0.1 for the KH and non-KH events respectively. Ma & Otto (2014) concluded that $\beta \approx 0.1 - 1$ in the magnetosheath is insufficient for a specific entropy increase of one to two orders of magnitude due to magnetic reconnection.

When calculating the mean specific entropy over the MVAB wave intervals (\mathcal{S}_{MVAB}), there is a significantly larger increase in the specific entropy (indicative of strong non-adiabatic heating) during the KHI events (Figures 4.10 (a)-(b)). Careful analysis was performed on the tails of the distributions from the MSP plasma regime relative to the

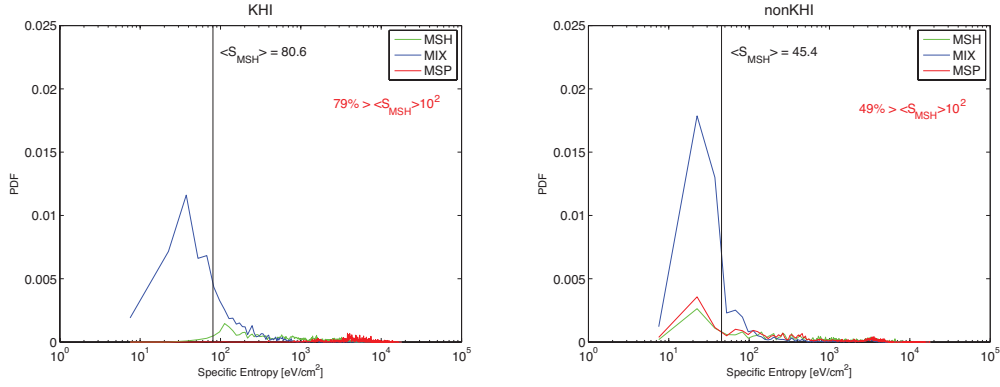


Figure 4.10: Specific entropy calculated during the ion-scale MVAB wave intervals (top panels) for the MSP (red), MIX (green) and MSH (blue) plasma for the KH (left panels) and non-KH events (right panels). The log-mean average of the global specific entropy (black line) is displayed for the KH and non-KH events.

log-mean average of the global MSH specific entropy $\langle \mathcal{S}_{global}^{MSH} \rangle$ (please see Table 4.1). Approximately 79% of the ion-scale wave intervals during KH events, the specific entropy in the MSP plasma revealed an increase of at least 2 orders of magnitude (relative to the global log-mean average specific entropy in the MSH), while during non-KHI events only $\approx 49\%$ showed a specific entropy increase of 2 orders of magnitude. This significant increase in the specific entropy from the MSH to MSP plasmas observed during the ion scale wave intervals suggests strong non-adiabatic heating. However, it should be noted that when considering only the cold component ions, DMSP ionospheric data mapped into the plasma sheet suggests that the specific entropy may only increase by a factor of 5 (Johnson & Wing, 2009) and that the approximate 2 order of magnitude increase shown by Borovsky & Cayton (2011) may be due to the influence of the hot ion population.

However, the global specific entropy \mathcal{S}_{global}^n – calculated at all time stamps, where n designates the plasma region – during the KH (and non-KH) is strikingly different than that taken from the MVAB intervals (see Figures 4.11 (a)-(b)). For instance, there exists a relatively large population of high specific entropy MSP plasma ($\mathcal{S}_{global}^{MSP} > 1$) during the

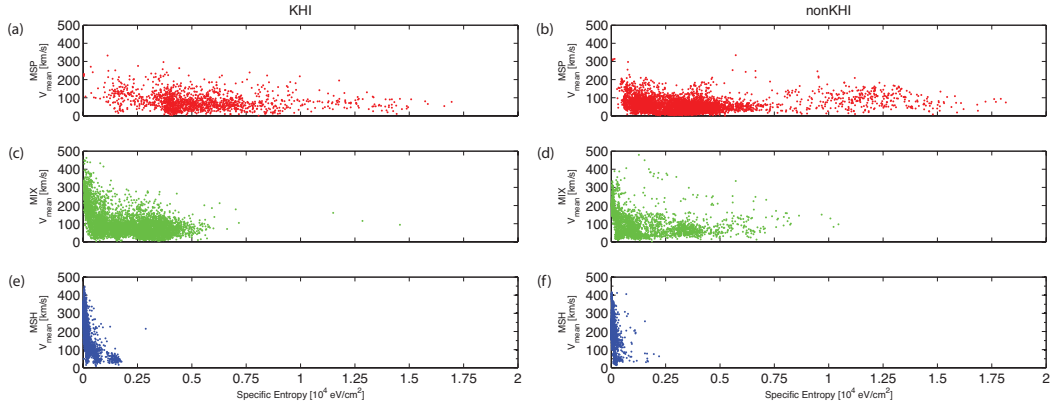


Figure 4.11: Global specific entropy vs mean plasma flow for KH (left panels) and non-KH events (right panels). The panels from top to bottom represent the MSP, MIX and MSH plasma regimes, respectively.

non-KH (the top right panel of Figure 4.11) events compared to the KH events (the top left panel of Figure 4.11). Furthermore a larger percentage of MSP data points are observed to have specific entropy values greater than $\langle \mathcal{S}_{global}^{MSH} \rangle$ by at least two orders of magnitude for the non-KH events compared to the KH events (see Table 4.1). The calculated log-mean specific entropies $\langle \mathcal{S}_{global}^n \rangle$ are listed in Table 4.1 for the MSP, MIX and MSH plasma regions along with their ratios relative to the MSH $\langle \mathcal{S}_{global}^n \rangle / \langle \mathcal{S}_{global}^{MSH} \rangle$ and the percentage of data points greater than $\langle \mathcal{S}_{global}^{MSH} \rangle$ by at least 2 orders of magnitude both globally (P_{global}^n) and for the ion scale wave intervals (P_{MVAB}^n). Another interesting feature is how the ratios of global log-mean specific entropies are strikingly similar for the KH and non-KH events as shown in Table 4.1.

Comparisons between the global and MVAB interval log-mean specific entropies are provided in Table 4.2. Interestingly for each plasma region, the ratio of the log-mean specific entropies between the global and ion scale wave intervals ($\langle \mathcal{S}_{MVAB}^n / \mathcal{S}_{global}^n \rangle$, where n represents the plasma region) calculated during the KH events is much closer to unity when compared to the non-KH events (see diagonals from Table 4.2). For example, in

Table 4.1: Details on the global specific entropy across the MSP, MIX and MSH plasma regimes.

	n	$\langle \mathcal{S}_{global}^n \rangle$	P_{global}^n ^a	P_{MVAB}^n ^b	$\frac{\langle \mathcal{S}_{global}^n \rangle}{\langle \mathcal{S}_{global}^{MSH} \rangle}$
KHI {	MSP	4.87×10^3	26%	79%	60
	MIX	1.27×10^3	0.058%	7.5%	16
	MSH	80.6	0%	0%	1
non-KHI {	MSP	2.89×10^3	71%	49%	64
	MIX	754	30%	45%	17
	MSH	45.4	.0050%	23.5%	1

^a P_{global}^n := % global data points greater than $\langle \mathcal{S}_{global}^{MSH} \rangle$ by at least two orders of magnitude.

^b P_{MVAB}^n := integral of \mathcal{S}_{global}^n greater than $\langle \mathcal{S}_{global}^{MSH} \rangle$ by at least two orders of magnitude.

Table 4.2: Log-mean specific entropy ratios relating the global and ion scale wave intervals. The bold values along the diagonals correspond to the ratio of the global log-mean specific entropy in plasma of type n to its corresponding MVAB value.

	n	$\frac{\langle \mathcal{S}_{MVAB}^n \rangle}{\langle \mathcal{S}_{global}^{MSP} \rangle}$	$\frac{\langle \mathcal{S}_{MVAB}^n \rangle}{\langle \mathcal{S}_{global}^{MIX} \rangle}$	$\frac{\langle \mathcal{S}_{MVAB}^n \rangle}{\langle \mathcal{S}_{global}^{MSH} \rangle}$
KHI {	MSP	1.00	3.83	60.3
	MIX	0.226	0.866	13.6
	MSH	0.0178	0.0683	1.08
non-KHI {	MSP	0.363	1.39	23.1
	MIX	0.384	1.47	24.4
	MSH	0.0526	0.202	3.35

the MSP plasma ($n = \text{MSP}$) $\langle \mathcal{S}_{MVAB}^{MSP} / \mathcal{S}_{global}^{MSP} \rangle$ is 1.00 and 0.363 for the KH and non-KH events respectively. This means that the specific entropy calculated in the ion-scale wave intervals offers a more quantitatively accurate description of the global specific entropy during the KH events compared to the non-KH events. In other words there is a better correlation between $\langle \mathcal{S}_{MVAB}^n \rangle$ and $\langle \mathcal{S}_{global}^n \rangle$ when KH is active.

4.4 Discussion

In the present work, ion scale properties for KH and non-KH events were compared. Cluster data from magnetopause crossings in the low-latitude flanks were binned according to their relative ion energies in order to compare ion scale wave properties in the magnetosphere, magnetosheath and mixed plasmas. These ion scale properties are compared to previous

observations of ion scale wave activity from Moore et al. (2016), specifically a FMW interval associated with ion heating inside a rolled-up KH vortex.

4.4.1 Broad Band Statistics

In Figures 4.1 (a) - (d), the degree of polarization ϵ above and below f_{ic} was shown for the KH and non-KH events. The peaks in the $|\epsilon|$ PDFs, at approximately ± 0.675 , are in good agreement with ion-scale wave activity from Moore et al. (2016), where ellipticities were calculated to be $\approx |0.57|$ and $\approx |0.66|$ from Cluster 1 and 4 respectively for right-handed FMW interval (which was identified with a two-spacecraft method), $\approx |0.35|$ and $\approx |0.60|$ for a double emission right-handed wave interval (likely a KAW below f_{ic} and a FMW above f_{ic} respectively, which were identified with single spacecraft method) and $\approx |0.57|$ for a left-handed interval (likely a KAW, which was identified with single spacecraft method). Without the ability to accurately assess the handedness of these waves in a statistical manner, the weight of right to left handedness in the degree of polarization between the KH and non-KH events remains indistinguishable.

The magnetic compressibility was presented in § 4.2.2; when considering only the significant wave power across all frequencies ($0.05 \text{ Hz} \leq f \leq 2.7 \text{ Hz}$), there is an amplification in the transverse wave power at the MIX region during the KH events (see Figure 4.2 (c)). This amplification is consistent with observations of mode conversion from MHD surface waves to KAWs at the magnetopause (Johnson & Cheng, 1997; Johnson et al., 2001), considering data binned in the MIX regime are best representative of observations taken nearest to the actual magnetopause when compared to those binned into the MSP and MSH regimes. No such amplification in the MIX regime occurs for the non-KH events. It may be that there are more KAWs present during the KH events.

4.4.2 Ion-Scale Wave Intervals

Ion-scale waves identified using a sliding window MVAB were shown in § 4.3 with their perspective properties.

In Figures 4.4 (a) - (c) the comparison in the total magnetic wave power between the KH and non-KH events was presented for the MSP, MIX and MSH plasmas respectively. There is an apparent transition in the comparisons between the low power band of quasi-perpendicular waves from the MSH to the MIX and MSP plasmas where observations go from non-KH to KH dominant respectively. In the MSH plasma the low power waves are non-KH dominant for all propagation angles. In the MIX and MSP plasmas the low power oblique waves are KH dominant, where the KH dominance extends to the high power waves in the MSP. Furthermore, there are relatively more KH dominant high power wave observations for in the MIX and MSP plasma regions.

The lower power waves shown in the MIX and MSP plasma regime for the quasi-perpendicular waves are consistent with the observed quasi-perpendicular FMW observed inside the center of the KH vortex from Moore et al. (2016). The quasi-perpendicular ($\theta_{kB} = 85^\circ, 88^\circ$) FMWs observed on June 6th 2002 by Moore et al. (2016) in the center of a KH vortex has a magnetic wave amplitude range of approximately $0.3 - 0.6 nT/Hz^{1/2}$ which corresponds to $|\delta B_{tot}|^2 \approx 0.09 - 0.36 nT^2/Hz$. Recall that the binning algorithm discussed earlier sets approximately 75% of the FMW interval into the MIX bin and the remaining 25% into the MSP bin.

The difference in total integrated Poynting flux S_{int} between the KH and non-KH events for the MSP, MIX and MSH plasmas was depicted in Figures 4.5 (a) - (c) respectively. There is a clear non-KH dominance in the available wave energy among the quasi-perpendicular waves in the MSH. However, a transition occurs in the MIX plasma, where the wave energy among the quasi-perpendicular waves becomes KH dominant for the lower band of S_{int} .

This transition accumulates to KH dominant quasi-perpendicular waves for all S_{int} . This appears to be connected to the enhancement of KH dominant quasi-perpendicular wave power in the MIX and MSP plasmas from the MSH discussed above. This transition in the total magnetic wave power and total integrated Poynting flux suggests that more quasi-perpendicular waves and their associated wave energy are more accessible to the MSP plasma when KHI is active. KAWs can heat ions stochastically (Johnson & Cheng, 2001) and have been shown to transfer significant energy into the magnetosphere (Chaston et al., 2007) when KHI is active. KH vortex associated FMWs have also been shown to heat cold component ions (Moore et al., 2016).

The KH dominant observations of quasi-perpendicular waves in the MSP and MIX plasma, shown in Figures 4.7 (a) and (b) respectively, might not appear to be consistent with the S_{int} from the FMW interval at first glance, however when considering the MVAB window length compared to the actual FMW interval duration, the results are in good agreement: The FMW interval is approximately 18.4 s in duration with a local average $f_{ic} \approx 0.3 Hz$ (Moore et al., 2016). Because the MVAB window length is dependent upon f_{ic} and search is limited to $[f_{(j_{ic}-10)}, f_{(j_{ic}+10)}]$, the window range over the FMW interval is bound by an approximate 0.20 – 0.45 Hz restriction. This restricts the possible MVAB window lengths passing over the FMW interval to approximately 2.2–5 s, which corresponds to a maximum of 27% of the actual FMW interval length. A crude estimation assumes that only 27% of the actual FMW S_{int} is recorded in the 2-d distribution plot of the S_{int} versus propagation angle, which is approximately only $1.2 \times 10^6 keVcm^{-2}$. This scaled estimate makes the KHI dominant wave observations in the MSP and MIX plasma regimes consistent with the FMW observations from Moore et al. (2016).

In Figure 4.6, the scaled wave electric to wave magnetic field ratio \mathcal{P} was presented for the FMW wave interval, which includes data from the MSP and MIX plasmas. The distribution is shown to be quite broad (approximately $0 \leq \mathcal{P} \leq 8$) near the local ion

cyclotron frequency ($f_{ic} \approx 0.3 Hz$). Additionally, the comparison of \mathcal{P} between the KH and non-KH events were provided for the MSP, MIX and MSH plasmas in Figures 4.7 (a)-(c). In the MSH plasma, the KH dominant distribution consist of a narrow band ($\mathcal{P} \leq 2$) for all propagation angles. Perpendicular KAW observations have been shown to have a wave electric to wave magnetic field ratio scaled by the local Alfvén velocity to be greater than one (Chaston et al., 2007; Chaston et al., 2012). It would appear that the narrow band of KH-dominant quasi-parallel, electromagnetic wave observations in the MSH do not carry a significant amount of wave energy relative to the other quasi-perpendicular ion-scale waves observed during non-KH events.

Similarly to the wave power and Poynting flux distributions, there is a transition from the KH dominant trend in the MSH beginning in the MIX plasma, where the \mathcal{P} distribution begins to widen (especially for the quasi-perpendicular component) in the MIX plasma and broadens even further in the MSP plasma. The broad KH dominant distributions in \mathcal{P} at oblique angles ($\theta_{kB} = 50^\circ - 90^\circ$) for the MSP and MIX plasma regimes are consistent with the FMW \mathcal{P} -dispersion in the vicinity of the local ion cyclotron frequency. The portion of the KH dominant \mathcal{P} distributions near unity among the quasi-perpendicular waves in the MIX and MSP plasmas is consistent with both the FMW interval and KAWs.

Presented in Figures 4.8 (a)-(b) and Figures 4.9 (a)-(b) were the plasma beta profiles for the ion-scale wave intervals and global plasma beta profiles for the MSH plasma β_{global}^{MSH} respectively. It was shown that although the β_{global}^{MSH} is statistically lower during the KH events, it is not sufficiently low (required $\beta \ll 1$), so that reconnection and associated shocks could account for the level of observed non-adiabtic heating (Ma & Otto, 2014).

Furthermore, the high global beta in the MSH during the non-KH events might explain why KHI is inactive. Compressibility and magnetic tension are known to stabilize KHI (Miura & Pritchett, 1982); compressibility can result from high plasma pressure and velocity in the magnetosheath.

In the later portion of § 4.3.5, results from the global and ion-scale wave intervals were shown and discussed. It was shown from Figures 4.10 (a)-(b) that there is significant increase in the specific entropy related to the ion-scale wave intervals during the KH events. One conclusion that is drawn is that there is more non-adiabatic heating across the magnetopause associated with ion-scale wave activity when KHI is active. Although from a global perspective, there is a larger increase in specific entropy from the MSH to the MIX and MSP plasmas during the non-KH events, it should be noted that the specific entropy calculation does not differentiate between the cold and hot component ions. In fact, southward IMF can contribute to the formation of a hot and tenuous plasma sheet (Wing & Newell, 2002). Plasma energization in the plasma sheet related to substorm activity is well known (Hones et al., 1976) – ion (Runov et al., 2009; Hietala et al., 2015) and electron (Runov et al., 2009) heating has been shown in plasma flow channels in the magnetotail. Furthermore, a hot and tenuous plasma sheet would have a higher specific entropy than a cold and dense plasma sheet. From Table 4.3, the time-lagged OMNI data shows that several of the non-KH events possess a significant southward component in the IMF of the upstream solar wind which may drive reconnection in the magnetotail and generate bursty bulk flows.

There is significant evidence of strong non-adiabatic heating directly related to ion-scale wave activity when KHI is active. Furthermore quasi-perpendicular waves and their associated energy are more accessible to the MSP plasma when KHI is active. Overall, the global plasma beta in the MSH plasma regime is lower during the KH events when compared to the non-KH events, although not sufficiently low (required $\beta < 0.1$), so that reconnection and associated shocks could account for the level of observed non-adiabatic heating (Ma & Otto, 2014). These results suggest that ion scale waves, such as observed and studied in detail by Moore et al. (2016) could strongly contribute to this significant non-adiabatic heating observed across the magnetopause during KHI events. Moore et al.

(2016) observed the specific entropy increase by a factor of ≈ 3 over the short FMW interval observed inside of a KH vortex, and ≈ 1.4 orders of magnitude relative to the magnetosheath during the entire two minute duration of the ion scale wave activity. The temperature of the cold-component ion population during this brief wave period increased by 2 keV.

4.5 Effects of Solar Wind Speed on Plasma Parameters

It has been shown that certain plasma parameters in the magnetosheath can be effected by solar wind flows. Wang et al. (2012) revealed a correlation between magnetosheath ion temperatures (T_i), and ion to electron temperature ratios from a statistical study using 4 years of THEMIS data. They showed that higher solar wind speeds ($|V| > 450 \text{ km/s}$) correspond to higher ion temperatures in the magnetosheath whereas lower solar wind speeds ($|V| < 450 \text{ km/s}$) correspond to lower ion temperatures. In this section we explore the plausibility of contamination in the plasma parameters due to initial solar wind conditions by exploring how solar fast and slow wind speeds effect the seed population in the magnetosheath.

Average solar wind conditions are calculated from time-lagged OMNI data by averaging over time scales comparable to each event and are listed in Table 4.3. The "fast" solar wind speeds are highlighted in bold. In the context of this section fast and slow solar wind speeds are defined as $|V| > 400 \text{ km/s}$ and $|V| < 400 \text{ km/s}$, respectively. There are a fair distribution of slow and fast solar winds speeds for both the KH and non-KH events, with an outlier residing in the non-KH event list where the average solar wind speed is larger than 700 km/s . It should be noted that removing this fast solar wind outlier (June 3rd 2003) diminishes a significant portion of the high specific entropy population that is observed in

4.5. EFFECTS OF SOLAR WIND SPEED ON PLASMA PARAMETERS

Table 4.3: Average time-lagged solar wind data from OMNI.

	Date [yyyy-mm-dd]	\vec{B} [nT]	\vec{V} [km/s]	n [cm ⁻³]	T [10 ⁶ K]	$ B $ [nT]	$ V $ [km/s]
KHI {	2001-07-03	<3.88, -5.40, -0.52>	<-402.27, -15.62, -11.24>	8.11	0.09	8.49	403.03
	2001-11-20	<-3.06, 0.58, 2.75>	<-388.68, -41.87, -21.30>	3.82	0.10	4.20	391.50
	2002-06-06	<0.96, -4.95, -0.16>	<-367.12, -13.46, -11.08>	4.13	0.02	5.16	367.57
	2002-06-13	<2.79, -3.39, -4.62>	<-368.44, -0.34, -26.72>	5.81	0.05	6.78	369.57
	2004-06-19 ^a	<-0.52, 3.73, 1.08>	<-472.56, 8.29, 8.27>	3.05	0.12	4.52	472.99
	2004-06-21	<0.96, 2.30, 1.21>	<-408.91, -2.82, 5.93>	3.67	0.06	3.70	409.13
non-KHI {	2003-06-03	<-4.16, 2.24, -1.26>	<-782.42, 9.00, 19.27>	3.05	0.30	6.99	784.08
	2004-11-16	<2.02, -4.90, 1.95>	<-428.69, 19.00, 16.11>	7.26	0.16	7.37	430.00
	2004-11-27	<-2.36, 2.68, -4.05>	<-421.57, -21.99, -4.67>	5.40	0.08	6.43	422.62
	2005-06-28	<-2.18, 2.32, 0.10>	<-375.06, -5.55, 20.80>	9.41	0.05	3.38	375.70
	2007-06-04	<3.42, 1.84, 1.77>	<-478.45, 36.66, -2.14>	4.73	0.13	4.73	479.94
	2007-06-06	<-1.97, -0.31, -1.45>	<-347.99, 1.88, -7.79>	3.96	0.03	2.50	348.12
	2007-06-06	<-2.03, 1.20, -0.80>	<-337.68, -1.77, -3.58>	4.14	0.03	2.67	337.76
	2009-06-03	<0.79, 0.45, 1.51>	<-303.62, -0.69, -4.02>	7.67	0.02	2.28	303.67
	2009-06-26	<3.29, 0.80, -0.49>	<-449.43, 25.56, -2.55>	2.92	0.10	3.50	450.19

^aThis event was considered PS by Moore (2012) due to differing techniques in averaging solar wind data.

the MSP plasma during the non-KH events (right panel of Figure 4.11), however the effects on P_{global} and P_{MVAB} from Table 4.1 are minute.

For solar wind a solar wind speed of 748 km/s and southward IMF the magnetosphere is under heavy driving, likely resulting in substorm activity or bursty bulk flows in the magnetotail which can increase the hot population of ions in the magnetotail.

Statistical mapping of the magnetosheath specific entropy in the magnetosheath interplanetary medium (MIPM) is performed using 5 years of THEMIS and OMNI data (Dimmock & Nykyri, 2013; Dimmock et al., 2014; Dimmock et al., 2015; Dimmock, Pulkkinen, et al., 2016). The specific entropy dependence on the solar wind speed can be seen in Figure 4.12, where the overall mean specific entropy in the magnetosheath is higher during fast (right panel) solar wind speeds compare to slow (left panel) solar wind speeds. There are noticeable enhancements in the mean specific entropy adjacent to the magnetopause (inner boundary) for both the solar wind speeds. However, comparing Figures 4.12 (a)-(b), this enhancement appears slightly wider for the fast solar wind, especially for the tailward populations.

Although the magnitude of the solar wind velocity seems to be correlated to the specific entropy in the magnetosheath plasma, it is unlikely that these effects contribute to the relative specific entropy increases observed in either the global or MVAB wave intervals

4.5. EFFECTS OF SOLAR WIND SPEED ON PLASMA PARAMETERS

discussed in § 4.3.5. This is mostly because the $\langle \mathcal{S}_{global}^{MSH,KHI} \rangle$ is in fact higher than $\langle \mathcal{S}_{global}^{MSH,nonKHI} \rangle$ even though the average solar wind speed for all of the KH events is lower than that of the non-KH events.

Plasma beta dependence on the solar wind speed is depicted in Figures 4.13 (a)-(b) and 4.14 (a)-(b) for the mean and minimum plasma beta, respectively, where at first glance the plasma beta is larger for slower wind speeds in the central magnetosheath and near the bow shock. For both solar wind speeds, the lowest mean and minimum plasma beta populations are located in the vicinity of the magnetopause corresponding to the enhancements in the mean specific entropy from Figures 4.12 (a)-(b).

There appears to be little solar wind speed dependence on the mean plasma beta when comparing the region adjacent to the magnetopause in Figures 4.13 (a)-(b) except for a slightly wider low minimum beta population for the fast solar wind, especially farther tailward; this is more evident when comparing Figures 4.14 (a)-(b). Saturating the color bar from Figures 4.14 (a)-(b) gives a more detailed description of the minimum plasma beta range along the magnetopause depicted in Figures 4.15 (a)-(b). In Figures 4.14 (a)-(b), there are more populations of very low plasma beta ($\beta < 0.1$) when the solar wind is fast (Figure 4.14 (b)) compared to when it is slow (Figure 4.14 (a)).

This data suggests that there is a correlation between the specific entropy enhancements in the magnetosheath along the magnetopause and the plasma beta, with subtle variation when considering solar wind speed. The plasma beta adjacent to the magnetopause is slightly lower for faster solar wind and corresponds to larger enhancements in the specific entropy along the magnetosheath side of the magnetopause. On average, the plasma beta along the magnetopause is not sufficiently low ($\beta < 0.1$) to account for a significant increase in the specific entropy in the magnetosphere from magnetic reconnection (Ma & Otto, 2014). However, there exists a larger population that might satisfy the low plasma beta requirement when the solar wind is fast – Ma & Otto (2014) showed $\beta = 0.025$ in the inflow region

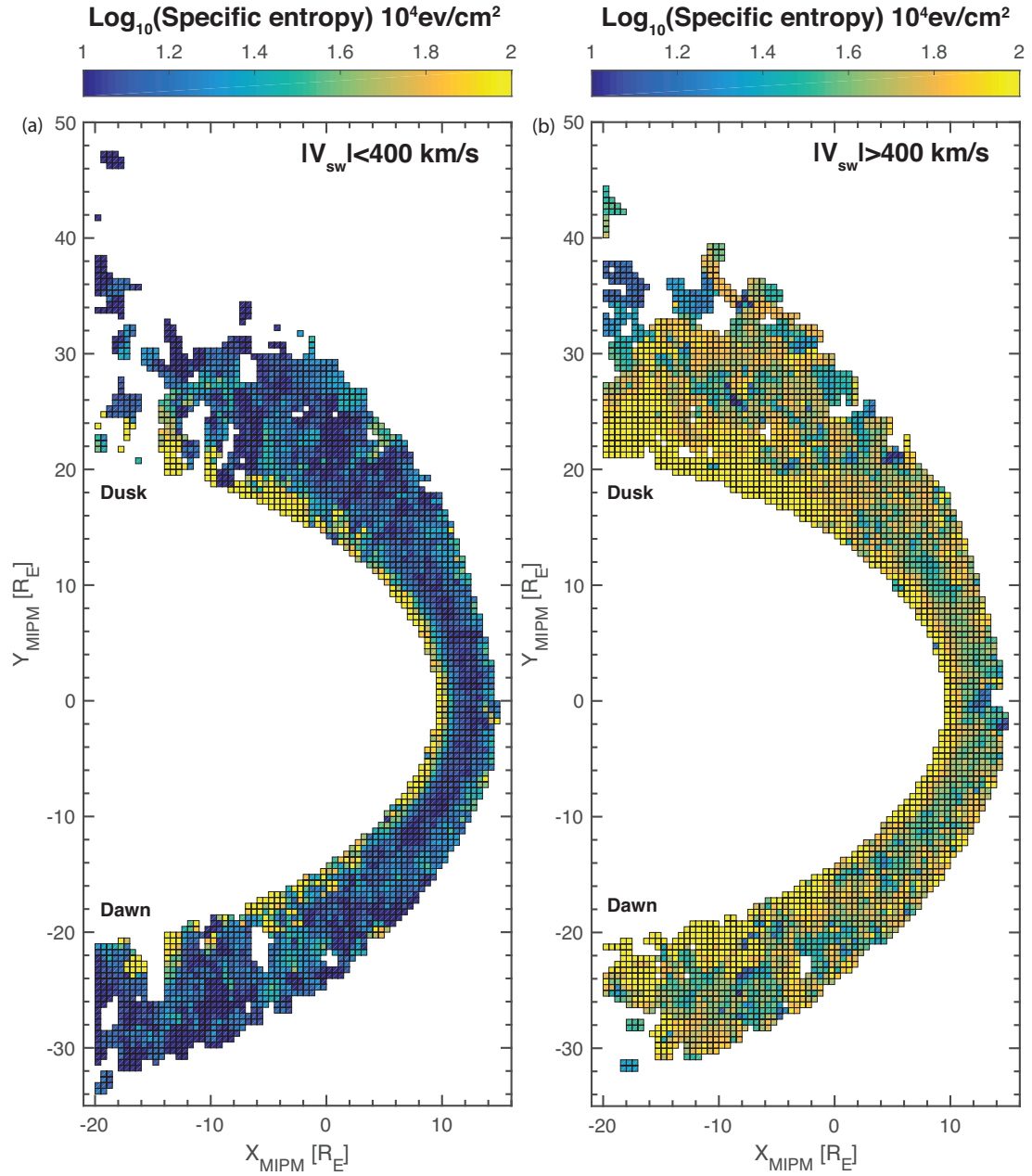


Figure 4.12: Mean of the mean specific entropy maps for slow (left panel) and fast (right panel) solar wind using THEMIS data.

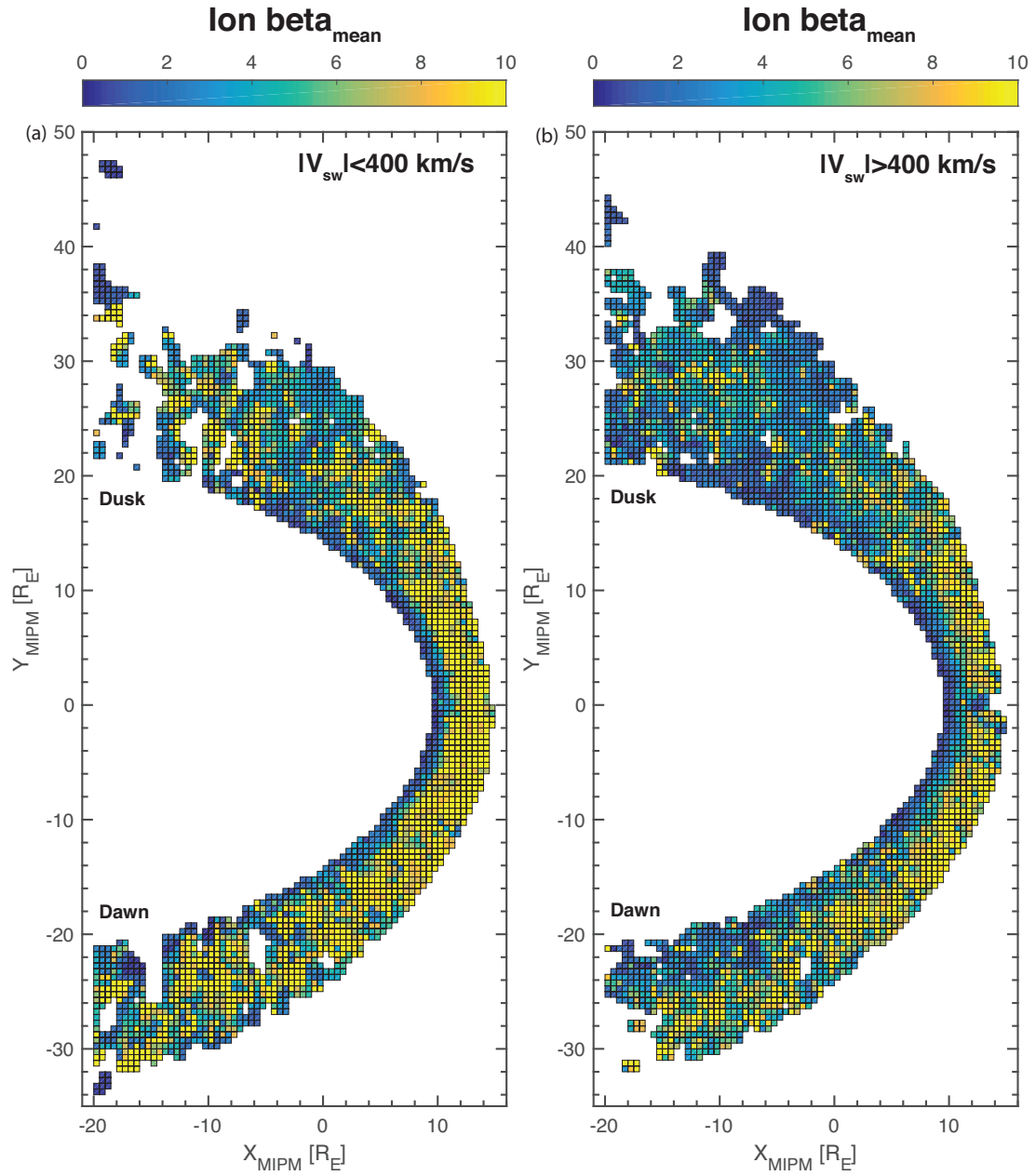


Figure 4.13: Mean of the mean plasma beta maps for slow (left panel) and fast (right panel) solar wind using THEMIS data.

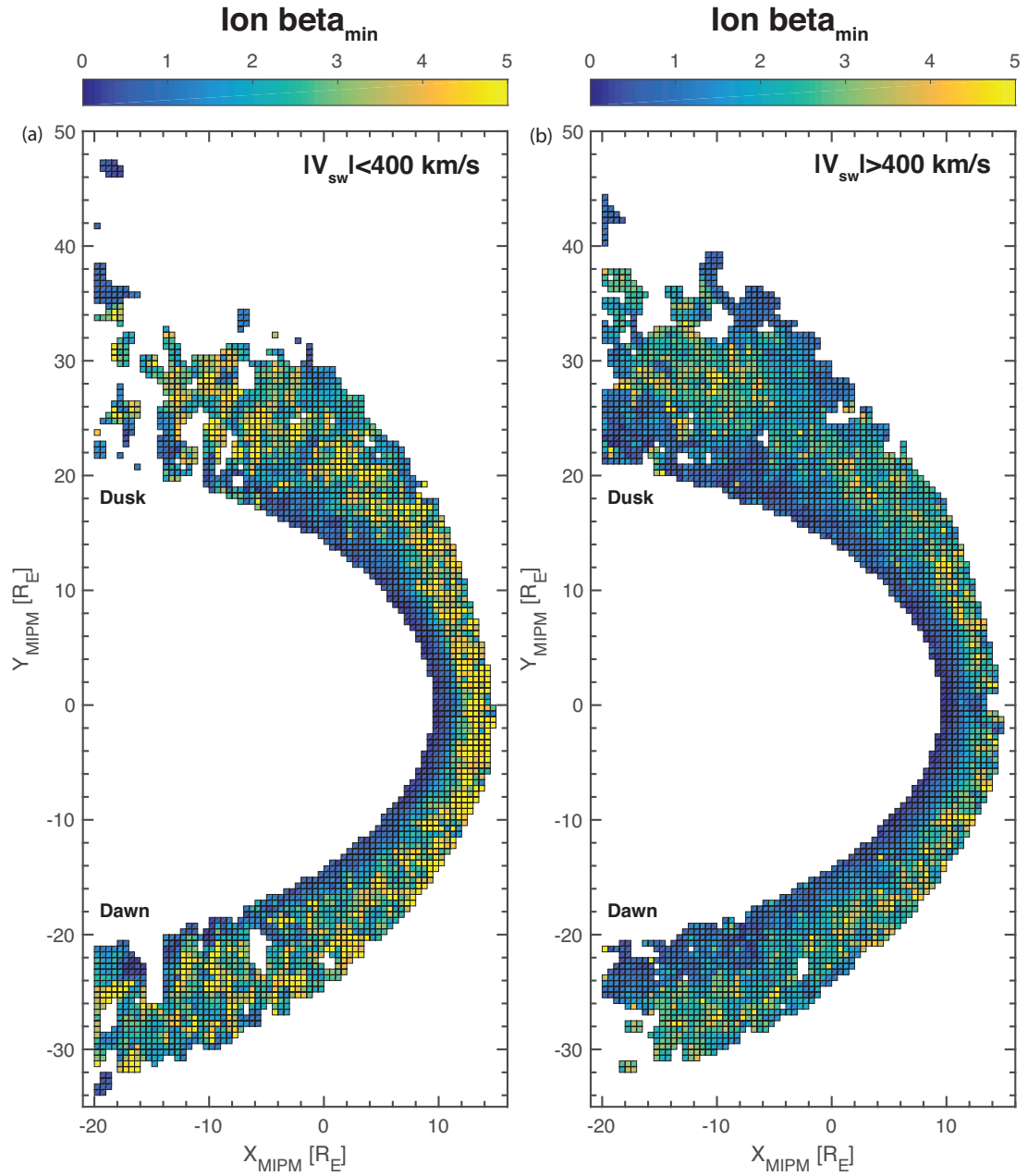


Figure 4.14: Mean of the minimum plasma beta maps for slow (left panel) and fast (right panel) solar wind using THEMIS data.

4.5. EFFECTS OF SOLAR WIND SPEED ON PLASMA PARAMETERS

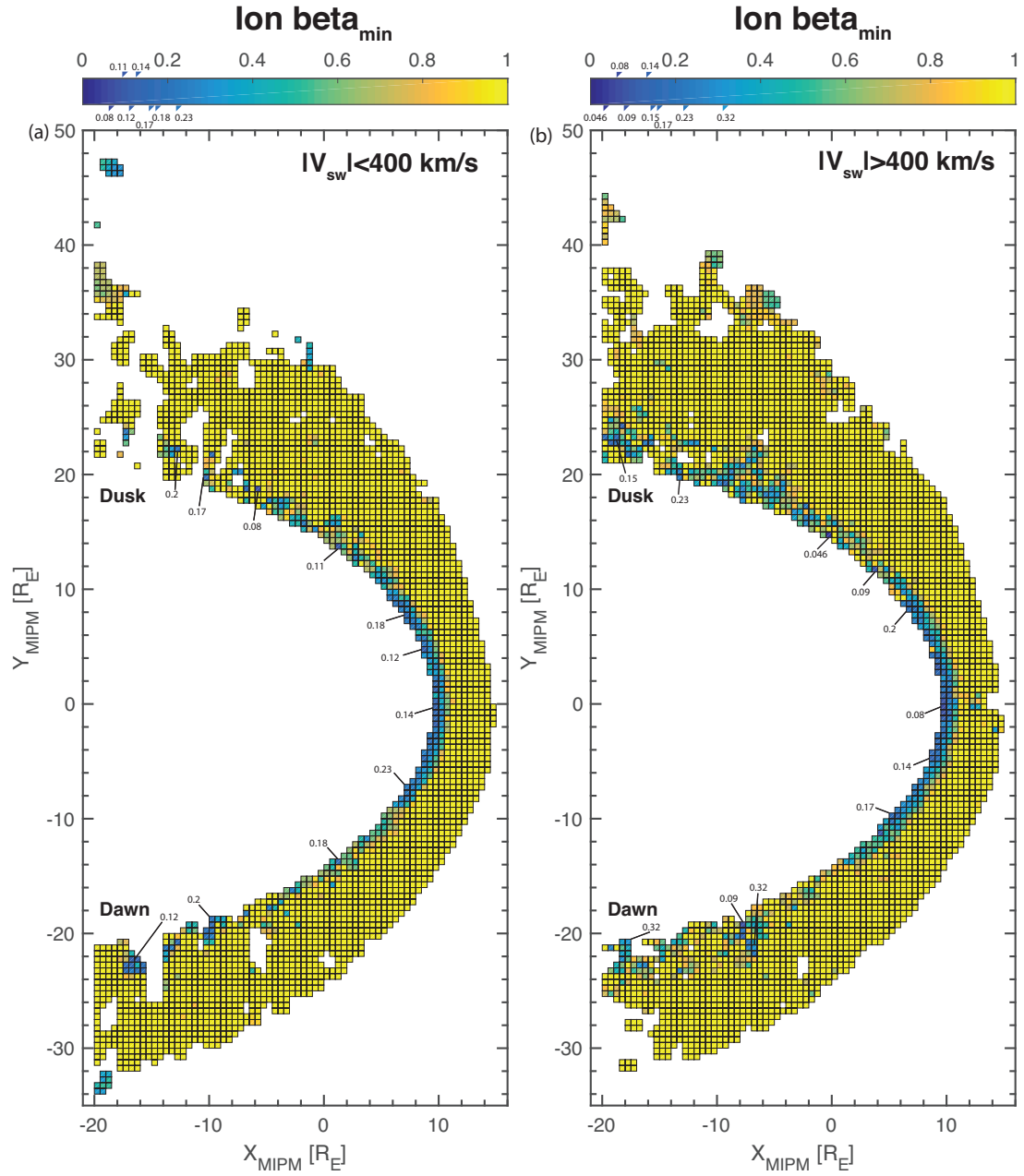


Figure 4.15: Saturated scale of the mean of the minimum plasma beta maps for slow (left panel) and fast (right panel) solar wind using THEMIS data.

(magnetosheath) was sufficiently low to increase the specific entropy in the outflow region (magnetosphere) by a factor of 4. It is most likely that the global specific increase for the non-KH events is produced in part by magnetic reconnection and substorm activity.

4.6 Doppler Shift Effects

In an aim to estimate possible Doppler effects, we use the higher end of the wavelength range from the FMW interval from Moore et al. (2016) ($200 \text{ km} \leq \lambda \leq 2000 \text{ km}$) corresponding to the ion-cyclotron frequency range such that a moderate Doppler shift will result. Thus a wavelength of $\lambda = 2000 \text{ km}$ is chosen (Appendix A.2 shows the most extreme Doppler shift effects for $\lambda = 200 \text{ km}$) for the Doppler shift equation $\omega_p = \omega_{sc} - 2\pi\hat{k}/\lambda \cdot \vec{v}_{flow}$, where ω_p is the plasma frame angular frequency, ω_{sc} is the spacecraft frame angular frequency, \hat{k} is the propagation direction and \vec{v}_{bulk} is the plasma flow in the spacecraft frame. Because the propagation direction vector \hat{k} is determined via MVAB, there is a 180° ambiguity with respect to the background magnetic field. As such, the estimation of the Doppler effect is split into the two extreme cases where \hat{k} is parallel or anti-parallel to \vec{v}_{bulk} such that $\omega_p = \omega_{sc} \mp 2\pi\hat{k}/\lambda \cdot \vec{v}_{flow}$.

Figures 4.16, 4.17 and 4.18 show how the possible Doppler shifts may effect the 2-d mean magnetic wave power, total integrated Poynting flux and mean scaled $\delta E/\delta B$ comparative distributions. The left, middle and right columns from Figures 4.16, 4.17 and 4.18 correspond to an parallel Doppler shift, no Doppler shift and anti-parallel Doppler shift respectively.

Taking into account the parallel Doppler shift has an insignificant effect on the properties of the 2-d mean magnetic wave power, total integrated Poynting flux and mean scaled $\delta E/\delta B$ comparative distributions (see the leftmost columns of Figures 4.16, 4.17 and 4.18). Similarly, the estimated anti-parallel Doppler shift has an insignificant effect on the proper-

ties of the 2-d mean magnetic wave power, total integrated Poynting flux and mean scaled $\delta E/\delta B$ comparative distributions (see the rightmost columns of Figures 4.16, 4.17 and 4.18).

When considering the Doppler shift for an ion-scale wave ($\lambda = 2000 \text{ km}$), the resulting effect on the ion-scale wave properties are insignificant. This suggests that the results discussed in § 4.4 are valid in the plasma frame.

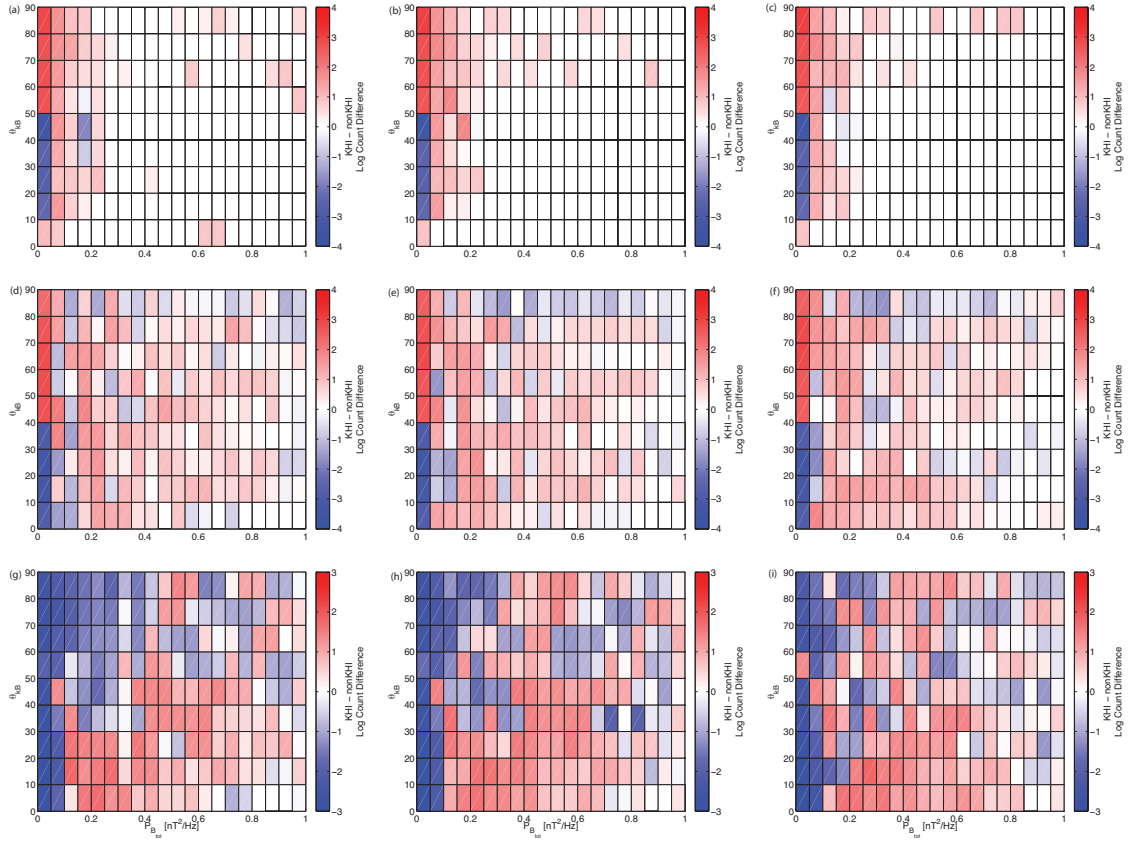


Figure 4.16: Estimated parallel \hat{k} (left columns) and anti-parallel \hat{k} (right columns) Doppler effects on the 2-d comparative distributions of mean total power (P_{tot}) versus propagation angle (θ_{kB}) between KHI and non-KHI events; center columns are the non-Doppler shifted distributions. The panels from top to bottom represent the MSP, MIX and MSH plasma regimes, respectively.

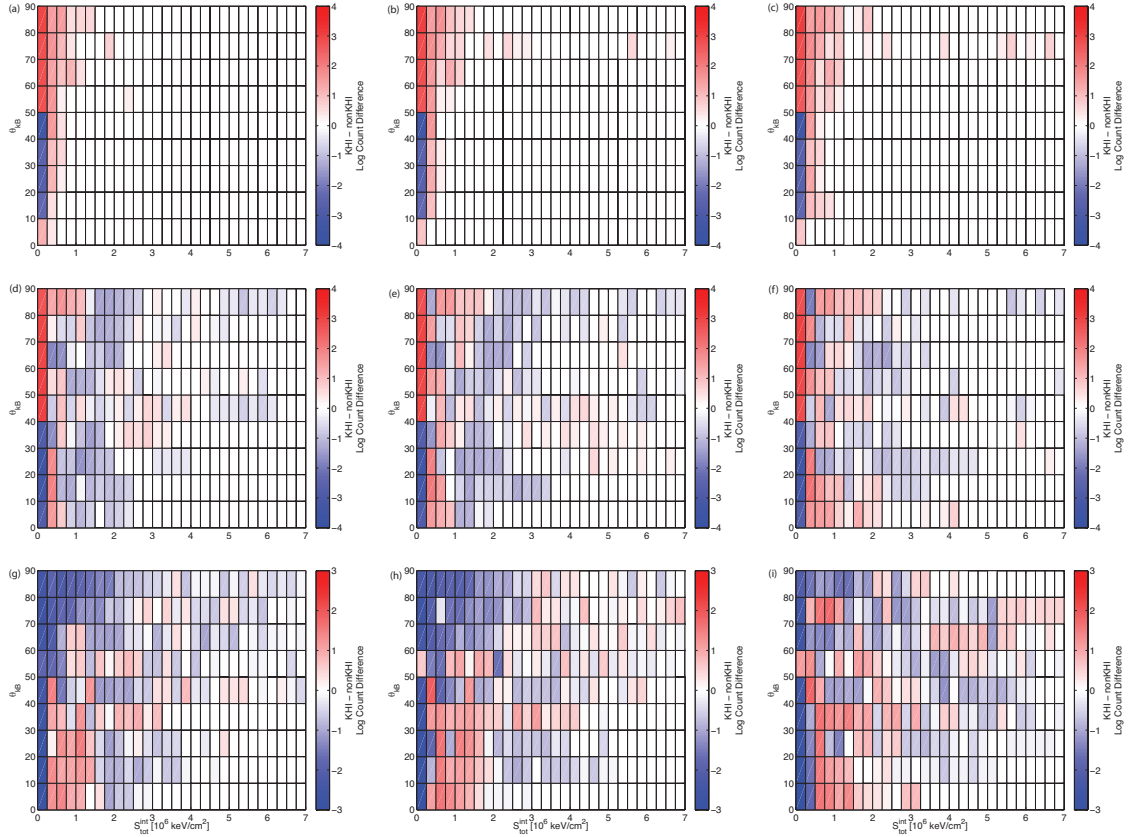


Figure 4.17: Estimated parallel \hat{k} (left columns) and anti-parallel \hat{k} (right columns) Doppler effects on the 2-d comparative distribution of the integrated Poynting flux versus propagation angle (S_{int} versus θ_{kB}); center columns are the non-Doppler shifted distributions. The panels from top to bottom represent the MSP, MIX and MSH plasma regimes, respectively.

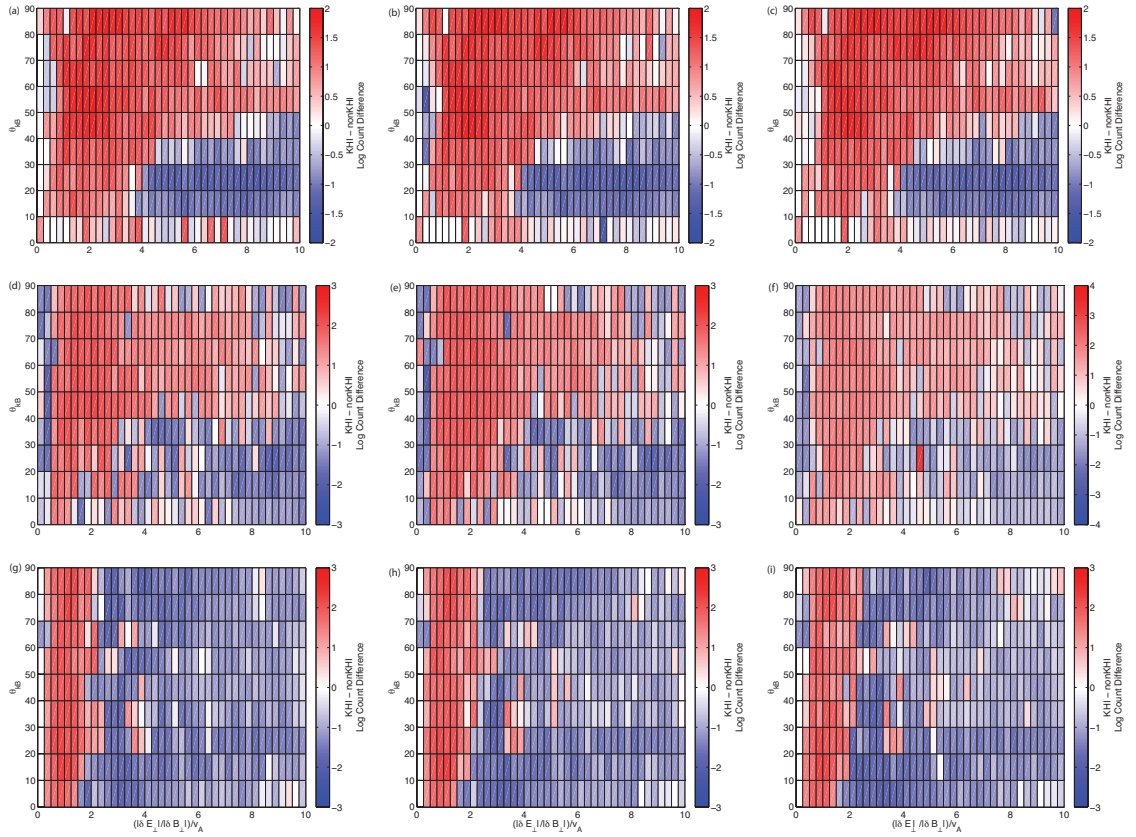


Figure 4.18: Estimated parallel \hat{k} (left columns) and anti-parallel \hat{k} (right columns) Doppler effects on the 2-d comparative distributions of scaled mean $\delta E/\delta B$ polarization versus propagation angle; center columns are the non-Doppler shifted distributions. The panels from top to bottom represent the MSP, MIX and MSH plasma regimes, respectively.

Chapter 5

Summary

5.1 Case Study

The observations described in this study show a cross-scale evolution from the ULF range to the ω_{ci} -range where the cold-component ions are energized. These observations are consistent with previous studies that portray an increased amount of wave power across multiple scales at the dawn-flank and may very well be one of the primary mechanisms at play responsible for the 30-40% increased temperature of the cold-component ions in the dawnside plasma sheet.

Observations on June 6th 2002 are consistent with typical KHI signatures and are reproduced qualitatively with simulations. We detect, and provide strong evidence in the form of an experimental dispersion relation, of a magnetosonic wave inside a KH vortex characterized by a total pressure minimum. The observed magnetosonic wave packet propagates almost perpendicularly to the ambient field in vicinity of the ion cyclotron frequency, is short-lived and has adequate energy to provide ≈ 2 keV energy increase for the cold-component ions of magnetosheath origin. The present observation of a large relative amplitude ($\delta B/B$)

≈ 33 percent), 200-2,000 km wavelength magnetosonic wave packet, generated by a 36,000 km wavelength Kelvin-Helmholtz wave is consistent with cross-scale energy transport. This finding could have a profound, cross disciplinary application to a broad range of systems which experience velocity shear and where KHI can form. For example, similar cross-scale mechanisms may contribute to the heating of the solar corona (Foullon et al., 2011) and also play a role in other astrophysical plasmas. Although here the cross-scale heating occurred in a natural plasma environment, where the observed wave length ratio between the fluid and ion scale wave is in the range of ≈ 20 -200, it would be important to study this further in the controlled man-made devices such as the Large Plasma Device (LAPD) where the KHI has been successfully generated (Horton et al., 2005). Especially compelling would be to investigate an optimal parameter regime and velocity shear layer and magnetic field geometries where the FMWs radiated by the KHI can heat the plasma most effectively. These efforts may also be beneficial for the understanding the cross-scale energy transport in man-made fusion devices (Ongena et al., 2016).

5.2 Statistical Study

This present work identified ion-scale wave properties associated with magnetopause crossings in the the low latitude flanks during periods where KHI was active and inactive and addressed the ubiquity of non-adiabatic heating to KHI. The conclusions can be summarized as follows:

1. Increase in the specific entropy associated with ion-scale waves is more pronounced when KHI is present.
2. Global specific entropy profiles show a stronger increase from MSH to MSP for the non-KH events, most likely due to a hot and tenuous plasma sheet.

3. MSH plasma beta is globally lower ($\beta < 1$) when KHI is present, however not sufficiently low enough to account for non-adiabatic heating from reconnection and associated shocks.
4. The mean total magnetic wave power observed during the FMW interval in Moore et al. (2016) falls within the range of KH dominant observations of quasi-perpendicular propagating waves in the MIX and MSP plasma.
5. In the MIX and MSP plasma, the estimated total integrated Poynting flux calculated during the FMW interval in Moore et al. (2016) falls within the range of KH dominant observations of quasi-perpendicular propagating waves.
6. The broad distributions in the $\delta E/\delta B$ ratio scaled by the local Alfvén velocity for the KH-dominant quasi-perpendicular ion-scale wave activity is consistent with the FMW interval.
7. The strong KH dominant scaled $\delta E/\delta B$ range greater than unity supports the existence of KAWs in the MSP, MIX and MSH plasmas.
8. Peaks in the degree of polarization during KH and non-KH events are consistent with the ion scale waves observed by Moore et al. (2016).
9. When considering the significant magnetic wave power, the magnetic compressibility profiles show an amplification in the transverse magnetic wave power in the MIX plasma consistent with mode conversion from from surface MHD to KAWs.
10. More wave energy from obliquely propagating waves are is available to the MSP when KHI is active.
11. Solar wind effects on the source MSH plasma is an unlikely cause of the specific entropy associated with the ion-scale waves in the MSP plasma when KHI is active.

In summary, there is a clear association between non-adiabatic heating and ion scale wave activity when KHI is active. Among the ion scale wave activity, a distinct KH-dominance is shown for quasi-perpendicular waves whose properties are consistent with recently observed FMW activity and KAWs. Although the specific entropy is shown to increase from the MSH to MSP when KHI is inactive, the plasma sheet may already be populated by hot and tenuous plasma due to substorm activity.

These findings may shed significant light on the origins of the plasma sheet temperature asymmetry of cold-component ions and non-adiabatic heating across the magnetopause. Energy provided in the form of a velocity shear can drive fluid scale KH waves at the magnetopause. Previously, it has been shown that there is a sufficient energy deficit – left-over from the twisting of magnetic lines and plasma compression from the KH motion – comparable to ion scale FMW emissions capable of energizing ions via harmonic cyclotron resonance. These results suggest that waves, consistent with KH vortex associated FMW activity and KAWs, may play a significant role in the cross-scale energy transport between fluid and ion scales. However more work is needed to uncover the mechanism by which these waves are generated inside the pressure wells of the KH vortices. For instance, the local 2-D MHD model used in this research contain the necessary physics for MHD magnetosonic waves to propagate in the simulation plane, however this is limited to low frequency ranges ($\omega \leq \omega_{ic}$) and the kinetic distribution functions cannot be provided by the MHD output data. Therefore, fully kinetic modeling or hybrid modeling with kinetic ions of KHI at the magnetopause should be analyzed in order to determine the typical ion distribution functions that are generated inside the vortex centers.

Chapter 6

Discussion and Future Work

Although here the cross-scale heating occurred in a natural plasma environment, where the observed wave length ratio between the fluid and ion scale wave is in the range of ≈ 20 -200, it would be important to study this further in the controlled man-made devices such as the Large Plasma Device (LAPD) where the KHI has been successfully generated (Horton et al., 2005). Especially compelling would be to investigate an optimal parameter regime and velocity shear layer and magnetic field geometries where the FMWs radiated by the KHI can heat the plasma most effectively. These efforts may also be beneficial for the understanding the cross-scale energy transport in man-made fusion devices (Ongena et al., 2016).

The present finding contributes to the understanding of the specific entropy increase at the magnetopause and on the origin of the asymmetry of the cold-component ions in the plasma sheet. However, it would be significant to extend this work to electron scales. It has been shown that the ion to electron temperature ratio T_i/T_e remains relatively constant across the magnetopause from the magnetosheath plasma to the plasma sheet, while the temperature and specific entropy for the ions and electrons increase dramati-

cally (Wang et al., 2012). This “stagnant” ratio suggests that both the magnetosheath ions and electrons undergo heating to similar proportions upon entry into the magnetosphere (Wang et al., 2012). In other words, it is as if the electrons know when the ions are heated. Interestingly, at higher k -values (on electron scales) the magnetosonic mode becomes a Whistler wave (Krauss-Varban et al., 1994) which may interact and energize electrons. It may be that the FMWs generated inside the KH vortices – which can heat ions – are coupled to electron-scale Whistler modes which in turn heat the electrons. Future work is needed in order to quantify if the magnetosonic-whistler branch continues to the electron scales with sufficiently high Poynting flux in the real system. The recently launched Magnetospheric Multi-Scale (MMS) mission provides superior measurement cadence and has the capability to extend the presently measured magnetosonic dispersion relation to higher k -values. These technical capabilities, paired with well suited orbital parameters, indicate that these data should be an ideal candidate for such studies and therefore significantly contribute to addressing these unresolved questions. Finally, it would be desirable to construct a laboratory experiment of this mechanism and investigate the parameter regime to yield maximum ion and electron heating.

The near-Earth environment is an ideal laboratory for studying phenomena that would otherwise not allow for in-situ measurements like the solar corona (Retino, 2016). Furthermore, KHI is one the main mechanisms resulting from the Sun’s interaction with the magnetopause (Retino, 2016). Of equal significance, this cross-scale mechanism may be fundamental in contributing to the heating of the solar corona, where significant shear flows are present and KHI can form (Nykyri & Foullon, 2013; Foullon et al., 2013), and therefore warrant further detailed investigation. Similar to the sudden increase in ion temperatures across the magnetopause, where the magnetospheric ions are approximately 50 times hotter than the magnetosheath ions, the temperature increase from the visible surface of the Sun to the solar corona is staggering (Borovsky & Cayton, 2011).

From fusion research applications to solving one of the most pressing problems in astrophysical plasmas, uncovering the specific mechanism generating ion-scale fast magnetosonic waves inside Kelvin-Helmholtz vortices allowing cross-scale energy transport is crucial.

Appendix A

Appendix

A.1 Binning and Sorting Statistical Figures and Summary Plots

A.1.1 KHI Events

The figures containing the format similar to that shown in Figure A.1 depict qualitative determination of the MSH, MIX and MSP threshold values. The omni-directional ion energy spectrograms rotated into flux-energy space for the entire event interval length are plotted in the Top Panel; the Middle Panel shows the histogram of observed ion energies tallied from each time step over the entire event length; and the weighted mean average of the ion energy is plotted relative to the plasma regime threshold in the Bottom Panel – the blue, green and red lines represent the energy thresholds for the MSH, MIX and MSP plasma regimes respectively.

The figures sharing the same format as shown in Figure A.2 depict the output of the binning algorithm. The bin in which each time step has been sorted into based upon its

*A.1. BINNING AND SORTING STATISTICAL FIGURES AND SUMMARY
PLOTS*

subsequent weighted mean average is plotted in the Bottom Panel – the blue, green and red lines represent the MSH, MIX and MSP plasma regimes respectively.

A.1. BINNING AND SORTING STATISTICAL FIGURES AND SUMMARY PLOTS

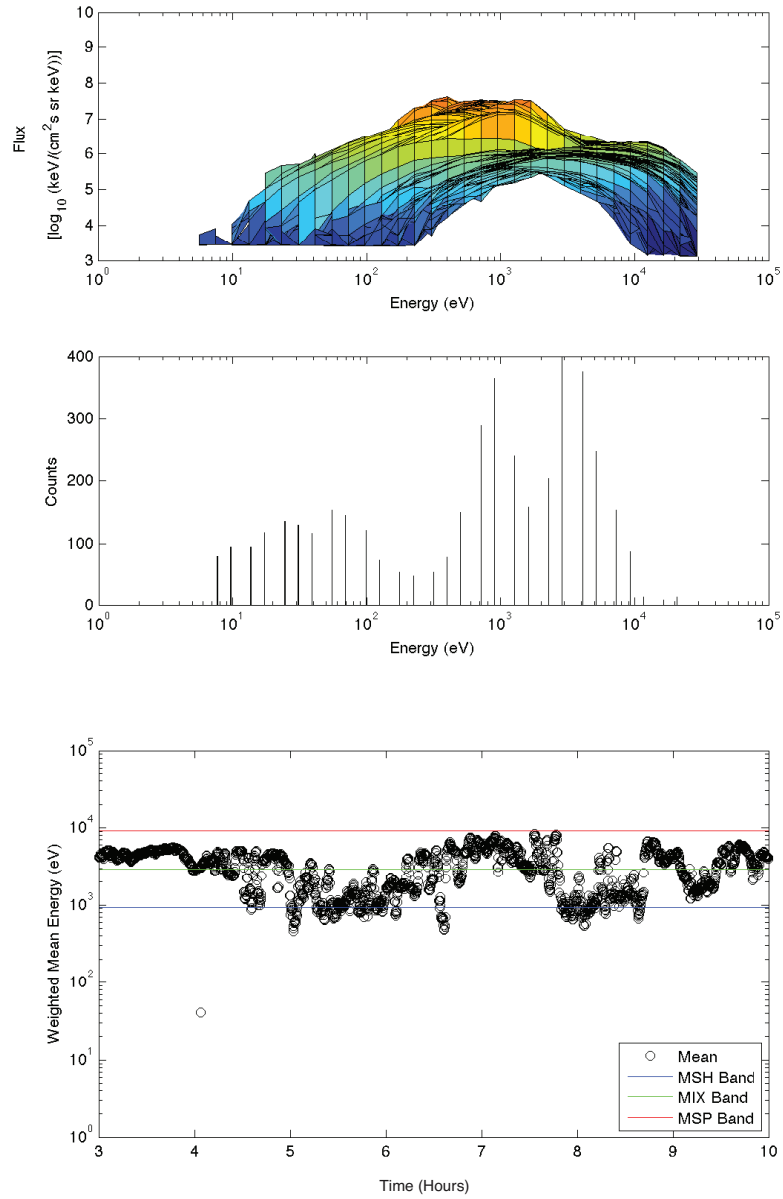


Figure A.1: Energy band statistics and sorting for July 3rd 2001 Event.

A.1. BINNING AND SORTING STATISTICAL FIGURES AND SUMMARY PLOTS

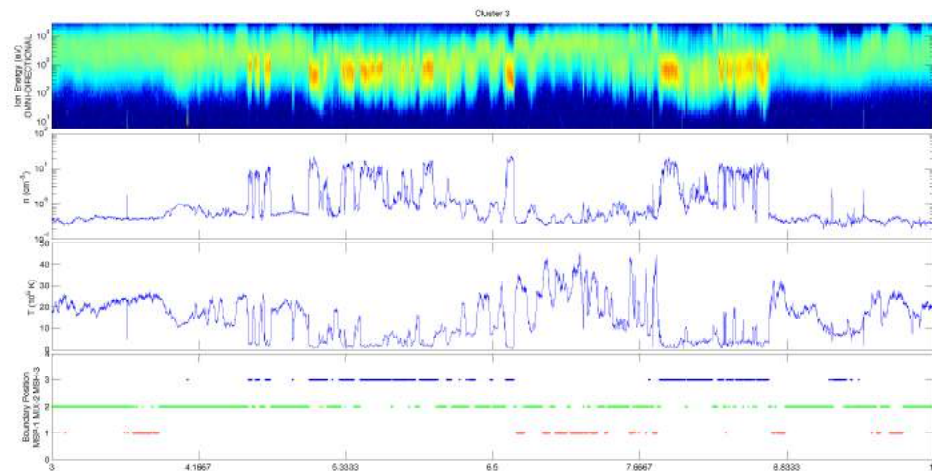


Figure A.2: July 3rd 2001 Event summary and boundary position.

A.1. BINNING AND SORTING STATISTICAL FIGURES AND SUMMARY PLOTS

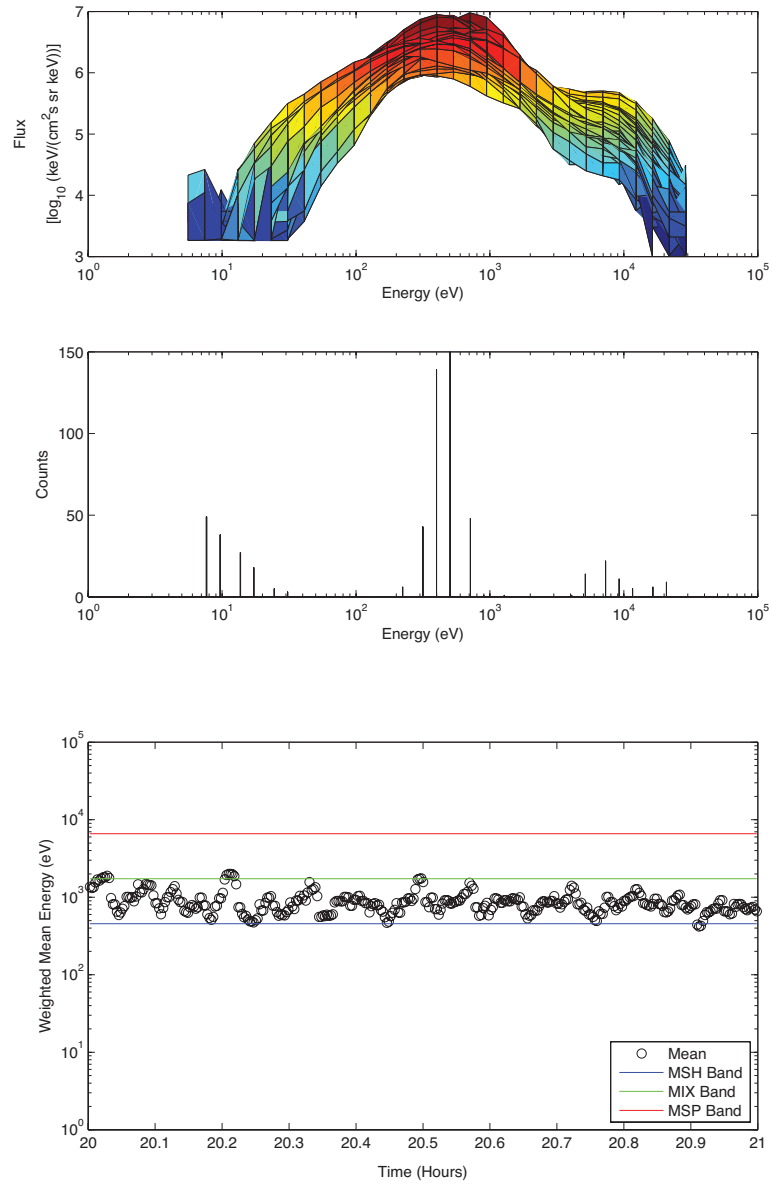


Figure A.3: Energy band statistics and sorting for November 20th 2001 Event.

A.1. BINNING AND SORTING STATISTICAL FIGURES AND SUMMARY PLOTS

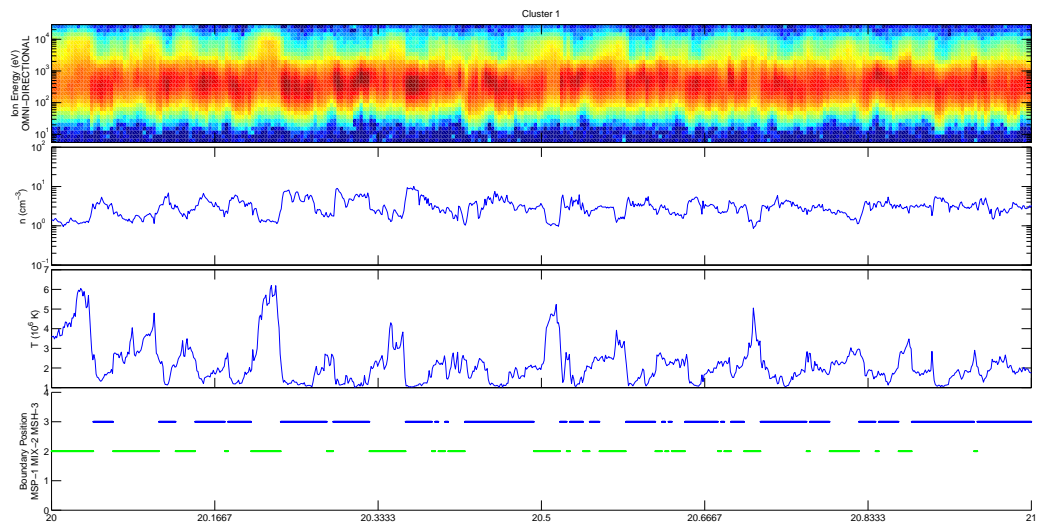


Figure A.4: November 20th 2001 Event summary and boundary position.

A.1. BINNING AND SORTING STATISTICAL FIGURES AND SUMMARY PLOTS

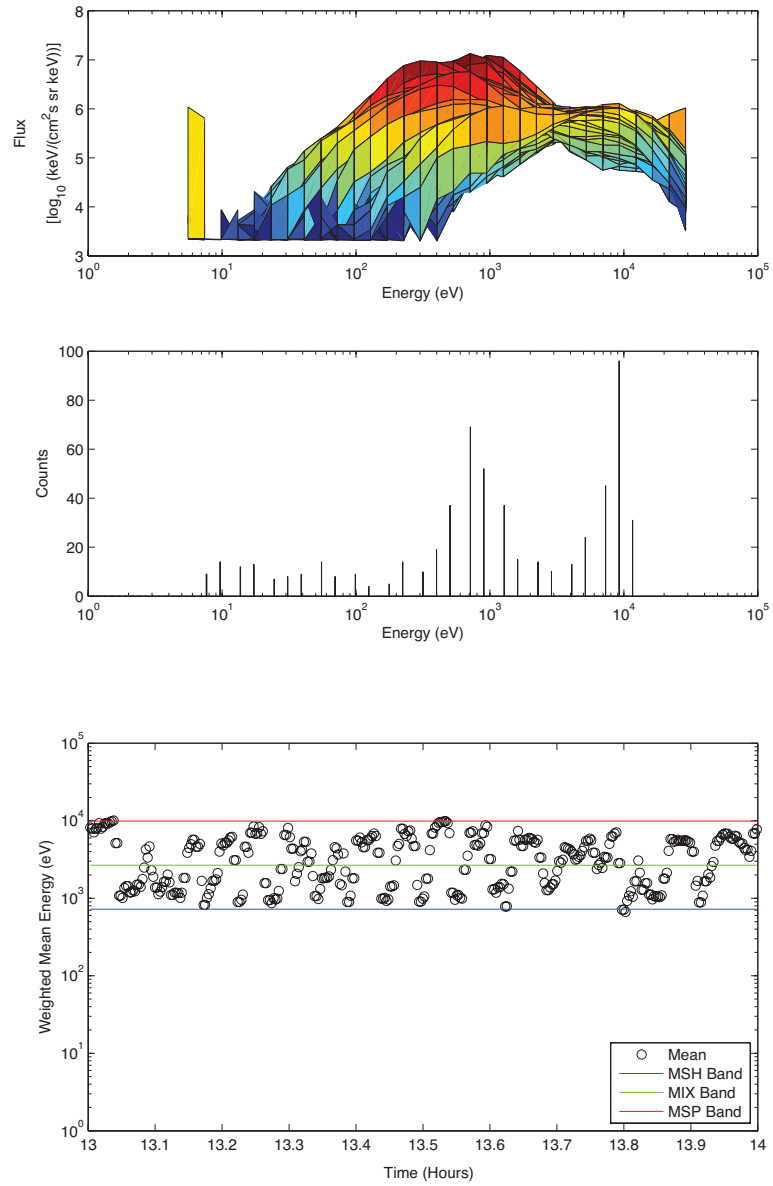


Figure A.5: Energy band statistics and sorting for June 6th 2002 Event.

A.1. BINNING AND SORTING STATISTICAL FIGURES AND SUMMARY PLOTS

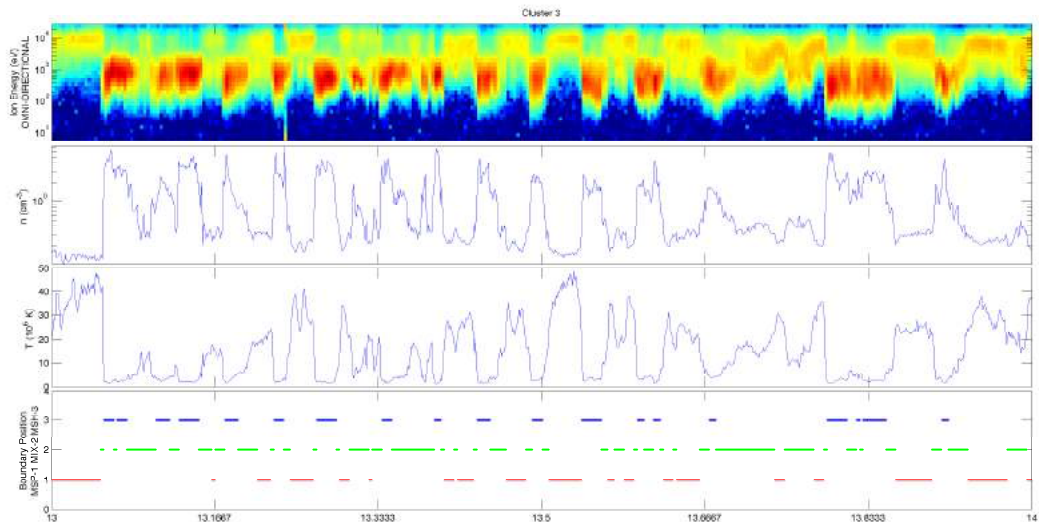


Figure A.6: June 6th 2002 Event summary and boundary position.

A.1. BINNING AND SORTING STATISTICAL FIGURES AND SUMMARY PLOTS

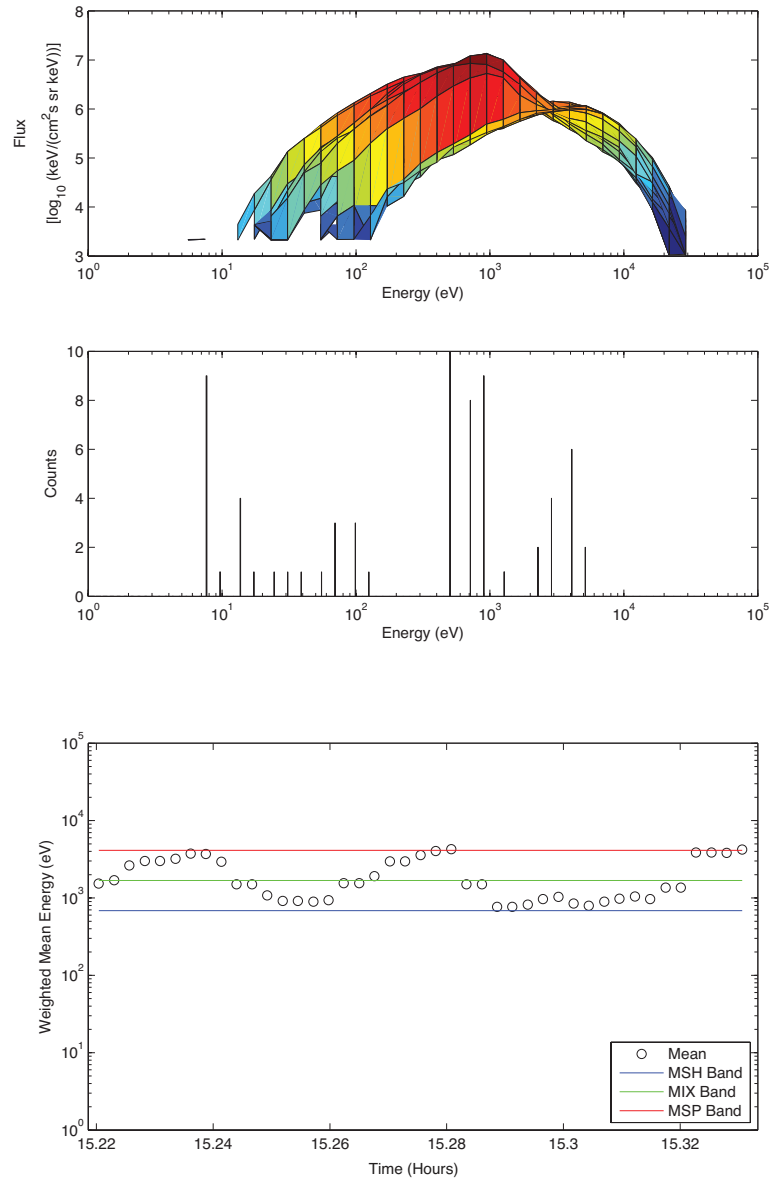


Figure A.7: Energy band statistics and sorting for June 13th 2002 Event.

A.1. BINNING AND SORTING STATISTICAL FIGURES AND SUMMARY PLOTS

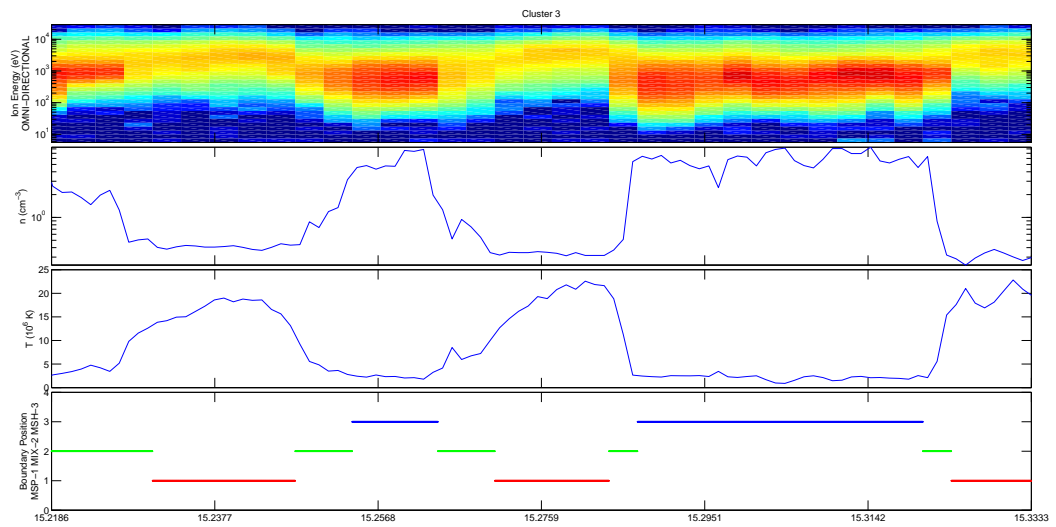


Figure A.8: June 13th 2002 Event summary and boundary position.

A.1. BINNING AND SORTING STATISTICAL FIGURES AND SUMMARY PLOTS

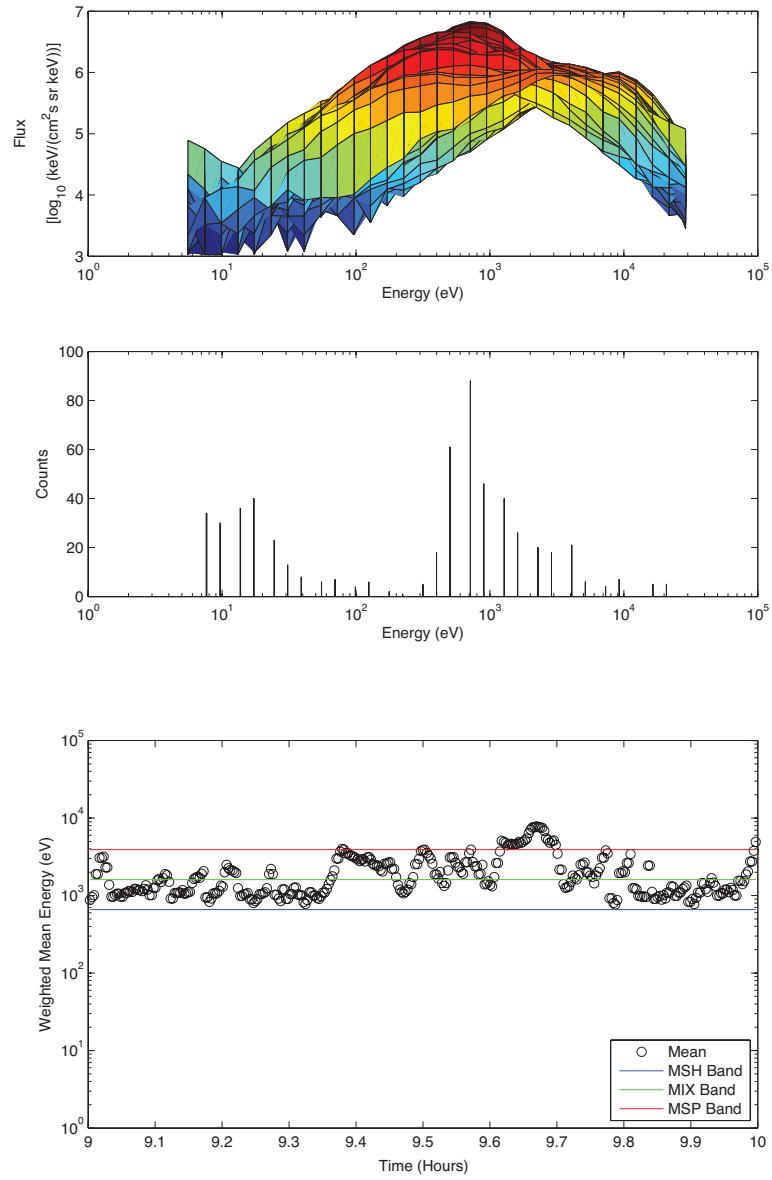


Figure A.9: Energy band statistics and sorting for June 19th 2004 Event.

A.1. BINNING AND SORTING STATISTICAL FIGURES AND SUMMARY PLOTS

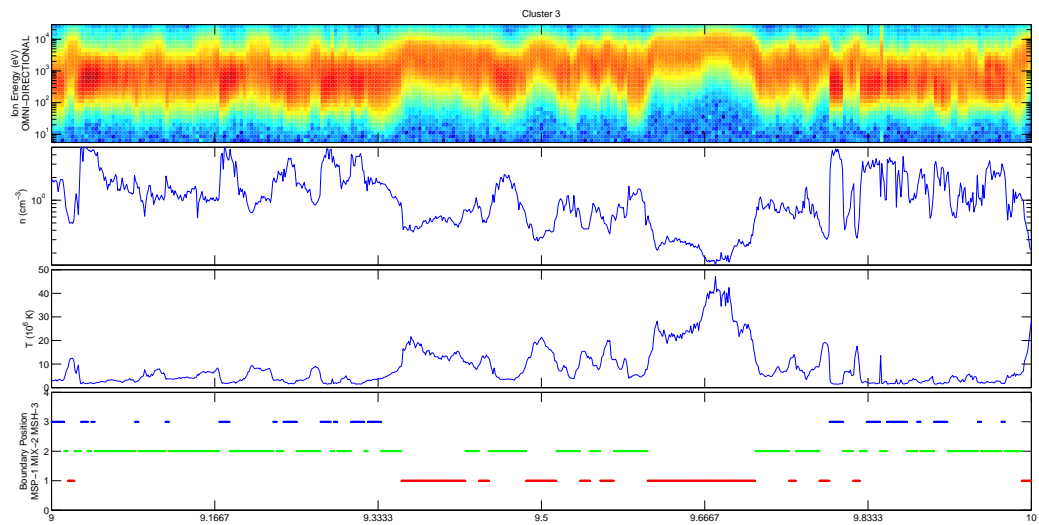


Figure A.10: June 19th 2004 Event summary and boundary position.

A.1. BINNING AND SORTING STATISTICAL FIGURES AND SUMMARY PLOTS

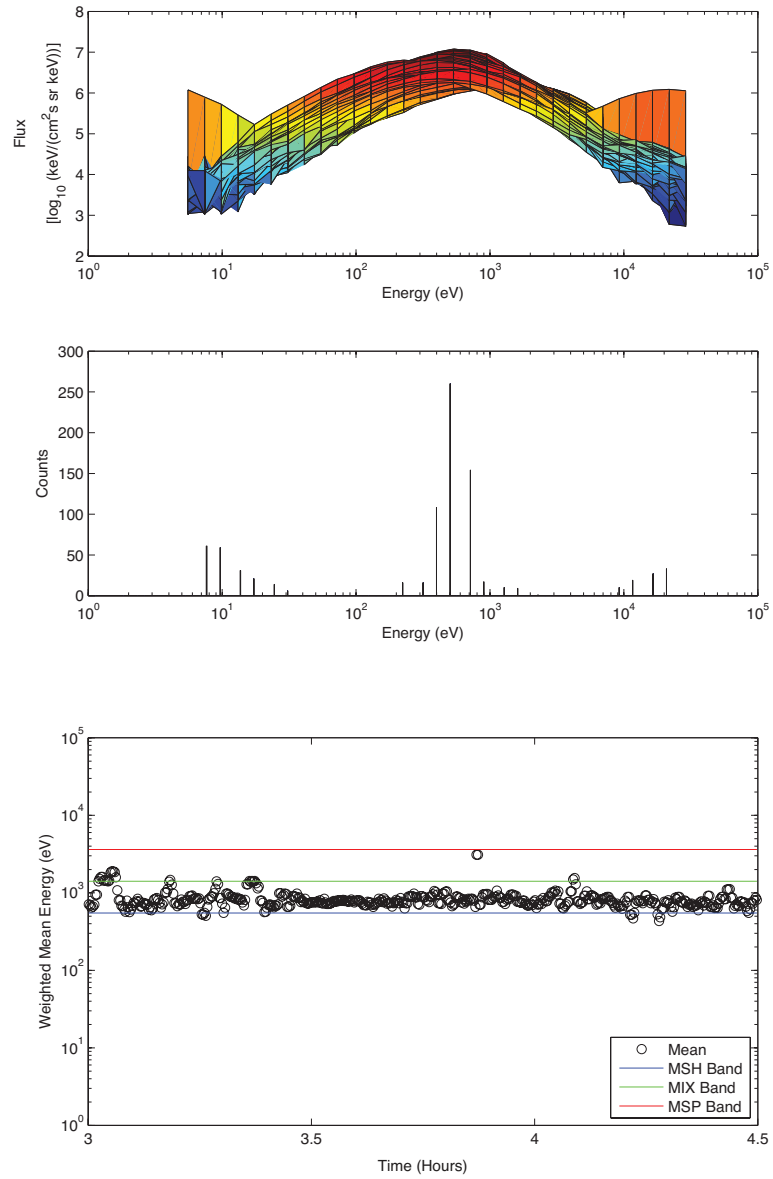


Figure A.11: Energy band statistics and sorting for June 21st 2004 Event.

A.1. BINNING AND SORTING STATISTICAL FIGURES AND SUMMARY PLOTS

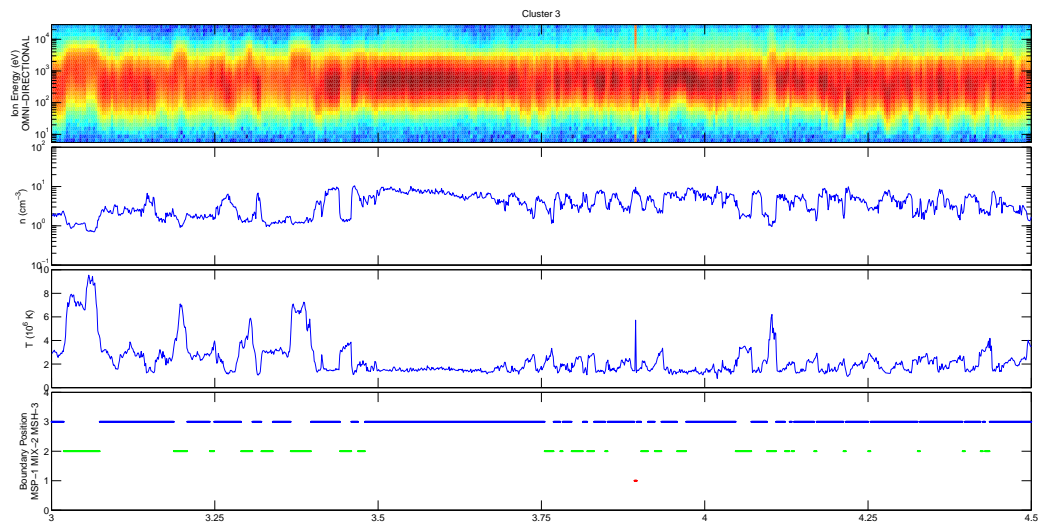


Figure A.12: June 21st 2004 Event summary and boundary position.

A.1.2 Non-KHI Events

A.1. BINNING AND SORTING STATISTICAL FIGURES AND SUMMARY PLOTS

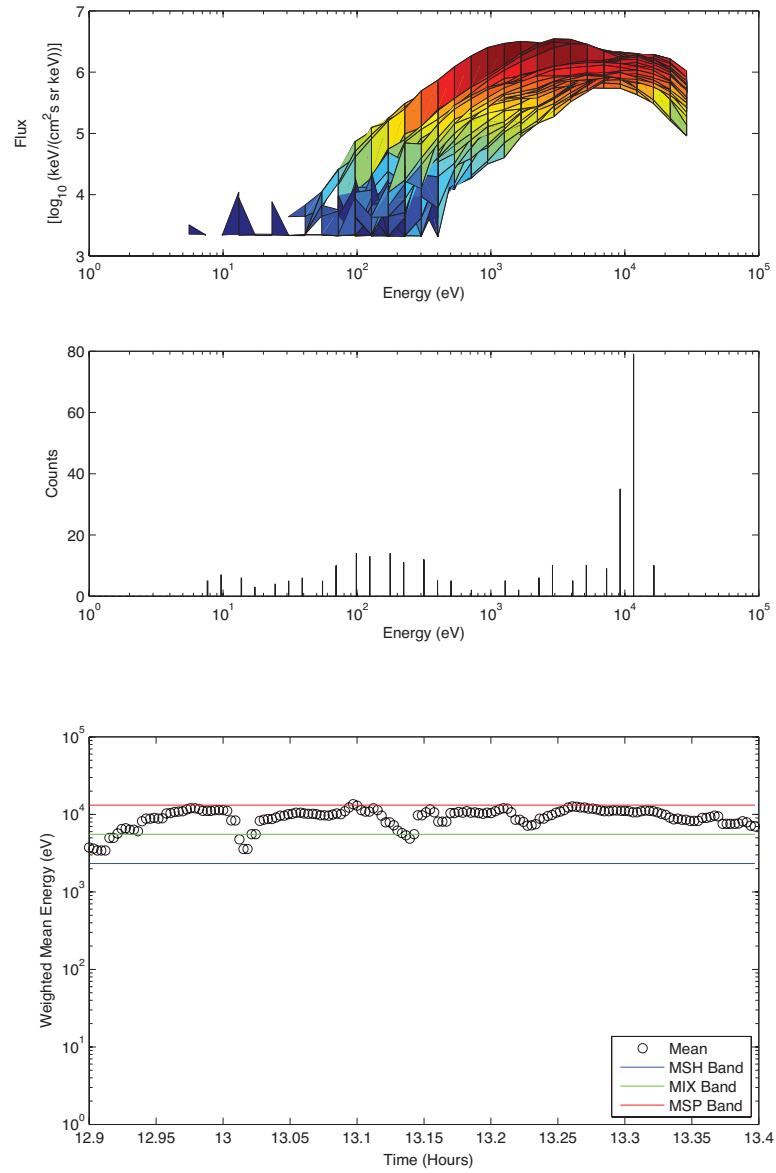


Figure A.13: Energy band statistics and sorting for June 3rd 2003 Event.

A.1. BINNING AND SORTING STATISTICAL FIGURES AND SUMMARY PLOTS

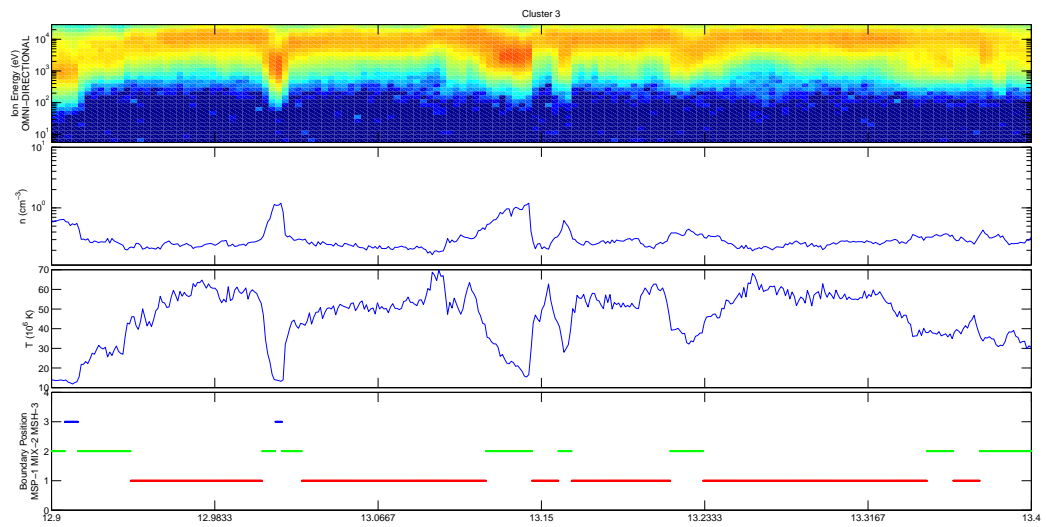


Figure A.14: June 3rd 2003 Event summary and boundary position.

A.1. BINNING AND SORTING STATISTICAL FIGURES AND SUMMARY PLOTS

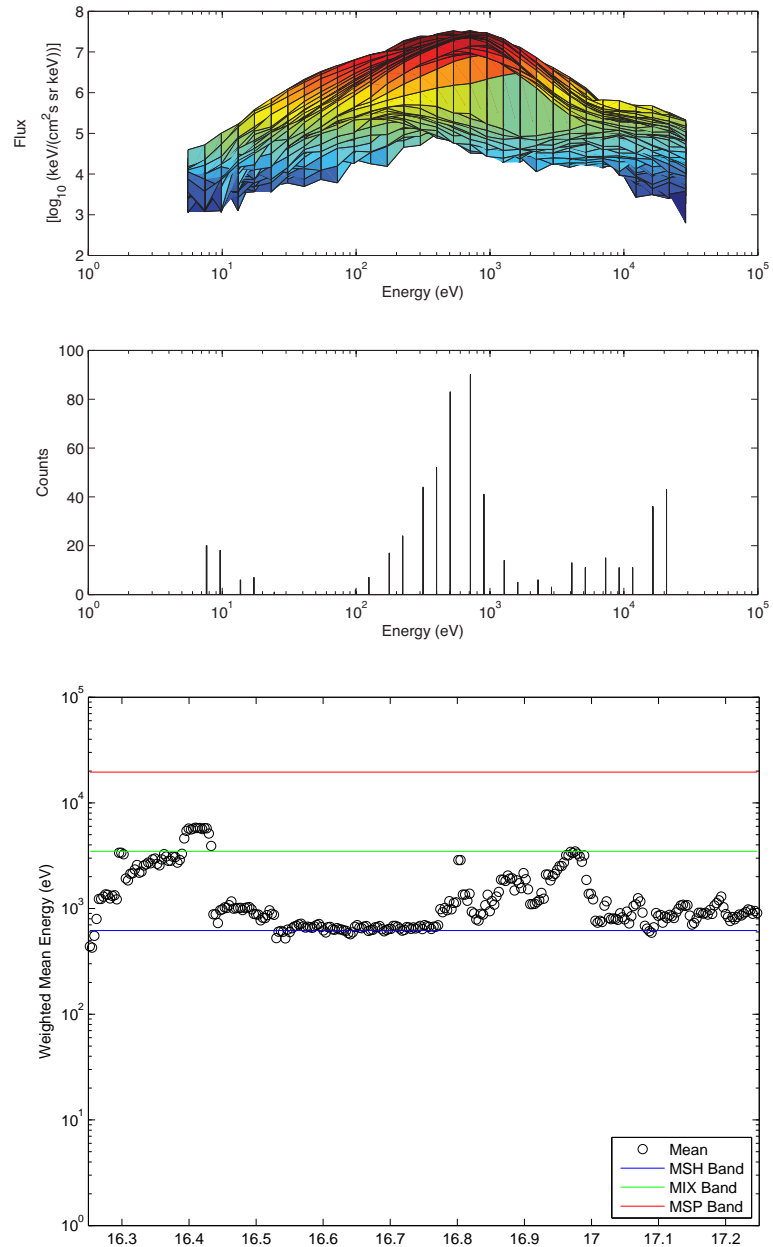


Figure A.15: Energy band statistics and sorting for November 16th 2004 Event.

A.1. BINNING AND SORTING STATISTICAL FIGURES AND SUMMARY PLOTS

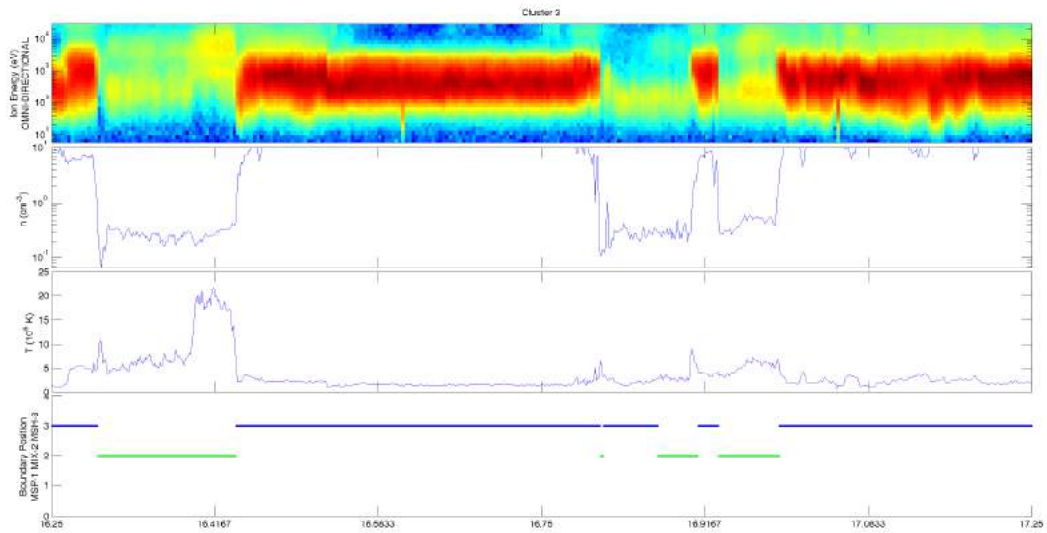


Figure A.16: November 16th 2004 Event summary and boundary position.

A.1. BINNING AND SORTING STATISTICAL FIGURES AND SUMMARY PLOTS

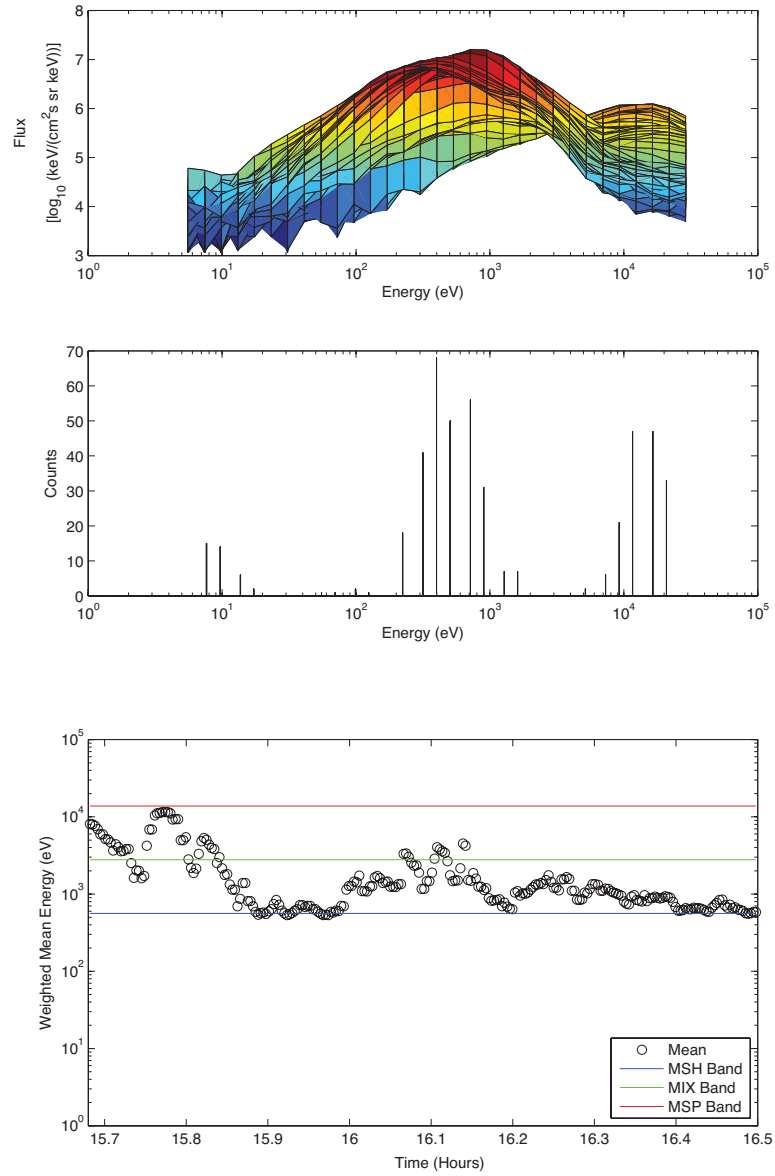


Figure A.17: Energy band statistics and sorting for November 27th 2004 Event.

A.1. BINNING AND SORTING STATISTICAL FIGURES AND SUMMARY PLOTS

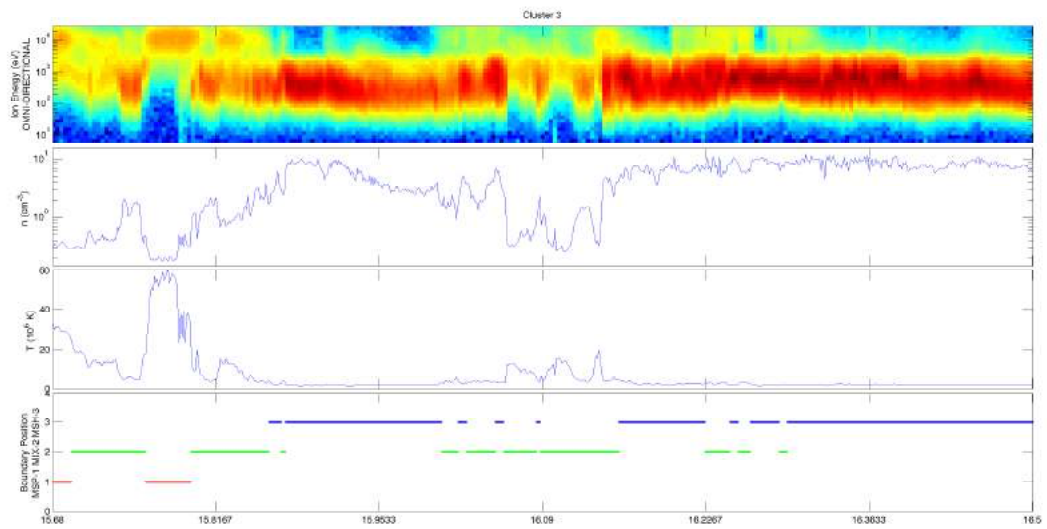


Figure A.18: November 27th 2004 Event summary and boundary position.

A.1. BINNING AND SORTING STATISTICAL FIGURES AND SUMMARY PLOTS

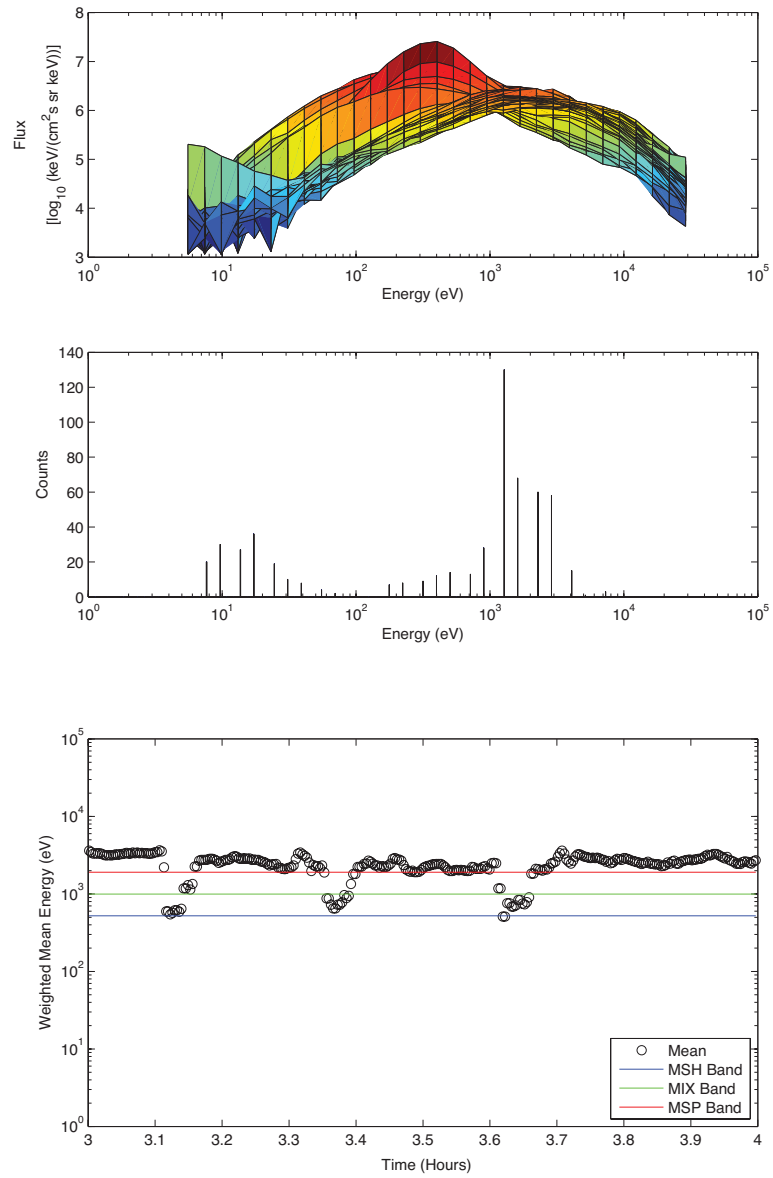


Figure A.19: Energy band statistics and sorting for June 28th 2005 Event.

A.1. BINNING AND SORTING STATISTICAL FIGURES AND SUMMARY PLOTS

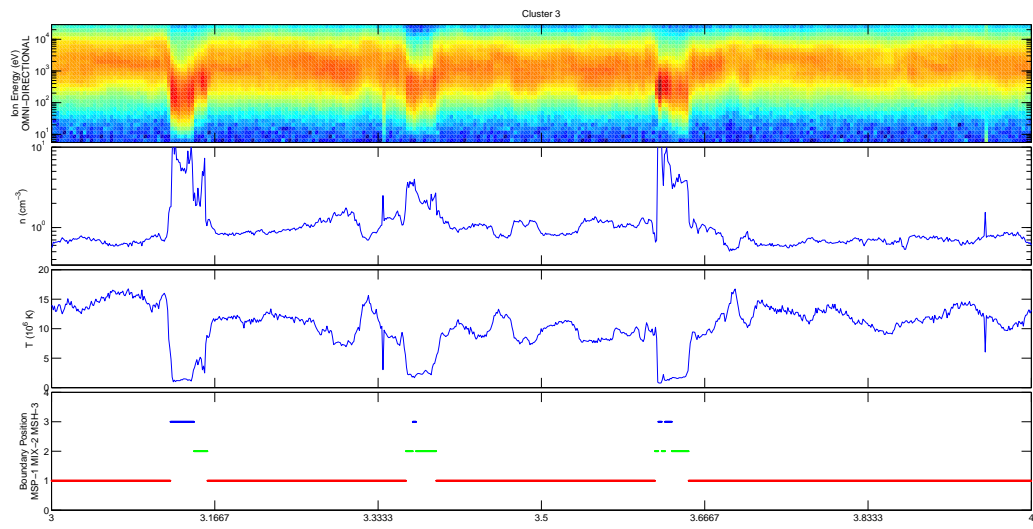


Figure A.20: June 28th 2005 Event summary and boundary position.

A.1. BINNING AND SORTING STATISTICAL FIGURES AND SUMMARY PLOTS

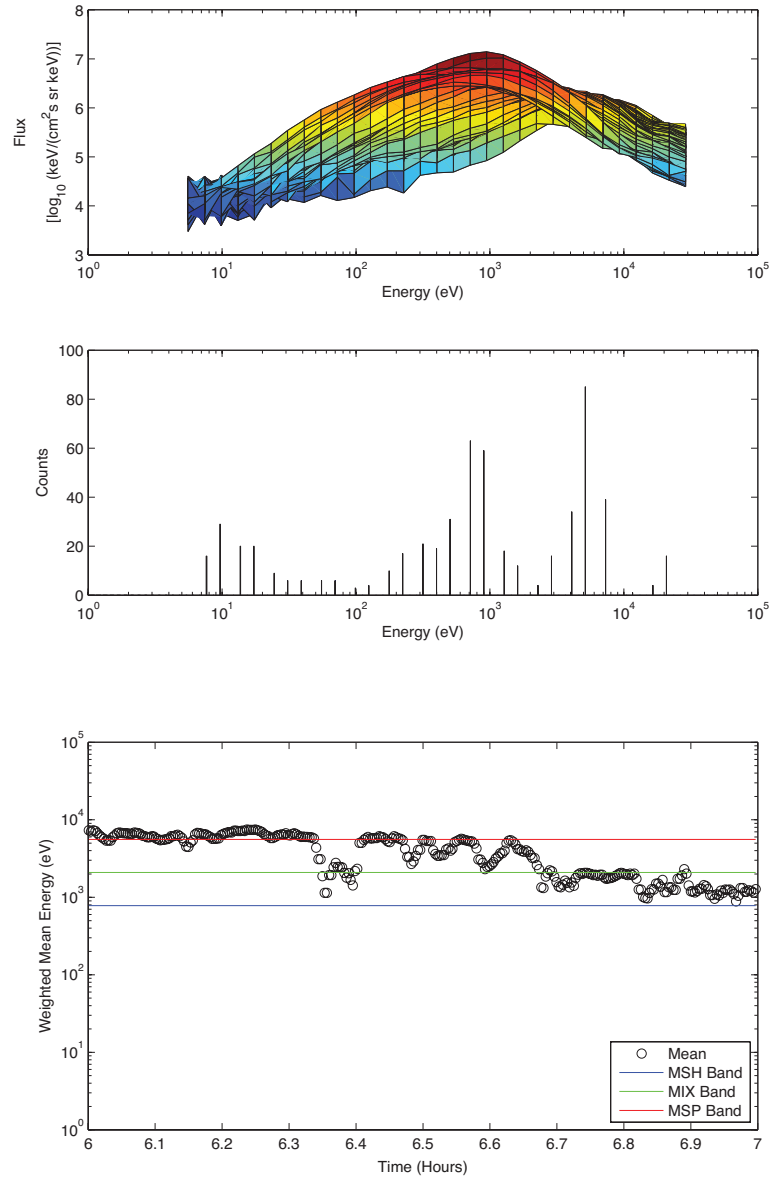


Figure A.21: Energy band statistics and sorting for June 4th 2007 Event.

A.1. BINNING AND SORTING STATISTICAL FIGURES AND SUMMARY PLOTS

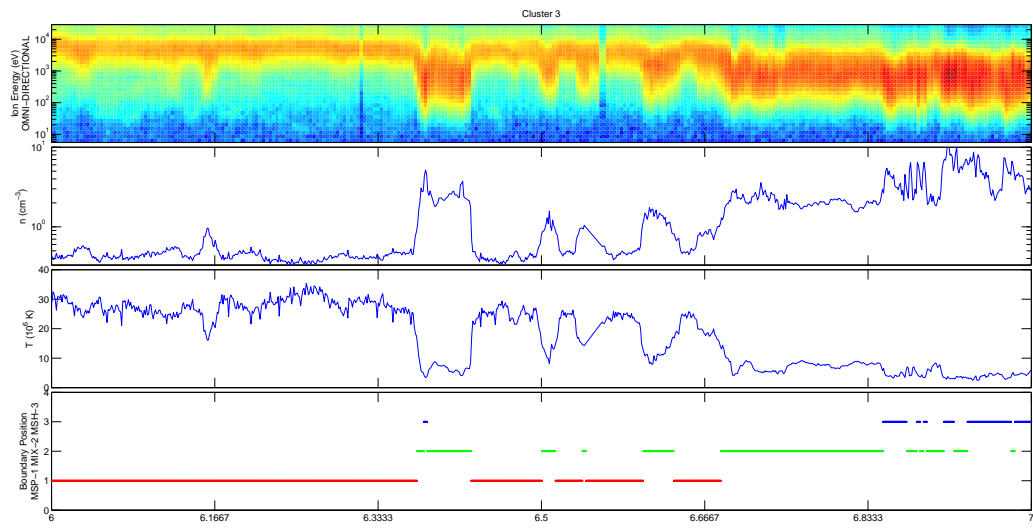


Figure A.22: June 4th 2007 Event summary and boundary position.

A.1. BINNING AND SORTING STATISTICAL FIGURES AND SUMMARY PLOTS

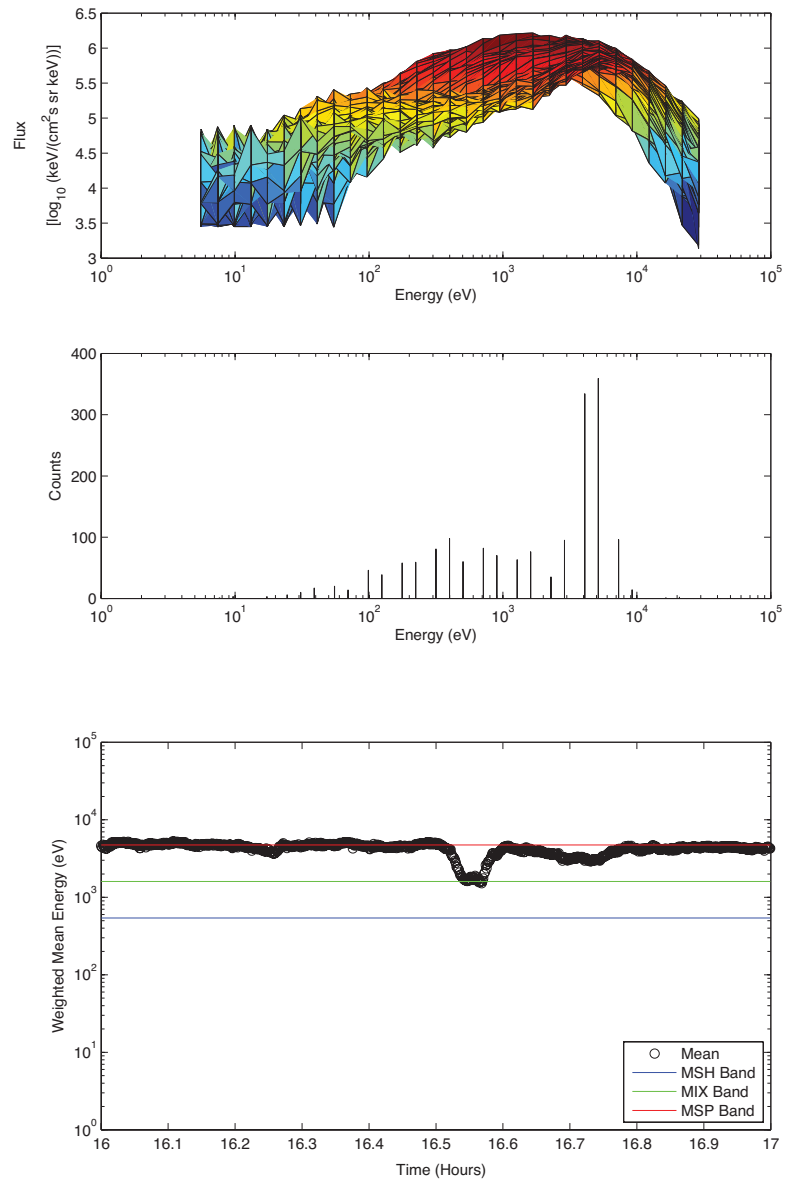


Figure A.23: Energy band statistics and sorting for June 6th 2007 Event A.

A.1. BINNING AND SORTING STATISTICAL FIGURES AND SUMMARY PLOTS

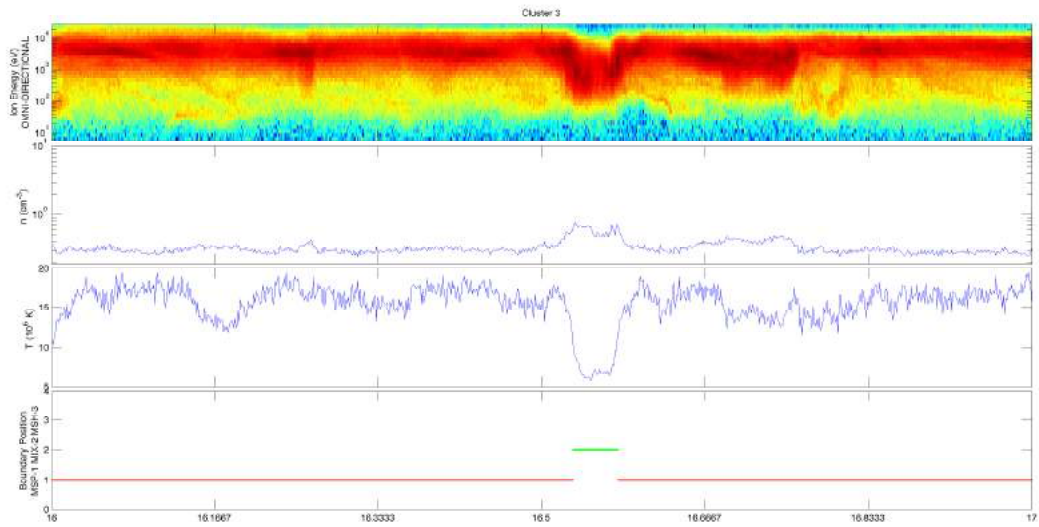


Figure A.24: June 6th 2007 Event A summary and boundary position.

A.1. BINNING AND SORTING STATISTICAL FIGURES AND SUMMARY PLOTS

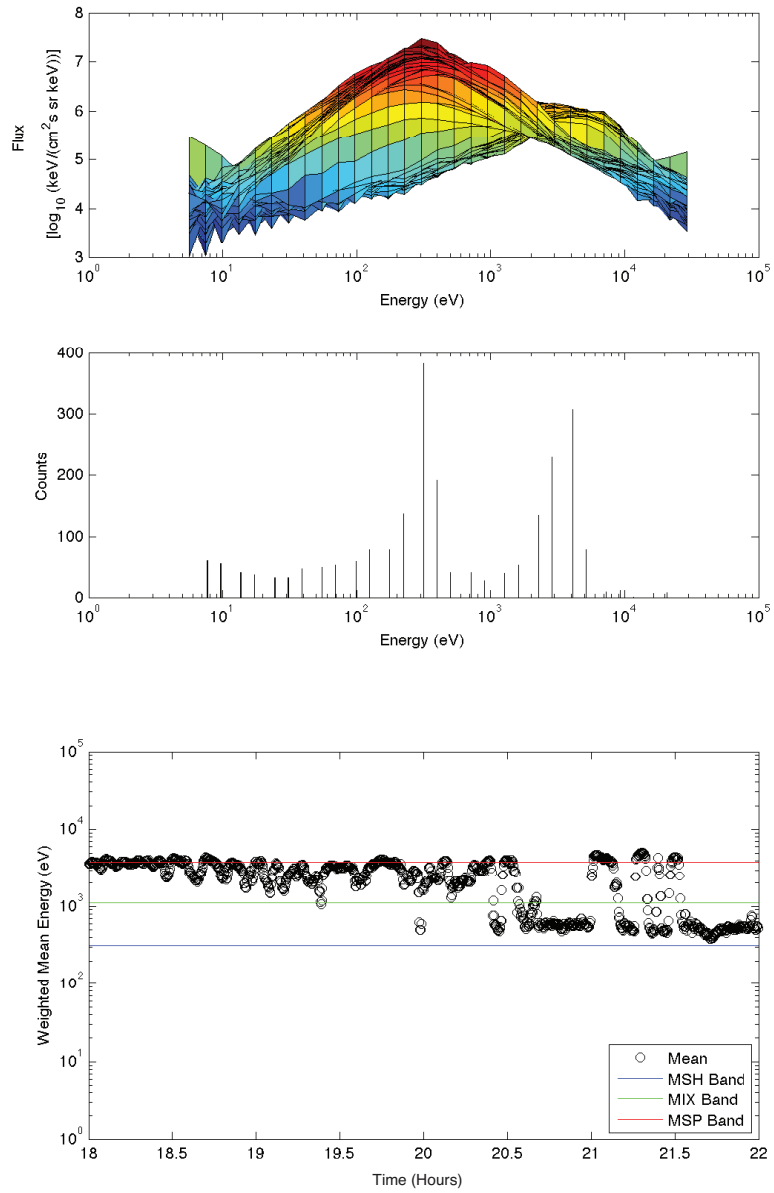


Figure A.25: Energy band statistics and sorting for June 6th 2007 Event B.

A.1. BINNING AND SORTING STATISTICAL FIGURES AND SUMMARY PLOTS

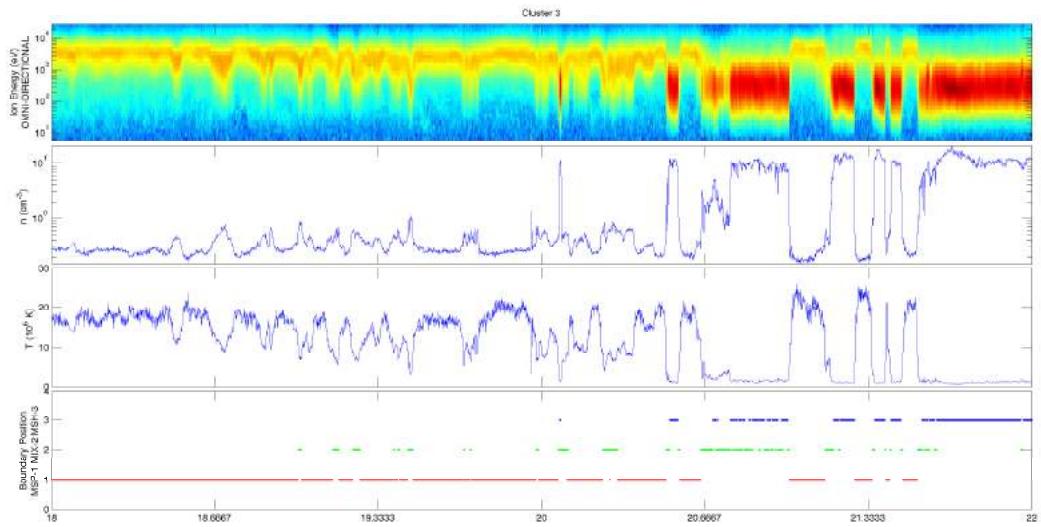


Figure A.26: June 6th 2007 Event B summary and boundary position.

A.1. BINNING AND SORTING STATISTICAL FIGURES AND SUMMARY PLOTS

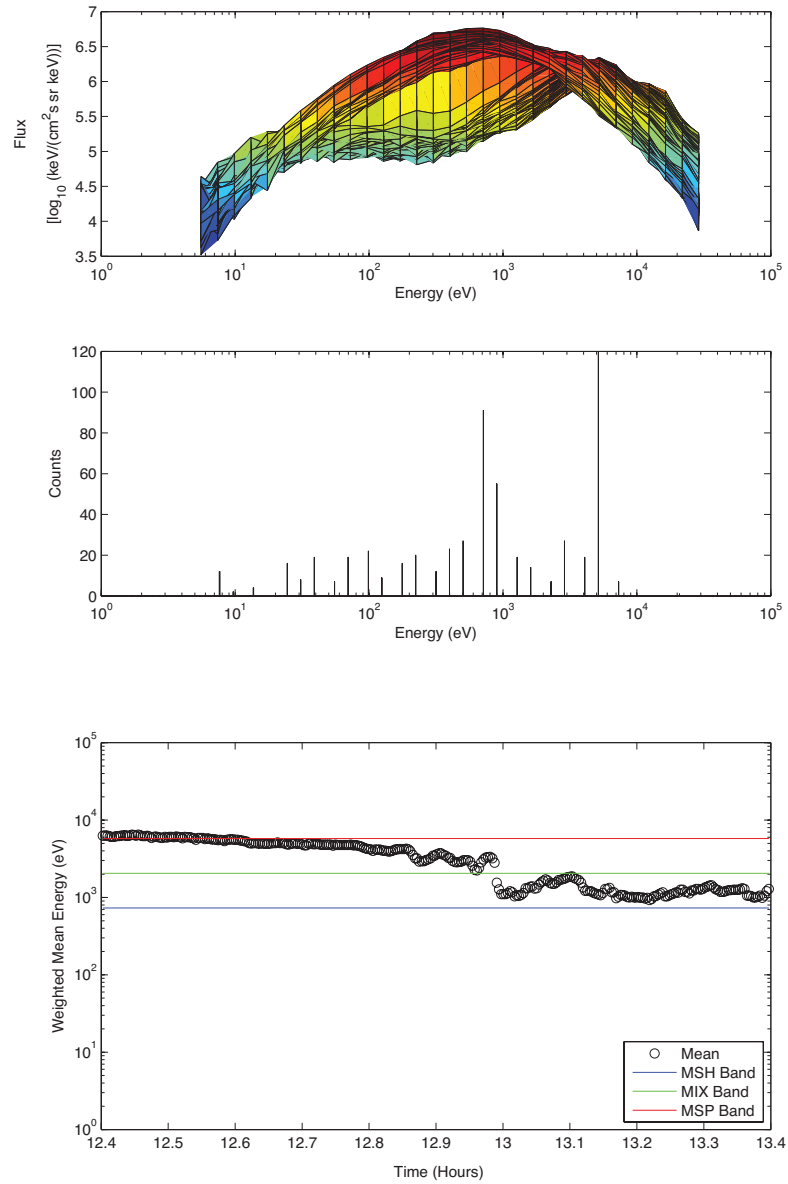


Figure A.27: Energy band statistics and sorting for June 3rd 2009 Event.

A.1. BINNING AND SORTING STATISTICAL FIGURES AND SUMMARY PLOTS

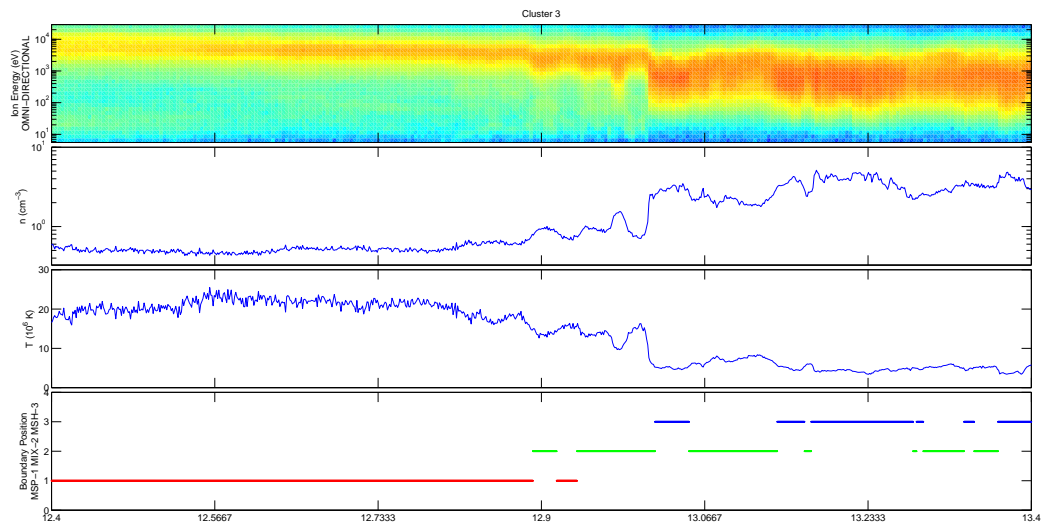


Figure A.28: June 3rd 2009 Event summary and boundary position.

A.2 Extreme Doppler Shift Effects

In an aim to estimate possible Doppler effects, we use the end of the wavelength range from the FMW interval from Moore et al. (2016) ($200 \text{ km} \leq \lambda \leq 2000 \text{ km}$) such that an extreme Doppler shift will result. Thus a wavelength of $\lambda = 200 \text{ km}$ is chosen for the Doppler shift equation $\omega_p = \omega_{sc} - 2\pi\hat{k}/\lambda \cdot \vec{v}_{flow}$, where ω_p is the plasma frame angular frequency, ω_{sc} is the spacecraft frame angular frequency, \hat{k} is the propagations direction and \vec{v}_{bulk} is the plasma flow in the spacecraft frame. Because the propagation direction vector \hat{k} is determined via MVAB, there is a 180° ambiguity with respect to the background magnetic field. As such, the estimation of the Doppler effect is split into the two extreme cases where \hat{k} is parallel or anti-parallel to \vec{v}_{bulk} such that $\omega_p = \omega_{sc} \mp 2\pi\hat{k}/\lambda \cdot \vec{v}_{flow}$.

Figures A.31, A.32 and A.33 show how the possible extreme Doppler shifts may effect the 2-d mean magnetic wave power, total integrated Poynting flux and mean scaled $\delta E/\delta B$ comparative distributions. The left, middle and right columns from Figures A.31, A.32 and A.33 correspond to an anti-parallel Doppler shift, no Doppler shift and parallel Doppler shift respectively.

Taking into account both extreme cases of the Doppler shift change the trends discussed in the ion-scale distributions in the MSH plasma. The most noticeable consequences of such extreme Doppler shift estimates are in the P_{tot} and S_{int} distributions. Specifically the anti-parallel and parallel Doppler shift estimates in the MIX plasma push the quasi-perpendicular portion of the P_{tot} into a range inconsistent with the June 6th 2002 FMW observations (see the middle row of panels from Figure A.31). Similarly the anti-parallel and parallel Doppler shift estimates in the MIX plasma push the quasi-perpendicular portion of the S_{int} into a range inconsistent with the June 6th 2002 FMW observations (see Figures A.32 (d) and (f)). When accounting for the extreme parallel Doppler shift on the \mathcal{P} distribution in the MSH plasma (Figure A.33 (i)), there is little evidence of KAW activity that was evidenced

A.2. EXTREME DOPPLER SHIFT EFFECTS

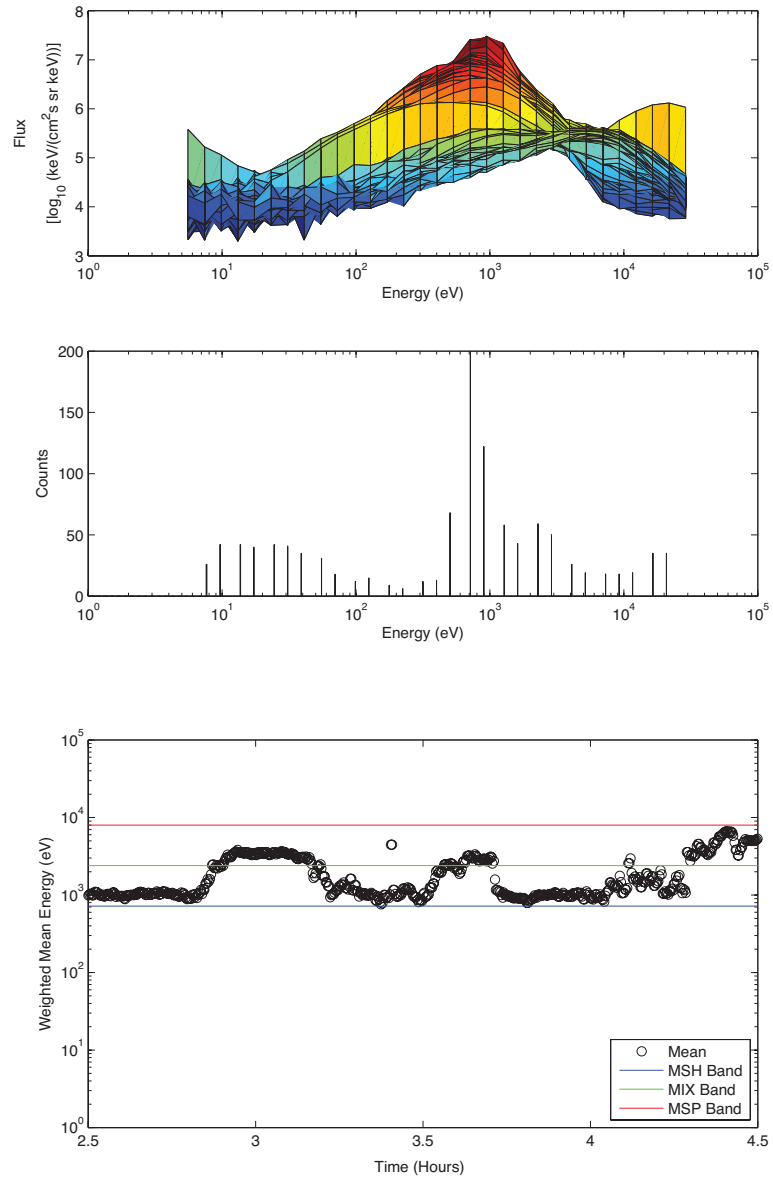


Figure A.29: Energy band statistics and sorting for June 26th 2009 Event.

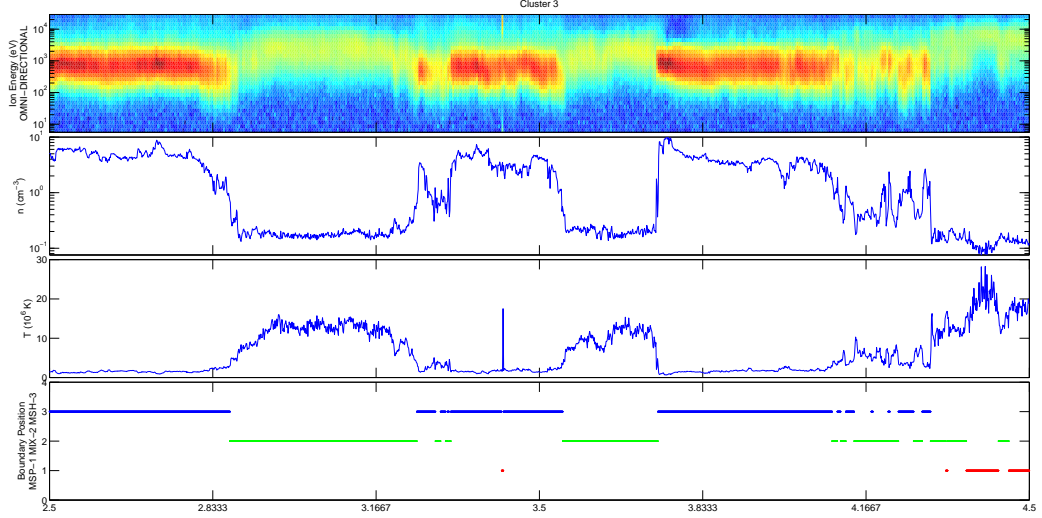


Figure A.30: June 26th 2009 Event summary and boundary position.

by the KH-dominant band near unity for the anti-parallel and zero Doppler shift cases in Figures A.33 (g) and (h) respectively.

Although accounting for possible Doppler shift effects causes changes in the results from the main text – most notably in the MIX P_{tot} and S_{int} distributions – these are for very extreme cases for a singular wavelength which most likely corresponds to frequencies well outside of the ion-cyclotron frequency and thus considerable weight should not be placed on these results.

A.2. EXTREME DOPPLER SHIFT EFFECTS

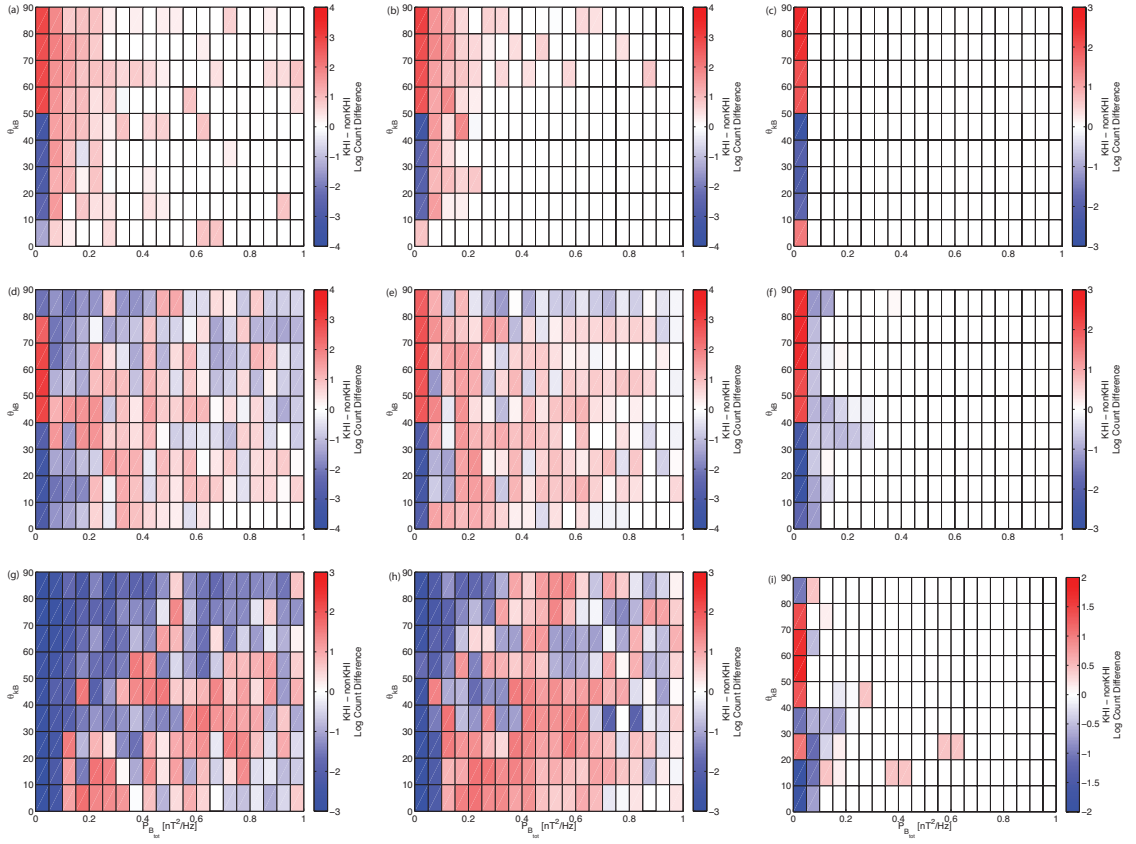


Figure A.31: Estimated parallel \hat{k} (left columns) and anti-parallel \hat{k} (right columns) Extreme Doppler effects on the 2-d comparative distributions of mean total power (P_{tot}) versus propagation angle (θ_{kB}) between KHI and non-KHI events; center columns are the non-Doppler shifted distributions. The panels from top to bottom represent the MSP, MIX and MSH plasma regimes, respectively.

A.2. EXTREME DOPPLER SHIFT EFFECTS

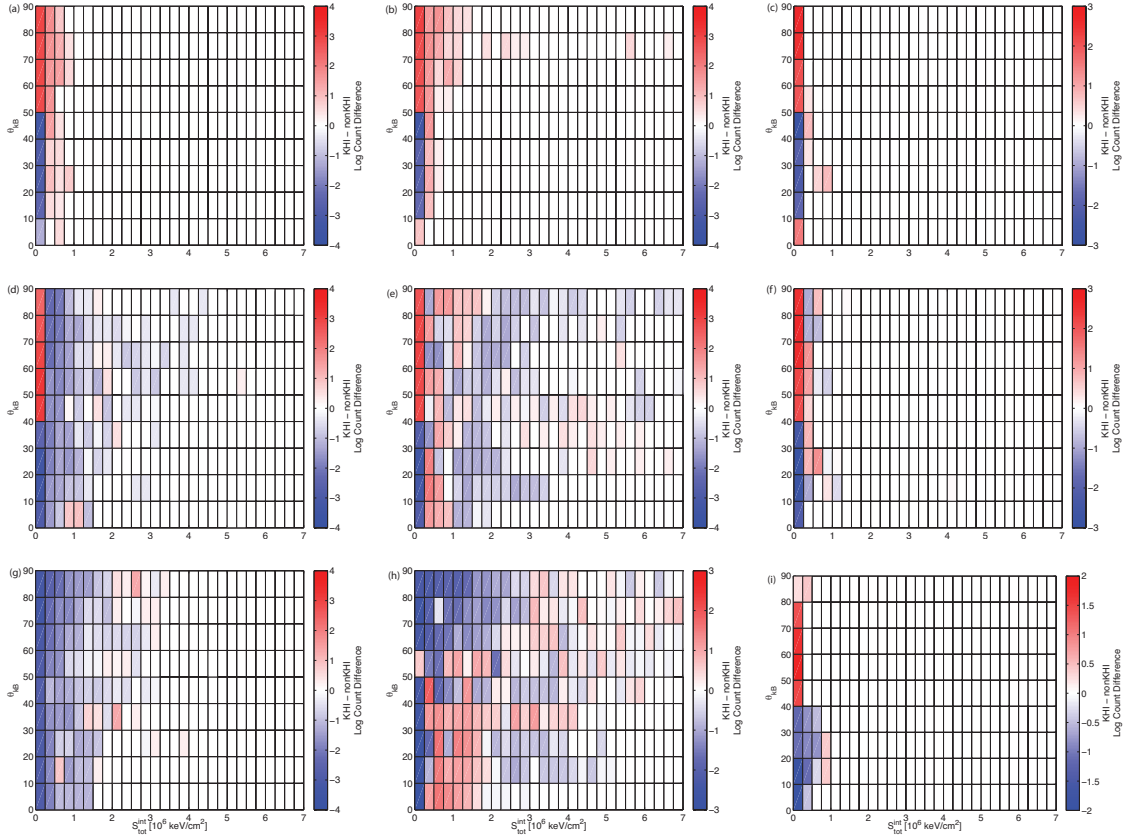


Figure A.32: Estimated parallel \hat{k} (left columns) and anti-parallel \hat{k} (right columns) Extreme Doppler effects on the 2-d comparative distribution of the integrated Poynting flux versus propagation angle (S_{int} versus θ_{kB}); center columns are the non-Doppler shifted distributions. The panels from top to bottom represent the MSP, MIX and MSH plasma regimes, respectively.

A.2. EXTREME DOPPLER SHIFT EFFECTS

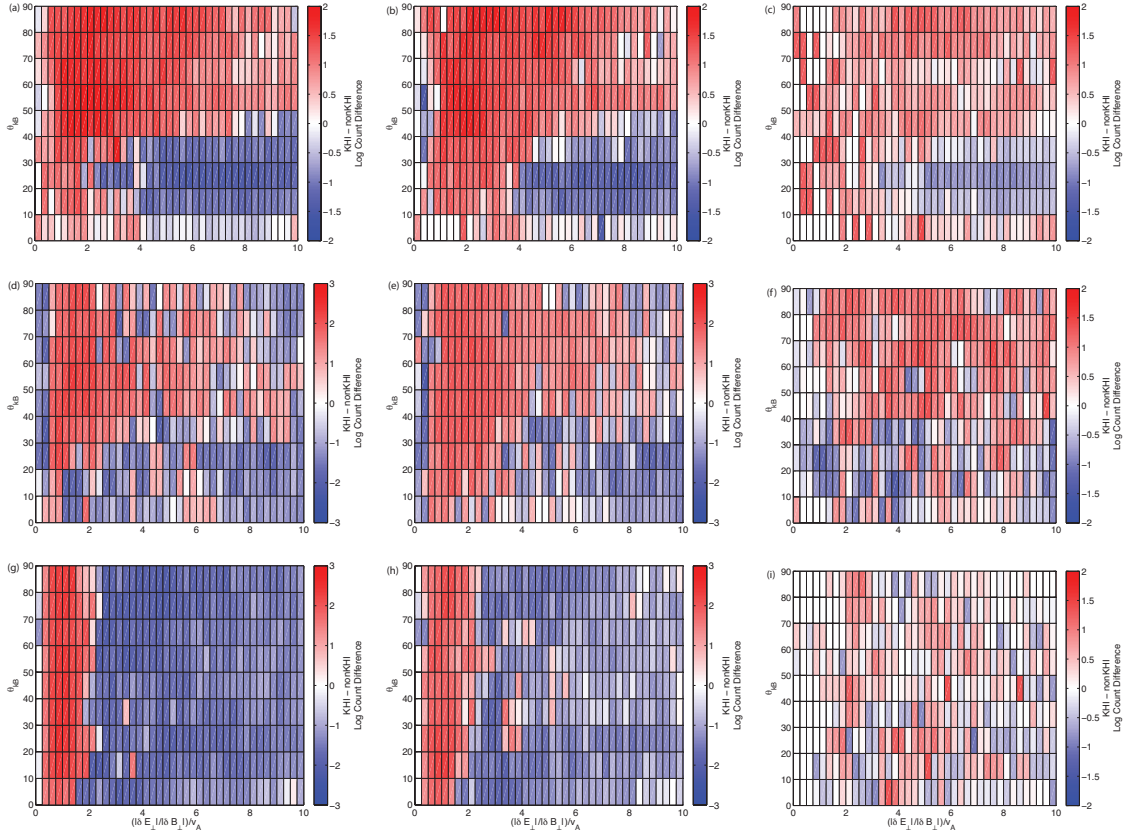


Figure A.33: Estimated parallel \hat{k} (left columns) and anti-parallel \hat{k} (right columns) Extreme Doppler effects on the 2-d comparative distributions of scaled mean $\delta E / \delta B$ polarization versus propagation angle; center columns are the non-Doppler shifted distributions. The panels from top to bottom represent the MSP, MIX and MSH plasma regimes, respectively.

References

- Adamson, E., Nykyri, K., & Otto, A. (2016, July). The Kelvin-Helmholtz instability under Parker-Spiral Interplanetary Magnetic Field conditions at the magnetospheric flanks. *Advances in Space Research*, *58*, 218-230. doi: 10.1016/j.asr.2015.09.013
- Alfvén, H. (1942, October). Existence of Electromagnetic-Hydrodynamic Waves. *Nature*, *150*, 405-406. doi: 10.1038/150405d0
- Alfvén, H. (1943). On the Existence of Electromagnetic-Hydrodynamic Waves. *Arkiv for Astronomi*, *29*, 1-7.
- Axford, W. I., & Hines, C. O. (1961). A unifying theory of high-latitude geophysical phenomena and geomagnetic storms. *Canadian Journal of Physics*, *39*, 1433. doi: 10.1139/p61-172
- Balikhin, M. A., de Wit, T. D., Alleyne, H. S. C. K., Woolliscroft, L. J. C., Walker, S. N., Krasnosel'skikh, V., ... Baumjohann, W. (1997). Experimental determination of the dispersion of waves observed upstream of a quasi-perpendicular shock. *Geophys. Res. Lett.*, *24*, 787-790. doi: 10.1029/97GL00671

-
- Balikhin, M. A., Shprits, Y. Y., Walker, S. N., Chen, L., Cornilleau-Wehrin, N., Dandouras, I., ... Weiss, B. (2015, July). Observations of discrete harmonics emerging from equatorial noise. *Nature Communications*, *6*, 7703. doi: 10.1038/ncomms8703
- Baumjohann, W., Paschmann, G., & Cattell, C. A. (1989). Average plasma properties in the central plasma sheet. *Journal of Geophysical Research: Space Physics*, *94*(A6), 6597–6606. Retrieved from <http://dx.doi.org/10.1029/JA094iA06p06597> doi: 10.1029/JA094iA06p06597
- Birn, J., Drake, J. F., Shay, M. A., Rogers, B. N., Denton, R. E., Hesse, M., ... Pritchett, P. L. (2001). Geospace environmental modeling (gem) magnetic reconnection challenge. *Journal of Geophysical Research: Space Physics*, *106*(A3), 3715–3719. Retrieved from <http://dx.doi.org/10.1029/1999JA900449> doi: 10.1029/1999JA900449
- Bittencourt, J. (2004). *Fundamentals of Plasma Physics, 3rd Edition* (Bittencourt, J.A., Ed.).
- Blanco-Cano, X., Omid, N., & Russell, C. T. (2006, October). Macrostructure of collisionless bow shocks: 2. ULF waves in the foreshock and magnetosheath. *Journal of Geophysical Research (Space Physics)*, *111*, 10205. doi: 10.1029/2005JA011421
- Boardsen, S. A., Gallagher, D. L., Gurnett, D. A., Peterson, W. K., & Green, J. L. (1992, October). Funnel-shaped, low-frequency equatorial waves. *Journal of Geophysical Research*, *97*, 14967. doi: 10.1029/92JA00827

- Boardsen, S. A., Sundberg, T., Slavin, J. A., Anderson, B. J., Korth, H., Solomon, S. C., & Blomberg, L. G. (2010, June). Observations of Kelvin-Helmholtz waves along the dusk-side boundary of Mercury's magnetosphere during MESSENGER's third flyby. *Geophys. Res. Lett.*, *37*, 12101. doi: 10.1029/2010GL043606
- Boller, B. R., & Stolov, H. L. (1973). Explorer 18 study of the stability of the magnetopause using a kelvin-helmholtz instability criterion. *Journal of Geophysical Research*, *78*(34), 8078–8086. Retrieved from <http://dx.doi.org/10.1029/JA078i034p08078> doi: 10.1029/JA078i034p08078
- Borovsky, J. E., & Cayton, T. E. (2011, June). Entropy mapping of the outer electron radiation belt between the magnetotail and geosynchronous orbit. *Journal of Geophysical Research (Space Physics)*, *116*, 6216. doi: 10.1029/2011JA016470
- Carozzi, T. D., Thid, B., Leyser, T. B., Komrakov, G., Frolov, V., Grach, S., & Sergeev, E. (2001). Full polarimetry measurements of stimulated electromagnetic emissions: First results. *Journal of Geophysical Research: Space Physics*, *106*(A10), 21395–21407. Retrieved from <http://dx.doi.org/10.1029/2001JA900004> doi: 10.1029/2001JA900004
- Chaston, C. C., Bonnell, J. W., Clausen, L., & Angelopoulos, V. (2012). Energy transport by kinetic-scale electromagnetic waves in fast plasma sheet flows. *Journal of Geophysical Research: Space Physics*, *117*(A9), n/a–n/a. Retrieved from <http://dx.doi.org/10.1029/2012JA017863> (A09202) doi: 10.1029/2012JA017863

- Chaston, C. C., Wilber, M., Mozer, F. S., Fujimoto, M., Goldstein, M. L., Acuna, M., ... Fazakerley, A. (2007, October). Mode Conversion and Anomalous Transport in Kelvin-Helmholtz Vortices and Kinetic Alfvén Waves at the Earth's Magnetopause. *Physical Review Letters*, *99*(17), 175004. doi: 10.1103/PhysRevLett.99.175004
- Chen, Q., Otto, A., & Lee, L. C. (1997). Tearing instability, kelvin-helmholtz instability, and magnetic reconnection. *Journal of Geophysical Research: Space Physics*, *102*(A1), 151–161. Retrieved from <http://dx.doi.org/10.1029/96JA03144> doi: 10.1029/96JA03144
- Cheng, C. Z., & Johnson, J. R. (1999, January). A kinetic-fluid model. *Journal of Geophysical Research*, *104*, 413-428. doi: 10.1029/1998JA900065
- Colpitts, C. A., Cattell, C. A., Kozyra, J. U., & Parrot, M. (2012). Satellite observations of banded vlf emissions in conjunction with energy-banded ions during very large geomagnetic storms. *Journal of Geophysical Research: Space Physics*, *117*(A10), n/a–n/a. Retrieved from <http://dx.doi.org/10.1029/2011JA017329> (A10211) doi: 10.1029/2011JA017329
- Cowee, M. M., Winske, D., & Gary, S. P. (2010, June). Hybrid simulations of plasma transport by Kelvin-Helmholtz instability at the magnetopause: Density variations and magnetic shear. *Journal of Geophysical Research (Space Physics)*, *115*, 6214. doi: 10.1029/2009JA015011
- Dimmock, A. P., Balikhin, M. A., Walker, S. N., & Pope, S. A. (2013, August). Dispersion of low frequency plasma waves upstream of the quasi-perpendicular

- terrestrial bow shock. *Annales Geophysicae*, *31*, 1387-1395. doi: 10.5194/angeo-31-1387-2013
- Dimmock, A. P., & Nykyri, K. (2013). The statistical mapping of magnetosheath plasma properties based on themis measurements in the magnetosheath interplanetary medium reference frame. *Journal of Geophysical Research: Space Physics*, *118*(8), 4963–4976. Retrieved from <http://dx.doi.org/10.1002/jgra.50465> doi: 10.1002/jgra.50465
- Dimmock, A. P., Nykyri, K., Karimabadi, H., Osmane, A., & Pulkkinen, T. I. (2015, April). A statistical study into the spatial distribution and dawn-dusk asymmetry of dayside magnetosheath ion temperatures as a function of upstream solar wind conditions. *Journal of Geophysical Research (Space Physics)*, *120*, 2767-2782. doi: 10.1002/2014JA020734
- Dimmock, A. P., Nykyri, K., Osmane, A., & Pulkkinen, T. I. (2016, July). Statistical mapping of ULF Pc3 velocity fluctuations in the Earth's dayside magnetosheath as a function of solar wind conditions. *Advances in Space Research*, *58*, 196-207. doi: 10.1016/j.asr.2015.09.039
- Dimmock, A. P., Nykyri, K., & Pulkkinen, T. I. (2014). A statistical study of magnetic field fluctuations in the dayside magnetosheath and their dependence on upstream solar wind conditions. *Journal of Geophysical Research: Space Physics*, *119*(8), 6231–6248. Retrieved from <http://dx.doi.org/10.1002/2014JA020009> doi: 10.1002/2014JA020009

- Dimmock, A. P., Pulkkinen, T. I., Osmane, A., & Nykyri, K. (2016, May). The dawn-dusk asymmetry of ion density in the dayside magnetosheath and its annual variability measured by THEMIS. *Annales Geophysicae*, *34*, 511-528. doi: 10.5194/angeo-34-511-2016
- Dombrowski, M. P., LaBelle, J., Rowland, D. E., Pfaff, R. F., & Kletzing, C. A. (2012). Interpretation of vector electric field measurements of bursty langmuir waves in the cusp. *Journal of Geophysical Research: Space Physics*, *117*(A9), n/a–n/a. Retrieved from <http://dx.doi.org/10.1029/2012JA017741> (A09209) doi: 10.1029/2012JA017741
- Dougal, E. R., Nykyri, K., & Moore, T. W. (2013, November). Mapping of the quasi-periodic oscillations at the flank magnetopause into the ionosphere. *Annales Geophysicae*, *31*, 1993-2011. doi: 10.5194/angeo-31-1993-2013
- Dungey, J. W. (1961, January). Interplanetary Magnetic Field and the Auroral Zones. *Physical Review Letters*, *6*, 47-48. doi: 10.1103/PhysRevLett.6.47
- Eastman, T. E., & Hones, E. W., Jr. (1979, May). Characteristics of the magnetospheric boundary layer and magnetopause layer as observed by Imp 6. *Journal of Geophysical Research*, *84*, 2019-2028. doi: 10.1029/JA084iA05p02019
- Eastwood, J. P., Balogh, A., Dunlop, M. W., Horbury, T. S., & Dandouras, I. (2002, November). Cluster observations of fast magnetosonic waves in the terrestrial foreshock. *Geophysical Research Letters*, *29*, 2046. doi: 10.1029/2002GL015582

-
- Eastwood, J. P., Balogh, A., Lucek, E. A., Mazelle, C., & Dandouras, I. (2003, July). On the existence of Alfvén waves in the terrestrial foreshock. *Annales Geophysicae*, *21*, 1457-1465. doi: 10.5194/angeo-21-1457-2003
- Eastwood, J. P., Balogh, A., Lucek, E. A., Mazelle, C., & Dandouras, I. (2005, November). Quasi-monochromatic ULF foreshock waves as observed by the four-spacecraft Cluster mission: 1. Statistical properties. *Journal of Geophysical Research (Space Physics)*, *110*, 11219. doi: 10.1029/2004JA010617
- Eastwood, J. P., Balogh, A., Mazelle, C., Dandouras, I., & Rème, H. (n.d.). Oblique propagation of 30 s period fast magnetosonic foreshock waves: A Cluster case study. *Geophysical Research Letters*.
- Egeland, A., & Burke, W. J. (2012, August). The ring current: a short biography. *History of Geo- and Space Sciences*, *3*, 131-142. doi: 10.5194/hgss-3-131-2012
- Eriksson, S., Hasegawa, H., Teh, W.-L., Sonnerup, B. U. ., McFadden, J. P., Glassmeier, K.-H., ... Carlson, C. W. (2009). Magnetic island formation between large-scale flow vortices at an undulating postnoon magnetopause for northward interplanetary magnetic field. *Journal of Geophysical Research: Space Physics*, *114*(A1), n/a-n/a. Retrieved from <http://dx.doi.org/10.1029/2008JA013505> (A00C17) doi: 10.1029/2008JA013505
- Eriksson, S., Lavraud, B., Wilder, F. D., Stawarz, J. E., Giles, B. L., Burch, J. L., ... Goodrich, K. A. (2016). Magnetospheric multiscale observations of magnetic reconnection associated with kelvin-helmholtz waves. *Geophysical Research Letters*,

- 43(11), 5606–5615. Retrieved from <http://dx.doi.org/10.1002/2016GL068783> (2016GL068783) doi: 10.1002/2016GL068783
- Fairfield, D. H. (1967). The ordered magnetic field of the magnetosheath. *Journal of Geophysical Research*, 72(23), 5865–5877. Retrieved from <http://dx.doi.org/10.1029/JZ072i023p05865> doi: 10.1029/JZ072i023p05865
- Fairfield, D. H., Farrugia, C. J., Mukai, T., Nagai, T., & Fedorov, A. (2003, December). Motion of the dusk flank boundary layer caused by solar wind pressure changes and the Kelvin-Helmholtz instability: 10-11 January 1997. *Journal of Geophysical Research*, 108, 1460. doi: 10.1029/2003JA010134
- Fairfield, D. H., Otto, A., Mukai, T., Kokubun, S., Lepping, R. P., Steinberg, J. T., ... Yamamoto, T. (2000). Geotail observations of the Kelvin-Helmholtz instability at the equatorial magnetotail boundary for parallel northward fields. *Journal of Geophysical Research*, 105, 21159–21174. doi: 10.1029/1999JA000316
- Farrugia, C. J., Sandholt, P. E., & Burlaga, L. F. (1994, October). Auroral activity associated with Kelvin-Helmholtz instability at the inner edge of the low-latitude boundary layer. *Journal of Geophysical Research*, 99, 19. doi: 10.1029/94JA00926
- Fletcher, C. A. (1988). *Computational techniques for fluid dynamics 2*. New York, NY, USA: Springer-Verlag New York, Inc.
- Foullon, C., Verwichte, E., Nakariakov, V. M., Nykyri, K., & Farrugia, C. J. (2011, March). Magnetic Kelvin-Helmholtz Instability at the Sun. *Astrophys. J. Lett.*, 729, L8. doi: 10.1088/2041-8205/729/1/L8

-
- Foullon, C., Verwichte, E., Nykyri, K., Aschwanden, M. J., & Hannah, I. G. (2013, April). Kelvin-Helmholtz Instability of the CME Reconnection Outflow Layer in the Low Corona. *Astrophys. J.*, *767*, 170. doi: 10.1088/0004-637X/767/2/170
- Fujimoto, M., & Terasawa, T. (1994, May). Anomalous ion mixing within an MHD scale Kelvin-Helmholtz vortex. *Journal of Geophysical Research*, *99*, 8601-8613. doi: 10.1029/93JA02722
- Fujimoto, M., & Terasawa, T. (1995, July). Anomalous ion mixing within an MHD scale Kelvin-Helmholtz vortex. 2: Effects of inhomogeneity. *Journal of Geophysical Research*, *100*, 12025. doi: 10.1029/94JA02219
- Fujimoto, M., Terasawa, T., Mukai, T., Saito, Y., Yamamoto, T., & Kokubun, S. (1998, March). Plasma entry from the flanks of the near-Earth magnetotail: Geotail observations. *Journal of Geophysical Research*, *103*, 4391-4408. doi: 10.1029/97JA03340
- Ganguli, G., Slinker, S., Gavrishchaka, V., & Scales, W. (2002, May). Low frequency oscillations in a plasma with spatially variable field-aligned flow. *Physics of Plasmas*, *9*, 2321-2329. doi: 10.1063/1.1445181
- Ganguli, G., Tejero, E., Crabtree, C., Amatucci, W., & Rudakov, L. (2014, January). Generation of electromagnetic waves in the very low frequency band by velocity gradient. *Physics of Plasmas*, *21*(1), 012107. doi: 10.1063/1.4862032
- Hasegawa, A. (1976, October). Particle acceleration by MHD surface wave and formation of aurora. *Journal of Geophysical Research*, *81*, 5083-5090. doi: 10.1029/JA081i028p05083

-
- Hasegawa, A., & Chen, L. (1976, December). Kinetic processes in plasma heating by resonant mode conversion of Alfvén wave. *Physics of Fluids*, *19*, 1924-1934. doi: 10.1063/1.861427
- Hasegawa, A., & Mima, K. (1978, March). Anomalous transport produced by kinetic Alfvén wave turbulence. *Journal of Geophysical Research*, *83*, 1117-1123. doi: 10.1029/JA083iA03p01117
- Hasegawa, H., Fujimoto, M., Maezawa, K., Saito, Y., & Mukai, T. (2003, April). Geotail observations of the dayside outer boundary region: Interplanetary magnetic field control and dawn-dusk asymmetry. *Journal of Geophysical Research (Space Physics)*, *108*, 1163. doi: 10.1029/2002JA009667
- Hasegawa, H., Fujimoto, M., Phan, T.-D., Rème, H., Balogh, A., Dunlop, M. W., . . . TanDokoro, R. (2004, August). Transport of solar wind into Earth's magnetosphere through rolled-up Kelvin-Helmholtz vortices. *Letters to Nature*, *430*, 755-758. doi: 10.1038/nature02799
- Hasegawa, H., Fujimoto, M., Saito, Y., & Mukai, T. (2004, March). Dense and stagnant ions in the low-latitude boundary region under northward interplanetary magnetic field. *Geophysical Research Letters*, *31*, 6802. doi: 10.1029/2003GL019120
- Hasegawa, H., Fujimoto, M., Takagi, K., Rème, H., Saito, Y., & Mukai, T. (2005, December). Detection of Rolled-up Kelvin-Helmholtz Vortices From Single-Spacecraft Data. *AGU Fall Meeting Abstracts*, A3.
- Hasegawa, H., Fujimoto, M., Takagi, K., Saito, Y., Mukai, T., & Rème, H. (2006, September). Single-spacecraft detection of rolled-up Kelvin-Helmholtz vortices at

-
- the flank magnetopause. *Journal of Geophysical Research (Space Physics)*, *111*, 9203-+. doi: 10.1029/2006JA011728
- Hasegawa, H., Retinò, A., Vaivads, A., Khotyaintsev, Y., André, M., Nakamura, T. K. M., ... Canu, P. (2009, December). Kelvin-Helmholtz waves at the Earth's magnetopause: Multiscale development and associated reconnection. *Journal of Geophysical Research (Space Physics)*, *114*, 12207. doi: 10.1029/2009JA014042
- Henry, Z., Nykyri, K., Dimmock, A., & Moore, T. (2017). On the dawn-dusk asymmetry of the Kelvin-Helmholtz instability: THEMIS observations. *Journal of Geophysical Research*, in preparation.
- Hietala, H., Drake, J. F., Phan, T. D., Eastwood, J. P., & McFadden, J. P. (2015). Ion temperature anisotropy across a magnetotail reconnection jet. *Geophysical Research Letters*, *42*(18), 7239–7247. Retrieved from <http://dx.doi.org/10.1002/2015GL065168> (2015GL065168) doi: 10.1002/2015GL065168
- Holzer, R. E., Mcleod, M. G., & Smith, E. J. (1966). Preliminary results from the ogo 1 search coil magnetometer: Boundary positions and magnetic noise spectra. *Journal of Geophysical Research*, *71*(5), 1481–1486. Retrieved from <http://dx.doi.org/10.1029/JZ071i005p01481> doi: 10.1029/JZ071i005p01481
- Hones, E. W., Jr., Higbie, P. R., & Palmer, I. D. (1976, August). Energetic protons of magnetospheric origin in the plasma sheet associated with substorms. *Journal of Geophysical Research*, *81*, 3866–3874. doi: 10.1029/JA081i022p03866

- Horton, W., Perez, J. C., Carter, T., & Bengtson, R. (2005, February). Vorticity probes and the characterization of vortices in the Kelvin-Helmholtz instability in the large plasma device experiment. *Physics of Plasmas*, *12*(2), 022303. doi: 10.1063/1.1830489
- Hwang, K.-J., Kuznetsova, M. M., Sahraoui, F., Goldstein, M. L., Lee, E., & Parks, G. K. (2011, August). Kelvin-Helmholtz waves under southward interplanetary magnetic field. *Journal of Geophysical Research (Space Physics)*, *116*, 8210. doi: 10.1029/2011JA016596
- Johnson, J. R., & Cheng, C. Z. (1997, June). Kinetic Alfvén waves and plasma transport at the magnetopause. *Geophysical Research Letters*, *24*, 1423-1426. doi: 10.1029/97GL01333
- Johnson, J. R., & Cheng, C. Z. (2001, December). Stochastic ion heating at the magnetopause due to kinetic Alfvén waves. *Geophysical Research Letters*, *28*, 4421-4424. doi: 10.1029/2001GL013509
- Johnson, J. R., Cheng, C. Z., & Song, P. (2001, January). Signatures of Mode Conversion and Kinetic Alfvén Waves at the Magnetopause. *Geophysical Research Letters*, *28*, 227-230. doi: 10.1029/2000GL012048
- Johnson, J. R., & Wing, S. (2009, September). Northward interplanetary magnetic field plasma sheet entropies. *Journal of Geophysical Research (Space Physics)*, *114*, A00D08. doi: 10.1029/2008JA014017
- Juusola, L. (2015). *Multipole model of the earth's magnetic field*. University Lecture. Retrieved from

-
- http://helios.fmi.fi/~juusola1/geomagnetism/Lectures/Chapter4_multipole.pdf
- Kavosi, S., & Raeder, J. (2015). Ubiquity of Kelvin-Helmholtz waves at Earth's magnetopause. *Nature Commun*, *6*, 7019. doi: doi:10.1038/ncomms8019
- Kavosi, S., & Raeder, J. (2015, 05 11). Ubiquity of kelvin-helmholtz waves at earth's magnetopause. *Nature Communications*, *6*. Retrieved from <http://dx.doi.org/10.1038/ncomms8019>
- Khrabrov, A. V., & Sonnerup, B. U. Ö. (1998, June). *Magnetic variance analysis for small-amplitude waves and flux transfer events on a current sheet* (Vol. 103). doi: 10.1029/98JA00615
- King, J. H., & Papitashvili, N. E. (2005, February). Solar wind spatial scales in and comparisons of hourly Wind and ACE plasma and magnetic field data. *Journal of Geophysical Research (Space Physics)*, *110*, 2104. doi: 10.1029/2004JA010649
- Kivelson, M. G., & Russell, C. T. (1995). *Introduction to Space Physics*.
- Korotova, G. I., Sibeck, D. G., & Rosenberg, T. (2009, January). Geotail observations of FTE velocities. *Annales Geophysicae*, *27*, 83-92. doi: 10.5194/angeo-27-83-2009
- Krauss-Varban, D., Omidi, N., & Quest, K. B. (1994, April). Mode properties of low-frequency waves: Kinetic theory versus Hall-MHD. *Journal of Geophysical Research*, *99*, 5987-6009. doi: 10.1029/93JA03202
- Lavraud, B., Thomsen, M. F., Taylor, M. G. G. T., Wang, Y. L., Phan, T. D., Schwartz, S. J., ... Balogh, A. (2005, June). Characteristics of the magnetosheath

- electron boundary layer under northward interplanetary magnetic field: Implications for high-latitude reconnection. *Journal of Geophysical Research (Space Physics)*, *110*, 6209. doi: 10.1029/2004JA010808
- Lee, L. C., Johnson, J. R., & Ma, Z. W. (1994, September). Kinetic Alfvén waves as a source of plasma transport at the dayside magnetopause. *Journal of Geophysical Research*, *99*, 17405. doi: 10.1029/94JA01095
- Lembege, B., Ratliff, S. T., Dawson, J. M., & Ohsawa, Y. (1983, July). Ion heating and acceleration by strong magnetosonic waves. *Physical Review Letters*, *51*, 264-267. doi: 10.1103/PhysRevLett.51.264
- Lessard, M. R., Hudson, M. K., & Lühr, H. (1999, March). A statistical study of Pc3-Pc5 magnetic pulsations observed by the AMPTE/Ion Release Module satellite. *Journal of Geophysical Research*, *104*, 4523-4538. doi: 10.1029/1998JA900116
- Li, W., Raeder, J., Dorelli, J., Øieroset, M., & Phan, T. D. (2005, April). Plasma sheet formation during long period of northward IMF. *Geophysical Research Letters*, *32*, 12. doi: 10.1029/2004GL021524
- Lockwood, M., & Wild, M. N. (1993). On the quasi-periodic nature of magnetopause flux transfer events. *Journal of Geophysical Research: Space Physics*, *98*(A4), 5935-5940. Retrieved from <http://dx.doi.org/10.1029/92JA02375> doi: 10.1029/92JA02375
- London, I. C. (2009). *Discovery of the 'travelling magnetopause erosion region'*. Retrieved 2017-04-12, from

- <https://www.ucl.ac.uk/mssl/space-plasma-physics/nuggets/mssl-plasma-nuggets/owen>
- Longmore, M., Schwartz, S. J., Geach, J., Cooling, B. M. A., Dandouras, I., Lucek, E. A., & Fazakerley, A. N. (2005, November). Dawn-dusk asymmetries and sub-Alfvénic flow in the high and low latitude magnetosheath. *Annales Geophysicae*, *23*, 3351-3364. doi: 10.5194/angeo-23-3351-2005
- Luhmann, J. G., Russell, C. T., & Elphic, R. C. (1986, February). Spatial distributions of magnetic field fluctuations in the dayside magnetosheath. *Journal of Geophysical Research*, *91*, 1711-1715. doi: 10.1029/JA091iA02p01711
- Lui, A. T. Y., Venkatesan, D., & Murphree, J. S. (1989, May). Auroral bright spots on the dayside oval. *Journal of Geophysical Research*, *94*, 5515-5522. doi: 10.1029/JA094iA05p05515
- Ma, X., & Otto, A. (2014). Nonadiabatic heating in magnetic reconnection. *Journal of Geophysical Research: Space Physics*, *119*(7), 5575–5588. Retrieved from <http://dx.doi.org/10.1002/2014JA019856> doi: 10.1002/2014JA019856
- Ma, X., Otto, A., & Delamere, P. A. (2014, February). Interaction of magnetic reconnection and Kelvin-Helmholtz modes for large magnetic shear: 1. Kelvin-Helmholtz trigger. *Journal of Geophysical Research (Space Physics)*, *119*, 781-797. doi: 10.1002/2013JA019224
- Mann, I. R., Wright, A. N., Mills, K. J., & Nakariakov, V. M. (1999, January). Excitation of magnetospheric waveguide modes by magnetosheath flows. *J. Geophys. Res.*, *104*, 333-354. doi: 10.1029/1998JA900026

- Masters, A., Achilleos, N., Kivelson, M. G., Sergis, N., Dougherty, M. K., Thomsen, M. F., ... Coates, A. J. (2010, July). Cassini observations of a Kelvin-Helmholtz vortex in Saturn's outer magnetosphere. *Journal of Geophysical Research (Space Physics)*, *115*, 7225. doi: 10.1029/2010JA015351
- McPherron, R. L. (1991). Physical processes producing magnetospheric substorms and magnetic storms. In J. A. Jacobs (Ed.), *Geomagnetism* (Vol. 4, p. 593-739).
- Meredith, N. P., Horne, R. B., & Anderson, R. R. (2008, June). Survey of magnetosonic waves and proton ring distributions in the Earth's inner magnetosphere. *Journal of Geophysical Research (Space Physics)*, *113*, 6213. doi: 10.1029/2007JA012975
- Min, K., & Liu, K. (2015, April). Fast magnetosonic waves driven by shell velocity distributions. *Journal of Geophysical Research (Space Physics)*, *120*, 2739-2753. doi: 10.1002/2015JA021041
- Miura, A. (1987, April). Simulation of Kelvin-Helmholtz instability at the magnetospheric boundary. *Journal of Geophysical Research*, *92*, 3195-3206. doi: 10.1029/JA092iA04p03195
- Miura, A., & Pritchett, P. L. (1982, September). Nonlocal stability analysis of the MHD Kelvin-Helmholtz instability in a compressible plasma. *Journal of Geophysical Research*, *87*, 7431-7444. doi: 10.1029/JA087iA09p07431
- Moore, T. W. (2012). *Identifying Signatures of Plasma Waves and Reconnection Associated with Kelvin-Helmholtz Activity* (Unpublished master's thesis). Embry-Riddle Aeronautical University, U.S.A..

-
- Moore, T. W., Nykyri, K., & Dimmock, A. P. (2016, 09 05). Cross-scale energy transport in space plasmas. *Nat Phys, advance online publication*, -. Retrieved from <http://dx.doi.org/10.1038/nphys3869>
- Nakamura, T. K., Hayashi, D., Fujimoto, M., & Shinohara, I. (2004, April). Decay of MHD-Scale Kelvin-Helmholtz Vortices Mediated by Parasitic Electron Dynamics. *Physical Review Letters*, *92*(14), 145001. doi: 10.1103/PhysRevLett.92.145001
- Ness, N. F., & Wilcox, J. M. (1965). Sector structure of the quiet interplanetary magnetic field. *Science*, *148*(3677), 1592–1594. Retrieved from <http://science.sciencemag.org/content/148/3677/1592> doi: 10.1126/science.148.3677.1592
- Nishida, A., & Nagayama, N. (1973). Synoptic survey for the neutral line in the magnetotail during the substorm expansion phase. *Journal of Geophysical Research*, *78*, 3782. doi: 10.1029/JA078i019p03782
- Nishino, M. N., Fujimoto, M., Terasawa, T., Ueno, G., Maezawa, K., Mukai, T., & Saito, Y. (2007, June). Temperature anisotropies of electrons and two-component protons in the dusk plasma sheet. *Annales Geophysicae*, *25*, 1417-1432. doi: 10.5194/angeo-25-1417-2007
- Nishino, M. N., Fujimoto, M., Ueno, G., Mukai, T., & Saito, Y. (2007, October). Origin of temperature anisotropies in the cold plasma sheet: Geotail observations around the Kelvin-Helmholtz vortices. *Annales Geophysicae*, *25*, 2069-2086. doi: 10.5194/angeo-25-2069-2007

-
- Němeček, Z., afrnkov, J., Zastenker, G., Pioft, P., & Jelnek, K. (2002). Low-frequency variations of the ion flux in the magnetosheath. *Planetary and Space Science*, 50(56), 567 - 575. doi: [http://dx.doi.org/10.1016/S0032-0633\(02\)00036-3](http://dx.doi.org/10.1016/S0032-0633(02)00036-3)
- Nykyri, K. (2011). *Plasma waves*. University Lecture.
- Nykyri, K. (2013, August). Impact of MHD shock physics on magnetosheath asymmetry and Kelvin-Helmholtz instability. *Journal of Geophysical Research (Space Physics)*, 118, 5068-5081. doi: 10.1002/jgra.50499
- Nykyri, K. (2017). Impact of magnetosheath fluctuations on the KHI and reconnection produced by KHI. *Journal of Geophysical Research*, in preparation.
- Nykyri, K., Cargill, P. J., Lucek, E. A., Horbury, T. S., Balogh, A., Lavraud, B., ... Rème, H. (2003, December). Ion cyclotron waves in the high altitude cusp: CLUSTER observations at varying spacecraft separations. *Geophysical Research Letters*, 30, 2263. doi: 10.1029/2003GL018594
- Nykyri, K., & Dimmock, A. (2016). Statistical study of the ulf pc4-pc5 range fluctuations in the vicinity of earths magnetopause and correlation with the low latitude boundary layer thickness. *Advances in Space Research*, -. Retrieved from <http://www.sciencedirect.com/science/article/pii/S0273117716000065>
doi: <http://dx.doi.org/10.1016/j.asr.2015.12.046>
- Nykyri, K., Dimmock, A. P., Pulkkinen, T. I., Otto, A., & Ma, X. (2016, October). Impact of Magnetosheath Velocity Fluctuations on Kelvin-Helmholtz Instability. *in preparation for Journal of Geophysical Research (Space Physics)*, in preparation.

- Nykyri, K., & Foullon, C. (2013, August). First magnetic seismology of the CME reconnection outflow layer in the low corona with 2.5-D MHD simulations of the Kelvin-Helmholtz instability. *Geophys. Res. Lett.*, *40*, 4154-4159. doi: 10.1002/grl.50807
- Nykyri, K., & Otto, A. (2001, September). Plasma transport at the magnetospheric boundary due to reconnection in Kelvin-Helmholtz vortices. *Geophysical Research Letters*, *28*, 3565-3568. doi: 10.1029/2001GL013239
- Nykyri, K., & Otto, A. (2004, March). Influence of the Hall term on KH instability and reconnection inside KH vortices. *Annales Geophysicae*, *22*, 935-949. doi: 10.5194/angeo-22-935-2004
- Nykyri, K., Otto, A., Adamson, E., Dougal, E., & Mumme, J. (2011, March). Cluster observations of a cusp diamagnetic cavity: Structure, size, and dynamics. *Journal of Geophysical Research (Space Physics)*, *116*, 3228. doi: 10.1029/2010JA015897
- Nykyri, K., Otto, A., Lavraud, B., Mouikis, C., Kistler, L. M., Balogh, A., & Rème, H. (2006, October). Cluster observations of reconnection due to the Kelvin-Helmholtz instability at the dawnside magnetospheric flank. *Annales Geophysicae*, *24*, 2619-2643. doi: 10.5194/angeo-24-2619-2006
- Øieroset, M., Raeder, J., Phan, T. D., Wing, S., McFadden, J. P., Li, W., ... Balogh, A. (2005, April). Global cooling and densification of the plasma sheet during an extended period of purely northward IMF on October 22-24, 2003. *Geophysical Research Letters*, *32*, 12. doi: 10.1029/2004GL021523

-
- Ongena, J., Koch, R., Wolf, R., & Zohm, H. (2016, 05). Magnetic-confinement fusion. *Nat Phys*, *12*(5), 398–410.
- Otto, A. (1990, May). 3D resistive MHD computations of magnetospheric physics. *Computer Physics Communications*, *59*, 185-195. doi: 10.1016/0010-4655(90)90168-Z
- Otto, A., & Fairfield, D. H. (2000). Kelvin-Helmholtz instability at the magnetotail boundary: MHD simulation and comparison with Geotail observations. *Journal of Geophysical Research*, *105*, 21175-21190. doi: 10.1029/1999JA000312
- Otto, A., & Nykyri, K. (2003). Kelvin-Helmholtz instability and magnetic reconnection: Mass transport at the LLBL. *Washington DC American Geophysical Union Geophysical Monograph Series*, *133*, 53-62. doi: 10.1029/133GM05
- Palermo, F., Faganello, M., Califano, F., & Pegoraro, F. (2011, June). Kelvin-Helmholtz vortices and secondary instabilities in super-magnetosonic regimes. *Annales Geophysicae*, *29*, 1169-1178. doi: 10.5194/angeo-29-1169-2011
- Parker, E. N. (1958, November). Dynamics of the Interplanetary Gas and Magnetic Fields. *The Astrophysical Journal*, *128*, 664. doi: 10.1086/146579
- Paschmann, G., & Daly, P. W. (1998). Analysis Methods for Multi-Spacecraft Data. ISSI Scientific Reports Series SR-001, ESA/ISSI, Vol. 1. ISBN 1608-280X, 1998. *ISSI Scientific Reports Series*, *1*.
- Paschmann, G., Haerendel, G., Papamastorakis, I., Sckopke, N., Bame, S. J., Gosling, J. T., & Russell, C. T. (1982, April). Plasma and magnetic field characteristics

- of magnetic flux transfer events. *Journal of Geophysical Research*, *87*, 2159-2168.
doi: 10.1029/JA087iA04p02159
- Paschmann, G., Papamastorakis, I., Sckopke, N., Haerendel, G., Sonnerup, B. U. O., Bame, S. J., ... Elphic, R. C. (1979, November). Plasma acceleration at the earth's magnetopause - Evidence for reconnection. *Nature*, *282*, 243-246. doi: 10.1038/282243a0
- Paularena, K. I., Richardson, J. D., Kolpak, M. A., Jackson, C. R., & Siscoe, G. L. (2001, November). A dawn-dusk density asymmetry in Earth's magnetosheath. *Journal of Geophysical Research*, *106*, 25377-25394. doi: 10.1029/2000JA000177
- Peñano, J. R., & Ganguli, G. (1999, August). Ionospheric Source for Low-Frequency Broadband Electromagnetic Signatures. *Physical Review Letters*, *83*, 1343-1346. doi: 10.1103/PhysRevLett.83.1343
- Peñano, J. R., & Ganguli, G. (2000, April). Generation of ELF electromagnetic waves in the ionosphere by localized transverse dc electric fields: Subcyclotron frequency regime. *Journal of Geophysical Research*, *105*, 7441-7458. doi: 10.1029/1999JA000303
- Peñano, J. R., & Ganguli, G. (2002, February). Correction to "Generation of ELF electromagnetic waves in the ionosphere by localized transverse dc electric fields: Subcyclotron frequency regime" by J. R. Peñano and G. Ganguli. *Journal of Geophysical Research (Space Physics)*, *107*, 1031. doi: 10.1029/2001JA000280
- Perraut, S., Roux, A., Robert, P., Gendrin, R., Sauvaud, J.-A., Bosqued, J.-M., ... Korth, A. (1982, August). A systematic study of ULF waves above F/H plus/ from

- GEOS 1 and 2 measurements and their relationships with proton ring distributions. *Journal of Geophysical Research*, *87*, 6219-6236. doi: 10.1029/JA087iA08p06219
- Pope, S. A., Balikhin, M. A., Zhang, T. L., Fedorov, A. O., Gedalin, M., & Barabash, S. (2009, April). Giant vortices lead to ion escape from Venus and re-distribution of plasma in the ionosphere. *Geophysical Research Letter*, *36*, 7202. doi: 10.1029/2008GL036977
- Potter. (1973). *Computational Physics* (John Wiley, Ed.).
- Pu, Z.-Y., & Kivelson, M. G. (1983, February). Kelvin-Helmholtz instability at the magnetopause. I - Solution for compressible plasmas. II - Energy flux into the magnetosphere. *Journal of Geophysical Research*, *88*, 841-861. doi: 10.1029/JA088iA02p00841
- Pu, Z. Y., Yei, M., & Liu, Z. X. (1990). Generation of vortex-induced tearing mode instability at the magnetopause. *Journal of Geophysical Research: Space Physics*, *95*(A7), 10559–10566. Retrieved from <http://dx.doi.org/10.1029/JA095iA07p10559> doi: 10.1029/JA095iA07p10559
- Retino, A. (2016, 12). Space plasmas: A journey through scales. *Nat Phys*, *12*(12), 1092–1093. Retrieved from <http://dx.doi.org/10.1038/nphys3976>
- Rezeau, L., Morane, A., Perraut, S., Roux, A., & Schmidt, R. (1989, January). Characterization of Alfvénic fluctuations in the magnetopause boundary layer. *Journal of Geophysical Research*, *94*, 101-110. doi: 10.1029/JA094iA01p00101

-
- Roennmark, K. (1982, June). *Waves in homogeneous, anisotropic multicomponent plasmas (WHAMP)* (Tech. Rep.).
- Rossi, C., Califano, F., Retinò, A., Sorriso-Valvo, L., Henri, P., Servidio, S., . . . Rezeau, L. (2015). Two-fluid numerical simulations of turbulence inside kelvin-helmholtz vortices: Intermittency and reconnecting current sheets. *Physics of Plasmas*, *22*(12). doi: <http://dx.doi.org/10.1063/1.4936795>
- Runov, A., Angelopoulos, V., Sitnov, M. I., Sergeev, V. A., Bonnell, J., McFadden, J. P., . . . Auster, U. (2009). Themis observations of an earthward-propagating dipolarization front. *Geophysical Research Letters*, *36*(14), n/a–n/a. Retrieved from <http://dx.doi.org/10.1029/2009GL038980> (L14106) doi: 10.1029/2009GL038980
- Russell, C. T. (1971). Geophysical coordinate transformations. *Cosmic Electrodynamics*, *2*, 184-196.
- Russell, C. T., & Elphic, R. C. (1978, December). Initial ISEE magnetometer results - Magnetopause observations. *Space Science Reviews*, *22*, 681-715. doi: 10.1007/BF00212619
- Russell, C. T., & Elphic, R. C. (1979). Isee observations of flux transfer events at the dayside magnetopause. *Geophysical Research Letters*, *6*(1), 33–36. Retrieved from <http://dx.doi.org/10.1029/GL006i001p00033> doi: 10.1029/GL006i001p00033
- Russell, C. T., Le, G., & Kuo, H. (1996). The occurrence rate of flux transfer events. *Advances in Space Research*, *18*, 197-205. doi: 10.1016/0273-1177(95)00965-5

-
- Russell, C. T., Petrinec, S. M., Zhang, T. L., Song, P., & Kawano, H. (1997). The effect of foreshock on the motion of the dayside magnetopause. *Geophysical Research Letters*, *24*, 1439-1441. doi: 10.1029/97GL01408
- Shevyrev, N. N., & Zastenker, G. N. (2005, January). Some features of the plasma flow in the magnetosheath behind quasi-parallel and quasi-perpendicular bow shocks. *Planetary and Space Science*, *53*, 95-102. doi: 10.1016/j.pss.2004.09.033
- Shevyrev, N. N., Zastenker, G. N., & Du, J. (2007, December). Statistics of low-frequency variations in solar wind, foreshock and magnetosheath: INTERBALL-1 and CLUSTER data. *Planetary and Space Science*, *55*, 2330-2335. doi: 10.1016/j.pss.2007.05.014
- Shevyrev, N. N., Zastenker, G. N., Eiges, P. E., & Richardson, J. D. (2006). Low frequency waves observed by Interball-1 in foreshock and magnetosheath. *Advances in Space Research*, *37*, 1516-1521. doi: 10.1016/j.asr.2005.07.072
- Siscoe, G. L., Davis, L., Smith, E. J., Coleman, P. J., & Jones, D. E. (1967). Magnetic fluctuations in the magnetosheath: Mariner 4. *Journal of Geophysical Research*, *72*(1), 1-17. Retrieved from <http://dx.doi.org/10.1029/JZ072i001p00001> doi: 10.1029/JZ072i001p00001
- Sonett, C. P., Judge, D. L., Sims, A. R., & Kelso, J. M. (1960). A radial rocket survey of the distant geomagnetic field. *Journal of Geophysical Research*, *65*(1), 55-68. Retrieved from <http://dx.doi.org/10.1029/JZ065i001p00055> doi: 10.1029/JZ065i001p00055

- Sonnerup, B. U. O., & Cahill, L. J., Jr. (1967, January). Magnetopause Structure and Attitude from Explorer 12 Observations. *J. Geophys. Res.*, *72*, 171. doi: 10.1029/JZ072i001p00171
- Sonnerup, B. U. O., Paschmann, G., Papamastorakis, I., Sckopke, N., Haerendel, G., Bame, S. J., ... Russell, C. T. (1981, November). Evidence for magnetic field reconnection at the earth's magnetopause. *Journal of Geophysical Research*, *86*, 10049-10067. doi: 10.1029/JA086iA12p10049
- Sonnerup, B. U. Ö., & Scheible, M. (1998). Minimum and Maximum Variance Analysis. *ISSI Scientific Reports Series*, *1*, 185-220.
- Stasiewicz, K., Bellan, P., Chaston, C., Kletzing, C., Lysak, R., Maggs, J., ... Wahlund, J.-E. (2000, May). Small Scale Alfvénic Structure in the Aurora. *Space Science Reviews*, *92*, 423-533.
- Stenuit, H., Fujimoto, M., Fuselier, S. A., Sauvaud, J.-A., Wing, S., Fedorov, A., ... Pedersen, A. (2002, October). Multispacecraft study on the dynamics of the dusk-flank magnetosphere under northward IMF: 10-11 January 1997. *Journal of Geophysical Research (Space Physics)*, *107*, 1333. doi: 10.1029/2002JA009246
- Stix, T. H. (1992). *Waves in plasmas*.
- Sundberg, T., Boardsen, S. A., Slavin, J. A., Anderson, B. J., Korth, H., Zurbuchen, T. H., ... Solomon, S. C. (2012, April). MESSENGER orbital observations of large-amplitude Kelvin-Helmholtz waves at Mercury's magnetopause. *Journal of Geophysical Research (Space Physics)*, *117*, 4216. doi: 10.1029/2011JA017268

-
- Taylor, M. G. G. T., Hasegawa, H., Lavraud, B., Phan, T., Escoubet, C. P., Dunlop, M. W., ... Wild, J. A. (2012). Spatial distribution of rolled up kelvin-helmholtz vortices at earth's dayside and flank magnetopause. *Annales Geophysicae*, *30*(6), 1025–1035. Retrieved from <http://www.ann-geophys.net/30/1025/2012/> doi: 10.5194/angeo-30-1025-2012
- Taylor, M. G. G. T., Hasegawa, H., Lavraud, B., Phan, T., Escoubet, C. P., Dunlop, M. W., ... Wild, J. A. (2012, June). Spatial distribution of rolled up Kelvin-Helmholtz vortices at Earth's dayside and flank magnetopause. *Annales Geophysicae*, *30*, 1025-1035. doi: 10.5194/angeo-30-1025-2012
- Taylor, M. G. G. T., & Lavraud, B. (2008, June). Observation of three distinct ion populations at the Kelvin-Helmholtz-unstable magnetopause. *Annales Geophysicae*, *26*, 1559-1566. doi: 10.5194/angeo-26-1559-2008
- Taylor, M. G. G. T., Lavraud, B., Escoubet, C. P., Milan, S. E., Nykyri, K., Dunlop, M. W., ... Zhang, T. L. (2008). The plasma sheet and boundary layers under northward IMF: A multi-point and multi-instrument perspective. *Advances in Space Research*, *41*, 1619-1629. doi: 10.1016/j.asr.2007.10.013
- Tejero, E. M., Amatucci, W. E., Ganguli, G., Cothran, C. D., Crabtree, C., & Thomas, E., Jr. (2011, May). Spontaneous Electromagnetic Emission from a Strongly Localized Plasma Flow. *Physical Review Letters*, *106*(18), 185001. doi: 10.1103/PhysRevLett.106.185001
- Terasawa, T., Fujimoto, M., Mukai, T., Shinohara, I., Saito, Y., Yamamoto, T., ... Lepping, R. P. (1997). Solar wind control of density and temperature in the

-
- near-Earth plasma sheet: WIND/GEOTAIL collaboration. *Geophysical Research Letters*, *24*, 935-938. doi: 10.1029/96GL04018
- Terasawa, T., & Nambu, M. (1989a, May). Ion heating and acceleration by magnetosonic waves via cyclotron subharmonic resonance. *Geophysical Research Letters*, *16*, 357-360. doi: 10.1029/GL016i005p00357
- Terasawa, T., & Nambu, M. (1989b, May). Ion heating and acceleration by magnetosonic waves via cyclotron subharmonic resonance. *Geophysical Research Letters*, *16*, 357-360. doi: 10.1029/GL016i005p00357
- Treumann, R., & Baumjohann, W. (1997). *Advanced space plasma physics*. Imperial College Press.
- University, B. (2017). *Physics of aurorae*. Retrieved 2017-01-27, from <http://www.bu.edu/csp/PASS/science/aurora.html>
- Walker, S. N., Balikhin, M. A., Shklyar, D. R., Yearby, K. H., Canu, P., Carr, C. M., & Dandouras, I. (2015). Experimental determination of the dispersion relation of magnetosonic waves. *Journal of Geophysical Research: Space Physics*, n/a–n/a. Retrieved from <http://dx.doi.org/10.1002/2015JA021746> (2015JA021746) doi: 10.1002/2015JA021746
- Walsh, B. (2014). Magnetopause boundary conditions and modes of SW-M coupling. In *Geospace environment modelling summer workshop*. Portsmouth, Virginia.
- Walsh, B. M., Sibeck, D. G., Wang, Y., & Fairfield, D. H. (2012). Dawn-dusk asymmetries in the earth's magnetosheath. *Journal of Geophysical Research: Space Physics*, *117*(A12). doi: 10.1029/2012JA018240

- Wang, C.-P., Gkioulidou, M., Lyons, L. R., & Angelopoulos, V. (2012). Spatial distributions of the ion to electron temperature ratio in the magnetosheath and plasma sheet. *Journal of Geophysical Research: Space Physics*, *117*(A8), n/a–n/a. Retrieved from <http://dx.doi.org/10.1029/2012JA017658> (A08215) doi: 10.1029/2012JA017658
- Wing, S., Johnson, J. R., & Fujimoto, M. (2006, December). Timescale for the formation of the cold-dense plasma sheet: A case study. *Geophysical Research Letters*, *33*, 23106. doi: 10.1029/2006GL027110
- Wing, S., Johnson, J. R., Newell, P. T., & Meng, C.-I. (2005, August). Dawn-dusk asymmetries, ion spectra, and sources in the northward interplanetary magnetic field plasma sheet. *Journal of Geophysical Research (Space Physics)*, *110*, 8205. doi: 10.1029/2005JA011086
- Wing, S., & Newell, P. T. (2002). 2d plasma sheet ion density and temperature profiles for northward and southward imf. *Geophysical Research Letters*, *29*(9), 21-1–21-4. Retrieved from <http://dx.doi.org/10.1029/2001GL013950> doi: 10.1029/2001GL013950
- Yan, G. Q., Mozer, F. S., Shen, C., Chen, T., Parks, G. K., Cai, C. L., & McFadden, J. P. (2014, July). Kelvin-Helmholtz vortices observed by THEMIS at the duskside of the magnetopause under southward interplanetary magnetic field. *Geophysical Research Letters*, *41*, 4427-4434. doi: 10.1002/2014GL060589
- Yao, Y., Chaston, C. C., Glassmeier, K.-H., & Angelopoulos, V. (2011, May). Electromagnetic waves on ion gyro-radii scales across the magnetopause. *Geophysical*

Research Letters, 38, 9102. doi: 10.1029/2011GL047328

Zastenker, G. N., Nozdrachev, M. N., Němeček, Z., Šafránková, J., Paularena, K. I., Richardson, J. D., ... Mukai, T. (2002, April). Multispacecraft measurements of plasma and magnetic field variations in the magnetosheath: Comparison with Spreiter models and motion of the structures. *Planetary and Space Science*, 50, 601-612. doi: 10.1016/S0032-0633(02)00039-9

Zieger, B., Retinò, A., Nakamura, R., Baumjohann, W., Vaivads, A., & Khotyaintsev, Y. (2011, November). Jet front-driven mirror modes and shocklets in the near-Earth flow-braking region. *Geophysical Research Letters*, 38, 22103. doi: 10.1029/2011GL049746